Efficient Error-Controllable High-Order Electromagnetic Modelling of Scattering on Electrically Large Targets with the Locally Corrected Nyström Method

by

Mohammad Shafieipour

A Thesis submitted to the Faculty of Graduate Studies of

The University of Manitoba

in partial fulfilment of the requirements of the degree of

DOCTOR OF PHILOSOPHY

Department of Electrical and Computer Engineering
University of Manitoba
Winnipeg, Manitoba, Canada

Abstract

This dissertation is about efficient computation of the electromagnetic fields with the locally corrected Nyström (LCN) method as a point-based boundary element method (BEM). The concept of surface integral equations is discussed and the electric field integral equation (EFIE) is derived from the Maxwell's equations. The basics of Rao-Wilton-Glisson (RWG) method-of-moments (MoM) and the LCN method are reviewed.

Due to its point-based nature, the LCN discretization of the EFIE has some advantages over discretizing the EFIE by the MoM which is an element-based (or basis-based) BEM. On the other hand, due to maturity of the MoM, a large body of work is available to resolve the numerical issues arising in MoM while there has been less work related to the relatively new LCN. To combine the benefits of the LCN method and the classical RWG MoM, equivalence between these BEMs are established and their exact relationships are derived. Both the vector-potential EFIE and the mixed-potential EFIE are covered.

Various aspects of achieving HO convergence to the correct answer using high-order (HO) LCN method are discussed. In particular, the patch size limitation, predicting the optimal degrees of freedom for a desired accuracy, and the effect of dynamic range in the solution are discussed both analytically and numerically to provide concrete motivations towards HO LCN.

The benefits of an HO BEM can not be realized unless an HO geometry representation is used in conjunction with the BEM. Non-uniform rational b-spline (NURBS) surfaces are the most widely adopted HO geometry modelling technique in various disciplines due to their many advantages. However, a typical mesh created out of NURBS surfaces contain both triangular and quadrilateral elements while formulating LCN based on Gaussian quadrature rules on triangular elements have limitations. A new class of Newton-Cotes quadrature rules for triangles is proposed to facilitate incorporating NURBS surfaces into the HO LCN.

Author's Publications

All publications prepared during this Ph.D. work have authors other than the author of this thesis (Mohammad Shafieipour). This is primarily because this research was preceded by a project during which the LCN solver based on [1] was developed and the same code was used in this research program as a base to implement and test the new contributions. As a result, in addition to the respective advisor (Prof. Vladimir Okhmatovski), Drs. Jeffrey and Aronsson were regularly consulted during this Ph.D. work. To honour these valuable discussions and the development of the original LCN code, these professionals are listed in almost all of the published work.

The author contributed to publishing the following work while pursuing the Ph.D. degree.

Articles in International Journals

1. **M. Shafieipour**, J. Aronsson, I. Jeffrey, C. Nui, and V. Okhmatovski, "On New Triangle Quadrature Rules for the Locally Corrected Nyström Method Formulated on NURBS Generated Bézier Surfaces in 3D," *IEEE Transactions on Antennas and Propagation*, Under Review.

2. **M. Shafieipour**, J. Aronsson, I. Jeffrey, and V. Okhmatovski, "Exact Relationship between the Locally Corrected Nyström Method and RWG Moment Method for the Mixed-Potential Integral Equation," *IEEE Transactions on Antennas and Propagation*,vol. 63, no. 11, pp. 4932-4943, November 2015.

3. **M. Shafieipour**, I. Jeffrey, J. Aronsson, and V. Okhmatovski, "On the Equivalence of RWG Method of Moments and the Locally Corrected Nyström Method for Solving the Electric Field Integral Equation," *IEEE Transactions on Antennas and Propagation*,vol. 62, no. 2, pp. 772-782, February 2014.

4. I. Jeffrey, J. Aronsson, **M. Shafieipour**, and V. Okhmatovski, "Error Controllable Solutions of Large Scale Problems in Electromagnetics: MLFMA Accel-

erated Locally Corrected Nyström Solutions of CFIE in 3D," *IEEE Antennas and Propagation Magazine*, vol. 55, no. 3, pp. 294-308, June 2013.

Articles in Conference Proceedings

1. **Mohammad Shafieipour**, Jonatan Aronsson, and Vladimir Okhmatovski, "On Error Controlled Computing of the Near Electromagnetic Fields in the Shade Regions of Electrically Large 3D Objects," *Intl. Symp. Electromagnetic Theory (EMTS),* Espoo, Finland. August 2016 (Accpeted).

2. **M. Shafieipour**, and V. Okhmatovski, "Error-Controlled Boundary Element Modeling of 3D Plasmonic Nano-Structures via Higher-Order Locally Corrected Nyström Method," *IEEE International Symposium on Antennas and Propagation and North American Radio Science Meeting,* Vancouver, BC, Canada, July 2015.

3. **M. Shafieipour**, J. Aronsson, C.Niu, I. Jeffrey, and V. Okhmatovski,"Error-Controllable Higher-Order Electromagnetic Analysis of Complex 3D Interconnects with Boundary Element Locally Corrected Nyström Method," *IEEE Workshop on Signal and Power Integrity,* Ghent, Belgium, May 2014.

4. Vladimir Okhmatovski, **Mohammad Shafieipour**, and Jonatan Aronsson,"New Era Algorithms and Supercomputers: Forging the Third Industrial Revolution," *G20 Youth Forum,* Garmisch-Partenkirchen, Germany, 7-11 May 2014.

5. **M. Shafieipour**, I. Jeffrey, J. Aronsson, and V. Okhmatovski, "Parallel Fast HO Solution of Large-Scale Scattering Problems via MLFMA Accelerated LCN discretization of MFIE," *Applied Computational Electromagnetic Society,* Monterey, CA, April 2013.

6. Jonatan Aronsson, **Mohammad Shafieipour**, and Vladimir Okhmatovski, "Study of Preconditioners For RWG MoM Analysis of Large Scale Scatterers Containing Junctions with Open Surfaces and Delta-Gap Voltage Sources," *Applied Computational Electromagnetic Society,* Columbus, OH, April 2012.

7. J. Aronsson, **M. Shafieipour**, and V. Okhmatovski, "Solution of large multiscale EMC problems with method of moments accelerated via low-frequency MLFMA," *IEEE Intl. Symp. Electromagnetic Compatibility,* Long Beanch, CA, August 2011.

Conference Abstracts

1. T. Killian, **M. Shafieipour**, V. Okhmatovski, M. Horn, D. Faircloth, I. Jeffrey, and J. Aronsson, "Large Scale Electromagnetic Scattering Problems Solved

Using The Locally Corrected Nyström Method and Adaptive Cross Approximation," *IEEE International Symposium on Antennas and Propagation and North American Radio Science Meeting,* Vancouver, BC, Canada, July 2015.

2. **M. Shafieipour**, C. Niu, and V. Okhmatovski, "Higher-Order Locally Corrected Nyström Solution of the Combined Field Integral Equation Based on Geometric Modelling with NURBS," *IEEE International Symposium on Antennas and Propagation and USNC-URSI Radio Science Meeting,* Memphis, Tennessee, July 2014.

3. **M. Shafieipour**, C. Niu, and V. Okhmatovski, "Accuracy Study of Low- and High-Order Numerical Techniques for Analysis of Scattering on Plasmonic Nanosphere at THz Frequencies," *IEEE International Symposium on Antennas and Propagation and USNC-URSI Radio Science Meeting,* Memphis, Tennessee, July 2014.

4. **M. Shafieipour**, I. Jeffrey, J. Aronsson, and V. Okhmatovski, "Point-based Discretization of the Mixed-Potential RWG MoM via the Nyström Method," *IEEE International Symposium on Antennas and Propagation and USNC-URSI Radio Science Meeting,* Memphis, Tennessee, July 2014.

5. D. Faircloth, T. Killian, M. Horn, **M. Shafieipour**, I. Jeffrey, J. Aronsson, and V. Okhmatovski, "Fast Direct Higher-Order Solution of Complex Large Scale Electromagnetic Scattering Problems via Locally Corrected Nyström Discretization of CFIE," *IEEE International Symposium on Antennas and Propagation and USNC-URSI Radio Science Meeting,* Memphis, Tennessee, July 2014.

6. **M. Shafieipour**, I. Jeffrey, J. Aronsson, and V. Okhmatovski, "Parallel Fast HO Solution of Large-Scale Scattering Problems via MLFMA Accelerated LCN discretization of EFIE," *IEEE International Symposium on Antennas and Propagation and USNC-URSI Radio Science Meeting,* Orlando, Florida, July 2013.

7. **M. Shafieipour** and V. Okhmatovski, "Current Continuity Enforcement in First Order Locally Corrected Nyström Method via RWG Moment Method," *IEEE International Symposium on Antennas and Propagation and USNC-URSI Radio Science Meeting,* Chicago, IL, July 2012.

Contributions

There are four scientific contributions included in this thesis. They are listed below.

Contribution #1 presented in Chapter 3: On the Equivalence of RWG Method of Moments and the Locally Corrected Nyström Method for Solving the Electric Field Integral Equation, *Reprint form IEEE Transactions on Antennas and Propagation. (Published)*

The equivalence of Rao-Wilton-Glisson (RWG) method-of-moments (MoM) and the first-order locally corrected Nyström (LCN) method is established. The resulting numerical scheme is a point-based discretization of the vector-potential electric field integral equation (EFIE) and is termed RWG-via-LCN. Due to the current continuity enforcing nature of the RWG basis functions, RWG-via-LCN ensures current continuity and produces more accurate results than the first-order LCN while forming a 4 times smaller and better conditioned matrix.

Contribution #2 presented in Chapter 4: Exact Relationship between the Locally Corrected Nyström Scheme and RWG Moment Method for the Mixed-Potential Integral Equation, *Reprint form IEEE Transactions on Antennas and Propagation. (Published)*

As an extension to the work presented in Chapter 3, the relationship between first- and zeroth-order LCN and the RWG MoM has been established and used to derive the current continuity enforcing point-based discretizaion of the mixed-potential (MP) EFIE. It is shown that in addition to the effect of current continuity enforcement on first-order LCN, analytical cancellation of line charge integrals appearing in the MP EFIE formulation, has a great impact on the accuracy of the resulting numerical method named MP RWG-via-LCN.

Contribution #3 presented in Chapter 5: On Achieving High-Order Convergence to the Correct Answer with the Locally Corrected Nysröm Method, *Appearing herein for the first time.*

The patch size limitation for the high-order (HO) LCN is explained based on the Nyquist criterion. It is shown that the patch size is not only limited by the frequency, but also the order of the discretization. Also, a new method for predicting the optimal number of unknowns for a desired accuracy in HO LCN is proposed. Finally, HO imperative in electromagnetic simulations has been demonstrated by analysing the analytical and numerical solutions of scattering from an electrically large sphere with large dynamic range in the solution using Mie series, RWG MoM and HO LCN.

Contribution #4 presented in Chapter 6: On New Triangle Quadrature Rules for the Locally Corrected Nyström Method Formulated on NURBS Generated Bézier Surfaces in 3D, *Reprint form IEEE Transactions on Antennas and Propagation (Under Review).*

It has been shown that incorporating non-uniform rational b-spline (NURBS) surfaces into boundary element methods (BEM) can increase the computational efficiency. In order to combine the LCN method with NURBS, the LCN method has to be formulated on both quadrilateral and triangular elements, as NURBS generated Bézier meshes include both triangular and quadrilateral elements. Formulating LCN on triangles has limitations due to the lack of LCN appropriate arbitrary order quadrature rules for triangles. A new family of quadrature rules for triangles has been proposed to be used in LCN for orders from 0 to 9, inclusively.

Acknowledgments

It is safe to say that without the support, expertise, enthusiasm, professionalism, ample knowledge, and comprehensive understanding of the subject, provided by my advisor Dr. Vladimir Okhmatovski, accomplishments presented in this dissertation would not have been possible. The privilege of being his graduate student for more than 4 years, not only taught me the concepts presented herein, but also changed my view as to how the mankind has accumulated knowledge and technology to shape the world to what we see today. Over the years, I am convinced that his scientific contributions might, and probably will, change the course of human development leading to a better future for us and the generations to come.

I would like to thank my internal (University of Manitoba) examining committee; Dr. Joe LoVetri and Dr. Bing-Chen Wang for their efforts in evaluating my Ph.D. work. I owe immense gratitude to Prof. LoVetri for reminding me at the very beginning of this research program that having a focused mindset towards graduation is very important. Now that I am preparing this thesis, I understand that this suggestion of his might be the best of suggestions when someone enters the not-so-smooth path of a Ph.D. program.

My external examiner Dr. Stephen D. Gedney from the University of Colorado fascinated me by his great comments, suggestions, and corrections. Although as the external examiner, he had a relatively short time to read and provide his feedback about the work, his contribution to improving the quality of the thesis can not be overlooked. So much so that I decided to add a section in the final chapter (Section 7.2) to preserve his feedback in its original form, while addressing the suggestions and corrections from my point-of-view.

Special thanks to my friends and colleagues; Dr. Jonatan Aronsson, Dr. Ian Jeffrey, Anton Menshov, Chen Nui, and Farhad Sheikhhossieni for their collaborations and support.

I would like to extend my thanks to the National Science and Engineering Research Council of Canada and University of Manitoba Faculty of Graduate Studies for fund-

ing my research. Also, special thanks to IERUS Technologies, Inc. and the CEM-Works, Inc. for their collaborations during this research. And of course, many thanks to Compute Canada for providing the computing resources at WestGrid throughout this research program.

Finally, I would like to thank my family for their support, emotionally as well as financially. My wife Leila, has always been my last resort of energy for overcoming difficulties in life.

Table of Contents

List of Figures

List of Tables

Chapter 1

Introduction

By *Mohammad Shafieipour* in partial fulfilment of the requirements of the degree of *Doctor of Philosophy (Ph.D.)*, March 2016.

1.1 Motivation

On May 16th, 2011, Human Rights Council of the United Nations General Assembly declared access to the Internet a basic human right that enables individuals to "exercise their right to freedom of opinion and expression" [2]. Such powerful statement by the UN would not have been possible without abundant production of efficient and easy-to-use electronic devices which owes its availability to rapid simulation of electromagnetic fields propagating in tiniest electronic chips to massive base stations. This example, among others, demonstrates that numerical techniques used to provide such simulations are an important part of today's human life. In this Ph.D. thesis we study existing and novel techniques for such numerical analysis, namely, computational electromagnetic (CEM) analysis of three-dimensional (3D) scattering problems.

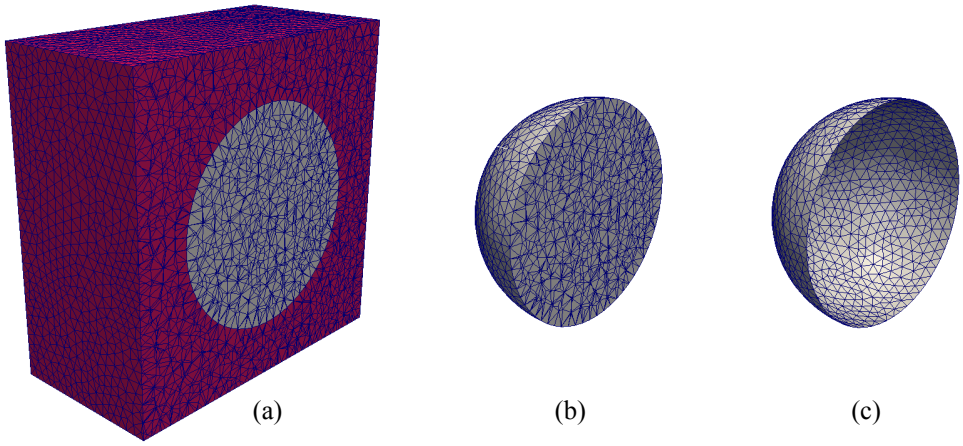

Figure 1.1: DE (a) vs. IE (b,c) discretizaion of a scattering problem which has a homogeneous (e.g. metallic) sphere as the scattering object in a homogeneous medium (e.g. free-space). a) is the cross section of the volumetric mesh that discretizes the object and the surrounding medium and can be used in DE techniques, b) is the cross section of the volumetric mesh that discretizes the object and can be used in volume IE techniques, c) is the cross section of the surface mesh that discretizes the boundary of the object and can be used in boundary element techniques.

1.1.1 Formulation

There are in general two types of formulations applicable to scattering problems; differential equation (DE) based formulations [3, 4] and integral equation (IE) based formulations [5]. While they both originate in Maxwell's equations, they have a fundamental difference in that DE based methods are formulated for the electromagnetic fields in the entire space while IE techniques involve unknown field quantities only on the surface of the scatterer or in its volume. These fields can then be used to evaluate the electromagnetic fields everywhere else. As a result, discretization of the DEs of CEM involves volume meshes including both the scatterer and the surrounding space (Fig 1.1.a) whereas the IE techniques only discretize the scatterer itself (Figs 1.1.b and 1.1.c). Furthermore, in solving DEs an electromagnetic field propagates from

point A to point B through discretized space. Thus in every step of the propagation a small amount of error is added to the solution leading to large phase errors in larger examples. Therefore, as the size of the problem is increased, denser discretizations are required to maintain the same error leading to even larger problem size. In contrast, in IE methods propagation of fields from point A to point B is performed using Green's functions which are commonly in the form of a closed-form and exact expression. Therefore, IE methods eliminate discretization dispersion errors to a large extent.

Form the above discussion, it is tempting to conclude that "in general" an IE method requires less computational resources (computational time and memory) to solve a given scattering problem than a DE technique would require for the same problem. This however, is not true for all cases. The reason for it is that in DEs the pertinent electromagnetic interactions are local in nature and lead to a sparse matrix equation as a result of discretization. Interactions in IEs, on the other hand, are global and result in a dense system of equations. Thus when solving a particular scattering problem, an IE method might end up using more computational resources than a DE technique as solving a dense matrix may become computationally more expensive than solving sparse matrix equation of a larger size. Besides, Green's function for a particular problem might not be available and deriving Green's functions can lead to complicated mathematical challenges (e.g. in inhomogeneous and/or nonlinear media). Nevertheless, DE techniques can not practically be applied to certain electrically large problems as dense discretization of the entire domain results in very large number of unknowns (trillions of unknowns according to my observations) making them unsolvable even with today's powerful state of the art supercomputers. On the other hand, assuming that the Green's function for such problem is available, so-

lutions can be realized by taking advantage of the reduction in number of unknowns through IE techniques and solving the resultant dense matrix using fast iterative or direct matrix implicit algorithms which allow for solving dense matrices up to billions of unknowns [5–14].

In the class of IE formulations, both volume and surface based methods are available. Volume integral equation (VIE) formulations solve for the unknown field quantities within the volume of the scatterer (Fig 1.1.b) whereas surface integral equations (SIE) are formulated for the unknown field quantities on the boundary of the scatterer (Fig 1.1.c) and the resultant numerical methods are commonly referred to as boundary element methods (BEM). VIE techniques have been shown to be more efficient than BEMs in solving problems involving inhomogeneous dielectrics as well as thin layered homogenous non-conducting materials whereas BEMs based on SIE formulations are most efficient in computing the unknown fields in the presence of conducting materials and/or homogenous resonant dielectrics [5]. In this Ph.D. thesis we focus on the later and therefore we adopt BEMs based on SIE formulations.

1.1.2 Discretizaion

1.1.2.1 Rokhlin's Dogma

Choosing a proper mathematical formulation for the problem of interest is followed by using a proper discretization scheme in order to numerically obtain the solution. While Maxwell's equations are the foundations for mathematical formulation of electromagnetic problems, a set of rules envisioned by Prof. Vladimir Rokhlin[1] can be used to safeguard the integrity of scientific computing. These rules have been referred

[1]Prof. Rokhlin is best known for the introduction of the fast multipole method (FMM) in 1985 [15]. He is currently a professor of Computer Science and Mathematics at Yale University.

to as *Rokhlin's Dogma* and presented in the form of the following rules [16]

Methods must be fast (1.1)

Errors must be controlled (1.2)

Methods must be high order (1.3)

Discretizations must be point based (1.4)

Formulations must be well conditioned (1.5)

God did not invent polynomials, he invented exponentials (1.6)

Any violation from the above rules results in an inadequate CEM technique causing problems ranging from small inefficiencies to severe paralyzing effects. In [1], we excluded the rule (1.6) from the list as it seemed to us too abstract for such discussion. Our later understandings however, made us realize that even the rule (1.6) can be seen as a practical guideline for numerical techniques. In this Ph.D. dissertation, we will do our best to abide by these rules and will give reasons as to why any of these six rules should not be overlooked whenever our experience, our observation or previous work can explain.

1.1.2.2 High-Order LCN Imperative due to Rokhlin's Dogma

In order to numerically solve SIEs, they must be discretized. As SIEs integrate the unknown quantities residing on the boundary of the object, discretization should be done by approximating the integrals using appropriate sums over the boundary. However, in order to account for arbitrary shaped objects, transformations of integrals into sums can only be done by representing the object's boundary as small 2D discrete fragments commonly known as elements or patches. Figure 1.2 depicts various types of

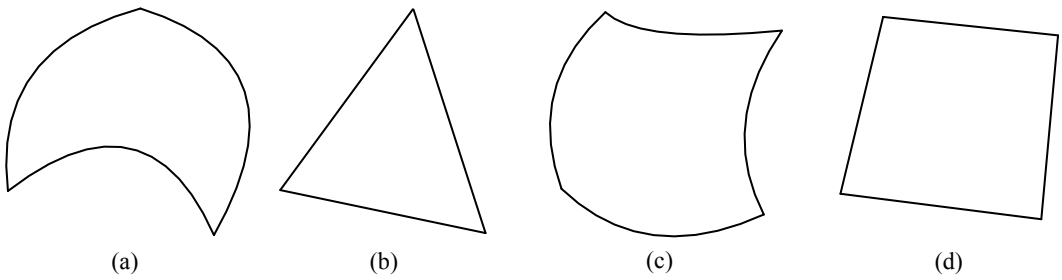

Figure 1.2: Different types of 2D elements used in an element-based discretization of SIEs.

2D elements. Once elements over the boundary are available, a preferred quadrature rule can be used to compute the integrals on the surface of these patches and by adding contributions from all patches, the unknown quantity can be evaluated. If low-order (LO) functions are used to approximate the solution on flat faceted elements (Fig. 1.2b,d), the resulting discretization scheme is referred to as a LO method. In contrast, a discretization scheme that allows for arbitrary order approximation of the solution based on high-order (HO) surface representation (Fig. 1.2a,c) is called an HO method[1]. While both LO and HO schemes can satisfy rule (1.2) by controlling the accuracy through mesh refinement, HO methods are exponentially more efficient [1, 17–20] as they can control the accuracy by applying HO quadrature rules in addition to reducing the size of the elements. In other words, HO schemes provide solutions which exhibit $\epsilon = \mathcal{O}(h^p)$ error in the solution where h is the characteristic size of the mesh elements and p is the order of the discretization, while LO methods can only provide solutions with error $\epsilon = \mathcal{O}(h)$. This is a manifestation of rule (1.3). Therefore, in this Ph.D. work we do not limit our discussion to classical LO techniques and will also discuss HO techniques.

[1]Sometimes in the CEM community, a method that either uses HO approximating functions or HO elements is called an HO method. However, for a method to exhibit exponential efficiency, it has to have both features [1, 17, 19, 20].

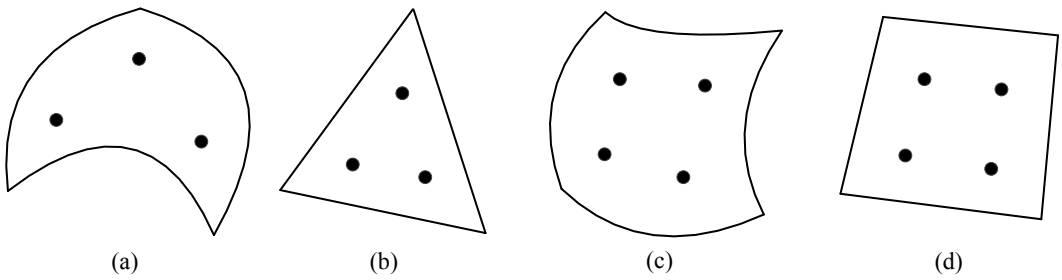

Figure 1.3: Different types of 2D elements used in a point-based discretization of SIEs.

Apart from being LO or HO, a discretization scheme can either be *point-based* or *element-based*. If the pertinent interactions are defined based on points (point-to-point interactions), the integrals are approximated only on specific set of points on a patch (Fig. 1.3) and the resultant method is referred to as a point-based method, otherwise the method is formulated using method-of-moments (MoM) [20–23] where interactions are defined based on elements and these methods are commonly referred to as element-based methods[1]. While element-based methods typically produce matrices with better conditioning compared to that of point-based methods, element-based methods suffer from two major disadvantages; 1) an MoM based interaction is computed by taking the inner product of the IE which needs computations of double integrations. This dramatically increases the matrix fill time specially if the method is HO [20], and 2) acceleration methods such as the multilevel fast multipole algorithm (MLFMA) can not efficiently accelerate element-based interactions as they do not allow for construction of imbalanced oct-tree structures. Point-based methods on the other hand, require computation of single reaction integrals which leads to significantly shorter matrix fill times compared to that of MoM at HOs, and further, these

[1]Please refer to Section 7.2.4.1 for more insight about the terms "point-based" and "element-based" mentioned by Prof. Gedney.

methods can efficiently be accelerated using the MLFMA by adapting the depth of the oct-tree to the disparity of the mesh [7, 24]. Therefore it is important to apply a point-based method in CEM which is a manifestation of rule (1.4). Despite the availability of point-matched MoM techniques [25, 26] which can efficiently be accelerated by the MLFMA, these techniques inherit the inner product testing from MoM and are not a suitable candidate for an HO scheme due to large matrix fill times. The locally corrected Nyström method (LCN) [18, 19] on the other hand, is a point-based method which inherently satisfies rule (1.4) and can efficiently provide HO solutions[1].

From the above discussion one can see that the HO LCN method equipped with fast iterative or fast direct solvers satisfies all rules in Rokhlin's Dogma with the exception that it does not guarantee rule (1.5). In order to accomplish better conditioned matrices several techniques have been suggested for particular examples [27–29] but a general solution is not available to date and constitutes an open research problem [1][2]. In this thesis, the LCN method is used to discretize SIEs of CEM and whenever necessary, error-controlled MLFMA acceleration based on Rokhlin's diagonal translators [1] is applied to solve large scale examples.

1.2 Purpose of Research

As was described above, the LCN method has several advantages compared with MoM. However, the existence of MoM in CEM originates in 1950s and as a result a significant amount of work can be found addressing numerical issues in MoM eclipsing the relatively new LCN (proposed in the 1990s) as a practical BEM method. Consequently, MoM remains the dominating BEM technique in the industry [30–32, 34, 35].

[1] See Prof. Gedney's comment in Section 7.2.4.2.
[2] Please refer to Section 7.2.4.3 for more information about this pointed out by Prof. Gedney.

In this thesis, several novel techniques are introduced in an attempt to close the gap between theoretical capabilities of the LCN and its practical use.

1.3 Computations

1.3.1 Commercial Software Packages

There are multiple commercial software packages available for EM simulations [30–32, 34, 35]. It is probably wise to say that for an EM software package to be comprehensive, it ideally needs to have both differential and integral equation techniques, both of which with the LO and HO capabilities. This is because for a particular problem of interest, either of these techniques might perform best. For the purpose of validating results for which analytical solutions are not available, in this thesis, we use the software *Wave3D* provided by *CEMWorks, Inc.* [35]. Other than the process of geometry creation, mesh generation, and visualization of the computed fields, its core is based on broadband MoM analysis accelerated with error-controllable Multilevel Fast Multipole Algorithm (MLFMA). Therefore, its results are conveniently compared with the results obtained from the techniques studied in this thesis. Nevertheless, other commercial software can also be used for the same analysis and there is no restriction on using Wave3D to validate results of this thesis.

1.3.2 Computing Platform

Most of the simulation results presented in this dissertation obtained by either parallel or serial computations, have been carried out on the advanced computing platform *Grex SGI Altix XE 1300 cluster* at WestGrid, part of the Compute Canada [37]. At the time of our simulations, Grex is equipped with 316 compute nodes, each

with two 6-core Intel Xeon X5650 2.66GHz processors (Intel Westmere architecture), 292 nodes of which have 48GB of memory and the other 24 nodes have 96GB of memory. In this research, the *Intel C++ Compiler* is used.

1.4 Outline of Thesis

This thesis has 7 chapters. They are summarized below:

- **Chapter 1**: A brief introduction and motivation of the work is given. Some detail about the utilized computing platform and commercial software is also provided.

- **Chapter 2**: The theory behind SIE formulations is reviewed and the electric field integral equation (EFIE) is derived from Maxwell's equations. The advantages of using Rao-Wilton-Glisson (RWG) basis functions in MoM when discretizing the EFIE is also reviewed. The author's point-of-view towards a simple description of the LCN method is also given in this chapter.

- **Chapter 3**: The equivalence of RWG MoM and LCN is established. The resulting numerical scheme is shown to be a point-based RWG MoM discretization of the vector-potential (VP) EFIE. It has a 4 times smaller and better conditioned matrix compared to that of the first-order LCN. It is preferred over the classical element-based MoM due to its point-based nature and at the same time it is computationally more efficient than the first-order LCN.

- **Chapter 4**: As an extension to the the work in Chapter 3, the exact relationship of the RWG MoM and LCN is derived for the mixed-potential (MP) EFIE by using first- and zeroth-order LCN to compute VP and scalar-potential terms of

the MP EFIE. Due to the analytical cancellation of the line charge contributions, it is shown that RWG MoM discretization of the MP EFIE is more accurate than discretizing the VP EFIE via the RWG MoM where the line charge contributions are left to be cancelled numerically.

- **Chapter 5**: The patch size limitation for HO LCN method is discussed in accordance with the Nyquist criterion. It is shown that the patch size is not only limited by the wavelength, but it is also related to the order of the discretization. A new method for predicting the optimal number of unknowns for a desired accuracy is proposed. The motivation towards HO LCN compared to LO methods is demonstrated by analysing solutions with large dynamic range.

- **Chapter 6**: A new set of quadrature rules to be applied to LCN on triangular Bézier elements is proposed based on equidistant Newton-Cotes quadrature formulae. Compared to existing Gaussian quadrature rules, they are more suitable for LCN as they prevent the EFIE from suffering from high condition numbers in the local correction system and the global impedance matrix. The new family of quadrature rules are stable and effective in LCN for orders from 0 to 9, inclusively.

- **Chapter 7**: The work presented in this dissertation is concluded in this chapter. Also, comments, corrections, and suggestions of the external examiner for the entire dissertation provided by Prof. Stephen D. Gedney are also addressed in this chapter. Finally, possible future research directions are discussed.

Chapter 2

Mathematical Formulation

By *Mohammad Shafieipour* in partial fulfilment of the requirements of the degree of *Doctor of Philosophy (Ph.D.)*, March 2016.

In this Chapter we review the theory behind surface integral equation (SIE) formulations. We first provide an overview of fundamental formulas needed for obtaining SIEs and then provide mathematical derivation of the electric field integral equation (EFIE). The chapter is finished by reviewing the advantages of using Rao-Wilton-Glisson (RWG) basis functions in discretizing the EFIE.

2.1 Fundamental Formulas

In this section we briefly discuss the fundamental formulas that are used to define SIE formulations, namely, Maxwell's and Helmholtz's Equations.

2.1.1 Maxwell's Equations

In 1873, James Clerk Maxwell published *A Treaties on Electricity and Magnetism*, his complete presentation of the laws of electromagnetics (EM) which is regarded as one of the greatest contributions in the 19th century and the most impactful discovery in the history of humanity (according to Einstein). In it, he mathematically formulated/corrected the EM laws that were discovered by Gauss, Faraday and Ampére through experiments. What is quite interesting (at least to me), is that for about a decade there was not a general understanding of his work as Maxwell made no effort to condense or simplify his work, aiming to be comprehensive rather than understandable. In the key chapter, entitled "General Equations of the Electromagnetic Field", he wrote:

> *These may be regarded as the principal relations among the quantities we have been considering, some could be combined, but our object is not to obtain compactness in the mathematical formulae.*

It was Oliver Heaviside who effectively discovered Maxwell's equations from about the thousand pages of Maxwell's treaties and presented them to the research community in 1883 similar to the form we know them today as four compact and understandable equations[1]. In this chapter, I will try to play Oliver's role rather than Maxwell's, that is to make SIE formulations understandable and compact, rather than trying to be comprehensive. For that, a large number of great texts already exist [5, 39–42].

Maxwell's equations can be written in various forms depending on the assumptions made for a particular problem. In this work, the EM fields are assumed to be produced by a time harmonic electric source whose current density is denoted by $\mathbf{J}(\mathbf{r})$ and its charge density is denoted by $\rho(\mathbf{r})$ where a time harmonic variation of $e^{j\omega t}$ is assumed.

[1] More interesting facts about Maxwell's equations as well as other great equations can be found in [38].

Therefore the electric and magnetic vector fields are denoted in their time harmonic forms by $\mathbf{E}(\mathbf{r})$ and $\mathbf{H}(\mathbf{r})$, respectively. Furthermore, the medium where the fields exist is assumed to be linear, isotropic and homogeneous. Under these assumptions, Maxwell's equations are written as [42]

$$\text{Gauss law: } \nabla \cdot \mathbf{E}(\mathbf{r}) = \frac{\rho(\mathbf{r})}{\epsilon} \tag{2.1}$$

$$\text{Gauss law–magnetic: } \nabla \cdot \mathbf{H}(\mathbf{r}) = 0 \tag{2.2}$$

$$\text{Faraday's law: } \nabla \times \mathbf{E}(\mathbf{r}) = -j\omega\mu\mathbf{H}(\mathbf{r}) \tag{2.3}$$

$$\text{Maxwell-Ampére law: } \nabla \times \mathbf{H}(\mathbf{r}) = j\omega\epsilon\mathbf{E}(\mathbf{r}) + \mathbf{J}(\mathbf{r}) \tag{2.4}$$

where ϵ is the electric permittivity and μ is the magnetic permeability of the medium. Equations (2.1)-(2.3) are named after their experimental discoverers but (2.4) is named after both Maxwell and the experimental discoverer (Ampére) as Maxwell not only formulated it, but he also corrected it[1].

2.1.2 Vector Helmholtz's (Wave) Equations

It is quite safe to say that the most important phenomena that was understood with the help of Maxwell's equations is the existence and propagation of EM waves. The equations that describe wave propagation are called vector *Helmholtz's equations* or simply vector *wave equations* and can be derived from Maxwell's equations as follows. By re-arranging Faraday's law (2.3), one can write

$$\mathbf{H}(\mathbf{r}) = \frac{-1}{j\omega\mu}[\nabla \times \mathbf{E}(\mathbf{r})] \tag{2.5}$$

[1] An interesting intuitive tutorial of Maxwell's equations can be found online [43].

If we substitute (2.5) into Maxwell-Ampére law (2.4) and assuming homogeneity of permeability μ, we get

$$\frac{-1}{j\omega\mu}[\nabla \times \nabla \times \mathbf{E}(\mathbf{r})] = j\omega\epsilon\mathbf{E}(\mathbf{r}) + \mathbf{J}(\mathbf{r}) \tag{2.6}$$

Multiplying the above equation by $(-j\omega\mu)$ we get

$$\nabla \times \nabla \times \mathbf{E}(\mathbf{r}) - k^2\mathbf{E}(\mathbf{r}) = -j\omega\mu\mathbf{J}(\mathbf{r}) \tag{2.7}$$

where $k^2 = \omega^2\mu\epsilon$. Equation (2.7) is called inhomogeneous Helmholtz's (wave) equation for the electric field[1]. Its left hand side enforces wave behaviour of the electric field which would propagate due to the excitation given on its right hand side. Under the assumption of homogeneous permittivity ε, it can also be shown that the wave equation for the magnetic field is

$$\nabla \times \nabla \times \mathbf{H}(\mathbf{r}) - k^2\mathbf{H}(\mathbf{r}) = \nabla \times \mathbf{J}(\mathbf{r}) \tag{2.8}$$

Equations (2.7) and (2.8) will later be used to derive Green's functions and SIEs.

2.2 Surface Integral Equations

One of the requirements for formulating IE methods is to find the appropriate Green's functions. Herein, we discuss two types of Green's functions; the dyadic Green's function of the electric type and the dyadic Green's function of the magnetic type, both for free-space.

[1]The wave equation is usually written in a different form by simplifying the first component of the left hand side of (2.7). In this chapter however, this form of the wave equation is chosen since it will be used later to derive Green's functions.

2.2.1 Free-Space Dyadic Green's Functions

2.2.1.1 Electric Type

The dyadic Green's function of the electric type $\overline{\mathbf{G}}_{e0}(\mathbf{r},\mathbf{r}')$ is, by definition, a dyadic operator[1] that relates the electric vector field $\mathbf{E}(\mathbf{r})$ to vector current $\mathbf{J}(\mathbf{r})$ by

$$\mathbf{E}(\mathbf{r}) = -j\omega\mu \int_V \overline{\mathbf{G}}_{e0}(\mathbf{r},\mathbf{r}') \cdot \mathbf{J}(\mathbf{r}')dV' \tag{2.9}$$

where V is the volume containing the current $\mathbf{J}(\mathbf{r})$ and the subscript "0" represents the free-space condition indicating that the volume is an unbounded homogeneous medium with constant permittivity and permeability. Substituting (2.9) in the wave equation in (2.7) we get

$$\begin{aligned} &- j\omega\mu \int_V \nabla \times \nabla \times \overline{\mathbf{G}}_{e0}(\mathbf{r},\mathbf{r}') \cdot \mathbf{J}(\mathbf{r}')dV' + j\omega\mu k^2 \int_V \overline{\mathbf{G}}_{e0}(\mathbf{r},\mathbf{r}') \cdot \mathbf{J}(\mathbf{r}')dV' \\ &= - j\omega\mu \mathbf{J}(\mathbf{r}) \end{aligned} \tag{2.10}$$

By using the definition of the Dirac delta function $\delta(\mathbf{r},\mathbf{r}')$ and the unit dyad[2] $\bar{\mathbf{I}}$ we can modify the second line and write

$$\begin{aligned} &- j\omega\mu \int_V \nabla \times \nabla \times \overline{\mathbf{G}}_{e0}(\mathbf{r},\mathbf{r}') \cdot \mathbf{J}(\mathbf{r}')dV' + j\omega\mu k^2 \int_V \overline{\mathbf{G}}_{e0}(\mathbf{r},\mathbf{r}') \cdot \mathbf{J}(\mathbf{r}')dV' \\ &= - j\omega\mu \int_V \bar{\mathbf{I}}\delta(\mathbf{r}-\mathbf{r}') \cdot \mathbf{J}(\mathbf{r}')dV' \end{aligned} \tag{2.11}$$

[1] A dyadic operator can be interpreted as a (3×3) matrix, similar to representing a vector as a matrix of (3×1).

[2] The unit dyad is a dyadic operator that does not change a vector. A general example is the (3×3) identity matrix, but it can have other forms in particular situations such as in [44].

For an arbitrary $\mathbf{J}(\mathbf{r})$, the above equation can only be satisfied if the following holds [40]

$$\nabla \times \nabla \times \overline{\mathbf{G}}_{e0}(\mathbf{r}, \mathbf{r}') - k^2 \overline{\mathbf{G}}_{e0}(\mathbf{r}, \mathbf{r}') = \bar{\mathbf{I}} \delta(\mathbf{r} - \mathbf{r}') \tag{2.12}$$

Therefore the dyadic Green's function of the electric type can be obtained by solving (2.12). It can be shown with different techniques [40] that the solution to (2.12) is

$$\begin{aligned} \overline{\mathbf{G}}_{e0}(\mathbf{r}, \mathbf{r}') &= (\bar{\mathbf{I}} + \frac{1}{k^2} \nabla\nabla) G_0(\mathbf{r}, \mathbf{r}') \\ &= \bar{\mathbf{I}} G_0(\mathbf{r}, \mathbf{r}') + \frac{1}{k^2} \nabla\nabla G_0(\mathbf{r}, \mathbf{r}') \end{aligned} \tag{2.13}$$

where the double gradient operator $\nabla\nabla$ produces a dyadic by acting on a scalar function and the unit dyad $\bar{\mathbf{I}}$ multiplied by the scalar function G_0 is also a dyadic term. The first term on the right hand side of (2.13) is sometimes referred to as the vector-potential component of the dyadic $\overline{\mathbf{G}}_{e0}$ and $\frac{1}{k^2}\nabla\nabla G_0(\mathbf{r}, \mathbf{r}')$ is sometimes called the scalar-potential component of the dyadic Green's function of the electric type. The scalar function G_0 is the free-space Green's function

$$G_0(\mathbf{r}, \mathbf{r}') = \frac{e^{-jk|\mathbf{r}-\mathbf{r}'|}}{4\pi|\mathbf{r} - \mathbf{r}'|}. \tag{2.14}$$

It can be shown that the dyadic Green's function of the electric type $\overline{\mathbf{G}}_{e0}(\mathbf{r}, \mathbf{r}')$ has the following symmetric properties [40]

$$\overline{\mathbf{G}}_{e0}(\mathbf{r}, \mathbf{r}') = \overline{\mathbf{G}}_{e0}(\mathbf{r}, \mathbf{r}')^T \tag{2.15}$$

$$\overline{\mathbf{G}}_{e0}(\mathbf{r}, \mathbf{r}') = \overline{\mathbf{G}}_{e0}(\mathbf{r}', \mathbf{r}) \tag{2.16}$$

where superscript T denotes transposition. These properties will be used in Section 2.2.2 to proof the equivalence principle.

2.2.1.2 Magnetic Type

Taking curl of the definition of the electric type dyadic Green's function (2.9) we get

$$\nabla \times \mathbf{E}(\mathbf{r}) = -j\omega\mu \int_V \nabla \times \overline{\mathbf{G}}_{e0}(\mathbf{r}, \mathbf{r}') \cdot \mathbf{J}(\mathbf{r}')dV' \tag{2.17}$$

Using Faraday's law (2.3) we can then write

$$\mathbf{H}(\mathbf{r}) = \int_V \nabla \times \overline{\mathbf{G}}_{e0}(\mathbf{r}, \mathbf{r}') \cdot \mathbf{J}(\mathbf{r}')dV' \tag{2.18}$$

which is the magnetic type counterpart for (2.9). Thus the dyadic Green's function of the magnetic type is obtained by

$$\overline{\mathbf{G}}_{m0}(\mathbf{r}, \mathbf{r}') = \nabla \times \overline{\mathbf{G}}_{e0}(\mathbf{r}, \mathbf{r}') \tag{2.19}$$

where $\overline{\mathbf{G}}_{e0}$ is defined in (2.13). Further, due to $\nabla \times \frac{1}{k^2}\nabla\nabla G_0(\mathbf{r}, \mathbf{r}') = 0$, (2.19) can be written as

$$\overline{\mathbf{G}}_{m0}(\mathbf{r}, \mathbf{r}') = \nabla \times \bar{\mathbf{I}} G_0(\mathbf{r}, \mathbf{r}'). \tag{2.20}$$

Since $\overline{\mathbf{G}}_{m0}$ is the curl of $\overline{\mathbf{G}}_{e0}$, it will have its own symmetry properties [40]

$$\overline{\mathbf{G}}_{m0}(\mathbf{r}, \mathbf{r}') = -\overline{\mathbf{G}}_{m0}(\mathbf{r}, \mathbf{r}')^T \tag{2.21}$$

$$\overline{\mathbf{G}}_{m0}(\mathbf{r}, \mathbf{r}') = -\overline{\mathbf{G}}_{m0}(\mathbf{r}', \mathbf{r}) \tag{2.22}$$

They will be needed in the next section to formulate the equivalence principle.

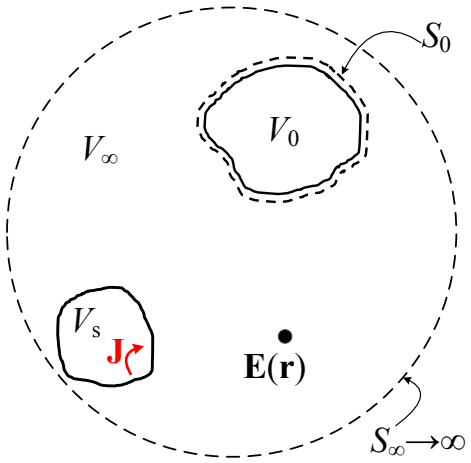

Figure 2.1: The vector BVP used to define the equivalence principle.

2.2.2 Equivalence Principle for the Electric Field

Consider the vector boundary value problem (BVP) shown in Fig. 2.1. The volume V_∞ is exterior to the object (scatterer) and has boundaries S_0 and a large spherical surface S_∞ whose radius approaches infinity ($S_\infty \to \infty$), thus it contains sources $\mathbf{J}$ supported by V_s but does not contain the scatterer which is bounded in V_0 with surface S_0. The electric field $\mathbf{E}(\mathbf{r})$ in the exterior region V_∞ satisfies the vector wave equation in (2.7). If we post-multiply (2.7) by the dyadic $\overline{\mathbf{G}}_{e0}$ we get

$$[\nabla \times \nabla \times \mathbf{E}(\mathbf{r})] \cdot \overline{\mathbf{G}}_{e0}(\mathbf{r}, \mathbf{r}') - k^2 \mathbf{E}(\mathbf{r}) \cdot \overline{\mathbf{G}}_{e0}(\mathbf{r}, \mathbf{r}') = -j\omega\mu \mathbf{J}(\mathbf{r}) \cdot \overline{\mathbf{G}}_{e0}(\mathbf{r}, \mathbf{r}') \qquad (2.23)$$

and if we pre-multiply (2.12) by the electric field $\mathbf{E}(\mathbf{r})$ we get

$$\mathbf{E}(\mathbf{r}) \cdot [\nabla \times \nabla \times \overline{\mathbf{G}}_{e0}(\mathbf{r}, \mathbf{r}')] - k^2 \mathbf{E}(\mathbf{r}) \cdot \overline{\mathbf{G}}_{e0}(\mathbf{r}, \mathbf{r}') = \mathbf{E}(\mathbf{r}) \cdot \overline{\mathbf{I}} \delta(\mathbf{r} - \mathbf{r}') \qquad (2.24)$$

By subtracting (2.24) from (2.23) and knowing that the operator unit dyad $\bar{\mathbf{I}}$ does not change a vector, we can then write

$$\begin{aligned}&[\nabla\times\nabla\times\mathbf{E}(\mathbf{r})]\cdot\overline{\mathbf{G}}_{e0}(\mathbf{r},\mathbf{r}')-\mathbf{E}(\mathbf{r})\cdot[\nabla\times\nabla\times\overline{\mathbf{G}}_{e0}(\mathbf{r},\mathbf{r}')]\\&=-j\omega\mu\mathbf{J}(\mathbf{r})\cdot\overline{\mathbf{G}}_{e0}(\mathbf{r},\mathbf{r}')-\mathbf{E}(\mathbf{r})\delta(\mathbf{r}-\mathbf{r}')\end{aligned}\tag{2.25}$$

Integrating the above equation over the exterior region V_∞ we get

$$\begin{aligned}&\int_{V_\infty}\Big\{[\nabla\times\nabla\times\mathbf{E}(\mathbf{r})]\cdot\overline{\mathbf{G}}_{e0}(\mathbf{r},\mathbf{r}')-\mathbf{E}(\mathbf{r})\cdot[\nabla\times\nabla\times\overline{\mathbf{G}}_{e0}(\mathbf{r},\mathbf{r}')]\Big\}\,dV\\&=-j\omega\mu\int_{V_\infty}\Big[\mathbf{J}(\mathbf{r})\cdot\overline{\mathbf{G}}_{e0}(\mathbf{r},\mathbf{r}')\Big]\,dV-\int_{V_\infty}[\mathbf{E}(\mathbf{r})\delta(\mathbf{r}-\mathbf{r}')]\,dV\end{aligned}\tag{2.26}$$

The left hand side of (2.26) has a form similar to the vector-dyadic Green's second identity [41]

$$\begin{aligned}&\int_V\Big[(\nabla\times\nabla\times\mathbf{A})\cdot\overline{\mathbf{D}}-\mathbf{A}(\nabla\times\nabla\times\overline{\mathbf{D}})\Big]\,dV\\&=\int_S\Big[(\hat{\mathbf{n}}\times\mathbf{A})\cdot(\nabla\times\overline{\mathbf{D}})+(\hat{\mathbf{n}}\times\nabla\times\mathbf{A})\cdot\overline{\mathbf{D}}\Big]\,dS\end{aligned}\tag{2.27}$$

where V is a volume enclosed by S and $\hat{\mathbf{n}}$ is the outward unit normal on S. In (2.26), V_∞ is enclosed by surfaces S_0 and S_∞ thus using the identity (2.27) it can be written as

$$\begin{aligned}&\int_{S_0+S_\infty}\Big\{[\hat{\mathbf{n}}(\mathbf{r})\times\mathbf{E}(\mathbf{r})]\cdot[\nabla\times\overline{\mathbf{G}}_{e0}(\mathbf{r},\mathbf{r}')]+[\hat{\mathbf{n}}(\mathbf{r})\times\nabla\times\mathbf{E}(\mathbf{r})]\cdot\overline{\mathbf{G}}_{e0}(\mathbf{r},\mathbf{r}')\Big\}\,dS\\&=-j\omega\mu\int_{V_\infty}\Big[\mathbf{J}(\mathbf{r})\cdot\overline{\mathbf{G}}_{e0}(\mathbf{r},\mathbf{r}')\Big]\,dV-\int_{V_\infty}[\mathbf{E}(\mathbf{r})\delta(\mathbf{r}-\mathbf{r}')]\,dV.\end{aligned}\tag{2.28}$$

In the BVP which we consider here, all sources $\mathbf{J}(\mathbf{r})$ are bound to be in V_s and no source exists at infinity. This has two consequences; 1) the integration of $[\mathbf{J}(\mathbf{r})\cdot\overline{\mathbf{G}}_{e0}(\mathbf{r},\mathbf{r}')]$ over V_∞ in (2.28) is the same as integrating it over V_s, and, 2) by applying

the radiation condition we have $\mathbf{E}(\mathbf{r}) \to 0$ and $\overline{\mathbf{G}}_{e0}(\mathbf{r}, \mathbf{r}') \to 0$ on S_∞ which eliminates the surface integral over S_∞ in (2.28) [40]. Consequently (2.28) can be written as

$$\begin{aligned} &\int_{S_0} \Big\{ [\hat{\mathbf{n}}(\mathbf{r}) \times \mathbf{E}(\mathbf{r})] \cdot [\nabla \times \overline{\mathbf{G}}_{e0}(\mathbf{r}, \mathbf{r}')] + [\hat{\mathbf{n}}(\mathbf{r}) \times \nabla \times \mathbf{E}(\mathbf{r})] \cdot \overline{\mathbf{G}}_{e0}(\mathbf{r}, \mathbf{r}') \Big\} \, dS \\ &= -j\omega\mu \int_{V_s} \Big[\mathbf{J}(\mathbf{r}) \cdot \overline{\mathbf{G}}_{e0}(\mathbf{r}, \mathbf{r}') \Big] \, dV - \int_{V_\infty} [\mathbf{E}(\mathbf{r}) \delta(\mathbf{r} - \mathbf{r}')] \, dV \end{aligned} \tag{2.29}$$

Using the definition of the dyadic Green's function of the magnetic type $\overline{\mathbf{G}}_{m0}$ in (2.20) and by applying $\hat{\mathbf{n}}(\mathbf{r})\times$ on Faraday's law $\hat{\mathbf{n}}(\mathbf{r}) \times \nabla \times \mathbf{E}(\mathbf{r}) = -j\omega\mu[\hat{\mathbf{n}}(\mathbf{r}) \times \mathbf{H}(\mathbf{r})]$, we can modify the first line of (2.29) and write

$$\begin{aligned} &\int_{S_0} \Big\{ [\hat{\mathbf{n}}(\mathbf{r}) \times \mathbf{E}(\mathbf{r})] \cdot \overline{\mathbf{G}}_{m0}(\mathbf{r}, \mathbf{r}') - j\omega\mu [\hat{\mathbf{n}}(\mathbf{r}) \times \mathbf{H}(\mathbf{r})] \cdot \overline{\mathbf{G}}_{e0}(\mathbf{r}, \mathbf{r}') \Big\} \, dS \\ &= -j\omega\mu \int_{V_s} \Big[\mathbf{J}(\mathbf{r}) \cdot \overline{\mathbf{G}}_{e0}(\mathbf{r}, \mathbf{r}') \Big] \, dV - \int_{V_\infty} [\mathbf{E}(\mathbf{r}) \delta(\mathbf{r} - \mathbf{r}')] \, dV \end{aligned} \tag{2.30}$$

Taking advantage of the delta function sifting property we have $\int_{V_\infty} [\mathbf{E}(\mathbf{r})\delta(\mathbf{r} - \mathbf{r}')] \, dV = \mathbf{E}(\mathbf{r}')$ if $(\mathbf{r}' \in V_\infty)$ since $\delta(\mathbf{r} - \mathbf{r}')$ cancels all values of the electric field except at $\mathbf{r}'$. On the other hand if $(\mathbf{r}' \notin V_\infty)$ or equivalently $(\mathbf{r}' \in V_0)$, we always have $\delta(\mathbf{r} - \mathbf{r}') = 0$ and consequently $\int_{V_\infty} [\mathbf{E}(\mathbf{r})\delta(\mathbf{r} - \mathbf{r}')] \, dV = 0$. Thus we can write

$$\begin{aligned} &\int_{S_0} \Big\{ [\hat{\mathbf{n}}(\mathbf{r}) \times \mathbf{E}(\mathbf{r})] \cdot \overline{\mathbf{G}}_{m0}(\mathbf{r}, \mathbf{r}') - j\omega\mu [\hat{\mathbf{n}}(\mathbf{r}) \times \mathbf{H}(\mathbf{r})] \cdot \overline{\mathbf{G}}_{e0}(\mathbf{r}, \mathbf{r}') \Big\} \, dS \\ &= -j\omega\mu \int_{V_s} \Big[\mathbf{J}(\mathbf{r}) \cdot \overline{\mathbf{G}}_{e0}(\mathbf{r}, \mathbf{r}') \Big] \, dV - \begin{cases} \mathbf{E}(\mathbf{r}'), & \mathbf{r}' \in V_\infty \\ 0, & \mathbf{r}' \in V_0 \end{cases} \end{aligned} \tag{2.31}$$

Usually in EM literature, the position vector $\mathbf{r}$ is used to indicate observation locations and $\mathbf{r}'$ is used for source locations. Thus we need to change the notation of (2.30)

from $\mathbf{r}$ to $\mathbf{r}'$ and vice versa

$$\begin{aligned}
&\int_{S_0} \Big\{ [\hat{\mathbf{n}}(\mathbf{r}') \times \mathbf{E}(\mathbf{r}')] \cdot \overline{\mathbf{G}}_{m0}(\mathbf{r}', \mathbf{r}) - j\omega\mu [\hat{\mathbf{n}}(\mathbf{r}') \times \mathbf{H}(\mathbf{r}')] \cdot \overline{\mathbf{G}}_{e0}(\mathbf{r}', \mathbf{r}) \Big\} \, dS' \\
&= -j\omega\mu \int_{V_s} \Big[\mathbf{J}(\mathbf{r}') \cdot \overline{\mathbf{G}}_{e0}(\mathbf{r}', \mathbf{r}) \Big] \, dV' - \begin{cases} \mathbf{E}(\mathbf{r}), & \mathbf{r} \in V_\infty \\ 0, & \mathbf{r} \in V_0 \end{cases}
\end{aligned} \tag{2.32}$$

By using the symmetry property of the dyadic Green's function of the magnetic type in (2.21) we can flip the order of the dot product in $[\hat{\mathbf{n}}(\mathbf{r}') \times \mathbf{E}(\mathbf{r}')] \cdot \overline{\mathbf{G}}_{m0}(\mathbf{r}', \mathbf{r})$ and write it as $-\overline{\mathbf{G}}_{m0}(\mathbf{r}', \mathbf{r}) \cdot [\hat{\mathbf{n}}(\mathbf{r}') \times \mathbf{E}(\mathbf{r}')]$ due to the transposition that takes place in flipping the order of the dot product. We can then use the other symmetry property of the same dyadic Green's function (2.22) to exchange $\mathbf{r}$ and $\mathbf{r}'$ of the Green's function and write the same component as $\overline{\mathbf{G}}_{m0}(\mathbf{r}, \mathbf{r}') \cdot [\hat{\mathbf{n}}(\mathbf{r}') \times \mathbf{E}(\mathbf{r}')]$. After applying similar algebraic manipulations on $\Big\{ [\hat{\mathbf{n}}(\mathbf{r}') \times \mathbf{H}(\mathbf{r}')] \cdot \overline{\mathbf{G}}_{e0}(\mathbf{r}', \mathbf{r}) \Big\}$ and $\Big\{ [\mathbf{J}(\mathbf{r}') \cdot \overline{\mathbf{G}}_{e0}(\mathbf{r}', \mathbf{r})] \Big\}$ using (2.15) and (2.16) we can re-write (2.32) as

$$\begin{aligned}
&\int_{S_0} \Big\{ \overline{\mathbf{G}}_{m0}(\mathbf{r}, \mathbf{r}') \cdot [\hat{\mathbf{n}}(\mathbf{r}') \times \mathbf{E}(\mathbf{r}')] - j\omega\mu \overline{\mathbf{G}}_{e0}(\mathbf{r}, \mathbf{r}') \cdot [\hat{\mathbf{n}}(\mathbf{r}') \times \mathbf{H}(\mathbf{r}')] \Big\} \, dS' \\
&= -j\omega\mu \int_{V_s} \Big[\overline{\mathbf{G}}_{e0}(\mathbf{r}', \mathbf{r}) \cdot \mathbf{J}(\mathbf{r}') \Big] \, dV' - \begin{cases} \mathbf{E}(\mathbf{r}), & \mathbf{r} \in V_\infty \\ 0, & \mathbf{r} \in V_0 \end{cases}
\end{aligned} \tag{2.33}$$

It is common to call tangential component of the electric field $\mathbf{E} \times \hat{\mathbf{n}}$ as the equivalent magnetic current $\mathbf{J}^{\mathrm{m}}$ and refer to the tangential component of the magnetic field $\hat{\mathbf{n}} \times \mathbf{H}$

as the equivalent electric current $\mathbf{J}^{\mathrm{e}}$[1]

$$\text{Electric current: } \mathbf{J}^{\mathrm{e}}(\mathbf{r}) = \hat{\mathbf{n}}(\mathbf{r}) \times \mathbf{H}(\mathbf{r}) \tag{2.34}$$

$$\text{Magnetic current: } \mathbf{J}^{\mathrm{m}}(\mathbf{r}) = \mathbf{E}(\mathbf{r}) \times \hat{\mathbf{n}}(\mathbf{r}) = -\hat{\mathbf{n}}(\mathbf{r}) \times \mathbf{E}(\mathbf{r}) \tag{2.35}$$

Using the above two definitions and by re-arranging (2.33) we get

$$\begin{aligned} &\int_{S_0} \left[\overline{\mathbf{G}}_{m0}(\mathbf{r},\mathbf{r}') \cdot \mathbf{J}^{\mathrm{m}}(\mathbf{r}') + j\omega\mu\overline{\mathbf{G}}_{e0}(\mathbf{r},\mathbf{r}') \cdot \mathbf{J}^{\mathrm{e}}(\mathbf{r}')\right] dS' \\ &- j\omega\mu \int_{V_s} \left[\overline{\mathbf{G}}_{e0}(\mathbf{r}',\mathbf{r}) \cdot \mathbf{J}(\mathbf{r}')\right] dV' = \begin{cases} \mathbf{E}(\mathbf{r}), & \mathbf{r} \in V_\infty \\ 0, & \mathbf{r} \in V_0 \end{cases} \end{aligned} \tag{2.36}$$

In (2.36), if we assume that the scatterer is absent, the surface integral vanishes and the resultant electric field is called the incident field $\mathbf{E}^{\mathrm{inc}}$

$$\mathbf{E}^{\mathrm{inc}}(\mathbf{r}) = -j\omega\mu \int_{V_s} \left[\overline{\mathbf{G}}_{e0}(\mathbf{r}',\mathbf{r}) \cdot \mathbf{J}(\mathbf{r}')\right] dV' \tag{2.37}$$

Therefore we can re-write (2.36) as

$$\int_{S_0} \left[\overline{\mathbf{G}}_{m0}(\mathbf{r},\mathbf{r}') \cdot \mathbf{J}^{\mathrm{m}}(\mathbf{r}') + j\omega\mu\overline{\mathbf{G}}_{e0}(\mathbf{r},\mathbf{r}') \cdot \mathbf{J}^{\mathrm{e}}(\mathbf{r}')\right] dS' + \mathbf{E}^{\mathrm{inc}}(\mathbf{r}) = \begin{cases} \mathbf{E}(\mathbf{r}), & \mathbf{r} \in V_\infty \\ 0, & \mathbf{r} \in V_0 \end{cases} \tag{2.38}$$

Equation (2.38) is called *equivalence principle for the electric field* with the following implications:

1. For the considered BVP, the electric field at any point outside the scatterer $\mathbf{E}(\mathbf{r})$

[1]The equivalent electric current $\mathbf{J}^{\mathrm{e}}$ is in fact the familiar electric current that flows on the surface of a conductor but the equivalent magnetic current $\mathbf{J}^{\mathrm{m}}$ does not have a physical meaning and is introduced for convenience.

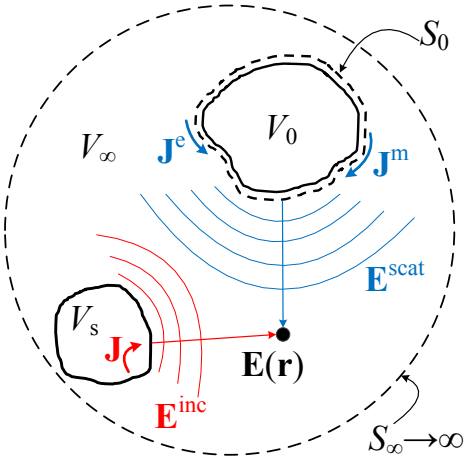

Figure 2.2: Illustration of the the equivalence principle for the electric field formulated in (2.38).

is produced by two contributions; 1) the primary sources $\mathbf{J}$ in V_s producing the incident electric field $\mathbf{E}^{\mathrm{inc}}$, and 2) the secondary sources $\mathbf{J}^{\mathrm{e}}, \mathbf{J}^{\mathrm{m}}$ induced on the surface of the scatterer S_0 producing the scattered electric filed $\mathbf{E}^{\mathrm{scat}}$. This is the vector electric field analogue with the *Huygens' principle*[1] As shown in Fig. 2.2, representation of the electric field (2.38) at arbitrary location $\mathbf{r}$ is nothing else but a superposition of spherical waves (Green's functions $\overline{\mathbf{G}}_{m0}$ and $\overline{\mathbf{G}}_{e0}$) emanating from each point of the surface S_0 just as was prescribed by Huygen.

2. For the considered BVP, the field representation in accordance with the equivalence principle at any point inside the scatterer is zero regardless of whether the scatterer is penetrable or not. This is called *extinction theorem.*

The equivalence principle shown in (2.38) is an important result and is used to derive EFIE as explained in the next section.

[1]The Huygen's principle which was first observed in 1678 states that every point of a wave front acts as a source of a secondary spherical wave.

2.2.3 Electric Field Integral Equation (EFIE)

From boundary conditions between free-space and perfect conductors we know that the electric field can only approach an ideally conducting surface normally and there is no tangential component of the electric field $\hat{\mathbf{n}} \times \mathbf{E} = 0$ on the surface of a perfect electric conductor (PEC) scatterer and hence there will not be any equivalent magnetic current $\mathbf{J}^{\mathrm{m}}$ produced on such surface

$$\hat{\mathbf{n}}(\mathbf{r}') \times \mathbf{E}(\mathbf{r}') = -\mathbf{J}^{\mathrm{m}}(\mathbf{r}') = 0,\ \mathbf{r}' \in S_0 \tag{2.39}$$

Thus for a PEC scatterer (object), the equivalence principle in (2.38) becomes

$$j\omega\mu \int_{S_0} [\overline{\mathbf{G}}_{e0}(\mathbf{r}, \mathbf{r}') \cdot \mathbf{J}^{\mathrm{e}}(\mathbf{r}')] dS' + \mathbf{E}^{\mathrm{inc}}(\mathbf{r}) = \begin{cases} \mathbf{E}(\mathbf{r}), & \mathbf{r} \in V_\infty \\ 0, & \mathbf{r} \in V_0 \end{cases} \tag{2.40}$$

In order to establish an IE on the surface of the object, $\hat{\mathbf{n}}(\mathbf{r})\times$ should be applied to (2.40)

$$\hat{\mathbf{n}}(\mathbf{r}) \times \left\{ j\omega\mu \int_{S_0} [\overline{\mathbf{G}}_{e0}(\mathbf{r}, \mathbf{r}') \cdot \mathbf{J}^{\mathrm{e}}(\mathbf{r}')] dS' + \mathbf{E}^{\mathrm{inc}}(\mathbf{r}) \right\} = \hat{\mathbf{n}}(\mathbf{r}) \times \begin{cases} \mathbf{E}(\mathbf{r}), & \mathbf{r} \in V_\infty \\ 0, & \mathbf{r} \in V_0 \end{cases} \tag{2.41}$$

To find the appropriate right hand side for (2.41), three scenarios should be considered

1. The observation point $\mathbf{r}$ is on S_0 as a limit from outside of the object ($\mathbf{r} \in S_0^+$)
2. The observation point $\mathbf{r}$ is on S_0 as a limit from inside of the object ($\mathbf{r} \in S_0^-$)
3. The observation point $\mathbf{r}$ is on S_0 right on the object's boundary ($\mathbf{r} \in S_0$)

Using the boundary condition in (2.39), we can see that in all three scenarios, the right hand side is actually zero

$$\hat{\mathbf{n}}(\mathbf{r}) \times \left\{ j\omega\mu \int_{S_0} [\overline{\mathbf{G}}_{e0}(\mathbf{r}, \mathbf{r}') \cdot \mathbf{J}^{\mathrm{e}}(\mathbf{r}')] dS' + \mathbf{E}^{\mathrm{inc}}(\mathbf{r}) \right\} = \begin{cases} 0, & \mathbf{r} \in S_0^+ \\ 0, & \mathbf{r} \in S_0^- \\ 0, & \mathbf{r} \in S \end{cases} \tag{2.42}$$

By re-arranging (2.42) we can write

$$j\omega\mu \left[\hat{\mathbf{n}}(\mathbf{r}) \times \int_{S_0} \overline{\mathbf{G}}_{e0}(\mathbf{r}, \mathbf{r}') \cdot \mathbf{J}^{\mathrm{e}}(\mathbf{r}') dS' \right] = -\hat{\mathbf{n}}(\mathbf{r}) \times \mathbf{E}^{\mathrm{inc}}(\mathbf{r}), \ \mathbf{r} \in S \tag{2.43}$$

This is the SIE for the electric field (i.e. EFIE) and can be discretized using IE numerical techniques such as the method-of-moments (MoM) [23] and the locally corrected Nyström (LCN) [19] method to find the equivalent electric current $\mathbf{J}^{\mathrm{e}}$ on the surface of the PEC. Once $\mathbf{J}^{\mathrm{e}}$ is found, the electric field $\mathbf{E}$ anywhere in the domain can be calculated using (2.40).

2.3 Discretizing the EFIE using MoM and RWG Basis Functions

In Chapter 3, we discuss discretizing the EFIE using both MoM and LCN in such a way that their equivalence can be established. In this section, a more familiar form of MoM is used to discretize the EFIE using Rao-Wilton-Glisson (RWG) basis functions and its relationship to the form of RWG MoM described in Chapter 3 is given. The advantages of using RWG basis functions in MoM are also reviewed.

2.3.1 The MoM System

The EFIE in (2.43) can be re-written in the following form

$$\mathbf{t}(\mathbf{r}) \cdot \int_{S_0} \overline{\mathbf{G}}(\mathbf{r}, \mathbf{r}') \cdot \mathbf{J}^{\mathrm{e}}(\mathbf{r}') dS' = -\mathbf{t}(\mathbf{r}) \cdot \mathbf{E}^{\mathrm{inc}}(\mathbf{r}),\ \mathbf{r} \in S \tag{2.44}$$

where $\mathbf{t}(\mathbf{r})$ is an arbitrary test vector which is tangential to S_0 and $\overline{\mathbf{G}}(\mathbf{r}, \mathbf{r}') = j\omega\mu\overline{\mathbf{G}}_{e0}(\mathbf{r}, \mathbf{r}')$. The procedure in which MoM converts the EFIE (2.44) to a matrix equation is by expanding the unknown function $\mathbf{J}^{\mathrm{e}}$ over a set of basis functions $[\mathbf{f}]$

$$\mathbf{J}^{\mathrm{e}}(\mathbf{r}) \simeq \sum_{n=1}^{N} I_n \mathbf{f}_n(\mathbf{r}) \tag{2.45}$$

and performing Galerkin's testing of the scattered field to form a set of algebraic system of equations

$$[Z] \cdot [I] = [V] \tag{2.46}$$

where $[I]$ contains the coefficients of expansion in (2.45), $[V]$ is the discrete samples of the excitation and $[Z]$ is the impedance matrix. Elements of $[V]$ are

$$[V]_m = -\langle \mathbf{E}^{\mathrm{inc}}, \mathbf{f}_m \rangle \quad m = 1, 2, ..., N \tag{2.47}$$

and the elements of $[Z]$ are the interactions between the basis $\mathbf{f}_n$ and test $\mathbf{f}_m$ functions which are defined as

$$[Z]_{m,n} = \langle \langle \overline{\mathbf{G}}, \mathbf{f}_n \rangle, \mathbf{f}_m \rangle, \quad m, n = 1, 2, ..., N. \tag{2.48}$$

In (2.47) and (2.48), the inner product $\langle \mathbf{x}, \mathbf{y} \rangle$ is defined as

$$\langle \mathbf{x}, \mathbf{y} \rangle \equiv \int_S \mathbf{x} \cdot \mathbf{y} dS \tag{2.49}$$

which is a symmetric operation [23].

2.3.2 The RWG Basis Functions

As shown above, one important part of discretizing EFIE via MoM, is to choose an appropriate basis function $\mathbf{f}$ to expand the unknown function $\mathbf{J}^{\mathrm{e}}$ in terms of basis functions. Defining a unique basis function for the entire domain S_0 is difficult. Therefore in RWG MoM, S_0 is subdivided into small triangular flat patches. Fig. 2.3 depicts discretization of an open surface (Fig. 2.3a) into a mesh of flat triangular elements (Fig. 2.3b). The highlighted edge in Fig. 2.3b, is an arbitrary edge in the mesh and it represents the red line depicted in the true geometry in Fig. 2.3a. From physics of EM fields, it is known that the unknown field $\mathbf{J}^{\mathrm{e}}$ over the PEC, should not result in spurious accumulation of charge density in the vicinity of this hypothetical line. Therefore, the current flowing into this line must be the same as the current flowing out of this line. In other words, the net current flowing into this hypothetical line should be zero, or equivalently current continuity should be preserved across the edge depicted in Fig. 2.3b. Defining basis functions that enforce continuity of current, will help accurately model the physics of the unknown field (i.e. $\mathbf{J}^{\mathrm{e}}$) yielding more accurate numerical results.

In 1982, S. M. Rao, D. R. Wilton, and A. W. Glisson, proposed the use of a special type of basis functions (later known as RWG basis functions due the authors' names)

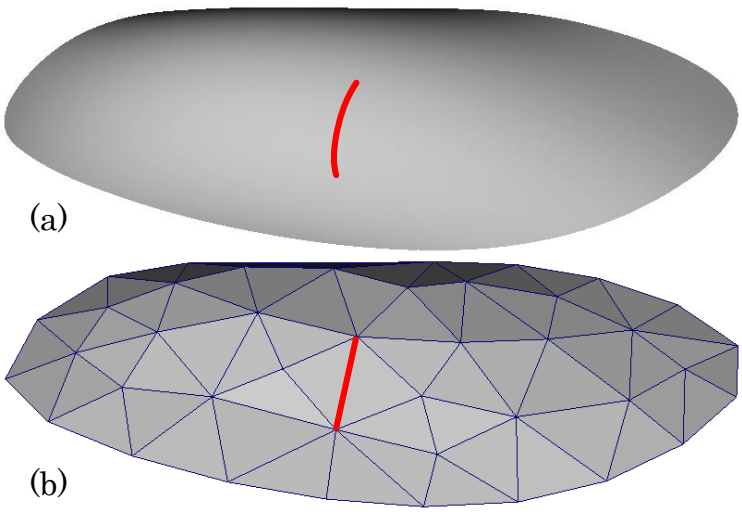

Figure 2.3: Discretization of an open surface PEC with the aid of flat triangular elements. The highlighted edge in (a) is an arbitrary curved hypothetical line on the true geometry, which is represented in the mesh (b) by a flat edge between two triangles. According to physics of EM fields, the unknown field of the EFIE ($\mathbf{J}^{\mathrm{e}}$) should not result in accumulation of charge on this edge. RWG basis functions ensure that all the non-boundary edges in (b) are free of charge and hence improve the accuracy of the numerical method.

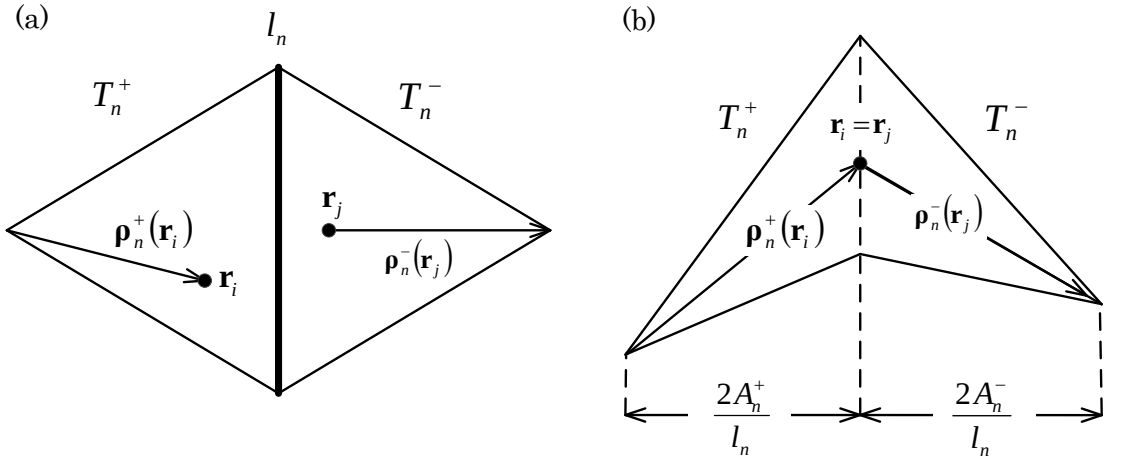

Figure 2.4: (a) Elements of RWG basis functions described in (2.50). (b) Depiction of the normal component of RWG basis functions.

when discretizing the EFIE via the MoM [23]. They are defined as

$$\mathbf{f}_n(\mathbf{r}) = \begin{cases} \frac{l_n}{2A_n^+}\boldsymbol{\rho}_n^+(\mathbf{r}), & \mathbf{r} \in T_n^+ \\ \frac{l_n}{2A_n^-}\boldsymbol{\rho}_n^-(\mathbf{r}), & \mathbf{r} \in T_n^- \\ 0, & \text{otherwise} \end{cases} \tag{2.50}$$

where $A_n^\pm$ is the area of triangle $T_n^\pm$, l_n is the length of the edge, and $\boldsymbol{\rho}_n^\pm(\mathbf{r})$ are the position vectors defined with respect to the free vertex of $T_n^\pm$ as depicted in Fig. 2.4. The RWG basis functions defined in (2.50), have the following important characteristics:

1. In a pair of triangles (Fig. 2.4a or b), the normal component of $\mathbf{f}_n$ is zero on all edges, except on the common edge which has length l_n.

2. On the common edge, the normal component of $\boldsymbol{\rho}_n^\pm$ has magnitude of $\frac{2A_n^\pm}{l_n}$ as seen in Fig. 2.4b. Therefore, the normal component of $\mathbf{f}_n$ is normalized to 1 in the vicinity of the common edge (e.g. $\mathbf{r}_i = \mathbf{r}_j$ in Fig. 2.4b) and is continuos

across the common edge.

The above characteristics, ensure that all edges of T_n^+ and T_n^- are free of line charges and hence no spurious charge will be produced as a result of using RWG basis functions in discretizing the EFIE. This can be further elaborated by analysing the surface charge density on the triangle pair shown in Fig. 2.4 which can be computed as the surface divergence of $\mathbf{f}_n$. By representing the RWG basis functions in (2.50) in the Cartesian coordinates, it can be shown that the surface divergence of $\mathbf{f}_n$ is (see Section 9.13 in [39])

$$\nabla_{\parallel} \cdot \mathbf{f}_n(\mathbf{r}) = \begin{cases} \frac{l_n}{A_n^+}, & \mathbf{r} \in T_n^+ \\ \frac{-l_n}{A_n^-}, & \mathbf{r} \in T_n^- \\ 0, & \text{otherwise} \end{cases} . \tag{2.51}$$

This shows that the charge density is independent of the position vector $\mathbf{r}$ in each triangle. Moreover, by summing (2.51) over the surface of T_n^+ and T_n^-, it can be seen that the net charge on the surface of each triangle pair is zero $\frac{l_n}{A_n^+} A_n^+ - \frac{l_n}{A_n^-} A_n^- = 0$ ensuring no spurious accumulation of charge over the triangle pair.

2.3.3 RWG versus Half RWG Basis Functions

By knowing that the RWG basis functions in (2.50) are defined for a pair of triangles and there are three basis functions (edges) associated with each triangle, for a closed geometry[1], the total number of RWG basis functions becomes $N = 1.5P$ where P is the total number of triangles. Therefore the matrix equation in (2.46) has the size of $N = 1.5P$, and the interactions defined in (2.48) may be referred to as RWG-to-RWG interactions. It is also possible to define RWG MoM discretization, based

[1]To simplify discussion, it is assumed that the geometry is closed.

on ramp-function $\mathbf{R}$ definition of RWG basis functions [51] which are defined on an individual triangle rather than a pair of triangles. In Chapter 3 we use ramp-functions in forming RWG MoM system as it facilitates establishing equivalence between RWG MoM and first-order LCN. By comparing the ramp-functions $\mathbf{R}_k$ in Fig. 3.1b and the RWG functions in Fig. 2.4, it is realized that depending on the direction of the nth RWG basis function on the pth triangle, the kth ramp-function is $\mathbf{R}_k^p = \pm\mathbf{f}_n$. Interactions defined based on $\mathbf{R}$ rather than $\mathbf{f}$ are referred to as ramp-to-ramp (or *half* RWG) interactions and can form a $3P$-size impedance matrix. As discussed in Chapter 3, such impedance matrix can be converted to $[Z]$ using sparse matrix converters.

2.4 Discretizing the EFIE using the LCN scheme

Chapters 3 and 4 are dedicated to establishing equivalence between RWG MoM and LCN discretizations of the EFIE in its vector-potential and mixed-potential forms. In doing so, the exact relationship of the first- and zeroth-order LCN to respectively vector-potential and scalar-potential in RWG MoM is derived. Reference [1] gives a clear description of the discretization of the EFIE using arbitrary order LCN using the standard approach [18, 19]. In order to avoid repetitions, we refer the reader to [1] for such discussion. In the next section, we give a somewhat new description of the LCN scheme for discretizing an arbitrary scalar kernel.

2.5 A New Way of Describing The Locally Corrected Nyström Method

In this section, we give a new approach to describing the LCN method for discretizing a general scalar kernel with the hope that it complements the already existing descriptions of the LCN method [1, 18, 19, 55].

2.5.1 History of LCN

Simply put, the locally-corrected Nyström (LCN) method is the generalization of the classical Nyström method so as to compute IEs with singular kernels. To elaborate, the Nyström method is an old procedure which was introduced in the year 1930 [52, 55] that converts an IE into a sum where appropriate quadrature rules are used to compute the sum. However, the Nyström method can not be used to numerically compute IEs with singular kernels. In 1998 [19], the Nyström method was generalized in order for it to be able to handle singular kernels such as the EFIE and the magnetic field integral equation (MFIE) by "locally correcting" the quadrature rule of interest. As such, this new method was given the name "locally-corrected" Nyström (LCN) method.

2.5.2 Quadrature Rules

Chances are, that the reader of this dissertation is already familiar with how quadrature rules are used, or even how they are defined. However, for the sake of a smooth understanding of the LCN method, we start from explaining how a quadrature rule for a 2D surface is used and defined. A quadrature rule can be used

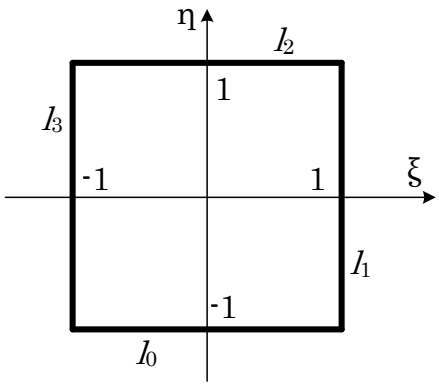

Figure 2.5: The canonical quadrilateral. Any quadrilateral in the 3D domain $\mathbf{r}(\xi, \eta)$ can be mapped into the canonical domain (ξ, η).

to approximate an integral over the canonical quadrilateral (Fig. 2.5) as follows[1]

$$\sum_{q=0}^{Q-1} w_q f(\xi_q, \eta_q) \simeq \int_{-1}^{1}\int_{-1}^{1} f(\xi, \eta) d\xi d\eta \tag{2.52}$$

where Q is the number of quadrature points over the 2D surface (ξ_q, η_q), w_q are the weights, and $f(\xi, \eta)$ is the known integrand and can be computed everywhere including (ξ_q, η_q). Note that any arbitrary quadrilateral can be mapped into the canonical quadrilateral using coordinate transformation in 3D (i.e. $\mathbf{r}(\xi, \eta) = (x, y, z)^T$) for a particular geometry modelling such as curvilinear elements [42, 96], non-uniform rational b-spline (NURBS) surfaces [122], Bézier elements [121, 122], or mapping a cube to an exact sphere [54]. Therefore (2.52) can be used to approximate integrals over an arbitrary 2D surface with 4 edges including both flat and curvilinear elements as depicted in Figs. 1.2c and 1.2d by applying the Jacobian of the transformation $\sqrt{g}$ from $f(\xi, \eta)$ to $f(\mathbf{r}(\xi, \eta))$ [1, 42]. By looking at (2.52) one can realize that in order to define a quadrature rule, for a given Q, one has to define/compute two sets of parameters.

[1]Note that quadrature rules can be applied to triangular 2D surfaces such as the work of Chapter 6, but here we limit our discussion to quadrilateral 2D elements.

1) The quadrature points with abscissas (ξ_q, η_q), and 2) the weights w_q at the quadrature points. It is possible to define the abscissas right on the boundary or outside of the canonical domain $|\xi|, |\eta| \geq 1$ [136], but such quadrature points are not suitable for LCN and therefore we assume $-1 < \xi, \eta < 1$. Once the quadrature abscissas are determined, one can use different methods to compute the corresponding quadrature weights. Depending on the position of the quadrature points, a 2D quadrature rule with Q points can exactly integrate polynomials of up to some degree over the 2D domain and usually as Q increases, so does the degree to which integration can be performed without any error (exact integration). It is to be noted that if a function can not be represented by a polynomial of finite degree (as the electromagnetic fields often are), using a quadrature rule to integrate such integrand will always result in numerical error. However, by increasing the order of the quadrature rule[1], one can approximate the integral to a prescribed accuracy which in turn increases the number of quadrature points Q and hence the computational complexity.

2.5.2.1 Obtaining 2D Quadrature Weights Analytically

One way to populate the surface of the 2D domain by quadrature points, is to use the product of 1D rules. Therefore it is important to discuss the order of 1D rules. If equidistant points are used, the corresponding 1D $\mathcal{Q}$ point quadrature rule is of order $\mathcal{P} = \mathcal{Q} - 1$ if $\mathcal{Q}$ is even. But if $\mathcal{Q}$ is odd these types of quadrature rules can exactly integrate polynomials of up to degree $\mathcal{P} = \mathcal{Q}$. Quadrature rules with equidistant points are also called Newton-Cotes rules [133, 134] and are the earliest forms of quadrature rules. Later, Gauss observed that by not restricting the quadrature abscissas on equidistant points, it is possible to create quadrature rules

[1] A quadrature rule is said to be of order n if it can exactly integrate polynomials of up to the nth degree.

Table 2.1: Quadrature abscissas $\mathcal{X}_i$ and weights $\mathcal{W}_i$ for 1D Gauss-Legendre rules having $\mathcal{Q}$ quadrature points.

$\mathcal{Q}$	i	$\mathcal{W}_i$	$\mathcal{X}_i$
1	0	2	0
2	0	1	-0.57735026918963
2	1	1	0.57735026918963
3	0	0.55555555555556	-0.77459666924148
3	1	0.88888888888889	0
3	2	0.55555555555556	0.77459666924148
4	0	0.34785484513745	-0.86113631159405
4	1	0.65214515486255	-0.33998104358486
4	2	0.65214515486255	0.33998104358486
4	3	0.34785484513745	0.86113631159405

that can provide better accuracy in terms of the number of quadrature points. In fact, one can analytically evaluate [55] both quadrature abscissas and weights for a 1D $\mathcal{Q}$ point quadrature rule that can integrate polynomials of up to degree $2\mathcal{Q}-1$ which is considerably higher than the order of Newton-Cotes rules. These types of quadrature rules are referred to as *Gauss-Legendre* quadrature rules and their product are typically used when numerical evaluation of integrals over quadrilaterals are performed. This is primality due to their high performance in terms of quadrature points (hence unknowns) with respect to the accuracy as well as the fact that arbitrary order Gauss-Legendre quadrate rules can be obtained. In other words, there is no limitation in increasing $\mathcal{Q}$ and obtaining a 1D Gauss-Legendre rule with order $2\mathcal{Q}-1$. Therefore, in this section we limit our discussion to Gauss-Legendre rules[1].

Table 2.1 tabulates the ith quadrature abscissa $-1 < \mathcal{X}_i < 1$ and weight $\mathcal{W}_i$ for a $\mathcal{Q}$ point 1D Gauss-Legendre rule. The tabulated $\mathcal{X}_i$ and $\mathcal{W}_i$ can be computed analytically for arbitrary values of $\mathcal{Q}$ [53]. If we use the 3-point 1D Gauss-Legendre rule in Table 2.1 in both dimensions of the 2D coordinate system (ξ, η), we are

[1] In Chapter 6 we apply Newton-Cotes rules to Bézier triangles which are in the form of degenerate quadrilaterals.

Table 2.2: The $Q = 9$ point 2D Gauss-Legendre quadrature abscissas (ξ_q, η_q) and weights w_q formed by the product of $\mathcal{Q} = 3$ point 1D Gauss-Legendre rule. Note that $\mathcal{W}_0 = 0.55555555555556$, $\mathcal{W}_1 = 0.88888888888889$, $\mathcal{W}_2 = 0.55555555555556$, $\mathcal{X}_0 = -0.77459666924148$, $\mathcal{X}_1 = 0$, and $\mathcal{X}_2 = 0.77459666924148$ are taken from 1D abscissas and weights of Table 2.1 for the case of $\mathcal{Q} = 3$. The same weights w_q can numerically be obtained with machine precision as explained in the next subsection (Section 2.5.2.2) and given in Equation (2.61).

$\mathcal{Q}$	Q	q	w_q	η_q	ξ_q
3	$\mathcal{Q}^2 = 9$	0	$\mathcal{W}_0 \cdot \mathcal{W}_0 = 0.30864197530865$	$\mathcal{X}_0$	$\mathcal{X}_0$
3	$\mathcal{Q}^2 = 9$	1	$\mathcal{W}_0 \cdot \mathcal{W}_1 = 0.49382716049383$	$\mathcal{X}_0$	$\mathcal{X}_1$
3	$\mathcal{Q}^2 = 9$	2	$\mathcal{W}_0 \cdot \mathcal{W}_2 = 0.30864197530865$	$\mathcal{X}_0$	$\mathcal{X}_2$
3	$\mathcal{Q}^2 = 9$	3	$\mathcal{W}_1 \cdot \mathcal{W}_0 = 0.49382716049383$	$\mathcal{X}_1$	$\mathcal{X}_0$
3	$\mathcal{Q}^2 = 9$	4	$\mathcal{W}_1 \cdot \mathcal{W}_1 = 0.79012345679013$	$\mathcal{X}_1$	$\mathcal{X}_1$
3	$\mathcal{Q}^2 = 9$	5	$\mathcal{W}_1 \cdot \mathcal{W}_2 = 0.49382716049383$	$\mathcal{X}_1$	$\mathcal{X}_2$
3	$\mathcal{Q}^2 = 9$	6	$\mathcal{W}_2 \cdot \mathcal{W}_0 = 0.30864197530865$	$\mathcal{X}_2$	$\mathcal{X}_0$
3	$\mathcal{Q}^2 = 9$	7	$\mathcal{W}_2 \cdot \mathcal{W}_1 = 0.49382716049383$	$\mathcal{X}_2$	$\mathcal{X}_1$
3	$\mathcal{Q}^2 = 9$	8	$\mathcal{W}_2 \cdot \mathcal{W}_2 = 0.30864197530865$	$\mathcal{X}_2$	$\mathcal{X}_2$

effectively creating 2D Gauss-Legendre rule using the product of 3-point 1D Gauss-Legendre rules. Such product results in a 2D Gauss-Legendre quadrature rule with the abscissas and weights tabulated in Table. 2.2 and depicted in Fig. 2.6.

In order to examine the performance of the 2D quadrature rule defined in Table 2.2, we consider integrating the polynomial $F^p(\xi, \eta)$ which has degree p and is formed by the sum of $K = (p+1)(p+2)/2$ functions that span the space of monomials[1]

$$\xi^i \eta^j,\ i = 0..p,\ j = 0..p - i. \tag{2.53}$$

[1]In this section, monomials $\xi^i \eta^j$ are used to facilitate easer implementation by the reader, Legendre polynomials can also be used in (2.53), (2.57), (2.58), and (2.65).

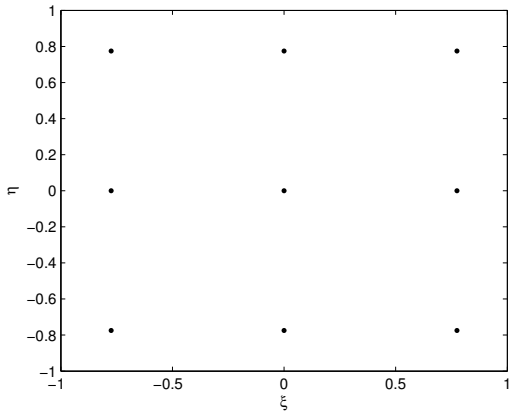

Figure 2.6: Depiction of the abscissas in Table 2.2.

It has the form of *binomial expansion* and for $p = 0..4$, the polynomial is

$$
\begin{aligned}
F^0(\xi,\eta) &= 1 \\
F^1(\xi,\eta) &= 1+\xi+\eta \\
F^2(\xi,\eta) &= 1+\xi+\eta+\xi^2+\xi\eta+\eta^2 \\
F^3(\xi,\eta) &= 1+\xi+\eta+\xi^2+\xi\eta+\eta^2+\xi^3+\xi^2\eta+\xi\eta^2+\eta^3 \\
F^4(\xi,\eta) &= 1+\xi+\eta+\xi^2+\xi\eta+\eta^2+\xi^3+\xi^2\eta+\xi\eta^2+\eta^3+\xi^4+\xi^3\eta+\xi^2\eta^2+\xi\eta^3+\eta^4.
\end{aligned}
\tag{2.54}
$$

Here, we use the quadrature rule of Table 2.2 on $F^p(\xi,\eta)$ with different values of p. Therefore in (2.52) we have $Q = 9$, $f(\xi,\eta) = F^p(\xi,\eta)$, and w_q, ξ_q, η_q that are tabulated in Table 2.2. The relative error is tabulated in Table 2.3 which is computed as

$$
\mathrm{Err}^p = \frac{|\sum_{q=0}^{8} w_q F^p(\xi_q,\eta_q) - \int_{-1}^{1}\int_{-1}^{1} F^p(\xi,\eta)d\xi d\eta|}{|\int_{-1}^{1}\int_{-1}^{1} F^p(\xi,\eta)d\xi d\eta|} \tag{2.55}
$$

where the double integration is done using adaptive integration routines to machine

Table 2.3: The relative error (2.55) associated with a $Q = 9$ point 2D Gauss-Legendre rule obtained from the product of 1D Gauss-Legendre rules with $\mathcal{Q} = 3$ points, when integrating an integrand of order p.

$\mathcal{Q}$	Q	p	Err^p
3	9	0	9.99200722162641E-015
3	9	1	1.01030295240889E-014
3	9	2	7.72715225139109E-015
3	9	3	7.72715225139109E-015
3	9	4	4.89404435344967E-015
3	9	5	4.89404435344967E-015
3	9	6	1.76039119804376E-002
3	9	7	1.76039119804377E-002

precision[1]. From Table 2.3, it can clearly be seen that a 9-point 2D Gauss-Legendre rule ($Q = 9$) that is created by the product of 3-point 1D Gauss-Legendre rules ($\mathcal{Q} = 3$), can exactly integrate the polynomial of up to the 5th degree ($p = 5$). This is consistent with the behaviour expected from a 2D Q-point Gauss-Legendre rule obtained from the product of $\mathcal{Q}$-point 1D Gauss-Legendre rules. In particular, if a 2D Gauss-Legendre rule uses $\mathcal{Q}$-point 1D Gauss-Legendre rules in both directions of the coordinate system, it is expected to exactly integrate polynomials of up to order $2\mathcal{Q} - 1$ over the 2D domain. Therefore, to integrate a polynomial of degree p, there exists a computationally optimal 2D Gauss-Legendre quadrature rule that can perform the integration over the 2D domain with machine precision.

[1]By recursively subdividing the integration domain (hence the term "adaptive"), quadrature rules such as Gauss-Legendre rules can provide results with machine precision due to reducing the size of the domain and irrespective of the order of the applied quadrature rule. The smaller the integration domain, the smaller the variations of the integrand over the considered domain. Therefore for an arbitrary small integration domain, practically *any* given function can exactly be approximated with polynomial of order p for which a quadrature rule of order p exists to exactly integrate it. Adaptive integration is accurate but time consuming as it applies quadrature rules to many small enough intervals in order to produce results with prescribed precision. Mathematical software packages (e.g. PTC Mathcad [36]) use adaptive integrations to compute an integral with an accuracy prescribed by the user.

2.5.2.2 Obtaining 2D Quadrature Weights Numerically

Instead of finding the quadrature weights and abscissas analytically demonstrated in the previous subsection, it is also possible to find the weights numerically by assuming that the quadrature abscissas are known. This can be obtained by solving the linear system

$$\begin{bmatrix} S_0^0 & S_1^0 & \dots & S_{Q-1}^0 \\ S_0^1 & S_1^1 & \dots & S_{Q-1}^1 \\ \vdots & \vdots & \ddots & \vdots \\ S_0^{K-1} & S_1^{K-1} & \dots & S_{Q-1}^{K-1} \end{bmatrix} \cdot \begin{bmatrix} w_0 \\ w_1 \\ \vdots \\ w_{Q-1} \end{bmatrix} = \begin{bmatrix} b_0 \\ b_1 \\ \vdots \\ b_{K-1} \end{bmatrix} \quad \Rightarrow \quad [S]^{-1} \cdot [b] = [w] \quad (2.56)$$

where the matrix on the left hand side $[S]$ is called the "Vandermonde Matrix" [6] and has entries

$$S_q^k = \xi_q^i \eta_q^j, \quad i = 0..p, \quad j = 0..p \tag{2.57}$$

This means that we have $k = 0...(p+1)^2 - 1$ and thus in (2.56) we have $K = (p+1)^2$. By choosing $Q = K$, the Vandermonde matrix becomes square. The order of the Vandermonde system in (2.56) is dictated by the order of the resulting polynomial in (2.57) and since $K = Q$, the order of the Vandermonde matrix is at least p as a polynomial complete to order p requires only $j = 0..p - i$ seen in (2.53) and (2.54). A 2D Vandermonde matrix can analytically be inverted [6]. However, due to its relatively small size, it is computationally efficient to obtain $[S]^{-1}$ numerically, by for example LU-Decomposition. Entries of the right hand side b_k are

$$b_k = \int_{-1}^{1} \int_{-1}^{1} \xi^i \eta^j d\xi d\eta, \quad i = 0..p, \quad j = 0..p \tag{2.58}$$

where the double integration can be computed adaptively using quadrature rules.

Now we solve the the linear system in (2.56) to obtain the weights of Table 2.2. Since $K = Q = 9$, $[S]$ becomes a (9×9) matrix which has order $p = 2$ as $i, j = 0, 1, 2$. Note that this order $p = 2$ is different from the order $2\mathcal{Q} - 1$ in which the resulting quadrature weights can exactly compute the polynomials of up to that order. Using (2.57) the resulting Vandermonde matrix is

$$[S] = \begin{bmatrix} 1 & 1 & 1 & 1 & 1 & 1 & 1 & 1 & 1 \\ -x_1 & -x_1 & -x_1 & 0 & 0 & 0 & x_1 & x_1 & x_1 \\ x_2 & x_2 & x_2 & 0 & 0 & 0 & x_2 & x_2 & x_2 \\ -x_1 & 0 & x_1 & -x_1 & 0 & x_1 & -x_1 & 0 & x_1 \\ x_2 & 0 & -x_2 & 0 & 0 & 0 & -x_2 & 0 & x_2 \\ -x_3 & 0 & x_3 & 0 & 0 & 0 & -x_3 & 0 & x_3 \\ x_2 & 0 & x_2 & x_2 & 0 & x_2 & x_2 & 0 & x_2 \\ -x_3 & 0 & -x_3 & 0 & 0 & 0 & x_3 & 0 & x_3 \\ x_4 & 0 & x_4 & 0 & 0 & 0 & x_4 & 0 & x_4 \end{bmatrix} \tag{2.59}$$

where $x_1 = 0.77459666924148$, $x_2 = 0.59999999999999$, $x_3 = 0.46475800154488$, and $x_4 = 0.35999999999999$. The values of the right hand side are computed using (2.58) and are

$$[b]^T = [4,\ 0,\ y_1,\ 0,\ 0,\ 0,\ y_1,\ 0,\ y_2] \tag{2.60}$$

where the transpose of the matrix is shown to save space, $y_1 = 1.33333333333333$,

and $y_2 = 0.44444444444444$. Finally the weights $[w]$ are computed by (2.56) as

$$[w] = \begin{bmatrix} 0.30864197530865 \\ 0.49382716049383 \\ 0.30864197530865 \\ 0.49382716049383 \\ 0.79012345679011 \\ 0.49382716049383 \\ 0.30864197530865 \\ 0.49382716049383 \\ 0.30864197530865 \end{bmatrix} \tag{2.61}$$

which are exactly (with machine precision) the same as those analytically found in Section 2.5.2.1 (Table 2.2).

2.5.3 The Nyström Method

Consider the integral equation

$$\phi(\mathbf{r}) = \int_S K(\mathbf{r}, \mathbf{r}') J(\mathbf{r}') ds' \tag{2.62}$$

which can be used to evaluate the unknown function J over the surface S where ϕ and K are known functions. Assuming that K is smooth, the Nyström method can be used to evaluate such integral equation by first discretizing the surface S into N_p smaller pieces (elements)

$$\phi(\mathbf{r}) = \sum_{p=1}^{N_p} \int_{S_p} K(\mathbf{r}, \mathbf{r}') J(\mathbf{r}') ds'. \tag{2.63}$$

Such geometry discretization is done as S is so large and $\int_S K(\mathbf{r},\mathbf{r}')J(\mathbf{r}')ds'$ in (2.62) can not be approximated using the quadrature rules explained in Section 2.5.2. Therefore, S is broken into N_p elements so that the value of $\int_{S_p} K(\mathbf{r},\mathbf{r}')J(\mathbf{r}')ds'$ in (2.63) can accurately be evaluated over S_p using quadrature rules as follows

$$\phi(\mathbf{r}_{q_m}) = \sum_{p=1}^{N_p}\sum_{q=1}^{N_q} w_{q_p} K(\mathbf{r}_{q_m},\mathbf{r}_{q_p})J(\mathbf{r}_{q_p}) \tag{2.64}$$

where $\mathbf{r}_{q_m}$ is the qth quadrature point on the observation patch m, $\mathbf{r}_{q_p}$ is the qth quadrature point on the source patch p, and w_{q_p} is the qth quadrature weight on the source element p. The system of linear algebraic equation in (2.64) has size $(N_pN_q \times N_pN_q)$ and can be numerically evaluated to obtain the the values of J at the quadrature points $J(\mathbf{r}_q)$.

It is important to note that the weights w_{q_p} in (2.64) are exactly the weights of the chosen quadrature rule such as the Gauss-Legendre rules discussed in Section 2.5.2. These weights are sometimes referred to as *regular* weights they belong to regular quadrature rules (e.g. Gauss-Legendre rules). Therefore, it is more efficient to obtain the weights for the Nyström method analytically (Section 2.5.2.1), store them in a lookup table and use them in (2.64).

2.5.4 The Generalized Nyström Method

The procedure of the Nyström method is valid so long as the kernel K in (2.62) to (2.64) is smooth. Therefore it can not be applied to problems with singular or near-singular kernels such as the Green's function of the EM. By analyzing the Nyström method, one can realize[1] that it is possible to generalize this method to a method that

[1]The structure of this entire section (Section 2.5) is laid out in its current form to facilitate this realization. This is a key point in understanding LCN and thus expressed explicitly here.

is applicable to any arbitrary kernel $\tilde{K}$ (singular or smooth) by numerically obtaining the weights (Section 2.5.2.2) where the desired kernel $\tilde{K}$ is applied to (2.58) to obtain the right hand side[1]

$$\tilde{b}_k = \int_{-1}^{1}\int_{-1}^{1} \tilde{K} \cdot \xi^i \eta^j d\xi d\eta, \quad i = 0..p, \quad j = 0..p \tag{2.65}$$

Subsequently, by using the values of (2.65), the following system can obtain weights $\tilde{w}_q$ capable of computing the integral with singular or non-singular kernels

$$\begin{bmatrix} S_0^0 & S_1^0 & \dots & S_{Q-1}^0 \\ S_0^1 & S_1^1 & \dots & S_{Q-1}^1 \\ \vdots & \vdots & \ddots & \vdots \\ S_0^{K-1} & S_1^{K-1} & \dots & S_{Q-1}^{K-1} \end{bmatrix} \begin{bmatrix} \tilde{w}_0 \\ \tilde{w}_1 \\ \vdots \\ \tilde{w}_{Q-1} \end{bmatrix} = \begin{bmatrix} \tilde{b}_0 \\ \tilde{b}_1 \\ \vdots \\ \tilde{b}_{K-1} \end{bmatrix} \tag{2.66}$$

where the entries of the Vandermonde matrix $[S]$ are the same as those in (2.57). Therefore the system of linear algebraic equations of the generalized Nyström Method can be written as

$$\phi(\mathbf{r}_{q_m}) = \sum_{p=1}^{N_p}\sum_{q=1}^{N_q} \tilde{w}_{q_p,q_m} J(\mathbf{r}_{q_p}) \tag{2.67}$$

where it is noticed that the weights $\tilde{w}_{q_p,q_m}$ are dependent on both the observation and source points. This means that unlike the Nyström method, these generalized weights $\tilde{w}_q$ can not be precomputed, but has to be computed for each pair of q_m and q_p and the desired kernel $\tilde{K}$, i.e. $\tilde{K}(\mathbf{r}_{q_m}, \mathbf{r}_{q_p})$. The Vandermonde matrix $[S]$ on the other hand is unique for a given order (quadrature abscissas) and its inverse can be precomputed and used to solve (2.66) for all cases of $\tilde{K}(\mathbf{r}_{q_m}, \mathbf{r}_{q_p})$. Therefore inverting $[S]$ numerically (e.g. LU-Decomposition) would not alter the computational efficiency

[1] In other words, the regular quadrature weights in Section 2.5.2.2 are obtained by assuming that $\tilde{K} = 1$ in (2.65) and are thus only applicable to smooth kernels.

of such method.

In this thesis, we call this procedure, the "generalized" Nyström method as it is a generalization of the Nyström method from smooth kernels to arbitrary kernels. It can also be called the "globally-corrected" Nyström method as opposed to the "locally-corrected" Nyström method explained next.

2.5.5 The Locally Corrected Nyström Method

The generalized Nyström Method, is not computationally efficient as it does not allow for the use of regular weights w_q in the system of linear algebraic equations. However, the Green's functions of the EM, become smooth as the distance between the source element p and observation point q_m grows. Therefore, the LCN method [19] suggests the use of the Nyström method when the separation between q_m and p is so large ($p \in$ far) that the kernel is smooth, and the use of the generalized Nyström method, when ($p \in$ near) and the weights has to be "locally-corrected"[1] due to the singular behaviour of the kernel for near source element p and observation point q_m. Mathematically this can be written as

$$\phi(\mathbf{r}_{q_m}) = \sum_{p\in\text{far}} \sum_{q=1}^{N_q} w_{q_p} K(\mathbf{r}_{q_m}, \mathbf{r}_{q_p}) J(\mathbf{r}_{q_p}) + \sum_{p\in\text{near}} \sum_{q=1}^{N_q} \tilde{w}_{q_p,q_m} J(\mathbf{r}_{q_p}) \tag{2.68}$$

where $\{\text{near}\} \cup \{\text{far}\} = \{1, ..., N_p\}$. The $(N_p N_q \times N_p N_q)$ system of linear algebraic equations in (2.68) can be solved to obtain the values of J at the quadrature points. The solution can then be interpolated locally (see (16)-(18) in [19]) over a given patch p to obtain the solution at an arbitrary point on S_p.

The order of the LCN method, is indicated by the order of the Vandermonde

[1] Locally-corrected as opposed to globally-corrected performed in the generalized Nyström method.

matrix p in (2.66). Typically, the characteristic size of the elements is denoted as h. The error in (2.68) behaves according to the convergence rate $\mathcal{O}(h^p)$[1] and thus by increasing N_p (h-refinement) and/or N_q (p-refinement) the accuracy of (2.68) can be increased to a prescribed precision.

2.6 Conclusion

In this chapter we reviewed the basic mathematical formulas behind SIE formulation techniques. In particular, we derived the EFIE all the way from Maxwell's equations in order to present a concise overview of how an integral equation formulation is derived. We also reviewed the nature of RWG basis functions and explained the motivation towards using them when discretizing the EFIE. A new way of describing the LCN method was also given as a complementary note to LCN descriptions available in the literature. In the following two chapters, RWG basis functions are used in conjunction with the LCN method when discretizing the vector-potential EFIE and the mixed-potential EFIE, respectively. The resulting numerical schemes combine the benefits of the RWG basis functions and the point-based nature of the LCN method.

[1] In Section 5.3.1 we show that in practice a more general convergence rate should be defined for LCN and we introduce an experimental procedure in Section 5.3.2 that can accurately approximate it.

Chapter 3

On the Equivalence of RWG Method of Moments and the Locally Corrected Nyström Method for Solving the Electric Field Integral Equation

Abstract

The first-order locally corrected Nyström (LCN) method for the electric field integral equation is modified to ensure continuity of the current between triangular elements of the mesh. Rao-Wilton-Glisson (RWG) basis functions are used to create a conversion matrix from the LCN representation of the current to the RWG method of moments (MoM) representation of the current in order to enforce continuity of current between adjacent triangular flat patches. Benefits of the method are two fold: first, it provides 4 times reduction in degrees of freedom and removes unacceptable error levels in first-order LCN implementations, second, the method can be viewed as a point-based discretization of the RWG MoM offering improved efficiency in its acceleration with the fast multipole algorithm.

3.1 Introduction

Today's design of wireless communication systems such as antennas and microwave circuits critically relies on accurate electromagnetic analysis. While there are many techniques available for such analysis in general, those based on the numerical solution of integral equations [1, 5, 17–23, 25, 26, 46–49] become an exclusive choice when pertinent models are electrically large [5]. Solutions to such problems have recently become possible due to the advent of fast iterative [5–9] and direct [10, 12, 14] matrix implicit algorithms.

Discretization of integral equations can be performed in either point-based [1, 18, 19, 25, 26, 47, 48] or element-based [17, 21–23] manners and under either low-order (LO) or higher-order (HO) approximations of the solution. HO solution methods have an advantage over their LO counterparts by being exponentially more efficient [1] when controlling the accuracy beyond one or two digits is required. The trade-off, however, is that HO methods may be substantially more difficult to implement as they require preservation of the desired accuracy throughout all stages of the numerical scheme including: the mesh based representation of the geometry, choice of basis functions approximating the unknown field, rules for integration of reaction integrals, evaluation of matrix-vector products, and possibly others [1].

Point-based methods are particularly suitable for efficient acceleration by the multilevel fast multipole algorithm (MLFMA) [19, 25, 26, 49] since they allow for the construction of an imbalanced oct-tree structure with the depth of the tree adapted to the disparity in point sampling density over the mesh [7, 24]. Classical element-based (or basis-based) method of moments (MoM) discretization schemes [20, 21, 23] do not allow for such adaptation without being cast into a point-based form [25, 26] and therefore render analysis of multiscale models inefficient even when fast algorithms

are employed. Because of this adaptivity point-based methods such as the locally corrected Nyström (LCN) method [1,18,19,46–49] or quadrature sampled MoM techniques [5,25,26] (aka point-matched MoM [18,20]) are the methods of choice when HO solutions of large multiscale problems are required. The major disadvantage of the LCN discretization is that it does not enforce current continuity across element boundaries unlike MoM discretization schemes for which construction of hierarchical basis function spaces can be used to maintain field continuity at all orders [21]. While enforcing continuity at the boundaries between elements makes only a minor impact on the solution accuracy at HOs, incorporating field continuity at LOs may affect the accuracy profoundly [1], [46]. Consequently, MoM achieves a certain accuracy with fewer unknowns when orders lesser than 3 are sought for the solution of the electric field integral equation (EFIE) in both 2D [46] and 3D [1]. Thus it is difficult to justify using LCN for the solution of the EFIE at LOs (i.e. order 1 and 2). In particular, a first-order LCN solution of the EFIE is often substantially less accurate when compared to its first-order Rao-Wilton-Glisson (RWG) MoM counterpart [1], despite using four times as many degrees of freedom per element[1].

Nevertheless, one can conclude from [18] that MoM and LCN are equivalent solutions if the following four conditions are met: (1) the same complete set of polynomials of order P is preserved in both dimensions of the surface coordinate system in MoM's basis functions as well as the LCN's local correction procedure yielding equal number of degrees of freedom in both methods, (2) the MoM's testing integrals are approximated with fixed-point quadratures of the same order P as the underlying quadrature rule of the LCN, (3) the same near and far regions are defined in both methods, and (4) the same numerical techniques are used to evaluate the near field integrals. Under

[1]See comment by Prof. Gedney in Section 7.2.6.1.

these conditions LCN can be viewed as a particular point-based discretization of a special case of MoM. In this paper, we extend this equivalence to the case of RWG MoM and first-order LCN discretizations on triangular elements by establishing an exact relationship between matrices of these two unequally sized systems. Such equivalence allows to eliminate the loss of accuracy in first-order LCN discretization of the EFIE and reduce the number of degrees of freedom. Specifically, sparse matrices are introduced such that their pre- and post-multiplications of the LCN generated impedance matrix produces exactly the RWG MoM impedance matrix. The latter is one quarter of the size of the original LCN impedance matrix and at the same time produces more accurate solutions due to current continuity enforcement. The introduced method can also be viewed as an alternative to the point-matched MoM for casting the element-based RWG MoM into the form of a point-based discretization which both preserves the continuity of current between adjacent mesh elements and is more suitable for acceleration by the MLFMA.

This chapter is organized as follows. Sections 3.2 and 3.3 present a description of the LCN method and RWG MoM, respectively. These sections provide sufficient details of the near and far contributions to the LCN and RWG MoM impedance matrices with the goal of explicitly identifying the relationship between the two systems. Section 3.4 provides derivations of basis conversion matrices that allow conversion from the LCN system to the RWG MoM system. Section 3.5 presents the numerical results demonstrating the exactness of the derived conversion from LCN to RWG MoM, and demonstrates the impact of enforcing continuity of current on the accuracy of the first-order LCN discretization of the EFIE and the conditioning of its impedance matrix.

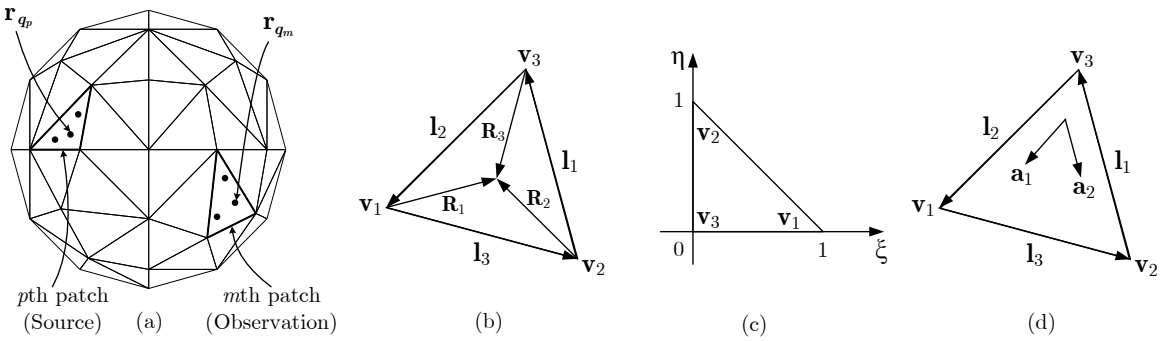

Figure 3.1: (a) Point-based discretization of a PEC scatterer using triangular flat patches (mesh), (b) "Half" RWG basis or ramp functions ($\mathbf{R}_1, \mathbf{R}_2, \mathbf{R}_3$), (c) Barycentric triangle, and (d) Covariant unitary vectors $\mathbf{a}_1$ and $\mathbf{a}_2$ on a flat triangular patch with reduced size ($a_1 = l_2,\ a_2 = l_1$).

3.2 The Locally Corrected Nyström Method

In this section we present the LCN formulation of the EFIE in order to compare it to the RWG MoM system. Additional details on the LCN method can be found in [19] and [18].

3.2.1 LCN Formulation

From the equivalence principle [39], the EFIE governing the induced electric current density on a PEC scatterer described by a surface S is expressed as

$$\mathbf{t}(\mathbf{r}) \cdot \int_S \overline{\mathbf{G}}(\mathbf{r}, \mathbf{r}') \cdot \mathbf{J}(\mathbf{r}') ds' = -\mathbf{t}(\mathbf{r}) \cdot \mathbf{E}^{\text{inc}}(\mathbf{r}),\ \mathbf{r} \in S \tag{3.1}$$

where $\overline{\mathbf{G}}$ is the dyadic Green's function[1] [40], $\mathbf{t}(\mathbf{r})$ is an arbitrary test vector tangential to S and $\mathbf{E}^{\text{inc}}$ is the incident electric field. The LCN method in general is capable of being formulated for practically arbitrary surface discretizations but in this work we

[1]Note that in Chapter 2, this dyadic Green's function is denoted as $\overline{\mathbf{G}}_{e0}$, but here the subscripts are omitted as this chapter only deals with the dyadic Green's function of the electric type in free-space.

restrict ourselves to triangular flat patches to establish its equivalence to RWG MoM. Thus, the surface S is discretized into N_p triangular flat patches

$$\mathbf{t}(\mathbf{r}) \cdot \sum_{p=1}^{N_p} \int_{S_p} \overline{\mathbf{G}}(\mathbf{r}, \mathbf{r}') \cdot \mathbf{J}(\mathbf{r}') ds' = -\mathbf{t}(\mathbf{r}) \cdot \mathbf{E}^{\text{inc}}(\mathbf{r}) \tag{3.2}$$

In the LCN method, testing is done by means of the covariant unitary vectors[1] tangential to the surface defined as in [42]

$$\mathbf{a}_1 = \frac{\partial \mathbf{r}}{\partial \xi}, \; \mathbf{a}_2 = \frac{\partial \mathbf{r}}{\partial \eta} \tag{3.3}$$

where the surface of the patch is locally defined by a two-dimensional space (ξ, η). Note that for a given flat patch, $\mathbf{a}_1$ and $\mathbf{a}_2$ are constant. Testing the vector integral equation in (3.2) yields a pair of scalar integral equations

$$\mathbf{a}_i^m \cdot \sum_{p=1}^{N_p} \int_{S_p} \overline{\mathbf{G}}(\mathbf{r}, \mathbf{r}') \cdot \mathbf{J}(\mathbf{r}') ds' = -\mathbf{a}_i^m \cdot \mathbf{E}^{\text{inc}}(\mathbf{r}) \tag{3.4}$$

where $i = 1, 2$ and the superscript m indicates that $\mathbf{a}_i^m$ corresponds to the observation patch m. In order to numerically solve (3.4), $\mathbf{J}$ is expanded over $\mathbf{a}_1$ and $\mathbf{a}_2$ ($\mathbf{J}(\mathbf{r}) = J^1(\mathbf{r})\mathbf{a}_1 + J^2(\mathbf{r})\mathbf{a}_2$)[2] and a set of observation points is enforced

$$\mathbf{a}_i^m \cdot \sum_{p=1}^{N_p} \int_{S_p} \overline{\mathbf{G}}(\mathbf{r}_{q_m}, \mathbf{r}') \cdot \left[J^1(\mathbf{r}')\mathbf{a}_1^p + J^2(\mathbf{r}')\mathbf{a}_2^p \right] ds' = -\mathbf{a}_i^m \cdot \mathbf{E}^{\text{inc}}(\mathbf{r}_{q_m}) \tag{3.5}$$

[1] Covariant unitary vectors do not necessarily have unit length and the term *unitary* is due to their relation to some other set of basis functions. This will be shown later in (3.34).

[2] Generally in the LCN method this is divided by the Jacobian $\sqrt{g}$ which is beneficial since it will cancel the Jacobian when the surface integral in (3.4) is mapped into barycentric (ξ, η) coordinates. In this work however, $\sqrt{g}$ is constant (twice the area) over triangular flat patches and will be omitted from our notation.

where the observation points $\mathbf{r}_{q_m}$ are chosen to be at the abscissa of the qth quadrature point on the observation patch m (Fig. 3.1a) which will result in a square system of equations when the integration in (3.5) is approximated by an N_q-point quadrature rule. Due to its singular behaviour, the kernel $\overline{\mathbf{G}}$ in (3.5) becomes a rapidly varying function as the separation between the source and observation patches decreases[1]. Thus the integral in (3.5) cannot be approximated to a desired precision with a fixed quadrature rule for the nearby source and observation triangles. This is circumvented by employing a "locally-corrected" quadrature rule such that a set of underlying polynomials weighted by the singular kernel are integrated exactly to a given precision[2] [19]. In the LCN method it is possible to use any arbitrary N_q-point quadrature rule. However, in this work we limit ourselves to a 3-point quadrature rule required for establishing its equivalence to RWG MoM. Hence (3.5) is discretized as

$$\begin{aligned}\sum_{p\in\text{far}(m)}\sum_{q_p=1}^{3}\left[\omega^{i1}_{q_m q_p}.J^1(\mathbf{r}_{q_p})+\omega^{i2}_{q_m q_p}.J^2(\mathbf{r}_{q_p})\right]+\\ \sum_{p\in\text{near}(m)}\sum_{q_p=1}^{3}\left[\tilde{\omega}^{i1}_{q_m q_p}.J^1(\mathbf{r}_{q_p})+\tilde{\omega}^{i2}_{q_m q_p}.J^2(\mathbf{r}_{q_p})\right]=-\mathbf{a}_i^m\cdot\mathbf{E}^{\text{inc}}(\mathbf{r}_{q_m})\end{aligned} \tag{3.6}$$

where $\omega^{ij}_{q_m q_p}$ and $\tilde{\omega}^{ij}_{q_m q_p}$ are the standard and locally-corrected weights, respectively, evaluated for observation point $\mathbf{r}_{q_m}$ and source point $\mathbf{r}_{q_p}$. Here, $i=1,2$ corresponds to testing with $\mathbf{a}_i$ and $j=1,2$ indicates the projection of current $\mathbf{J}$ on $\mathbf{a}_j$. The locally-corrected quadrature rule effectively "corrects" the standard 3-point quadrature scheme in order to evaluate the singular integrals. For consistency between the two sets of weights, the abscissa points of the locally-corrected quadrature rule with

[1]This is true for every individual observation point $\mathbf{r}_{q_m}$ and source patch p. However, throughout this paper and without loss of generality, we define near and far regions based on the distance between the centroids of the source and observation elements to simplify notations.

[2]See Prof. Gedney's comment in Section 7.2.6.2.

weights $\tilde{\omega}$ are chosen to be the same as those in the standard "regular" quadrature rule having weights ω. This ensures that the unknowns are the same and is required for implementing the MLFMA.

3.2.2 LCN System

The discretized EFIE in (3.6) is a linear system of $6N_p$ equations with $6N_p$ unknowns which can be written in matrix form as

$$[Z_{\text{LCN}}] \cdot [J] = [E] \tag{3.7}$$

where $[J]$ and $[E]$ are the vectors of unknown coefficients and the right-hand-side, respectively, and $[Z_{\text{LCN}}]$ is the impedance matrix and has the form

$$[Z_{\text{LCN}}] = \begin{bmatrix} [Z_{11}^{\text{far}}] & [Z_{12}^{\text{far}}] \\ [Z_{21}^{\text{far}}] & [Z_{22}^{\text{far}}] \end{bmatrix} + \begin{bmatrix} [Z_{11}^{\text{near}}] & [Z_{12}^{\text{near}}] \\ [Z_{21}^{\text{near}}] & [Z_{22}^{\text{near}}] \end{bmatrix} \tag{3.8}$$

where $[Z_{ij}^{\text{far}}]$ and $[Z_{ij}^{\text{near}}]$ are respectively filled with regular quadrature weights ω^{ij} and locally-corrected quadrature weights $\tilde{\omega}^{ij}$. In the standard LCN procedure, an iterative or a direct linear solver is applied to (3.7) without attempting to enforce continuity of the current.

3.2.3 LCN Local Interactions

3.2.3.1 Far field

Referring back to (3.6), the q_m, q_pth entry of a (3×3) matrix $[\omega^{ij}]$ defining the interactions between far patches m and p is simply

$$[\omega^{ij}]_{q_m,q_p} = \omega_{q_m}\omega_{q_p}\mathbf{a}_i^m \cdot \overline{\mathbf{G}}(\mathbf{r}_{q_m}, \mathbf{r}_{q_p}) \cdot \mathbf{a}_j^p \tag{3.9}$$

where ω_{q_n} is the standard quadrature weight associated with the abscissa point $\mathbf{r}_{q_n}$ on patch n. Note that unlike standard LCN, the observation weight ω_{q_m} is included in (3.9) (also later in (3.11)) in order to permit observation patch integrals analogous to RWG MoM[1]. A (6×6) element-to-element[2] (local) impedance matrix for far patches m and p can be defined as

$$[\omega] = \begin{bmatrix} [\omega^{11}] & [\omega^{12}] \\ [\omega^{21}] & [\omega^{22}] \end{bmatrix} \tag{3.10}$$

3.2.3.2 Near field

To solve for the weights $\tilde{\omega}^{ij}_{q_m q_p}$, a set of scalar basis functions $F_k(\mathbf{r})$ are distributed over the source patch such that $\mathbf{J}_k^j(\mathbf{r}) = F_k(\mathbf{r})\mathbf{a}_j$. In this work we limit ourselves up to order one basis functions $(k = 1, 2, 3)$ on triangular flat patches to establish LCN equivalence to RWG MoM. Thus, we use $F_1(\mathbf{r}) = 1$, $F_2(\mathbf{r}) = \xi(\mathbf{r})$ and $F_3(\mathbf{r}) = \eta(\mathbf{r})$ as the basis functions where ξ and η are barycentric coordinates defined on a triangle as shown in Fig. 3.1c. These basis functions formed by the monomials (ξ, η) are generally preferred on triangular patches due to their simplicity and effectiveness [19]

[1] See Prof. Gedney's comment in Section 7.2.6.3.

[2] The term *element-to-element* refers to the interactions between quadrature points on the source and observation elements (Fig. 3.1a) and should not be interpreted as LCN being an element-based method.

but here they are particularly adopted since they can be used to exactly represent RWG basis functions as shown later in (3.30). The (3×3) matrix of the locally-corrected quadrature weights $[\tilde{\omega}^{ij}]$ defining the interactions between near patches m and p can then be obtained by solving the system

$$\sum_{q_p=1}^{3} \tilde{\omega}^{ij}_{q_m q_p} F_{k'}(\mathbf{r}_{q_p}) = \omega_{q_m} \mathbf{a}_i^m \cdot \int_{S_p} \overline{\mathbf{G}}(\mathbf{r}_{q_m}, \mathbf{r}') \cdot \mathbf{J}^j_{k'}(\mathbf{r}') ds' \tag{3.11}$$

where $i, j \in \{1, 2\}$ and $q_m \in \{1, 2, 3\}$. The small linear (3×3) system of equations in (3.11) can be solved to determine the locally-corrected weights $\tilde{\omega}^{ij}_{q_m q_p}$ that will accurately integrate all currents described by $\mathbf{J}^j_{k'}(\mathbf{r}')$. In matrix form, (3.11) for $q_m, k' = 1, 2, 3$ can be written as

$$[L] \cdot [\tilde{\omega}^{ij}]^T = [\tilde{\boldsymbol{\kappa}}^j]^T \cdot [\mathbf{a}_i^m] \tag{3.12}$$

where superscript T denotes transposition and the $((3 \times 3) \times (3 \times 1))$[1] matrix $[\mathbf{a}_i^m] = [\mathrm{diag}(\mathbf{a}_i^m)]$ is local to patch m. The q_m, k'th entry of the $((3 \times 3) \times (3 \times 1))$ matrix $[\tilde{\boldsymbol{\kappa}}^j]$ is

$$[\tilde{\boldsymbol{\kappa}}^j]_{q_m, k'} = \omega_{q_m} \int_{S_p} \overline{\mathbf{G}}(\mathbf{r}_{q_m}, \mathbf{r}') \cdot \mathbf{J}^j_{k'}(\mathbf{r}') ds'. \tag{3.13}$$

In (3.12), $[L]$ is a (3×3) Vandermonde matrix [50] independent of both the source and observation patches[2] with the k, q_nth entry $[L]_{k,q_n} = F_k(\mathbf{r}_{q_n})$. We can now define

[1] The notation $((A \times B) \times (C \times D))$ indicates that the matrix has $(A \times C)$ elements and each element has $(B \times D)$ entries making the actual size of the matrix $(AB \times CD)$. The same convention is used throughout the paper.

[2] Generally in LCN, $[L]$ is dependent on the source patch due to the possibility of mixed-order basis function sets, but in this work we have a unique (3×3) matrix since we limited the work to $F_1(\mathbf{r})$, $F_2(\mathbf{r})$ and $F_3(\mathbf{r})$ required for the equivalence.

a (6×6) element-to-element impedance matrix for near patches m and p as

$$[\tilde{\omega}] = [\mathbf{a}_m]^T \cdot \left[[\tilde{\boldsymbol{\kappa}}^1] \, [\tilde{\boldsymbol{\kappa}}^2] \right] \cdot \left([F]^{-1} \right)^T \tag{3.14}$$

where the $((3 \times 3) \times (6 \times 1))$ matrix $[\mathbf{a}_m]$ is local to patch m and is defined as

$$[\mathbf{a}_m] = \left[\; [\mathrm{diag}(\mathbf{a}_1^m)] \, [\mathrm{diag}(\mathbf{a}_2^m)] \; \right] \tag{3.15}$$

In (3.14), the (6×6) matrix $[F]$ is

$$[F] = [\mathrm{diag}([L])] \tag{3.16}$$

and its inverse $[F]^{-1}$ can be obtained analytically as $[L]$ is a two-dimensional Vandermonde-type system [6]. We would like to note here that the form of $[\tilde{\omega}]$ in (3.14) is chosen to facilitate establishing equivalence between RWG MoM and LCN near interactions.

3.3 RWG Method of Moments

3.3.1 RWG MoM Formulation

Consider again (3.1) and (3.2). In RWG MoM, the surface current $\mathbf{J}(\mathbf{r}')$ is approximated using RWG basis function expansion on patch p

$$\mathbf{J}(\mathbf{r}') \simeq \sum_{k'=1}^{3} b_{k'}^p \mathbf{R}_{k'}^p(\mathbf{r}'), \; \mathbf{r}' \text{ in patch } p \tag{3.17}$$

where $b_{k'}^p$ are the current coefficients to be determined numerically. Since only a single triangular element is considered, $\mathbf{R}_1^p$, $\mathbf{R}_2^p$ and $\mathbf{R}_3^p$ are referred to as "half"

RWG basis or ramp functions (Fig. 3.1b) [51] as opposed to the conventional RWG basis functions which are defined for a pair of triangles and are formed by two ramp functions [23]. The ramp functions are chosen here since they facilitate establishing equivalence between first-order LCN and RWG MoM. By plugging (3.17) into (3.2), and knowing that the current coefficients $b_{k'}^{p}$ are constant over an individual cell, RWG MoM converts the EFIE into

$$\mathbf{t}(\mathbf{r}) \cdot \sum_{p=1}^{N_p} \sum_{k'=1}^{3} b_{k'}^{p} \int_{S_p} \overline{\mathbf{G}}(\mathbf{r}, \mathbf{r}') \cdot \mathbf{R}_{k'}^{p}(\mathbf{r}) ds' = -\mathbf{t}(\mathbf{r}) \cdot \mathbf{E}^{\text{inc}}(\mathbf{r}) \tag{3.18}$$

Next, Galerkin's testing is performed by taking the inner product of (3.18) with the three ramp functions $\mathbf{R}_{k}^{m}(\mathbf{r})$ on the observation triangle S_m

$$\int_{S_m} \mathbf{R}_{k}^{m}(\mathbf{r}) \cdot \left[\sum_{p=1}^{N_p} \sum_{k'=1}^{3} b_{k'}^{p} \int_{S_p} \overline{\mathbf{G}}(\mathbf{r}, \mathbf{r}') \cdot \mathbf{R}_{k'}^{p}(\mathbf{r}') ds' \right] ds = - \int_{S_m} \mathbf{R}_{k}^{m}(\mathbf{r}) \cdot \mathbf{E}^{\text{inc}}(\mathbf{r}) ds \tag{3.19}$$

where $k \in \{1, 2, 3\}$ and $m, p \in \{1, 2, ..., N_p\}$. The subscripts k, k' are the ramp index defined on the observation patch m and source patch p, respectively. Now a linear system can be formed by approximating the outer integrals on both sides of (4.3)

$$\begin{aligned} &\sum_{q_m=1}^{3} \omega_{q_m} \mathbf{R}_{k}^{m}(\mathbf{r}_{q_m}) \cdot \left[\sum_{p=1}^{N_p} \sum_{k'=1}^{3} b_{k'}^{p} \int_{S_p} \overline{\mathbf{G}}(\mathbf{r}_{q_m}, \mathbf{r}') \cdot \mathbf{R}_{k'}^{p}(\mathbf{r}') ds' \right] \\ &= - \sum_{q_m=1}^{3} \omega_{q_m} \mathbf{R}_{k}^{m}(\mathbf{r}_{q_m}) \cdot \mathbf{E}^{\text{inc}}(\mathbf{r}) \end{aligned} \tag{3.20}$$

where the first-order approximation (3-point quadrature rule) is used as it allows us to establish equivalence with the first-order LCN formulation.

3.3.2 RWG-MoM System

The linear system of equations in (3.20) can be written in matrix form as

$$[z] \cdot [b] = [v] \tag{3.21}$$

where $[b]$ (unknown coefficients) and $[v]$ (right-hand-side terms) are $(3N_p \times 1)$ matrices and $[z]$ is the $(3N_p \times 3N_p)$ impedance matrix. Even though the linear system defined in (3.21) can be solved as is, it does not produce satisfactory results since it does not enforce continuity of the current across triangle edges. Therefore RWG MoM enforces continuity of the current between elements by casting (3.21) into the form

$$\begin{aligned} \Big([u]^T \cdot [z] \cdot [u]\Big) \cdot [I] &= \Big([u]^T \cdot [v]\Big) \\ [Z] \cdot [I] &= [V] \end{aligned} \tag{3.22}$$

where the $(3N_p \times 1.5N_p)$ sparse matrix $[u]$ unifies ramp functions into RWG functions[1]. The $1.5N_p$-size linear system in (3.22) can be solved using an iterative or a direct linear solver to obtain $[I]$ and finally the ramp basis function coefficients are obtained by $[b] = [u] \cdot [I]$ which gives the solution to the current $\mathbf{J}(\mathbf{r}')$ via (3.17). It is important to realize that $[Z]$ in (3.22) is 4 times smaller than $[Z_{\text{LCN}}]$ in (3.7) but the RWG MoM linear system produces more accurate results since it preserves continuity of the current across cell boundaries.

[1] To simply discussion and without loss of generality, it is assumed that $3N_p$ is divisible by 2 and the geometry is closed. Since two ramp functions contribute to an RWG function, each column of $[u]$ has two non-zero entries; 1 if the ramp and RWG functions have the same direction, and -1 otherwise.

3.3.3 RWG MoM Local Interactions

To fill out the $(3N_p \times 3N_p)$ impedance matrix $[z]$, the left side of (3.20) is reduced to obtain the ramp-to-ramp (local) interactions between patches m and p

$$\sum_{q_m=1}^{3} \omega_{q_m} \mathbf{R}_k^m(\mathbf{r}_{q_m}) \cdot \int_{S_p} \overline{\mathbf{G}}(\mathbf{r}, \mathbf{r}') \cdot \mathbf{R}_{k'}^p(\mathbf{r}') ds' \tag{3.23}$$

3.3.3.1 Far field

In the case that the observation patch m and source patch p are well separated, the kernel of the integral in (3.23) is smooth and is approximated by a fixed-order quadrature rule. To establish equivalence with first-order LCN, the same first-order quadrature rule used for LCN is applied

$$\sum_{q_m=1}^{3} \omega_{q_m} \mathbf{R}_k^m(\mathbf{r}_{q_m}) \cdot \sum_{q_p=1}^{3} \omega_{q_p} \overline{\mathbf{G}}(\mathbf{r}_{q_m}, \mathbf{r}_{q_p}) \cdot \mathbf{R}_{k'}^p(\mathbf{r}_{q_p}) \tag{3.24}$$

In matrix form, the ramp-to-ramp (3×3) impedance matrix for far patches m and p can be expressed as

$$[z_{mp}^{\text{far}}] = [\mathbf{R}_m]^T \cdot [\overline{\mathbf{g}}] \cdot [\mathbf{R}_p] \tag{3.25}$$

where the q_m, q_pth element of the $((3 \times 3) \times (3 \times 3))$ matrix $[\overline{\mathbf{g}}]$ is

$$[\overline{\mathbf{g}}]_{q_m, q_p} = \omega_{q_m} \omega_{q_p} \overline{\mathbf{G}}(\mathbf{r}_{q_m}, \mathbf{r}_{q_p}) \tag{3.26}$$

and the $((3\times3)\times(3\times1))$ matrix $[\mathbf{R}_n]$ is local to the nth patch and its q_n, kth element is $[\mathbf{R}_n]_{q_n,k} = \mathbf{R}_k^n(\mathbf{r}_{q_n})$.

3.3.3.2 Near field

For the near field region, the convolutional integral in (3.23) must be performed to the desired precision (2 digits). Thus the contribution to the ramp-to-ramp (3×3) impedance matrix for near patches m and p is expressed as

$$[z_{mp}^{\text{near}}] = [\mathbf{R}_m]^T \cdot [\tilde{\mathbf{g}}] \tag{3.27}$$

where the q_m, k'th entry of the $((3 \times 3) \times (3 \times 3))$ matrix $[\tilde{\mathbf{g}}]$ is

$$[\tilde{\mathbf{g}}]_{q_m,k'} = \omega_{q_m} \int_{S_p} \overline{\mathbf{G}}(\mathbf{r}_{q_m}, \mathbf{r}') \cdot \mathbf{R}_{k'}^p(\mathbf{r}') ds'. \tag{3.28}$$

Note that the RWG MoM described above discretizes the vector-potential EFIE as opposed to the mixed-potential EFIE [56], where the dyadic kernel in (3.28) is decomposed into vector- and scalar-potentials and further simplification of the scalar-potential is possible [23]. The vector-potential EFIE is adopted here since it is the one used in the standard LCN formulation and is required for the sought equivalence.

3.4 RWG MoM via first-order LCN : RWG-via-LCN

In this section, we establish exact relationships between ramp-to-ramp RWG MoM impedance matrices $([z_{mp}^{\text{far}}], [z_{mp}^{\text{near}}])$ and the first-order element-to-element LCN impedance matrices $([\omega], [\tilde{\omega}])$ using local conversion matrices. The resulting convertors will then be used to derive RWG MoM from the first-order LCN discretization, hence the name "RWG-via-LCN". RWG-via-LCN is a discretization method that com-

bines the benefits of both the point-based LCN formulation and current continuity of RWG MoM.

3.4.1 RWG-via-LCN Formulation

By comparing (3.13) and (3.28) it is recognized that a relationship must be established between $\mathbf{J}^j_{k'}(\mathbf{r}')$ and $\mathbf{R}^p_{k'}(\mathbf{r}')$ in order to formulate RWG-via-LCN. Therefore we begin by relating the basis functions used in the two methods. Supressing the notational dependence on element p for simplicity, the three ramp functions $\mathbf{R}_k$ can be represented by a cyclic rotation

$$\mathbf{R}_{i+1}(\mathbf{r}) = \frac{l_{i+1}}{2A}[\mathbf{l}_{\underline{i+2}+1}\mathcal{S}_{\underline{i+1}+1}(\mathbf{r}) - \mathbf{l}_{\underline{i+1}+1}\mathcal{S}_{\underline{i+2}+1}(\mathbf{r})] \tag{3.29}$$

where $i \in \{0,1,2\}$ and the underline represents the modulo 2 operation ($\underline{x} = x \bmod 2$). In (3.29), $\mathcal{S}_1$, $\mathcal{S}_2$ and $\mathcal{S}_3$ are the element shape functions [57], l_k is the length of the vector defined on the kth edge $\mathbf{l}_k$ as shown in Fig. 3.1b and A is the triangle area. By mapping the triangle in Fig. 3.1b to the barycentric triangle (Fig. 3.1c) we have $\mathcal{S}_1 = \xi$, $\mathcal{S}_2 = \eta$ and $\mathcal{S}_3 = 1 - \xi - \eta$. Note also that $\mathbf{l}_1 = -\mathbf{a}_2$, $\mathbf{l}_2 = \mathbf{a}_1$ and $\mathbf{l}_3 = \mathbf{a}_2 - \mathbf{a}_1$ as depicted in Fig. 3.1d where the size of $\mathbf{a}_1$ and $\mathbf{a}_2$ are reduced to enhance visibility. Therefore we can rewrite (3.29) in terms of $F_k(\mathbf{r})$ and $\mathbf{a}_i$

$$\begin{aligned}
\mathbf{R}_1(\mathbf{r}) &= \frac{l_1}{2A}[-F_1(\mathbf{r})\mathbf{a}_1 + F_2(\mathbf{r})\mathbf{a}_1 + F_3(\mathbf{r})\mathbf{a}_2] \\
\mathbf{R}_2(\mathbf{r}) &= \frac{l_2}{2A}[-F_1(\mathbf{r})\mathbf{a}_2 + F_2(\mathbf{r})\mathbf{a}_1 + F_3(\mathbf{r})\mathbf{a}_2] \\
\mathbf{R}_3(\mathbf{r}) &= \frac{l_3}{2A}[F_2(\mathbf{r})\mathbf{a}_1 + F_3(\mathbf{r})\mathbf{a}_2].
\end{aligned} \tag{3.30}$$

Thus $[\mathbf{R}_n]$ in (3.25) can be written as

$$[\mathbf{R}_n] = [\mathbf{a}_n] \cdot [F]^T \cdot [\psi_n] \tag{3.31}$$

where $[\mathbf{a}_n]$ and $[F]$ are defined in (3.15) and (3.16), respectively. In (3.31), the (6×3) matrix $[\psi_n]$ belongs to patch n and is constructed using (3.30)

$$[\psi_n] = \begin{bmatrix} -1 & 0 & 0 \\ 1 & 1 & 1 \\ 0 & 0 & 0 \\ 0 & -1 & 0 \\ 0 & 0 & 0 \\ 1 & 1 & 1 \end{bmatrix} \cdot \begin{bmatrix} \frac{l_1}{2A} & 0 & 0 \\ 0 & \frac{l_2}{2A} & 0 \\ 0 & 0 & \frac{l_3}{2A} \end{bmatrix} \tag{3.32}$$

where the first three rows of $[\psi_n]$ represent $F_1(\mathbf{r})\mathbf{a}_1$, $F_2(\mathbf{r})\mathbf{a}_1$ and $F_3(\mathbf{r})\mathbf{a}_1$, the second three rows represent $F_1(\mathbf{r})\mathbf{a}_2$, $F_2(\mathbf{r})\mathbf{a}_2$ and $F_3(\mathbf{r})\mathbf{a}_2$, and the kth column is for $\mathbf{R}_k$.

Next, consider the reciprocal unitary vectors defined in [42] as follows[1]:

$$\mathbf{a}^1 = \mathbf{a}_2 \times \hat{\mathbf{n}},\ \mathbf{a}^2 = \hat{\mathbf{n}} \times \mathbf{a}_1 \tag{3.33}$$

where $\mathbf{a}_1, \mathbf{a}_2$ are defined in (3.3) and $\hat{\mathbf{n}}$ is normal to the surface. The reciprocal unitary vectors $\mathbf{a}^i$ in (3.33) are constant for a given flat patch and form a complete reciprocal vector basis function space with the unitary vectors of (3.3) on patch n such that

$$\mathbf{a}_n^i \cdot \mathbf{a}_j^n = \delta_{ij} \tag{3.34}$$

[1]See Prof. Gedney's correction to equation (3.33) in Section 7.2.6.4.

where $\mathbf{a}_n^i$ and $\mathbf{a}_i^n$ are defined for patch n and δ_{ij} is the Kronecker-Delta[1]. Using (3.34) one can show that

$$[I_6] = [\boldsymbol{\alpha}_n]^T \cdot [\mathbf{a}_n] \tag{3.35}$$

where $[I_i]$ is the $(i \times i)$ identity matrix and the $((3 \times 3) \times (6 \times 1))$ matrix $[\boldsymbol{\alpha}_n] = [[\text{diag}(\mathbf{a}_n^1)]\ [\text{diag}(\mathbf{a}_n^2)]]$ is local to patch n. It can also be shown that the operator $[\mathbf{a}_n] \cdot [\boldsymbol{\alpha}_n]^T$ is a $((3 \times 3) \times (3 \times 3))$ matrix local to patch n and satisfies[2]

$$[\mathbf{R}_p] = [\mathbf{a}_p] \cdot [\boldsymbol{\alpha}_p]^T \cdot [\mathbf{R}_p] \tag{3.36}$$

Transposing the above equation for patch m will result in

$$[\mathbf{R}_m]^T = [\mathbf{R}_m]^T \cdot [\boldsymbol{\alpha}_m] \cdot [\mathbf{a}_m]^T \tag{3.37}$$

The identities shown in (3.36) and (3.37) will be used in the definition of RWG-via-LCN local interactions explained next.

[1]Kronecker-Delta δ_{ij} is unity when $i = j$ and zero when $i \neq j$.

[2]Although $[\mathbf{a}_n] \cdot [\boldsymbol{\alpha}_n]^T$ is not $[I_9]$, it has (3×3) block diagonal elements with l^2 norm $= 1$ which act like the unit dyad on vectors tangential to the nth patch. This makes the operator local to patch n.

3.4.2 RWG-via-LCN Local Interactions

3.4.2.1 Far field

Substituting (3.36) and (3.37) into (3.25) and noticing that $[\mathbf{a}_m]^T \cdot [\overline{\overline{\mathbf{g}}}] \cdot [\mathbf{a}_p]$ is exactly equal to $[\omega]$ in (3.10) we arrive at

$$[z_{mp}^{\text{far}}] = [\mathbf{R}_m]^T \cdot [\boldsymbol{\alpha}_m] \cdot [\omega] \cdot [\boldsymbol{\alpha}_p]^T \cdot [\mathbf{R}_p] \tag{3.38}$$

Equation (3.38) can be used to convert LCN far interactions $[\omega]$ to RWG MoM far interactions $[z_{mp}^{\text{far}}]$. Fig. 3.2 depicts the construction of global transformation matrices from the local transformation provided above plus unifying ramp functions into RWG functions using $[u]$. Through (3.38), the ramp current coefficients $[b_p]$ can be converted to ramp coefficients at the quadrature points q_p using $[\mathbf{R}_p]$. Then LCN current coefficients $[J_p]$ can be obtained by $[\boldsymbol{\alpha}_p]^T$. Thus a transformation of unknowns from $[b_p]$ to $[J_p]$ is performed by

$$[J_p] = [\boldsymbol{\alpha}_p]^T \cdot [\mathbf{R}_p] \cdot [b_p] \tag{3.39}$$

If we substitute (3.31) into (3.39) and knowing that $[\boldsymbol{\alpha}_p]^T \cdot [\mathbf{a}_p]$ is the identity matrix (3.35), we can write

$$[b_p] = [\psi_p]^\dagger \cdot \left([F]^{-1}\right)^T \cdot [J_p] \tag{3.40}$$

where the superscript † represents the pseudo inverse and $[\psi_p]^\dagger$ can be computed by means of the the generalized inverse [58]. The transformation of unknowns from the ramp basis to the covariant basis (3.39) and vice versa (3.40) will be used in the near field transformations explained next.

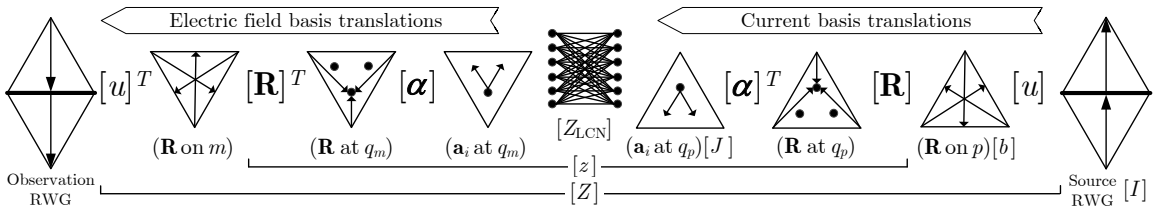

Figure 3.2: Basis translation interpretation of the RWG-via-LCN method (3.50). Reading from right to left, in the current translations, the source RWG current coefficients $[I]$ are converted to ramp current coefficients $[b]$ through $[u]$. With the aid of $[\mathbf{R}]$, the ramp current coefficients $[b]$ are converted to the coefficients of the ramps at the source quadrature points q_p. Then with the help of $[\boldsymbol{\alpha}]^T$, current coefficients $[J]$ of $\mathbf{a}_1$ and $\mathbf{a}_2$ are obtained. Note that in (3.50), conversion from $[b]$ to $[J]$ is done in one step using $[\mathcal{R}] = [\boldsymbol{\alpha}]^T \cdot [\mathbf{R}]$, but here both steps are shown to provide better insight. Translations of the electric field basis will occur in reverse order on the observation triangle m producing RWG electric field coefficients. In the process of conversion, the $(6N_p \times 6N_p)$ first-order LCN impedance matrix $[Z_{\mathrm{LCN}}]$ is converted to the $(3N_p \times 3N_p)$ half RWG MoM impedance matrix $[z]$. Then, by enforcing continuity of the current on $[z]$ the $(1.5N_p \times 1.5N_p)$ RWG MoM impedance matrix $[Z]$ is obtained. Using the depicted conversion, despite a point-based discretization of the EFIE in $[Z_{\mathrm{LCN}}]$, element-based current coefficients $[b]$ are determined and can be used to obtain the current anywhere on a patch using (3.17).

3.4.2.2 Near field

The three RWG MoM's ramp functions $\mathbf{R}_k$ in (3.30) can parametrically be related to the monomials F_i of the LCN method as follows

$$\mathbf{R}_k(\mathbf{r}) = \sum_{i=1}^{3} x_i^{k1}(\mathbf{r}) F_i(\mathbf{r}) \mathbf{a}_1 + \sum_{i=1}^{3} x_i^{k2}(\mathbf{r}) F_i(\mathbf{r}) \mathbf{a}_2 \tag{3.41}$$

where $k \in \{1, 2, 3\}$ and x_i^{kj} are members of $[\psi_n]$ in (3.32). By substituting (3.41) into (3.28) we can write

$$[\tilde{\mathbf{g}}] = \left[[\tilde{\boldsymbol{\kappa}}^1] \, [\tilde{\boldsymbol{\kappa}}^2] \right] \cdot [\psi_p] \tag{3.42}$$

where $[\tilde{\boldsymbol{\kappa}}^i]$ is identical to that defined in (3.13). If we multiply (3.40) by (3.42), $[\psi_p]$ and $[\psi_p]^\dagger$ will cancel from the right hand side and we get

$$[\tilde{\mathbf{g}}] \cdot [b_p] = \left[[\tilde{\boldsymbol{\kappa}}^1] \, [\tilde{\boldsymbol{\kappa}}^2] \right] \cdot \left([F]^{-1} \right)^T \cdot [J_p] \tag{3.43}$$

Pre-multiplying the left hand side by $[\mathbf{R}_m]$ and the right hand side by an equivalent matrix $[\mathbf{R}_m]^T \cdot [\boldsymbol{\alpha}_m] \cdot [\mathbf{a}_m]^T$ in (3.37) we obtain

$$[\mathbf{R}_m]^T \cdot [\tilde{\mathbf{g}}] \cdot [b_p] = [\mathbf{R}_m]^T \cdot [\boldsymbol{\alpha}_m] \cdot [\mathbf{a}_m]^T \cdot \left[[\tilde{\boldsymbol{\kappa}}^1] \, [\tilde{\boldsymbol{\kappa}}^2] \right] \cdot \left([F]^{-1} \right)^T \cdot [J_p] \tag{3.44}$$

Since $[\mathbf{a}_m]^T \cdot \left[[\tilde{\boldsymbol{\kappa}}^1] \, [\tilde{\boldsymbol{\kappa}}^2] \right] \cdot \left([F]^{-1} \right)^T$ is precisely $[\tilde{\omega}]$ in (3.14) we can write

$$[\mathbf{R}_m]^T \cdot [\tilde{\mathbf{g}}] \cdot [b_p] = [\mathbf{R}_m]^T \cdot [\boldsymbol{\alpha}_m] \cdot [\tilde{\omega}] \cdot [J_p] \tag{3.45}$$

Substituting (3.39) into (3.45) we get

$$[\mathbf{R}_m]^T \cdot [\tilde{\mathbf{g}}] \cdot [b_p] = [\mathbf{R}_m]^T \cdot [\boldsymbol{\alpha}_m] \cdot [\tilde{\omega}] \cdot [\boldsymbol{\alpha}_p]^T \cdot [\mathbf{R}_p] \cdot [b_p] \tag{3.46}$$

Eliminating $[b_p]$ from both sides and using (4.15) we finally get

$$[z_{mp}^{\text{near}}] = [\mathbf{R}_m]^T \cdot [\boldsymbol{\alpha}_m] \cdot [\tilde{\omega}] \cdot [\boldsymbol{\alpha}_p]^T \cdot [\mathbf{R}_p] \tag{3.47}$$

which can be used to exactly convert the LCN near interactions matrix $[\tilde{\omega}]$ to the RWG MoM near interactions matrix $[z_{mp}^{\text{near}}]$. It is interesting to realize that the conversions from first-order LCN to RWG MoM in far (3.38) and near (3.47) regions have the exact same form, making it possible to define a unified global conversion from LCN to RWG MoM explained next.

3.4.3 RWG-via-LCN System

Based on the transformations developed for local interactions in the previous section, we can form a $(3N_p \times 3N_p)$ matrix which is derived from $[Z_{\text{LCN}}]$ in (3.8) and is identical to $[z]$ defined in (3.21) by applying a global conversion from $[Z_{\text{LCN}}]$ to $[z]$

$$[z] = [\mathcal{R}]^T \cdot [Z_{\text{LCN}}] \cdot [\mathcal{R}] \tag{3.48}$$

where $[\mathcal{R}]$ is a $(6N_p \times 3N_p)$ matrix defined as

$$[\mathcal{R}] = \begin{bmatrix} [\mathcal{R}_1^1] & [0] & \dots & [0] \\ [0] & [\mathcal{R}_2^1] & \dots & [0] \\ \vdots & \vdots & \ddots & \vdots \\ [0] & [0] & \dots & \left[\mathcal{R}_{N_p}^1\right] \\ [\mathcal{R}_1^2] & [0] & \dots & [0] \\ [0] & [\mathcal{R}_2^2] & \dots & [0] \\ \vdots & \vdots & \ddots & \vdots \\ [0] & [0] & \dots & \left[\mathcal{R}_{N_p}^2\right] \end{bmatrix}. \tag{3.49}$$

In (3.49), every [0] represents a matrix of (3×3) zeros and $[\mathcal{R}_n^i]$ is a (3×3) matrix defined for the ith unitary vector on patch n with the q_n, kth entry $[\mathcal{R}_n^i]_{q_n,k} = \mathbf{a}_n^i \cdot \mathbf{R}_k^n(\mathbf{r}_{q_n})$. The global conversion formulated in (3.48) shows that the first-order LCN and MoM procedures are equivalent in the sense that an exact relationship between their matrices can be established. This is consistent with [18]. Note however, that here LCN and MoM systems under the study have different sizes and the introduced basis converter (3.49) is a non-square matrix which reduces the degrees of freedom unlike the equivalence shown in [18] for equally sized systems. The continuity of current on (3.48) is then enforced by forming a $(1.5N_p \times 1.5N_p)$ matrix

$$[Z] = [u]^T \cdot [\mathcal{R}]^T \cdot [Z_{\text{LCN}}] \cdot [\mathcal{R}] \cdot [u] \tag{3.50}$$

which is identical to $[Z]$ defined in (3.22). The RWG-via-LCN method (3.50) facilitates transformation of the LCN impedance matrix $[Z_{\text{LCN}}]$ to that of RWG MoM impedance matrix $[Z]$, thus enforcing continuity of current on the LCN method. The

stages of basis conversion are depicted in Fig. 3.2.

3.4.4 RWG-via-LCN Implementation

3.4.4.1 Cancellation of Line Integrals

To compute $[Z_{\text{LCN}}]$ in (3.50), the integration with the dyadic kernel in (3.13) needs to be numerically evaluated. Therefore, it is rewritten as [39]

$$[\tilde{\boldsymbol{\kappa}}^j]_{q_m,k'} = \frac{-j\eta_0\omega_{q_m}}{k_0}\left[k_0^2\cdot\int_{S_p} G(\mathbf{r}_{q_m},\mathbf{r}')\mathbf{J}^j_{k'}(\mathbf{r}')ds' + \nabla\int_{S_p}\nabla G(\mathbf{r}_{q_m},\mathbf{r}')\cdot\mathbf{J}^j_{k'}(\mathbf{r}')ds'\right] \tag{3.51}$$

where G is the free-space Green's function[1]. The first term on the right hand side of (3.51) has a singularity of $\mathcal{O}(1/R)$ and can analytically be computed to controllable accuracy since the triangle is flat [59]. It is also possible to use methods capable of handling both flat and curvilinear triangles [60,61]. By making use of vector identities, the second term can be separated into two parts (see formulas (92)-(94) in [19])

$$\begin{aligned}&\nabla\int_{S_p}\nabla G(\mathbf{r}_{q_m},\mathbf{r}')\cdot\mathbf{J}^j_{k'}(\mathbf{r}')ds' = \\ &\int_{S_p}\nabla G(\mathbf{r}_{q_m},\mathbf{r}')\left[\nabla'_{\|}\cdot\mathbf{J}^j_{k'}(\mathbf{r}')\right]ds' - \oint_{C_p}\left[\hat{e}'_p\cdot\mathbf{J}^j_{k'}(\mathbf{r}')\right]\left[\nabla G(\mathbf{r}_{q_m},\mathbf{r}')\right]dl'\end{aligned} \tag{3.52}$$

where C_p is the contour bounding S_p and $\hat{e}_p$ is the outward normal to C_p tangential to S. The first term on the right hand side of (3.52) is a surface integral which is hypersingular at vanishing separation of the source and observation elements but its order of singularity can be reduced to $\mathcal{O}(1/R)$ (see formulas (95)-(105) in [19] and (32)-(33) in [18]). Since triangles are flat, it can be computed to controllable accuracy

[1]Note that in Chapter 2, this Green's function is denoted as G_0, but here the subscript is omitted as this chapter assumes free-space.

by analytic evaluation of the singular integrals [59]. Other singularity cancellation schemes [60–62] applicable to both flat and curvilinear elements may also be used. Since it is assumed that the quadrature points are interior to S_p and do not lie on the contour C_p, the contour integral in (3.52) is non-singular and can be computed directly using adaptive quadrature. However, in the construction of $[Z]$ using (3.50), the contour integral computed in (3.52) will be cancelled numerically due to the properties of RWG basis functions that is enforced through the conversion. To understand why this cancellation occurs, we need to interpret the exact conversions that take place in relation (3.50). Fig. 3.2 depicts the interpretation of this transformation. From the figure, one may see that through current transformations, RWG coefficients $[I]$ are transformed to LCN coefficients $[J]$. Similarly, in the process of electric field transformations, LCN coefficients will be converted back to RWG coefficients. Thus, through the introduced transformations, $\mathbf{J}^j_{k'}(\mathbf{r}')$ in (3.52) will have the same properties as $\mathbf{R}^p_{k'}(\mathbf{r}')$ which is orthogonal to $\hat{e}'_p$ on two edges along C_p and has the same contribution with opposite sign from the adjacent triangle on the third edge. Consequently $\left[\hat{e}'_p \cdot \mathbf{J}^j_{k'}(\mathbf{r}')\right] = 0$ on two edges of the triangle and the line integrals vanish over these edges. The line integral on the other (third) edge is non-zero but will be cancelled numerically in (3.50) due to the same contribution with opposite sign from the neighbouring triangle. Thus the contour integral in (3.52) may be omitted when filling $[Z_{\text{LCN}}]$ in (3.50). In fact, $[\nabla'_{\parallel} \cdot \mathbf{J}^j_{k'}(\mathbf{r}')]$ is constant on triangular flat patches and (3.52) may be reduced to

$$\left(\nabla'_{\parallel} \cdot \mathbf{J}^j_{k'}\right) \int_{S_p} \nabla G(\mathbf{r}_{q_m}, \mathbf{r}') ds' \tag{3.53}$$

where $(\nabla'_{\parallel} \cdot \mathbf{J}^j_{k'})$ is local to patch p. We would like to note that (3.53) is not applicable to the local conversion of the near field (3.47) since $[z^{\text{near}}_{mp}]$ is defined based on ramp

functions and not RWG functions and preserves the third line integral discussed above.

3.4.4.2 Solving the System

Once the impedance matrix of the LCN method $[Z_{\text{LCN}}]$ is filled according to the descriptions given in this paper or any standard first-order LCN implementation [18, 19] on triangular flat patches, the sparse matrices $[\mathcal{R}]$ and $[u]$ are used according to (3.50) to obtain the RWG-via-LCN's impedance matrix $[Z]$ via sparse matrix-vector products with $\mathcal{O}(N)$ complexity. Then, the system (3.22) can be solved with $[V]$ directly determined by RWG MoM to obtain the numerical solution $[I]$. It is also possible to evaluate the excitation vector via the LCN's right-hand-side $[V] = [u]^T \cdot [\mathcal{R}]^T \cdot [E]$, to accommodate ease of implementation.

3.4.4.3 MLFMA Acceleration

RWG-via-LCN features an important attribute of the LCN scheme, namely the representation of the fundamental interactions in the point-based form. The point-to-point interactions defined in $[Z_{\text{LCN}}]$ (Fig. 3.2) constitute projections of vectors of the scattered electric field produced at the quadrature points by the vector point sources (electric dipoles) located at the same points. As a result, far interactions in the matrix-vector product $[Z_{\text{LCN}}] \cdot [J]$ can be calculated by applying MLFMA to the point interactions which is inherently an *N-body problem* [63]. When accelerating the computation of these interactions with the high frequency MLFMA based on plane wave field expansions, the fact that interactions are point-based, permits more levels to be used in the MLFMA tree when compared to basis-based MoM implementations [64] where the number of MLFMA's levels are limited by the size of the basis functions [26]. Further, accelerated algorithms for RWG-via-LCN can ex-

ploit imbalanced MLFMA trees where the depth is locally adapted to the density of discretization dictated by the model [24].

3.5 Numerical Results

3.5.1 RWG MoM vs. RWG-via-LCN

It is worth noting that all equations presented in Section 3.4 are exact and were numerically confirmed to be accurate down to machine precision. As a comprehensive example, Fig. 3.3 presents the relative deviation of $[Z]$ obtained by RWG-via-LCN (3.50) from its counterpart defined by RWG MoM (3.22), for far and near regions. The mesh has 32 elements producing a (48×48) matrix thus there are totally 48^2 points in the figure. It is clear that the deviations are due to machine precision. This supports the fact that the introduced transformations are exact and the two matrices are computationally equivalent. Thus RWG MoM and RWG-via-LCN yield identical solutions.

3.5.2 RWG-via-LCN vs. LCN

In all simulations herein, both LCN and RWG-via-LCN systems were solved directly by LU-decomposition in order to avoid introducing additional errors into the solutions, ensuring a reliable error analysis. The average and maximum relative errors of the surface transverse currents $\mathbf{J}$ evaluated by LCN and RWG-via-LCN methods

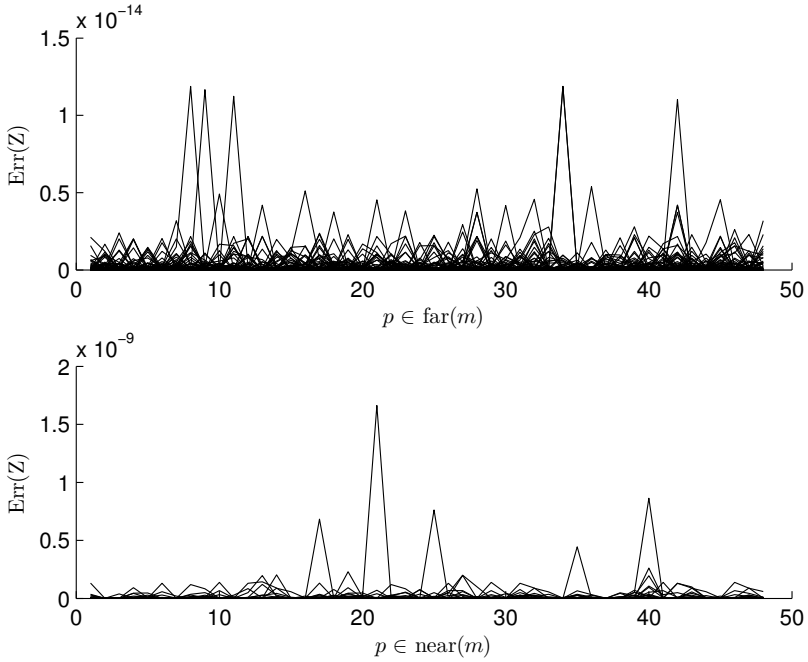

Figure 3.3: Comparison of the (48×48) impedance matrix [Z] obtained by RWG MoM (3.22) and its equivalent counterpart obtained by RWG-via-LCN (3.50) for far and near regions. There are a total of 48^2 points in the figure each corresponding to $\mathrm{Err}(Z_{i,j}) = |Z_{i,j}^{\text{RWG MoM}} - Z_{i,j}^{\text{RWG-via-LCN}}|/|Z_{i,j}^{\text{RWG MoM}}|$ where $i, j = 1, ..., 48$.

were calculated using

$$\begin{aligned} \text{MeanErr}(\mathbf{J}) &= \frac{1}{3N_p}\sum_{i=1}^{3N_p}\frac{\left|J_i^{\text{Num}}-J_i^{\text{Ref}}\right|}{|J_i^{\text{Ref}}|} \\ \text{MaxErr}(\mathbf{J}) &= \max\left[\frac{\left|J_i^{\text{Num}}-J_i^{\text{Ref}}\right|}{|J_i^{\text{Ref}}|}\right],\ i\in\{1,..,3N_p\} \end{aligned} \tag{3.54}$$

respectively, where J_i^{Num} is the current magnitude $|\mathbf{J}|$ at the quadrature points q_m approximated by the numerical solution (LCN or RWG-via-LCN) and J_i^{Ref} is the reference solution at q_m. Analysis of the surface current at the quadrature points q_m is required as LCN is a point-based method and solves for the currents at these points. Deviation from these points requires interpolation [19].

3.5.2.1 Uniform Discretization of a Sphere

The sphere we consider has a radius of $1m$ and is centered at the origin. It is discretized by 4,832 flat surface triangular elements with minimum element size[1] $h_{\min}=0.024m$, maximum element size $h_{\max}=0.065m$ and maximum deviation from the true radius $\epsilon = 1.74\times10^{-3}$. The sphere is excited by the volumetric current $\mathbf{j}=\mathbf{I}\ell\delta(\mathbf{r}-\mathbf{r}')$ of a radial electric dipole with moment $\mathbf{I}\ell=\hat{\mathbf{z}}\cdot 1A\cdot m$ located at $\mathbf{r}'=\hat{\mathbf{z}}\cdot 10$ meters.

Figure 3.4 depicts the time snapshot of the $\hat{\boldsymbol{\theta}}$-directed current density $\hat{\boldsymbol{\theta}}\Re[J_\theta(\theta)e^{-2i\pi ft}]$ at $t=0$ seconds obtained using LCN and RWG-via-LCN methods, due to a time-harmonic excitation at $f=100$MHz. From this figure, it is observed that the current obtained by the LCN method is notably non-smooth compared to the RWG-via-LCN solution. Fig. 3.5 plots the magnitude of the current shown in Fig. 3.4 against the Mie series solution [65] along the meridian of the sphere ($\theta=0^\circ\sim180^\circ$). It

[1]Element size is the radius of the circumscribing circle.

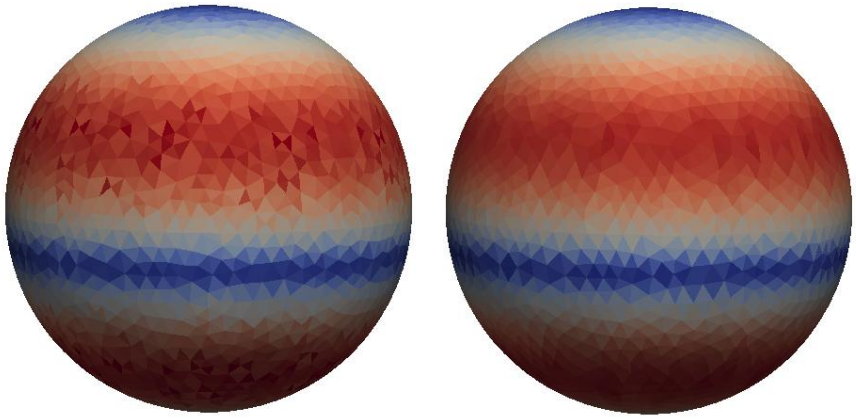

Figure 3.4: Comparison of the $\hat{\boldsymbol{\theta}}$-directed surface current numerically computed by LCN and RWG-via-LCN at $f = 100$MHz. The mesh has 4,832 triangular flat elements. Fig. 3.5 plots the magnitude of the same currents against Mie series as a function of θ.

can be seen that the LCN current deviates severely from the true solution whereas the RWG-via-LCN method provides a smoother solution due to current continuity enforcement. Fig. 3.6 plots the mean and maximum relative errors of the current produced using both LCN and RWG-via-LCN methods estimated by (3.54) at multiple frequencies ($h_{\max} < \lambda/10$) with the reference solution obtained analytically using Mie series. From this figure one can see that at higher frequencies the two methods have similar performance. For lower frequencies, enforcement of current continuity greatly influences the accuracy of the RWG-via-LCN method where the LCN method fails to provide satisfactory performance[1].

As was mentioned earlier, the impedance matrix of the RWG-via-LCN method $[Z]$ is 4 times smaller than that of the LCN method $[Z_{\text{LCN}}]$ due to current continuity enforcement. This lead not only to faster solution due to problem size reduction but

[1]See Prof. Gedney's comment in Section 7.2.6.5.

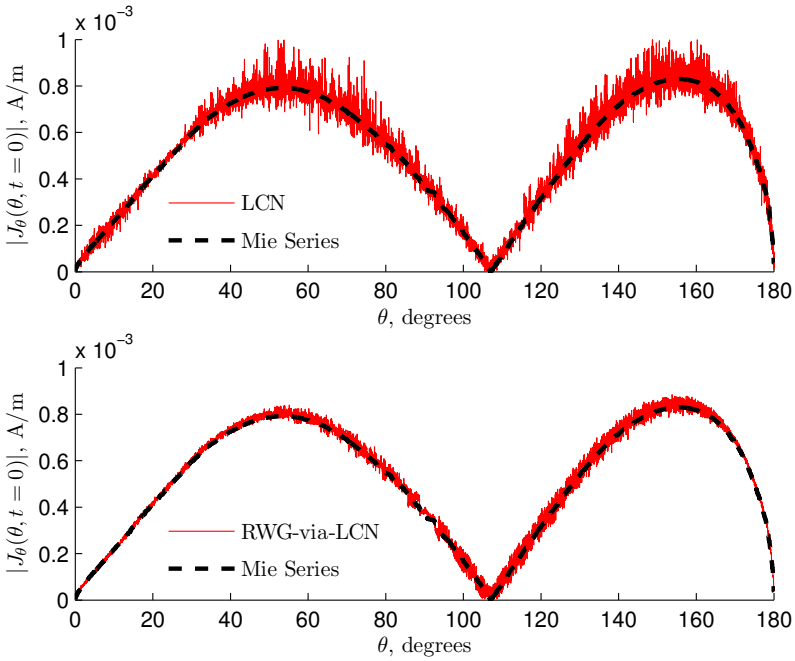

Figure 3.5: The magnitude of current density as a function of θ for numerical solutions (LCN and RWG-via-LCN) against the analytic solution (Mie series) at $f = 100$ MHz. Fig. 3.4 is the snapshot of the same current density on the surface of the sphere.

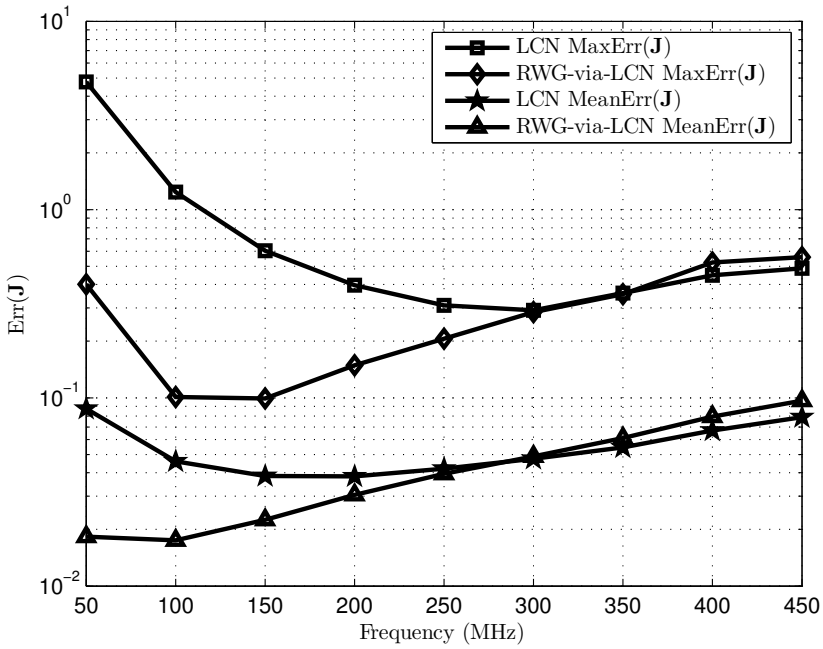

Figure 3.6: Mean and maximum relative errors in the current computed by (3.54) for scattering from a 4,832 element PEC sphere at different frequencies ($h_{\max} < \lambda/10$) using the LCN and RWG-via-LCN formulation of EFIE.

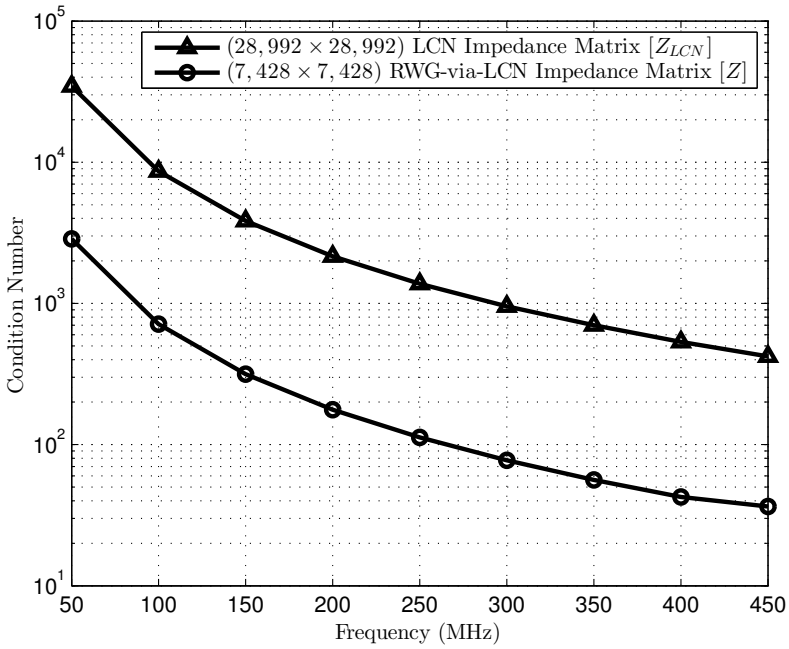

Figure 3.7: Condition numbers of the $(6N_p \times 6N_p)$ first-order LCN impedance matrix $[Z_{\text{LCN}}]$ and $(1.5N_p \times 1.5N_p)$ RWG-via-LCN impedance matrix $[Z]$ for the PEC sphere example with 4,832 triangular flat patches.

also improves the matrix condition number. Fig. 3.7 compares the condition numbers of the LCN and RWG-via-LCN impedance matrices at different frequencies. Improved conditioning of the matrix results in faster convergence of RWG MoM compared to the LCN when iterative matrix equation solvers are used.

3.5.2.2 Multiscale Discretization of an F5 Aircraft Model

In order to demonstrate the effect of current continuity on the LCN method for a practical multiscale geometry, we compared the results obtained by LCN and RWG-via-LCN methods for an F5 model (Figs. 3.8 to 3.10)[1] that fits within a cuboid with dimensions $(-4.09 \leq x \leq 4.09,\ -9.9013 \leq y \leq 4.2765,\ 0.0740475 \leq z \leq 3.35)$

[1]Note that these three figures are all depicted in Fig. 8 of [89] but have been separated herein to improve visibility.

in meters and meshed with 10,146 elements. The mesh has minimum element size $h_{\min} = 0.011m$ and maximum element size $h_{\max} = 0.311m$, making a large maximum to minimum element size ratio which ensures the multiscale nature of the problem [24]. The excitation is the same as in Section 3.5.2.1 but located at $\mathbf{r}' = \hat{\mathbf{y}} \cdot 10 + \hat{\mathbf{z}} \cdot 3$ meters. As a reference solution, a more highly discretized mesh (101,716 elements) simulated by the commercial tool *Wave3D* [35] was considered.

Figures 3.8 to 3.10 provide snapshots of the time-harmonic current density at $t = 0$s and $f = 50$MHz obtained by the three aforementioned methods. In these figures, part of the surface is magnified from a different angle for better visualization. It can be seen that the RWG-via-LCN method (Fig. 3.10) can produce a solution which agrees well with the reference solution (Fig. 3.8) and is visibly more accurate than the LCN solution (Fig. 3.9). Fig. 3.11 plots the mean relative error of the current produced using LCN and RWG-via-LCN methods for various frequencies ($k_0 h_{\max} < 1$) estimated by (3.54) with the reference solution obtained by Wave3D. Near the geometric edges in the model, the maximum relative error may exceed 100%. In such regions the error was capped at 100% in the calculation of MeanErr($\mathbf{J}$) in (3.54). Fig. 3.11 shows trends similar to those observed for the PEC sphere example provided in Fig. 3.6. Current continuity makes a great impact on the solution accuracy at lower frequencies.

3.6 Conclusion

In this work, a method for introducing current continuity into the first-order LCN formulation of the EFIE has been presented. The resulting system of equations has been shown to be equivalent to RWG MoM. The conversion from LCN to RWG MoM is exact and can easily be incorporated into existing LCN implementations in

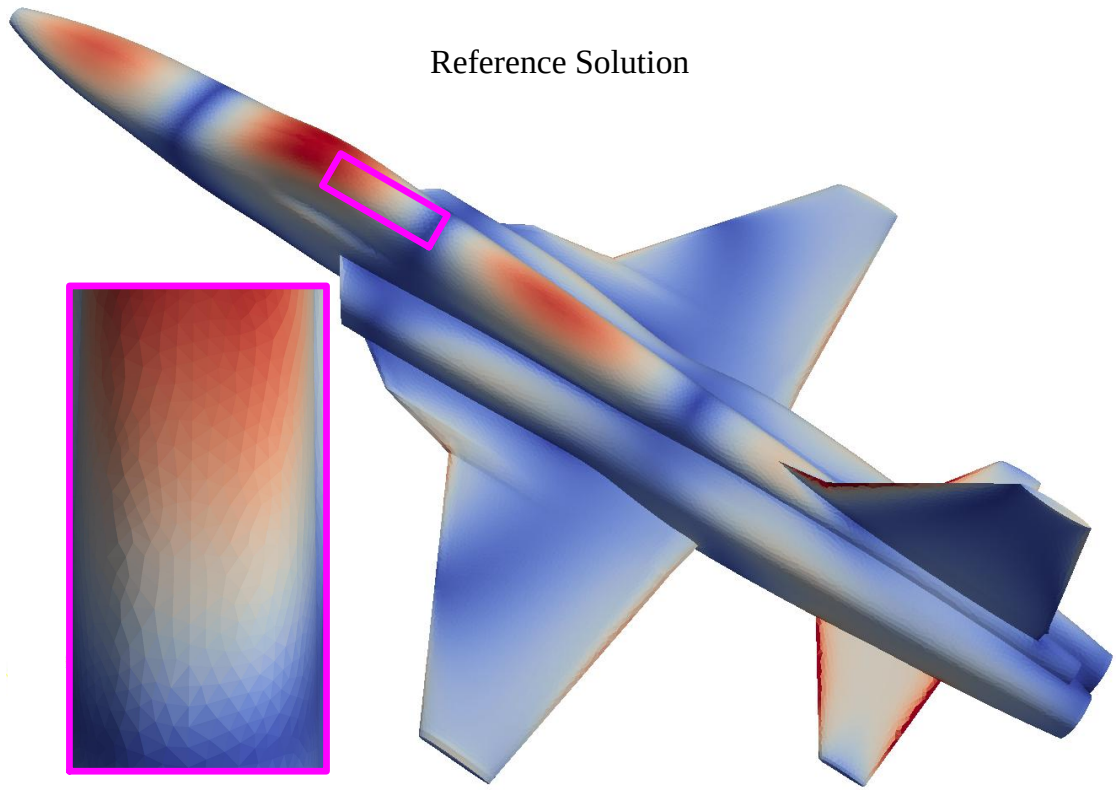

Figure 3.8: The surface current density at $t = 0$s numerically computed as the reference solution for Figs. 3.9 and 3.10. The solution is computed by a commercial tool (Wave3D) with a dense mesh (101,716 elements). The magnification has been done from a different angle for better visulization.

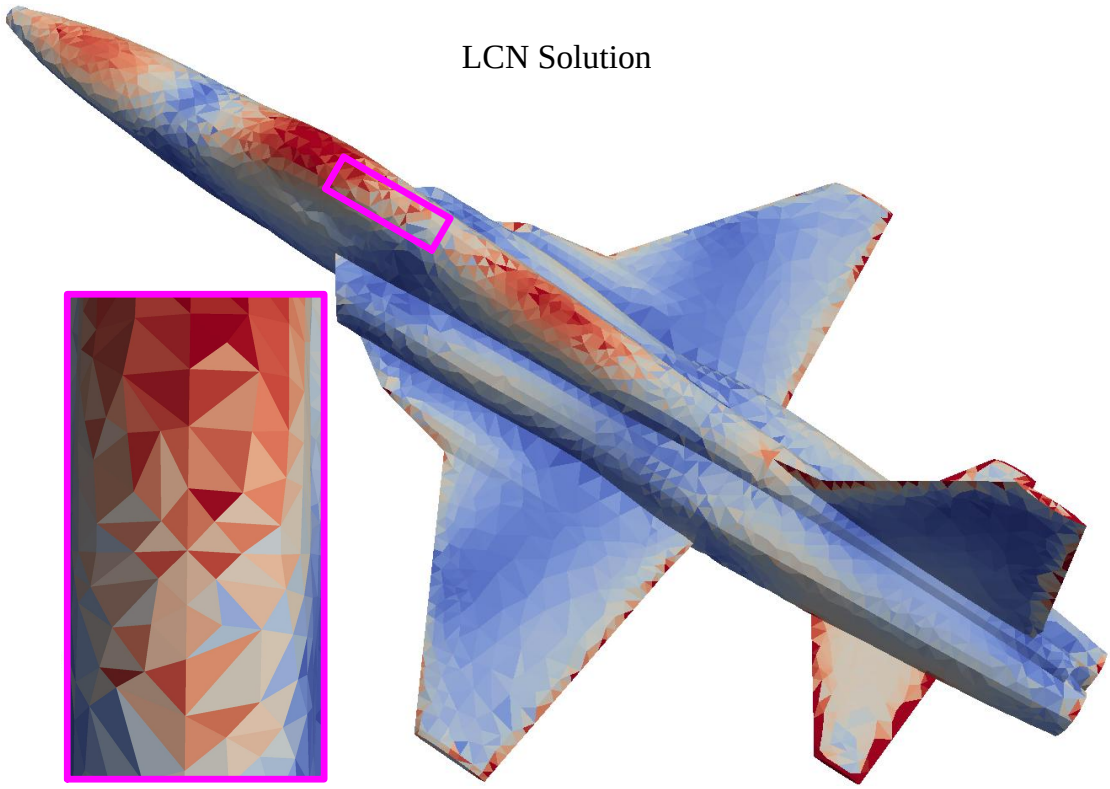

Figure 3.9: The surface current density at $t = 0$s numerically computed by the LCN method at $f = 50$MHz. The mesh has 10,146 triangular flat elements. The reference solution has been obtained by a commercial tool (Wave3D) with a much denser mesh (101,716 elements) and is depicted in Fig. 3.8. The RWG-via-LCN solution with the same mesh is depicted in Fig. 3.10. The magnification has been done from a different angle for better visulization.

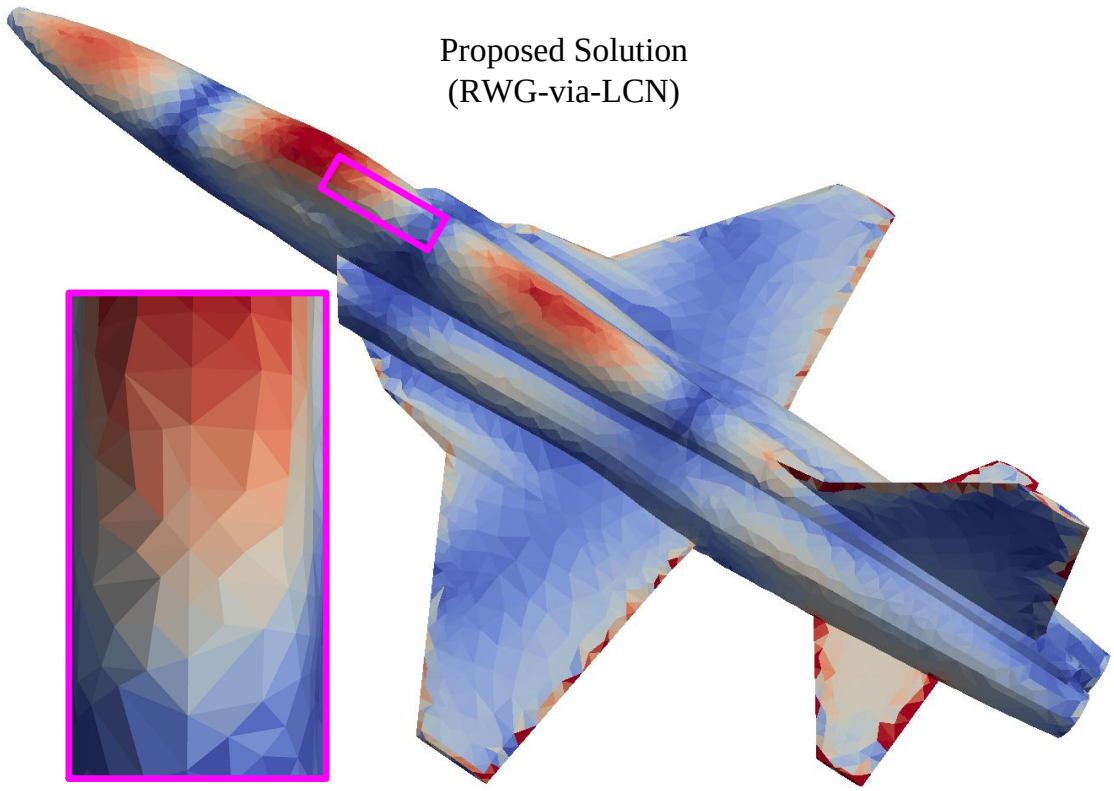

Figure 3.10: The surface current density at $t = 0$s numerically computed by the RWG-via-LCN method at $f = 50$MHz. The mesh has 10,146 triangular flat elements. The reference solution has been obtained by a commercial tool (Wave3D) with a much denser mesh (101,716 elements) and is depicted in Fig. 3.8. The LCN solution with the same mesh is depicted in Fig. 3.9. The magnification has been done from a different angle for better visulization.

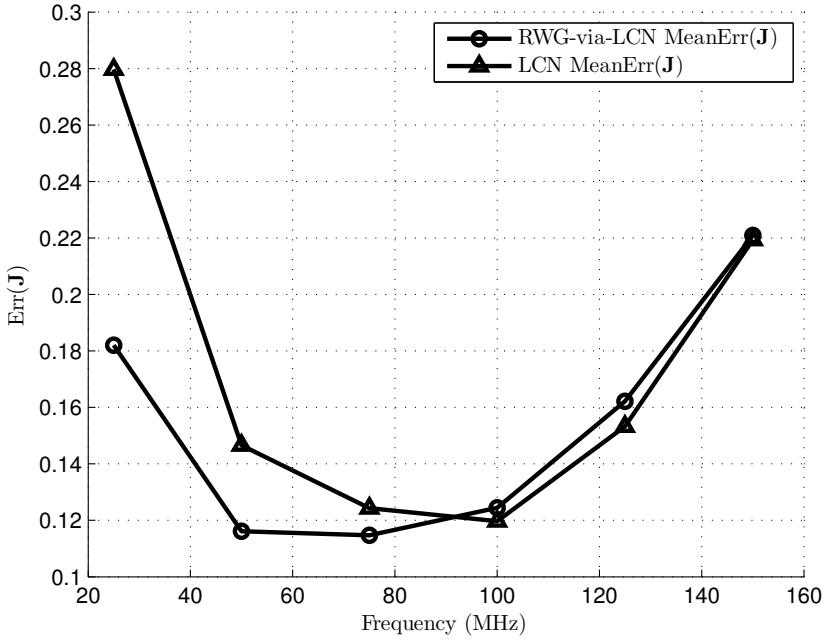

Figure 3.11: Mean relative error in the current for scattering from the F5 aircraft model shown in Figs. 3.8 to 3.10 at different frequencies ($k_0 h_{\max} < 1$) using the LCN and RWG-via-LCN formulation of the EFIE, when compared with the reference solution obtained by a commercial tool simulated on a much denser mesh.

$\mathcal{O}(N)$ operations. The advantage of the proposed RWG-via-LCN method over the standard first-order LCN method is that it produces more accurate results and at the same time has a 4 times reduction in degrees of freedom with improvement in the condition number of the impedance matrix. Its advantage over classical element-based RWG MoM is that the former is a point-based method and can be accelerated using an imbalanced-tree MLFMA implementation as an alternative to the point-matched RWG MoM. In order to achieve the equivalence between LCN and RWG MoM, the vector-potential EFIE was adopted. A point-based discretization of the RWG MoM for the mixed-potential EFIE via the Nyström method will be a subject of future work.

Chapter 4

Exact Relationship between the Locally Corrected Nyström Scheme and RWG Moment Method for the Mixed-Potential Integral Equation

Abstract

The exact relationship between the Rao-Wilton-Glisson (RWG) method-of-moments (MoM) and the locally corrected Nyström (LCN) method for the mixed-potential (MP) electric field integral equation (EFIE) is presented as an extension to our work where we established analogous exact relationship for solving the EFIE in its vector-potential (VP) form. It is shown that in order to achieve one such relationship for the MP EFIE, the first- and zeroth-order LCN methods must be respectively used for the discretization of the VP and scalar-potential terms of the MP EFIE. The resulting numerical scheme is a point-based RWG MoM discretization of the MP EFIE via the Nyström method. Due to the MP formulation of the EFIE, the proposed method establishes notably higher accuracy compared to either RWG MoM or LCN discretizations of the EFIE in the VP form. The increased accuracy is attributed to the analytical cancellation of the line charge contributions in the MP formulation as opposed to numerical cancellation inherent in the VP formulation of the EFIE. The detailed study and explanations of the above cancellations is presented along with their impact on the accuracy of the respective schemes for both canonical and realistic scattering targets at different frequencies.

4.1 Introduction

The moment method (MoM) [17,30,66], and the locally corrected Nyström (LCN) method [1,18,19,39], are established as accurate and economical numerical techniques for solving the general three-dimensional scattering [67], antenna placement and radiation [31], circuit analysis [32,33], electromagnetic compatibility, and other problems in computational electromagnetics (CEM) [68–75]. The economy of computational resources in the MoM and LCN are due to boundary element method (BEM) discretization of homogeneous regions [72,76] as opposed to the volumetric discretization of the regions required in schemes based on direct partial differential equation (PDE) discretizations including the finite-element method (FEM) [77], finite-difference-time-domain (FDTD) [78], finite integration technique [79], and others. Additional savings of computational resources in the MoM or LCN can be achieved for specialized applications that allow for abstraction of the complex environment into the pertinent Green's function [56, 80, 81]. The accuracy of the MoM/LCN solutions is attributed to the exact satisfaction of the radiation conditions [39] and description of the wave propagation phenomena across homogenous regions [5]. This is unlike discretization schemes based on the PDEs directly such as FEM and FDTD, where the wave propagation phenomena across electrically large regions leads to accumulation of the errors in the field approximation [5, 78].

The advantages offered by the MoM and LCN solutions are commonly plagued by numerical instabilities, inefficiencies, and errors unique to these BEM discretization schemes. Due to the maturity of the MoM dating back to the late 50s, a large body of work [5, 17, 20, 30, 64–66, 82–87] can be found alleviating numerical issues in MoM whereas there has been less work related to these issues addressing the relatively new LCN invented in the late 90s [19]. This is despite the fact that LCN has been

shown to offer various advantages compared to MoM such as cheaper error-controlled evaluation of the singular integrals [20], higher efficiency of acceleration with fast algorithms [5], and simple physically consistent handling of material junctions [72]. The LCN scheme, however, is known to be more prone to low-frequency breakdown [88] and producing ill-conditioned matrices [1] when solving for the electric field integral equation (EFIE). It is also substantially more inaccurate and inefficient in its first- and second-order forms compared to the RWG MoM when discretizing the EFIE [1, 89]. The above disadvantages have been partially responsible for the relatively slow adoption of LCN in the research community and leaving MoM to remain the dominating BEM technique in the industry [30–32, 34, 35].

In this work we propose a new methodology termed RWG-via-LCN which combines the benefits of the two BEM schemes by establishing an exact relationship between the LCN scheme and the RWG MoM. This work is a sequel to our work in [89] where we established such an exact relationship between the RWG MoM and first-order LCN solutions of the EFIE *in the vector-potential (VP) form* which here we refer to it as VP RWG-via-LCN. In this paper we develop analogous exact relationship between the RWG MoM and LCN solutions of the EFIE *in the mixed-potential (MP) form* yielding the MP RWG-via-LCN. Discretization of the MP EFIE (or simply MPIE) [56] offers higher accuracy of the solution and higher computational efficiency compared to the discretization schemes for the VP EFIE, be it MoM, LCN, or VP RWG-via-LCN. The reason for these benefits is due to the analytic (exact) cancellation of line integrals appearing in the MPIE when discretized with RWG MoM. In contrast, discretization schemes dealing with the VP EFIE, inherently require these cancellations to be performed numerically where more computational resources are required while additional error may be introduced into the numerical technique. In

order to establish the desired exact relationship between the RWG MoM and LCN discretizations of the MPIE, the first- and zeroth-order LCN schemes are used for discretization of the VP and scalar-potential (SP) terms of the MPIE, respectively. The constraints imposed on the RWG MoM discretization of the MPIE besides the obvious requirement of using the same meshes, include: a) establishing the same separation between the near and far interactions in the RWG MoM as well as in the first- and zeroth-order LCN discretizations, b) evaluation of the near interaction RWG MoM integrals in the VP and SP terms of the MPIE in exactly the same way as the calculation of the same integrals in local corrections of the two LCNs, and c) performing the discretization of the RWG MoM far interaction integrals of the MPIE's VP and SP terms with the first- and zeroth-order quadrature rules, respectively. Under these conditions, the zeroth- and first-order LCN discretization matrices can be used to produce the RWG MoM impedance matrix with machine precision. The resulting MP RWG-via-LCN discretization carries the advantages of LCN's point-based discretization such as more efficient acceleration by fast algorithms as well as the benefits stemming from the current continuity enforced RWG MoM. These benefits include a four times lower count of pertinent degrees of freedom (DOF) in RWG MoM compared to first-order LCN, its increased accuracy, better conditioning of the matrix, and lower computational complexity. The proposed MP RWG-via-LCN method can also be viewed as a mechanism for facilitating LCN with the techniques previously developed exclusively for the RWG MoM discretization of MPIE such as Calderon multiplicative preconditioning [82], Helmholtz decomposition techniques [83, 85, 86], multiresolution preconditioners [87] and others.

A new method of current continuity enforcement for the LCN method known as constrained LCN (CLCN) [90] has been proposed since the initial submission of this

work. In CLCN, current continuity is enforced by using auxiliary matrices obtained from non-trivial solutions of local continuity constraint systems. Consequently, current continuity enforcement can be applied to LCN impedance matrix at arbitrary orders. However, at higher orders the impact of current continuity on accuracy of the solution is known to diminish while it has a profound impact in low-order discretization schemes such as the classical zeroth- and first-order MoM and LCN. In this work we introduce a technique to enforce current continuity in LCN at these orders through its relationship with the classical MP RWG MoM. Besides the improvements of accuracy which results from the current continuity enforcement along with the analytical cancellation of the line integrals in MPIE, the relationship established in this work allows to link the low order LCN schemes to the techniques eliminating the low-frequency breakdown of the EFIE based on loop-tree, loop-star, and loop-charge decompositions as well as Calderon identity methods [82, 83, 85–87]. In the CLCN approach, however, such low-frequency breakdown elimination is enabled through the discretization of the augmented EFIE (AEFIE) instead of the original EFIE. Due to the separate discretization of surface charges as well as surface currents, the number of DOF in the solution of the AEFIE is twice that for the EFIE when discretized with CLCN. This makes the CLCN approach notably more expensive than the proposed MP RWG-via-LCN approach when low-frequency solutions are sought.

4.2 Mixed-Potential RWG Method-of-Moments

In this section, we describe RWG MoM discretization of the MP EFIE in a form that it can be related to the LCN method. The time-harmonic EFIE for a perfect

electric conductor (PEC) in dyadic form is [91]

$$\mathbf{t}(\mathbf{r}) \cdot \int_S \overline{\mathbf{G}}(\mathbf{r}, \mathbf{r}') \cdot \mathbf{J}(\mathbf{r}') ds' = -\mathbf{t}(\mathbf{r}) \cdot \mathbf{E}^{\text{inc}}(\mathbf{r}),\ \mathbf{r} \in S \tag{4.1}$$

where $\overline{\mathbf{G}}$ is the dyadic Green's function, $\mathbf{t}$ is a test vector tangential to S, $\mathbf{J}$ is the unknown surface current density, $\mathbf{E}^{\text{inc}}$ is the incident electric field, and $\mathbf{r}$ is the observation point on S. In (4.1) and throughout the paper, the $e^{+j2\pi f \mathtt{t}}$ is assumed and suppressed, where f is the frequency of the time-harmonic fields (and sources) and $\mathtt{t}$ denotes time. The RWG MoM approximates $\mathbf{J}$ using RWG basis functions. In this paper we use ramp (half RWG) function representation of RWG basis functions as it facilitates establishing exact relationship between RWG MoM and the LCN method [89]. The surface current $\mathbf{J}$ at an arbitrary location $\mathbf{r}'$ is represented as

$$\mathbf{J}(\mathbf{r}') \simeq \sum_{k'=1}^{3} b_{k'}^{p} \mathbf{R}_{k'}^{p}(\mathbf{r}') \tag{4.2}$$

where $b_{k'}^{p}$ are the current coefficients and $\mathbf{R}_{k'}^{p}$ are the ramp functions, both defined for arbitrary triangular flat patch p. By taking the inner product of (4.1) with $\mathbf{R}_{k}^{m}$ and discretizing the surface S into N_p elements we can write

$$\int_{S_m} \mathbf{R}_{k}^{m}(\mathbf{r}) \cdot \left[\sum_{p=1}^{N_p} \sum_{k'=1}^{3} b_{k'}^{p} \int_{S_p} \overline{\mathbf{G}}(\mathbf{r}, \mathbf{r}') \cdot \mathbf{R}_{k'}^{p}(\mathbf{r}') ds' \right] ds = -\int_{S_m} \mathbf{R}_{k}^{m}(\mathbf{r}) \cdot \mathbf{E}^{\text{inc}}(\mathbf{r}) ds \tag{4.3}$$

where k, k' are the ramp index defined on the surface of the observation patch S_m and source patch S_p, respectively, $k = 1, 2, 3$, and $m, p \in \{1, 2, ..., N_p\}$. From (4.3), one can define the ramp-to-ramp interactions between patches m and p as a (3×3) matrix

$$[z_{mp}] = \int_{S_m} \mathbf{R}_{k}^{m}(\mathbf{r}) \cdot \int_{S_p} \overline{\mathbf{G}}(\mathbf{r}, \mathbf{r}') \cdot \mathbf{R}_{k'}^{p}(\mathbf{r}') ds' ds, \quad k, k' = 1, 2, 3 \tag{4.4}$$

By decomposing $\overline{\mathbf{G}}$ into its VP and SP components, the ramp-to-ramp interaction of (4.4) can be written as $[z_{mp}] = [z^{\mathcal{A}}_{mp}] + [z^{\Phi}_{mp}]$ where $[z^{\mathcal{A}}_{mp}]$ is obtained by the VP component of the dyadic kernel

$$[z^{\mathcal{A}}_{mp}] = -j\eta_0 k_0 \int_{S_m} \mathbf{R}^m_k(\mathbf{r}) \cdot \int_{S_p} G(\mathbf{r},\mathbf{r}')\mathbf{R}^p_{k'}(\mathbf{r}')ds'ds, \qquad k,k' = 1,2,3 \tag{4.5}$$

and $[z^{\Phi}_{mp}]$ is obtained through the kernel's SP component which can be written as [39]

$$[z^{\Phi}_{mp}] = -\frac{j\eta_0}{k_0} \int_{S_m} \mathbf{R}^m_k(\mathbf{r}) \cdot \left[\nabla \int_{S_p} \nabla G(\mathbf{r},\mathbf{r}') \cdot \mathbf{R}^p_{k'}(\mathbf{r}')ds'\right] ds, \quad k,k' = 1,2,3 \tag{4.6}$$

where G is the free-space Green's function. The typical approach to mitigating the hypersingular kernel in (4.6) is by shifting the inner gradient operator to act onto the basis function [19, 89]

$$\begin{aligned}[z^{\Phi}_{mp}] = &-\frac{j\eta_0}{k_0} \int_{S_m} \mathbf{R}^m_k(\mathbf{r}) \cdot \oint_{C_p} \nabla G(\mathbf{r},\mathbf{r}') \left[\mathbf{R}^p_{k'}(\mathbf{r}') \cdot \hat{e}'_p\right] dl'ds \\ &-\frac{j\eta_0}{k_0} \int_{S_m} \mathbf{R}^m_k(\mathbf{r}) \cdot \int_{S_p} \nabla G(\mathbf{r},\mathbf{r}') \left[\nabla'_{\parallel} \cdot \mathbf{R}^p_{k'}(\mathbf{r}')\right] ds'ds \\ &k,k' = 1,2,3\end{aligned} \tag{4.7}$$

where C_n $(n = 1,2,...,N_p)$ is the contour bounding S_n and $\hat{e}_n$ is the outward normal to C_n tangential to S_n. The inner product testing with the differentiable ramp-functions $\mathbf{R}^m_k(\mathbf{r})$, facilitates the use of surface calculus identities [92] to shift the gradient operators in (4.7) to act on the test function. Subsequently, $[z^{\Phi}_{mp}]$ may be

obtained by a sum of four terms[1]

$$
\begin{aligned}
[z^{\Phi}_{mp}] =& \frac{j\eta_0}{k_0} \oint_{C_m} \mathbf{R}^m_k(\mathbf{r}) \cdot \hat{e}_m \oint_{C_p} G(\mathbf{r},\mathbf{r}') \mathbf{R}^p_{k'}(\mathbf{r}') \cdot \hat{e}'_p dl' dl \\
&+ \frac{j\eta_0}{k_0} \oint_{C_m} \mathbf{R}^m_k(\mathbf{r}) \cdot \hat{e}_m \int_{S_p} G(\mathbf{r},\mathbf{r}') \nabla'_{\parallel} \cdot \mathbf{R}^p_{k'}(\mathbf{r}') ds' dl \\
&+ \frac{j\eta_0}{k_0} \int_{S_m} \nabla_{\parallel} \cdot \mathbf{R}^m_k(\mathbf{r}) \oint_{C_p} G(\mathbf{r},\mathbf{r}') \mathbf{R}^p_{k'}(\mathbf{r}') \cdot \hat{e}'_p dl' ds \\
&+ \frac{j\eta_0}{k_0} \int_{S_m} \nabla_{\parallel} \cdot \mathbf{R}^m_k(\mathbf{r}) \int_{S_p} G(\mathbf{r},\mathbf{r}') \nabla'_{\parallel} \cdot \mathbf{R}^p_{k'}(\mathbf{r}') ds' ds, \quad k,k' = 1,2,3.
\end{aligned}
\tag{4.8}
$$

However, since a ramp-function $\mathbf{R}^n_o$ ($o = 1,2,3$) is orthogonal to $\hat{e}_n$ on two edges along C_n, the dot product $\mathbf{R}^n_o \cdot \hat{e}_n$ vanishes on these two edges. On the remaining edge, we have $\mathbf{R}^n_o \cdot \hat{e}_n = 1$ but the contribution from this ramp will be cancelled by a ramp from the adjacent triangle when current continuity is enforced by combining the two ramps into an RWG function. Therefore, the first three terms in (4.8) containing line charge contributions, can analytically be eliminated in RWG MoM. Furthermore, RWG basis functions help simplify the fourth term of (4.8) as the divergence of a ramp-function is constant over one triangle. This is commonly referred to as a *pulse*: $\nabla_{\parallel} \cdot \mathbf{R}^n_o = l^n_o / A^n$, where l^n_o is the length of the oth edge of the nth patch and A^n is the area of the nth triangle. Thus the SP component of the ramp-to-ramp interaction can be reduced to

$$
[z^{\varphi}_{mp}] = \frac{j\eta_0}{k_0} \frac{l^m_k l^p_{k'}}{A^m A^p} \int_{S_m} \int_{S_p} G(\mathbf{r},\mathbf{r}') ds' ds, \quad k,k' = 1,2,3 \tag{4.9}
$$

where the small letter φ is used in the notation to distinguish the reduced SP $[z^{\varphi}_{mp}]$ and the full term SP $[z^{\Phi}_{mp}]$ in (4.6) to (4.8). This convention has been used throughout the text. If the RWG MoM computes $[z^{\Phi}_{mp}]$ for its SP contribution, it discretizes the

[1]Note that the expression (4.8), is merely a transition between (4.7) and (4.9) and is never numerically evaluated in the context of RWG-via-LCN techniques. The VP RWG-via-LCN [89] discretizes (4.7), while the proposed MP RWG-via-LCN computes (4.9).

VP EFIE [56] yielding the VP RWG MoM [89]. Otherwise $[z^{\varphi}_{mp}]$ is computed as the SP contribution resulting in the RWG MoM discretization of the MPIE [23] and is referred to as the MP RWG MoM. In order to discretize (4.5) and (4.9), with the goal of establishing an exact relationship between MP RWG MoM and the LCN method, we first approximate the outer integrals over S_m using quadrature rules. The outer integral in (4.5) is approximated using a first-order (3-point) quadrature rule

$$[z^{\mathcal{A}}_{mp}] \simeq -j\eta_0 k_0 \sum_{q_m=1}^{3} \omega_{q_m} \mathbf{R}^m_k(\mathbf{r}_{q_m}) \cdot \int_{S_p} G(\mathbf{r}_{q_m}, \mathbf{r}') \mathbf{R}^p_{k'}(\mathbf{r}') ds', \quad k, k' = 1, 2, 3 \tag{4.10}$$

where ω_{q_m} is the quadrature weight associated with the abscissa point $\mathbf{r}_{q_m}$. The outer integral in (4.9) is discretized using a zeroth-order (1-point) quadrature rule

$$[z^{\varphi}_{mp}] \simeq \frac{j\eta_0}{k_0} \frac{l^m_k l^p_{k'}}{A^m A^p} \omega_{c_m} \int_{S_p} G(\mathbf{r}_{c_m}, \mathbf{r}') ds', \quad k, k' = 1, 2, 3 \tag{4.11}$$

where ω_{c_m} is the quadrature weight at the centroid of the triangle $\mathbf{r}_{c_m}$.

For a smooth kernel (G is smooth when source and observation triangles are sufficiently far apart[1]), fixed-point quadrature rules can be used to discretize (4.10) and (4.11). Approximating (4.10) and (4.11) using first- and zeroth-order rules, respectively, the ramp-to-ramp (3×3) impedance matrix for far patches m and p can be expressed as

$$[z^{\text{far}}_{mp}] = [l_m]^T \cdot \varphi \cdot [l_p] + [\mathbf{R}_m]^T \cdot [\overline{\boldsymbol{\mathcal{A}}}] \cdot [\mathbf{R}_p] \tag{4.12}$$

where the (1×3) matrix $[l_n]$ is local to patch n with entries $[l_n]_o = l^n_o$ and φ is the (1×1) scalar interaction between the centroids of the observation $\mathbf{r}_{c_m}$ and source $\mathbf{r}_{c_p}$

[1]Similar to [89], near and far regions are defined based on centroids of the elements for the sake of simplicity. Alternatively, near and far regions can be defined based on the minimum distance between the observation point and source patch.

elements

$$\varphi = \frac{j\eta_0}{k_0}\frac{1}{A^m A^p}\omega_{c_m}\omega_{c_p}G(\mathbf{r}_{c_m},\mathbf{r}_{c_p}) \tag{4.13}$$

In (4.12), $[\mathbf{R}_n]$ is a $((3\times 3)\times(3\times 1))$[1] matrix with the q_n,kth element $[\mathbf{R}_n]_{q_n,k} = \mathbf{R}_k^n(\mathbf{r}_{q_n})$, and $[\overline{\boldsymbol{\mathcal{A}}}]$ is a $((3\times 3)\times(3\times 3))$ matrix with its q_m,q_pth element as

$$[\overline{\boldsymbol{\mathcal{A}}}]_{q_m,q_p} = -j\eta_0 k_0 \omega_{q_m}\omega_{q_p}G(\mathbf{r}_{q_m},\mathbf{r}_{q_p})\bar{\mathbf{I}} \tag{4.14}$$

where $\bar{\mathbf{I}}$ is the unit dyad.

In the near field region, the convolutional integrals in (4.10) and (4.11) are singular and should be evaluated using singularity subtraction or cancellation techniques such as [59–61]. Thus the contribution to the ramp-to-ramp (3×3) impedance matrix for near patches m and p is

$$[z_{mp}^{\text{near}}] = [l_m]^T\cdot\tilde{\varphi}\cdot[l_p] + [\mathbf{R}_m]^T\cdot[\tilde{\boldsymbol{\mathcal{A}}}] \tag{4.15}$$

where the q_m,k'th element of the $((3\times 3)\times(3\times 1))$ matrix $[\tilde{\boldsymbol{\mathcal{A}}}]$ is defined as

$$[\tilde{\boldsymbol{\mathcal{A}}}]_{q_m,k'} = -j\eta_0 k_0\omega_{q_m}\int_{S_p} G(\mathbf{r}_{q_m},\mathbf{r}')\mathbf{R}_{k'}^p(\mathbf{r}')ds' \tag{4.16}$$

and the (1×1) scalar interaction between the centroid of the observation element $\mathbf{r}_{c_m}$ and source patch p is

$$\tilde{\varphi} = \frac{j\eta_0}{k_0}\frac{1}{A^m A^p}\omega_{c_m}\int_{S_p} G(\mathbf{r}_{c_m},\mathbf{r}')ds'. \tag{4.17}$$

[1]The notation $((A\times B)\times(C\times D))$ is borrowed from [89] indicating that the size of the matrix is $(AB\times CD)$ with $(A\times C)$ elements each of which having $(B\times D)$ entries.

Based on the local ramp-to-ramp interactions of (4.15) and (4.12), MP half RWG MoM system can be constructed followed by enforcement of current continuity similar to that of (21) and (22), respectively, in [89], to build the $1.5N_p$-size[1] MP RWG MoM linear system

$$\begin{aligned} ([Z^{\varphi}] + [Z^{\mathcal{A}}]) \cdot [I] &= [V] \\ [Z] \cdot [I] &= [V] \end{aligned} \tag{4.18}$$

where $[Z^{\varphi}]$ contains the SP terms and $[Z^{\mathcal{A}}]$ contains the VP terms of the MPIE's global impedance matrix $[Z]$. Note, that the above described MP RWG MoM formulation discretized with first- (3-point) and zeroth-order (1-point) rules in its vector- and scalar-potential terms, respectively, is one of the many forms of the MP RWG MoM which could be applied. This particular form of the MP RWG MoM, however, is special in the sense that it can be directly related to the point-based LCN formulation and is required to build the proposed MP RWG-via-LCN. If more accurate integration results are needed, mesh refinement can be applied as opposed to using more sample points in discretizing the VP and SP integrations.

4.3 The Locally Corrected Nyström Method

To formulate MP RWG-via-LCN, first- and zeroth-order LCN techniques should be constructed in a form that they can be related to the VP and SP contributions of the MP RWG MoM, respectively. One such first-order LCN formulation was presented in [89] and so we restrict ourselves to zeroth-order LCN here. The LCN formulation can be used to discretize an integral equation solving an unknown scalar quantity

[1]For the sake of simplicity and without loss of generality, it is assumed that the geometry is closed.

$\sigma(\mathbf{r}')$ over the surface S

$$\int_S K(\mathbf{r},\mathbf{r}')\sigma(\mathbf{r}')ds' = \phi^{\text{inc}}(\mathbf{r}), \quad \mathbf{r}\in S \tag{4.19}$$

where $\phi^{\text{inc}}(\mathbf{r})$ is the known excitation function and $K(\mathbf{r},\mathbf{r}')$ is the kernel that may or may not exhibit singular behaviour. Discretizing (4.19) over N_p elements we obtain

$$\sum_{p=1}^{N_p}\int_{S_p} K(\mathbf{r},\mathbf{r}')\sigma(\mathbf{r}')ds' = \phi^{\text{inc}}(\mathbf{r}), \quad \mathbf{r}\in S \tag{4.20}$$

Next, the integral over S_p should be discretized. Using a zeroth-order (1-point) quadrature rule yields a zeroth-order LCN. To facilitate computations of singular and near singular integrals through the local correction procedure, the discretization of the surface integral over S_p should be written for near and far interactions separately

$$\sum_{p\in\text{far(m)}} \omega\sigma(\mathbf{r}_{c_p}) + \sum_{p\in\text{near(m)}} \tilde{\omega}\sigma(\mathbf{r}_{c_p}) = \phi^{\text{inc}}(\mathbf{r}_{c_m}) \tag{4.21}$$

where ω is the regular weight describing the interactions between centroids of the source c_p and observation c_m patches

$$\omega = \omega_{c_m}\omega_{c_p}K(\mathbf{r}_{c_m},\mathbf{r}_{c_p}) \tag{4.22}$$

provided that m and p are far enough apart that K is smooth. In (4.22) and further below in (4.23), contrary to standard notation of the LCN [1,18,19], the observation weight ω_{c_m} is included in the LCN weights in order to allow for observation patch integrals analogous to RWG MoM. This convention was also used in [89]. The locally-corrected weight $\tilde{\omega}$ in (4.21), is obtained using a zeroth-order basis function $F(\mathbf{r}) = 1$. Therefore the Vandermonde matrix of the zeroth-order LCN becomes a (1×1) unity

matrix [1] and the LCN weights are obtained by

$$\tilde{\omega} = \omega_{c_m} \int_{S_p} K(\mathbf{r}_{c_m}, \mathbf{r}')ds'. \tag{4.23}$$

A zeroth-order LCN implementation would compute ω and $\tilde{\omega}$ for a desired kernel [18,73–75]. By solving the resulting N_p-size system $[Z_{\text{0th-LCN}}] \cdot [\sigma] = [\phi]$, the unknown coefficients are obtained.

4.4 Mixed-Potential RWG-via-LCN

4.4.1 Scalar-Potential Contribution via Zeroth-Order LCN

By comparing the scalar interactions of the MP RWG MoM in (4.13) and (4.17) with the zeroth-order LCN's regular and locally-corrected weights in (4.22) and (4.23), it is realized that by applying the following kernel

$$K(\mathbf{r}, \mathbf{r}') = \frac{j\eta_0}{k_0 A^m A^p} G(\mathbf{r}, \mathbf{r}') \tag{4.24}$$

to zeroth-order LCN, one can exactly reproduce the scalar interactions of the MP RWG MoM via the regular $\omega = \varphi$ and locally corrected weights $\tilde{\omega} = \tilde{\varphi}$, for far and near regions, respectively. Since triangles are flat, methods capable of handling both flat and curvilinear triangles are applicable to compute singular integrals of the near field [59–61]. Note, that when establishing the exact equality $\tilde{\omega} = \tilde{\varphi}$, one must use the same technique when computing the locally corrected weights (4.23) and the SP interactions in the MP RWG MoM (4.17), otherwise the equality is prone to approximations only as accurate as the least accurate integration result.

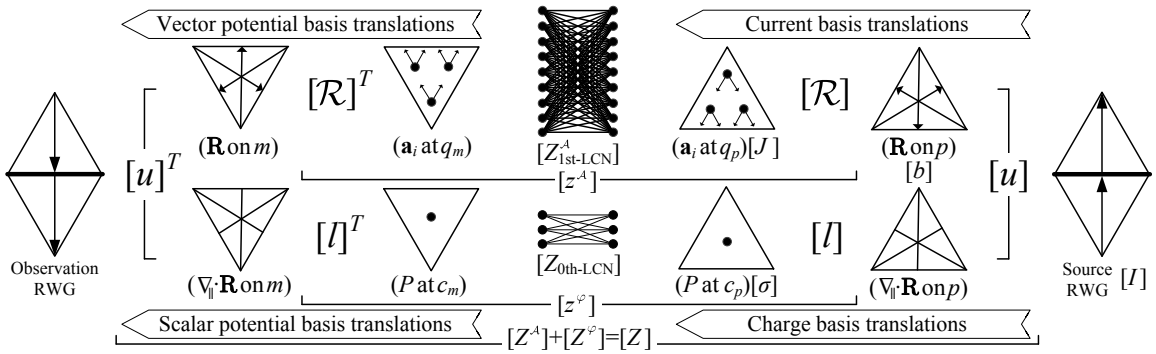

Figure 4.1: Basis translation interpretation of the MP RWG-via-LCN method formulated in (4.29) and (4.31). In the process of current basis translations, source RWG current coefficients $[I]$ will be converted to ramp current coefficients $[b]$ via the unifier $[u]$ which maps ramp-functions onto RWG functions. Then with the aid of $[\mathcal{R}]$, current coefficients of the first-order LCN $[J]$ are obtained. This will be followed by VP basis translations in the reverse order on the observation patch m to produce observation RWG VP coefficients. During this process the $(6N_p \times 6N_p)$ VP part of the first-order LCN matrix $[Z^{\mathcal{A}}_{\text{1st-LCN}}]$ with the kernel in (4.25) is converted to $(3N_p \times 3N_p)$ VP half RWG matrix $[z^{\mathcal{A}}]$ and subsequently $(1.5N_p \times 1.5N_p)$ VP RWG matrix $[Z^{\mathcal{A}}]$. For charge, basis conversion is from $[I]$ to $[b]$ similar to that of the current except that $[b]$ is the coefficients of dimensionless $\nabla_{\|}\cdot\mathbf{R}$, hence no arrow on the ramps. Then through $[l]$, coefficients of charge $[\sigma]$ are obtained for the centroid of the source triangle c_p. This will be followed by SP basis translations on the observation element m in the reverse order which results in observation RWG SP coefficients. During this process, the $(N_p \times N_p)$ zeroth-order LCN matrix $[Z_{\text{0th-LCN}}]$ with the kernel in (4.24) is converted to $(3N_p \times 3N_p)$ SP half RWG matrix $[z^{\varphi}]$ followed by enforcing current continuity which gives the $(1.5N_p \times 1.5N_p)$ SP RWG matrix $[Z^{\varphi}]$. Depending on the implementation preference, current continuity can be applied once $[Z] = [u]^T \cdot ([z^{\mathcal{A}}] + [z^{\varphi}]) \cdot [u]$, or separately on $[z^{\mathcal{A}}]$ and $[z^{\varphi}]$ matrices $[Z] = [Z^{\mathcal{A}}] + [Z^{\varphi}]$. In order to properly illustrate the proportionality of $[Z_{\text{0th-LCN}}]$ with respect to $[Z^{\mathcal{A}}_{\text{1st-LCN}}]$, interactions in $[Z^{\mathcal{A}}_{\text{1st-LCN}}]$ are depicted by ticker lines representing interactions for both $\mathbf{a}_1$ and $\mathbf{a}_2$ while each line in $[Z_{\text{0th-LCN}}]$ represents one interaction for P which is the inverse of the area of the triangle.

4.4.2 Vector-Potential Contribution via First-Order LCN

The equivalence of the first-order LCN and RWG MoM for the VP EFIE was shown in [89]. Using a similar approach and by applying the VP part of the dyadic kernel

$$\overline{\mathbf{G}}^{\mathcal{A}}(\mathbf{r},\mathbf{r}') = -j\eta_0 k_0 G(\mathbf{r},\mathbf{r}')\bar{\mathbf{I}} \tag{4.25}$$

to first-order LCN discretizaion, it can be shown that the VP contribution of the MP RWG MoM can be obtained using regular $[\omega^{\mathcal{A}}]$ and locally corrected $[\tilde{\omega}^{\mathcal{A}}]$ weights, for far and near regions, respectively. This is done by the basis conversions introduced in [89] which are used in the next section to define MP RWG-via-LCN's local interactions. Note that the superscript $\mathcal{A}$ is used in the notation of the LCN weights to indicate that they are obtained by only applying the VP part of the dyadic kernel (4.25).

4.4.3 Mixed-Potential RWG-via-LCN Local Interactions

Based on the exact representations of the SP and VP contributions to the MP RWG MoM discussed in sections 4.4.1 and 4.4.2, we can define local interactions of the MP RWG MoM $([z_{mp}^{\text{far}}], [z_{mp}^{\text{near}}])$ based on the local interactions of the first-order $([\omega^{\mathcal{A}}], [\tilde{\omega}^{\mathcal{A}}])$ and zeroth-order $(\omega, \tilde{\omega})$ LCN discretizations, yielding the MP RWG-via-LCN local interactions. For the far field region we have

$$[z_{mp}^{\text{far}}] = [l_m]^T \cdot \omega \cdot [l_p] + [\mathcal{R}_m]^T \cdot [\omega^{\mathcal{A}}] \cdot [\mathcal{R}_p] \tag{4.26}$$

where $[\mathcal{R}_n]$ is a (6×3) matrix defined as

$$[\mathcal{R}_n] = \begin{bmatrix} [\mathcal{R}_n^1] \\ [\mathcal{R}_n^2] \end{bmatrix} \tag{4.27}$$

with $[\mathcal{R}_n^i]$ being a (3×3) matrix defined for the ith unitary vector on patch n with its q_n, kth entry $[\mathcal{R}_n^i]_{q_n,k} = \mathbf{a}_n^i \cdot \mathbf{R}_k^n(\mathbf{r}_{q_n})$ where $\mathbf{a}_n^i$ is the reciprocal unitary vector local to patch n [89]. Similarly for the near field region we can write

$$[z_{mp}^{\text{near}}] = [l_m]^T \cdot \tilde{\omega} \cdot [l_p] + [\mathcal{R}_m]^T \cdot [\tilde{\omega}^{\mathcal{A}}] \cdot [\mathcal{R}_p] \tag{4.28}$$

Since (4.28) and (4.26) have the same form, it is possible to define unified global converter matrices for VP and SP contributions as explained in the sequel.

4.4.4 Mixed-Potential RWG-via-LCN System

A global transformation of first- and zeroth-order LCN matrices to the global $(1.5N_p \times 1.5N_p)$ impedance matrix of the MP RWG-via-LCN $[Z]$ has the following form

$$[Z] = [u]^T \cdot ([l]^T \cdot [Z_{\text{0th-LCN}}] \cdot [l] + [\mathcal{R}]^T \cdot [Z_{\text{1st-LCN}}^{\mathcal{A}}] \cdot [\mathcal{R}]) \cdot [u] \tag{4.29}$$

where $[u]$ unifies ramp functions onto RWG functions and $[\mathcal{R}]$ exactly converts RWG current coefficients to its first-order LCN counterpart, both of which are sparse matrices and explicitly defined in [89] (see (22) and (49) therein). Here, $[Z_{\text{0th-LCN}}]$ is the $(N_p \times N_p)$ zeroth-order LCN matrix and $[Z_{\text{1st-LCN}}^{\mathcal{A}}]$ is the $(6N_p \times 6N_p)$ VP part of the first-order LCN matrix which are filled with the kernels of (4.24) and (4.25),

respectively. Finally, $[l]$ is a $(N_p \times 3N_p)$ matrix defined as

$$[l] = \begin{bmatrix} [l_1] & [0] & \dots & [0] \\ [0] & [l_2] & \dots & [0] \\ \vdots & \vdots & \ddots & \vdots \\ [0] & [0] & \dots & \left[l_{N_p}\right] \end{bmatrix} \tag{4.30}$$

where every $[0]$ represents a matrix of (1×3) zeros. The stages of global transformations of (4.29) are depicted in Fig. 4.1.

4.4.5 Mixed-Potential RWG-via-LCN Implementation

4.4.5.1 Local Transformations

The global transformations formulated in (4.29) (also in (4.31) as well as (50) of [89]), while beneficial to understand the techniques, are not explicitly performed in practice. Instead, we fill out the $(1.5N_p \times 1.5N_p)$ RWG-via-LCN impedance matrix $[Z]$ by locally obtaining $[z_{mp}^{\text{far}}]$ and $[z_{mp}^{\text{near}}]$, and adding or subtracting the contribution to $[Z]$ based on the alignment of the corresponding RWG and ramp functions. While the complexity of a direct conversion form the global LCN matrix to the global RWG-via-LCN matrix (both MP and VP) is $\mathcal{O}(N)$, performing the conversion locally, eliminates the need for saving $(6N_p \times 6N_p)$ $[Z_{\text{1st-LCN}}^{\mathcal{A}}]$ and $(N_p \times N_p)$ $[Z_{\text{0th-LCN}}]$ matrices.

4.4.5.2 Multilevel Fast Multipole Algorithm (MLFMA) Acceleration

The proposed MP RWG-via-LCN method greatly facilitates acceleration of the RWG MoM with the MLFMA [24, 67] as it casts the interactions of the RWG basis functions into the point-based form established by the underlying LCN discretizations. As MLFMA is most efficient when applied to the acceleration of point-to-point

interactions, in the proposed scheme, the product of $[Z_{\text{0th-LCN}}]$ and $[Z^{\mathcal{A}}_{\text{1st-LCN}}]$ matrices with the vectors are accelerated with the MLFMA for scalar Helmholtz kernel. Evaluation of each x, y, and z component of the VP and SP at the observation quadrature points are handled separately with the scalar kernel MLFMA [93–95]. This approach is commonly termed as MP MLFMA as opposed to the dyadic MLFMA typically applied directly to the RWG basis-function-to-basis-function interactions.

4.4.5.3 Low-Frequency Stable Formulations

The low-frequency stable formulations available for RWG MoM through loop-tree, loop-star, loop-charge, and Calderon based techniques [82, 83, 85–87] become directly applicable to the LCN through the relationship established in this work. For that purpose, in the impedance matrix of the RWG MoM $[Z]$ (4.18), the SP contribution $[Z^{\varphi}]$ and the VP contribution $[Z^{\mathcal{A}}]$ are separately related to the LCN impedance matrices according to the following exact relations

$$\begin{aligned} [Z^{\varphi}] &= [u]^T \cdot [l]^T \cdot [Z_{\text{0th-LCN}}] \cdot [l] \cdot [u], \\ [Z^{\mathcal{A}}] &= [u]^T \cdot [\mathcal{R}]^T \cdot [Z^{\mathcal{A}}_{\text{1st-LCN}}] \cdot [\mathcal{R}] \cdot [u] \end{aligned} \tag{4.31}$$

which are also depicted in Fig. 4.1. Subsequently, the scalar- and vector-potential MP RWG MoM matrices ($[Z^{\varphi}], [Z^{\mathcal{A}}]$) can be directly used in the low-frequency stable formulations. Thus, the proposed MP RWG-via-LCN scheme combines the benefits of the point-based LCN discretization and low-frequency stable MoM formulations. Note, that this is unlike the standard LCN [18] and VP RWG-via-LCN [89] which discretize VP EFIE and can not be directly related to the low-frequency stable discretization schemes. It is important to mention also that the Helmholtz decomposition and preconditioning techniques based on RWG MoM low-frequency stable formula-

tions do not introduce additional unknowns into the formulation. This is unlike the methods based on the discretization of the AEFIE which discretize both current and charge and, thus, at least double the number of unknowns [88, 90].

4.5 Results and Discussion

In all simulations herein, the $\mathcal{O}(1/R)$ singularity in the zeroth-order LCN weights $\tilde{\omega}$ is integrated by analytical evaluation of the singular part of the free space Green's function $G_s(\mathbf{r}, \mathbf{r}') = 1/|\mathbf{r} - \mathbf{r}'|$ [59] and a zeroth-order approximation of its regular part $G_r(\mathbf{r}, \mathbf{r}') = [e^{-jk_0|\mathbf{r}-\mathbf{r}'|} - 1]/|\mathbf{r} - \mathbf{r}'|$ to fill out $[Z_{\text{0th-LCN}}]$. Matrix elements of $[Z^{\mathcal{A}}_{\text{1st-LCN}}]$ and the first-order LCN impedance matrix $[Z_{\text{1st-LCN}}]$ are computed to prescribed precision with relative error $\epsilon = 10^{-4}$ using Duffy transform [60] and adaptive quadrature [18, 89]. Herein, the final system of linear algebraic equations is solved directly by LU-decomposition. The results are quantified by means of relative error in the approximated surface current $\mathbf{J}$ defined as

$$\text{MeanErr}(\mathbf{J}) = \frac{1}{3N_p} \sum_{i=1}^{3N_p} \frac{\left| J_i^{\text{Num}} - J_i^{\text{Ref}} \right|}{|J_i^{\text{Ref}}|} \tag{4.32}$$

where J_i^{Num} and J_i^{Ref} are the current magnitudes $|\mathbf{J}|$ at the quadrature points of the first-order rule q_m obtained by the numerical and reference solutions, respectively.

4.5.1 Equivalence of MP RWG MoM and MP RWG-via-LCN

As the MP RWG-via-LCN conversions in (4.29) and (4.31) are exact, the proposed method establishes an exact relationship between LCN and MP RWG MoM, under the assumption that both LCN and MP RWG MoM consider the same near and far regions along with the same choice of singularity cancellation techniques for the SP and VP

contributions. Therefore the MP RWG-via-LCN impedance matrix $[Z]$ in (4.29) will be equivalent to the MP RWG MoM matrix in (4.18) to machine precision, irrespective of the accuracy in which the singular integrals are computed. Fig. 4.2 compares matrix elements from the MP RWG-via-LCN versus MP RWG MoM for a PEC sphere at 100MHz meshed with 32 triangles. Here, we use the same singularity cancellation techniques to fill out both matrices. Thus, as described above, we analytically evaluate G_s and apply zeroth-order approximation of G_r to compute SP contributions in both techniques (i.e. $\tilde{\omega}$ and $\tilde{\varphi}$), as well as the same adaptive integrations to compute VP contributions in both methods (i.e. $[\tilde{\omega}^{\mathcal{A}}]$ and $[\tilde{\boldsymbol{\mathcal{A}}}]$). While adaptive integrations of $[\tilde{\boldsymbol{\mathcal{A}}}]$ and $[\tilde{\omega}^{\mathcal{A}}]$ are expected to provide results with the requested 4 digits of precision, $\tilde{\varphi}$ and $\tilde{\omega}$ are 2 digits accurate due to the approximation of G_r. Nevertheless, as can be seen from the figure, the equivalence between MP RWG MoM and MP RWG-via-LCN is exact to machine precision, consistent with [18, 89].

4.5.2 Line Integral Cancellation in VP and MP RWG MoM

In order to understand the difference between VP and MP RWG-via-LCNs or equivalently VP and MP RWG MoMs, we need to look at how these techniques compute SP interactions. While MP RWG-via-LCN as well as the general case of MP RWG MoM [23] take advantage of exact cancellations of the terms containing line integrals in (4.8) to compute $[z^{\varphi}_{mp}]$ in (4.9), the VP RWG-via-LCN and VP RWG MoM by definition, attempt to achieve analogous cancellations numerically by computing $[z^{\Phi}_{mp}]$ in (4.7). Although VP RWG-via-LCN may use analytical cancellation of the source line integral over C_p in (4.7) (see also (51)-(53) in [89]), cancelling contributions containing line integrals over C_m in (4.8) is not analytically possible for VP RWG MoM. This is because, VP EFIE formulation based discretizations imply inner

product testing using δ-functions (i.e. point-based sampling) and since δ-functions are non-differentiable, the gradient operators in (4.7) can not be shifted onto them to reproduce (4.8). Therefore VP RWG MoM, LCN, and VP RWG-via-LCN do not only require more computational effort to compute SP interactions, they are also prone to errors in numerical line integrals[1] which impacts the accuracy of the solution depending on the frequency as demonstrated below.

To numerically study these cancellation mechanisms, we consider VP and MP RWG-via-LCN formulations in the quantitative analysis. However, since the analysis is based on the difference of RWG MoM discretization of the MPIE and VP EFIE formulations in general, based on (4.9) and (4.7), respectively, its results are relevant to an arbitrary form of RWG MoM when discretizing VP and MP EFIEs. Consider the electromagnetic scattering on a 1-meter radius PEC sphere uniformly discretized by $N_p = 5,948$ triangles and excited by $\hat{z}$-directed electric dipole with time-harmonic current situated 9 meters above the north pole of the sphere. As shown in Fig. 4.1, the impedance matrix of the MP RWG-via-LCN can be obtained by $[Z] = [Z^{\mathcal{A}}] + [Z^{\varphi}]$ and thus we fill out $(1.5N_p \times 1.5N_p)$ matrices $[Z^{\mathcal{A}}]$ and $[Z^{\varphi}]$ using (4.31) as well as the same size VP RWG-via-LCN impedance matrix of [89] which here, we refer to as $[Z^{\mathcal{A}+\Phi}]$ since it is built from $[z^{\mathcal{A}}_{mp}] + [z^{\Phi}_{mp}]$. The difference between matrix elements of MP RWG-via-LCN and VP RWG-via-LCN $[Z^{\Phi-\varphi}] = [Z^{\mathcal{A}+\Phi}] - [Z]$ can be used to quantify the error that appears in VP RWG-via-LCN due to the fact that it can not perfectly cancel test line integrals over C_m and thus reduce $[z^{\Phi}_{mp}]$ to $[z^{\varphi}_{mp}]$. The imperfection in cancellation of the test line integrals comes from its implicit nature

[1]If an RWG MoM implementation obtains SP contributions using (4.8), depending on the discretization, it may or may not exhibit imperfect test line integral cancellations. If a fixed-symmetric quadrature rule is applied along contours of the observation elements C_m, numerical cancellation of test line integrals in (4.8) can be achieved to machine precision, numerically. Otherwise, discretization of (4.8) is vulnerable to imperfect cancellation of test line integrals.

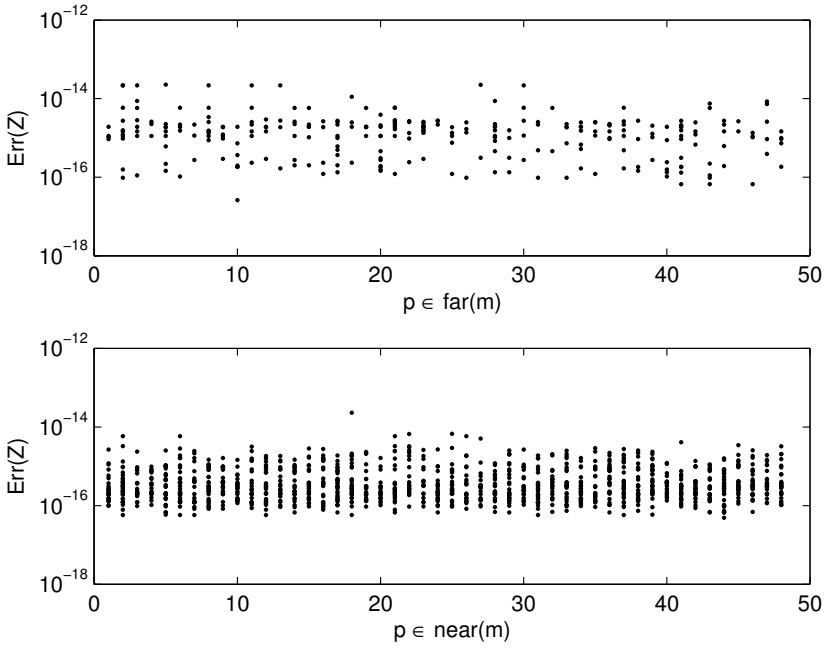

Figure 4.2: Comparison of the $(1.5N_p \times 1.5N_p)$ impedance matrix $[Z]$ of a 32 element PEC sphere at 100MHz obtained by the MP RWG-via-LCN (4.29) and MP RWG MoM (4.18). There are 48^2 points in the figure representing $\mathrm{Err}(Z_{i,j}) = |Z_{i,j}^{\text{MP RWG MoM}} - Z_{i,j}^{\text{MP RWG-via-LCN}}|/|Z_{i,j}^{\text{MP RWG MoM}}|$ where $i, j \in \{1, ..., 48\}$.

inherent to the VP RWG-via-LCN formulation. The latter discretizes scalar potential contribution in the form of (4.7) rather than (4.9), which allows for only imperfect implicit numerical cancellation of the test line integrals over C_m and leads to non-zero values of $[Z^{\Phi-\varphi}]$. Fig. 4.3 plots $|[Z^{\varphi}]_{4461,j}|$, $|[Z^{\mathcal{A}}]_{4461,j}|$, and $|[Z^{\Phi-\varphi}]_{4461,j}|$, which are the magnitudes of the 4461st row of the corresponding matrices sampled in increments of 60, i.e. at columns $(j = 1, 61, ..., 8881)$.

At 10kHz, the elements of $[z^{\varphi}]$ are numerically confirmed to be accurate with at least 4 digits of precision with average relative error $\epsilon = 10^{-5}$ when compared with the values of $[z^{\varphi}_{mp}]$ in (4.9) calculated to machine precision. Note that the conversion from $[Z_{\text{0th-LCN}}]$ to $[z^{\varphi}]$ is exact and this error is due to the approximation made in (4.11) plus the zeroth-order approximation of G_r. Although matrix components with maximum relative error 10^{-4} for $[z^{\varphi}]$ and $[z^{\mathcal{A}}]$ seem appropriate for the low-order RWG MoM[1], the imbalance due to the k_0^2 factor difference between $[z^{\mathcal{A}}_{mp}]$ and $[z^{\varphi}_{mp}]$ makes $|[Z^{\mathcal{A}}]_{4461,j}|$ about 8 digits of magnitude smaller than $|[Z^{\varphi}]_{4461,j}|$. This means that $[Z]$ will essentially lose the contribution of $[Z^{\mathcal{A}}]$ as the absolute error level of $[Z^{\varphi}]$ lies above $[Z^{\mathcal{A}}]$. This is because the absolute error level of $[Z^{\varphi}]$ is at least 10^{-4} due to error of $[z^{\varphi}]$ described above. Therefore, the MP RWG-via-LCN does not produce meaningful results at this frequency as shown later in Figs. 4.4 and 4.5. The VP RWG-via-LCN is also paralyzed at this frequency (Figs. 4.4 and 4.5), since $|[Z^{\Phi-\varphi}]_{4461,j}|$ is larger than $|[Z^{\mathcal{A}}]_{4461,j}|$ which is an indication that the contribution of $[z^{\mathcal{A}}_{mp}]$ will be lost in $[Z^{\mathcal{A}+\Phi}]$.

At 1MHz, the absolute error of $[z^{\varphi}]$ was numerically found to be $\epsilon = 10^{-7}$ and thus the absolute error level of $[Z^{\varphi}]$ at this frequency is at least 10^{-7}. This means that the level of $|[Z^{\mathcal{A}}]_{4461,j}|$ (observed from Fig. 4.3 to be about 10^{-5}) is 2 orders of magnitude

[1]Low-order methods are usually expected to provide field solutions with no more than 2 to 3 digits of precision [1].

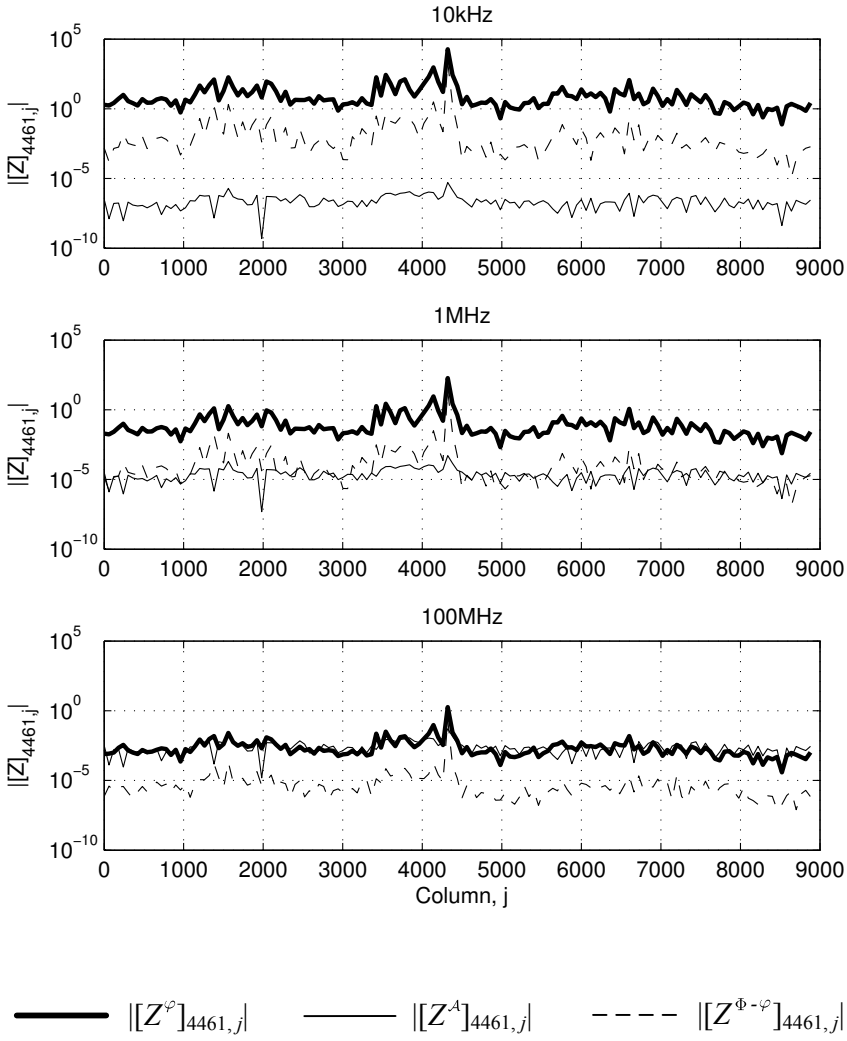

Figure 4.3: The magnitude of a single row of $(1.5N_p \times 1.5N_p)$ matrices generated for the $5,948$ element PEC sphere. Matrices $[Z^{\varphi}]$ and $[Z^{\mathcal{A}}]$ are used in the definition of the MP RWG-via-LCN matrix $[Z] = [Z^{\varphi}] + [Z^{\mathcal{A}}]$ while $[Z^{\Phi-\varphi}] = [Z^{\mathcal{A}+\Phi}] - [Z]$ quantifies the difference between $[Z]$ and the VP RWG-via-LCN matrix $[Z^{\mathcal{A}+\Phi}]$. The same mesh is used in Figs. 4.4, 4.5, and 4.6.

above the absolute error level of $|[Z^{\varphi}]_{4461,j}|$. Therefore, the MP RWG-via-LCN is expected to produce acceptable results at this frequency. The VP RWG-via-LCN on the other hand, still suffers from the imbalance in the vector- and scalar-potential terms due to the k_0^2 factor and fails to operate numerically. This is because $|[Z^{\Phi-\varphi}]_{4461,j}|$ is, on average, above the level of $|[Z^{\mathcal{A}}]_{4461,j}|$ and only about 2 orders of magnitude smaller than $|[Z^{\Phi}]_{4461,j}|$, $[Z^{\Phi}]$ being $[Z^{\mathcal{A}+\Phi}] - [Z^{\mathcal{A}}]$[1]. This means that despite the prescribed accuracy ($\epsilon = 10^{-4}$) imposed on the calculation of $[z_{mp}^{\Phi}]$, the resultant $[Z^{\Phi}]$ is only 2 digits accurate with respect to $[Z^{\varphi}]$ making the level of imperfectly canceled line integrals $[Z^{\Phi-\varphi}]$, on average, above the level of $[Z^{\mathcal{A}}]$. Hence, the VP contribution $[z_{mp}^{\mathcal{A}}]$ is still not recoverable in $[Z^{\mathcal{A}+\Phi}]$. The imperfection in line integral cancellation stems from the fact that $[Z^{\mathcal{A}+\Phi}]$ performs numerical cancellations that rely on the contribution from the adjacent triangle with opposite signs despite the fact that two adjacent triangles hold the scattered electric field on two different sets of observation points interior to each cell and not on the common edge. As a result, matrix elements in the VP formulation $[Z^{\mathcal{A}+\Phi}]$ are subject to additional inaccuracies when compared with matrix elements $[Z]$ in the MP formulation. Specifically, despite having two equivalent contributions with opposite signs at the same observation location (right on the edge), $[Z^{\mathcal{A}+\Phi}]$ implicitly sums these contributions at two different observation locations (at the internal quadrature points of the respective triangles) producing a less accurate SP contribution $[Z^{\Phi}]$ than the SP term $[Z^{\varphi}]$ in the MP formulation which assumes these cancellations analytically on the edge. This causes the numerical cancellation of analogous terms in $[Z^{\Phi}]$ with observation (outer) line integrals over C_m (i.e. the first two terms of (4.8)) to produce relative error level of near 10^{-2}, well above and irrespective of the 10^{-4} maximum error expected from the

[1]Note, $|[Z^{\Phi}]_{4461,j}|$ is not depicted in Fig. 4.3 as it would visually overlap with $|[Z^{\varphi}]_{4461,j}|$.

adaptive quadrature integration results. Further experiments showed that requesting more digits of precision (up to 9 digits) from the adaptive routines to evaluate inner integrals of (4.7), does not reduce this error which corroborates earlier statements that imperfect numerical cancellation of line integrals is independent of the source line integrals over C_p. In fact, numerical results showed that cancellation of the inner line integrals over the contour of the source triangle C_p (i.e. the third term in (4.8) as well as the first term on the right hand side of (4.7) appearing in VP RWG-via-LCN) is numerically performed down to machine precision with error level of 10^{-12} which supports that only the test line integrals in (4.8) implicitly contribute to the error of $[Z^{\Phi}]$ observed here. It is worth noting that applying special quadrature rules to the outer integral of (4.7) which have their quadrature points close to the edge of the triangle was tested in an attempt to mitigate this effect in VP RWG-via-LCN to no avail. This can be explained by the singular behaviour of the fields close to sharp edges.

Finally, at 100MHz, both VP and MP formulations perform with similar error levels. Although the $[z^{\varphi}]$ interactions were numerically evaluated to be only 3 digits accurate at this frequency[1], since the level of $|[Z^{\varphi}]_{4461,j}|$ is comparable with the level of $|[Z^{\mathcal{A}}]_{4461,j}|$, the MP RWG-via-LCN is expected to exhibit good performance. The VP RWG-via-LCN will also produce acceptable results since the level of $|[Z^{\Phi-\varphi}]_{4461,j}|$ lies well below (about 3 digits) the level of $|[Z^{\mathcal{A}}]_{4461,j}|$.

Fig. 4.4 depicts the time snapshots of the surface current at $\mathtt{t} = 0$s for the above discussed example and frequencies. Results are consistent with the described error mechanisms.

[1]Note that the analytical evaluation of G_s causes $[z^{\varphi}]$ to be more accurate at lower frequencies, since the lower the frequency, the less impact G_r and its zeroth-order approximation has in computing $[z^{\varphi}]$ elements.

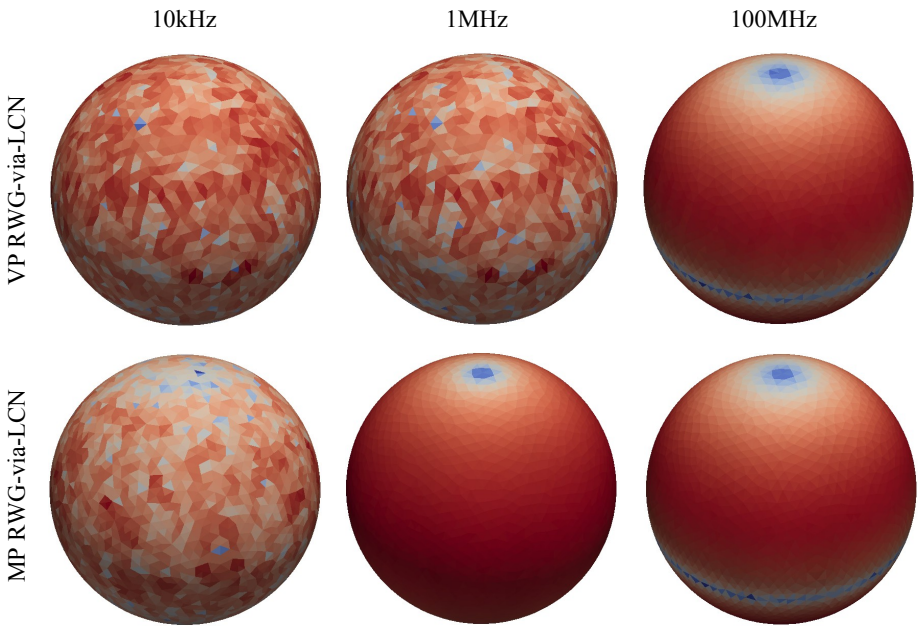

Figure 4.4: Time snapshots of the surface current density at $\mathtt{t} = 0$s computed by VP RWG-via-LCN (first row) and MP RWG-via-LCN (second row), corresponding to the plots of Fig. 4.3 at three frequencies. First, second, and third columns, correspond to 10kHz, 1MHz, and 100MHz, respectively. Results are quantified in Fig. 4.5.

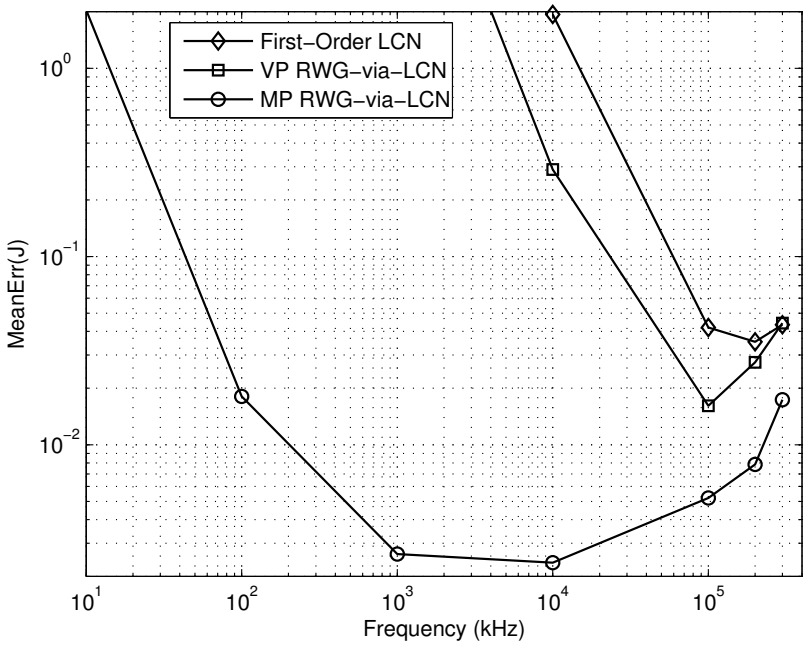

Figure 4.5: Mean relative error in the surface current MeanErr($\mathbf{J}$) computed by (4.32) for the 5,948 element PEC sphere example. Mie series is used as the reference solution.

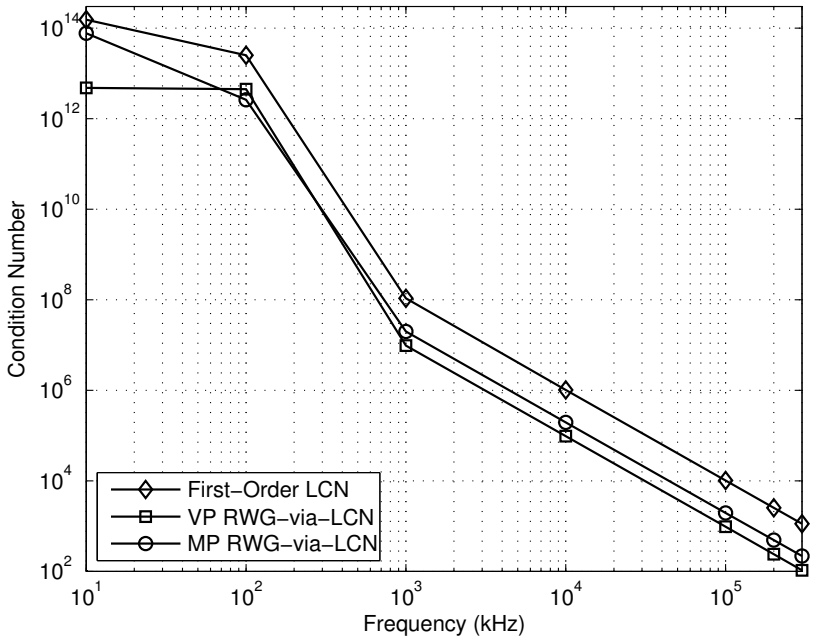

Figure 4.6: Condition numbers of the impedance matrices for the $5,948$ element PEC sphere used to produce Fig. 4.5.

Fig. 4.5 plots MeanErr($\mathbf{J}$) (4.32) produced by first-order LCN, VP RWG-via-LCN and MP RWG-via-LCN for the same sphere example at different frequencies where Mie series is used as the reference solution. The higher accuracy of the MP RWG-via-LCN compared with VP RWG-via-LCN and first-order LCN is evident as long as the low-frequency breakdown phenomena is not present. Specifically, the proposed MP RWG-via-LCN provides solutions with MeanErr($\mathbf{J}$) $< 2\%$ from $f = 100$kHz up to $f = 300$MHz but faces the low-frequency breakdown at 10kHz. The other two methods however, have MeanErr($\mathbf{J}$) $> 10\%$ at $f < 100$MHz due to the imbalance caused by the k_0^2 factor in SP and VP terms of the VP EFIE, described above. At higher frequencies where VP RWG-via-LCN and LCN can numerically operate ($f \geq 100$MHz), the VP RWG-via-LCN provides increasingly more accurate results compared to first-order LCN as the frequency decreases which is consistent with [89]. Nonetheless, the accuracy of the MP RWG-via-LCN is superior to both of the other methods at all frequencies while being computationally more efficient as it does not compute the contour integrals and requires fewer operations in computation of the SP contributions than either the VP RWG-via-LCN or first-order LCN.

Fig. 4.6 compares the 2-norm condition numbers of the impedance matrices used in creating Fig. 4.5. While there is improvement in the condition number from first-order LCN to MP RWG-via-LCN, the MP RWG-via-LCN has an increase in the condition number compared to that of the VP RWG-via-LCN. This increase however, is not severe and is well justified at lower frequencies where VP RWG-via-LCN suffers from high inaccuracies due to the imbalance in SP and VP terms of the VP EFIE. Moreover, as discussed in Section 4.4.5.3, the proposed MP RWG-via-LCN method can be combined with low-frequency stable formulations unlike LCN and VP RWG-via-LCN for which such techniques are not available.

4.5.3 Realistic Boeing 747 Model

The performance of the new technique was examined for a Boeing 747 airplane model, discretized with 9,810 triangles mesh. The model mesh has the ratio of maximum to minimum element size [24] of about 18. The excitation is a $\hat{z}$-directed electric dipole situated 3 meters above the tip of the aircraft. Figs. 4.7 to 4.10[1] are the time snapshots of the surface current induced on the surface of the aircraft at $\mathtt{t} = 0$s using the three techniques we are considering, as well as a reference solution (Fig. 4.7) obtained by a commercial tool, *Wave3D* [35]. Once again, the first-order LCN (Fig. 4.8) and VP RWG-via-LCN (Fig. 4.9) fail to operate at the low frequency ($f = 1$MHz) whereas the MP RWG-via-LCN (Fig. 4.10) maintains its accuracy. At the high frequency ($f = 100$MHz), both MP and VP RWG-via-LCNs provide acceptable results while first-order LCN shows visually less accurate results especially at the tail of the aircraft.

Fig. 4.11 plots the mean relative error of the computed current MeanErr($\mathbf{J}$) by the three techniques where *Wave3D* is used as the reference solution. Note however, that near the geometry edges, error is capped at 100% in calculating MeanErr($\mathbf{J}$) since maximum relative error may exceed 100% in such areas. Such a method of dealing with singular fields near the geometry edges in computing the average error (4.32), causes the error level to increase compared to what was shown in Fig. 4.5. However, this does not alter the comparison we are addressing here since all three methods under study use the same mesh. Similar behaviour as for the case of the sphere is observed for the realistic Boeing 747 model. At low frequencies, MP RWG-via-LCN performs much better than first-order LCN and VP RWG-via-LCN techniques, while at higher frequencies, both RWG-via-LCN solutions are more accurate than the

[1]Note that these four figures are all depicted in Fig. 7 of [132] but have been separated herein to improve visibility.

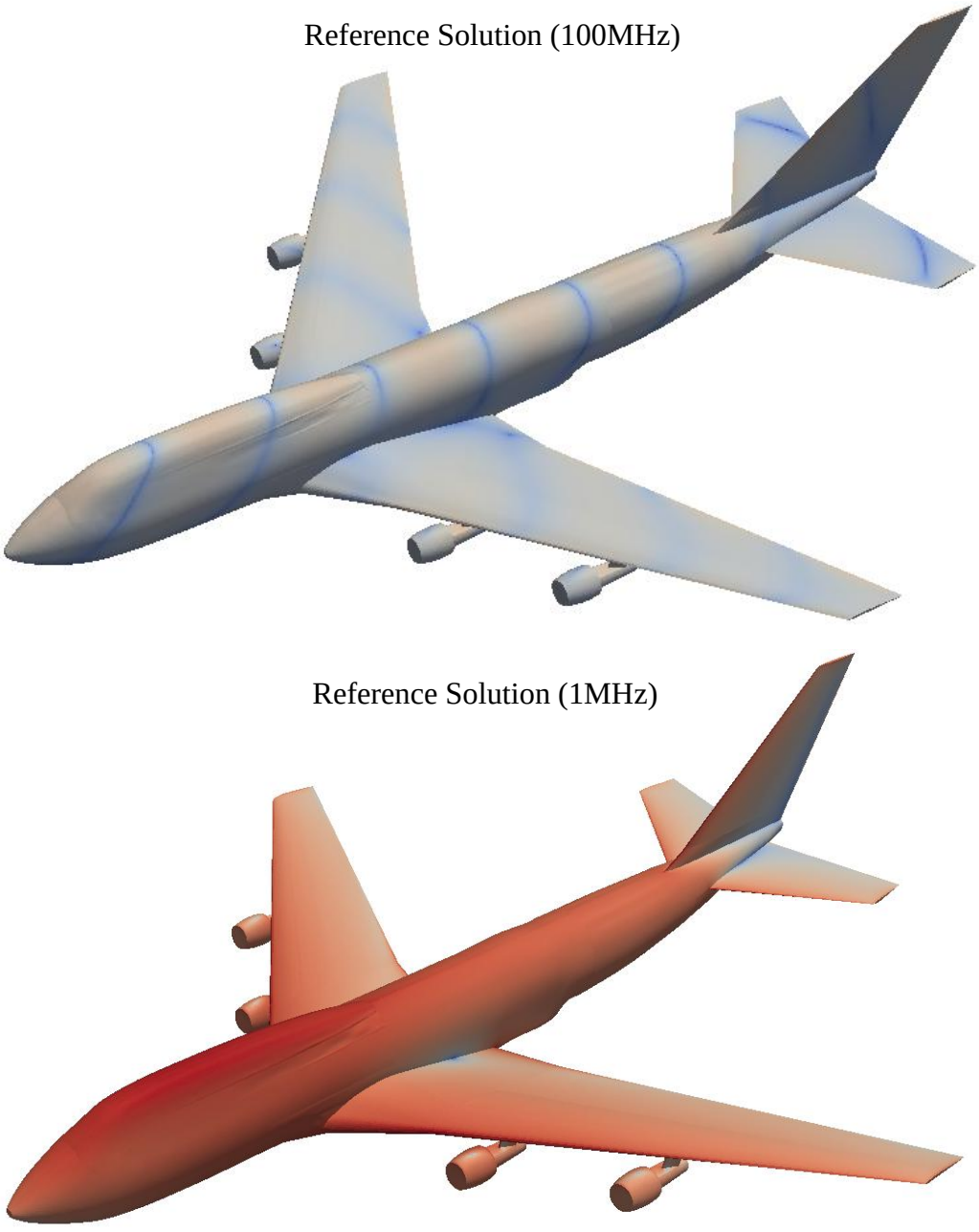

Figure 4.7: Time snapshots of the current density induced at $\mathtt{t} = 0$s on the surface of the Boeing 747 model obtained by Wave3D [35] using a $283,970$ element mesh as the reference solution for Figs 4.8 to 4.11.

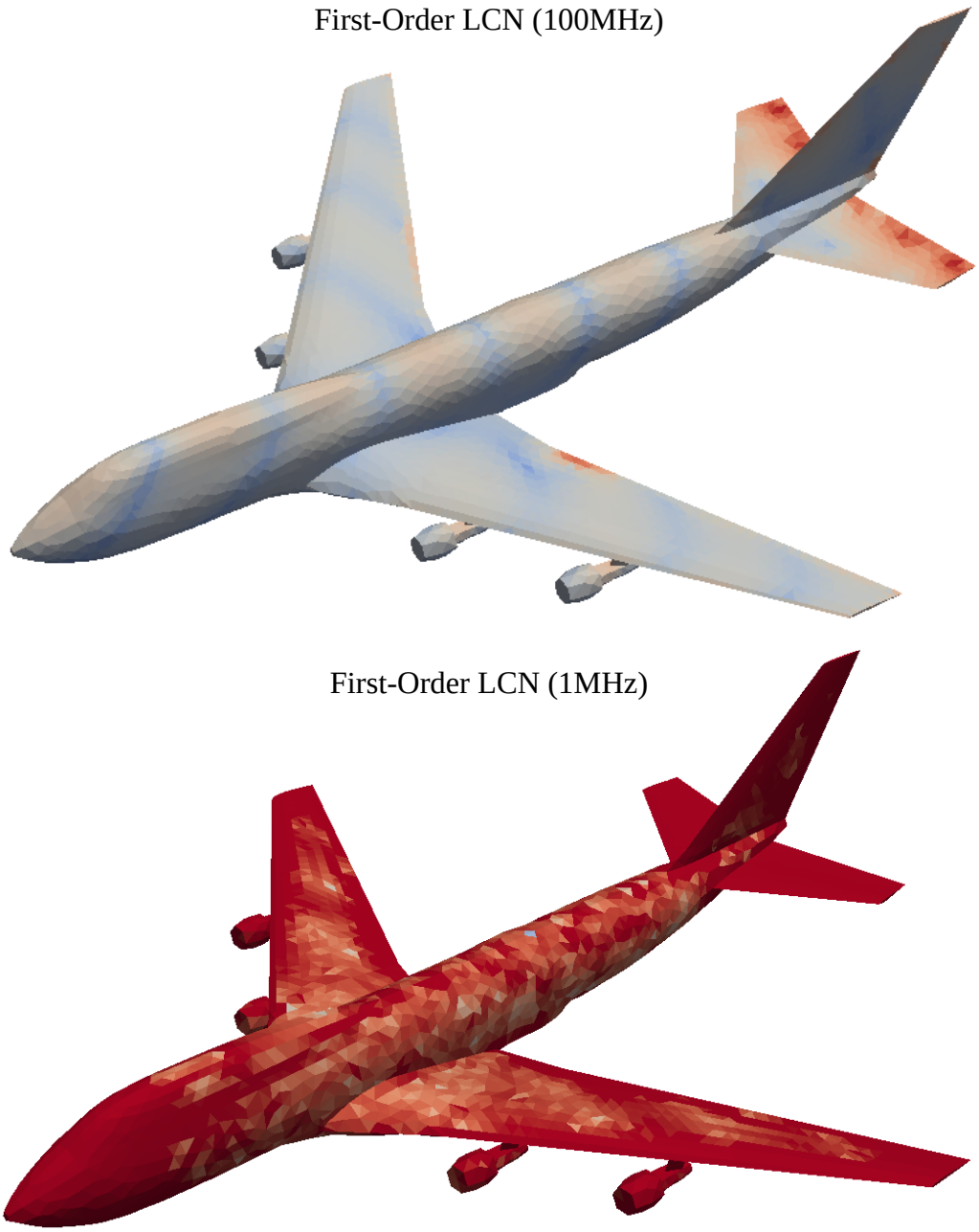

Figure 4.8: Time snapshots of the current density induced at $\mathtt{t} = 0$s on the surface of the Boeing 747 model obtained by First-order LCN with a mesh containing $9,810$ triangles. The reference solution is illustrated in Fig. 4.7 and is obtained by Wave3D [35] using a $283,970$ element mesh. The VP RWG-via-LCN and MP RWG-via-LCN solutions with the same mesh are depicted in Figs. 4.9 and 4.10, respectively. Results are quantified in Fig. 4.11.

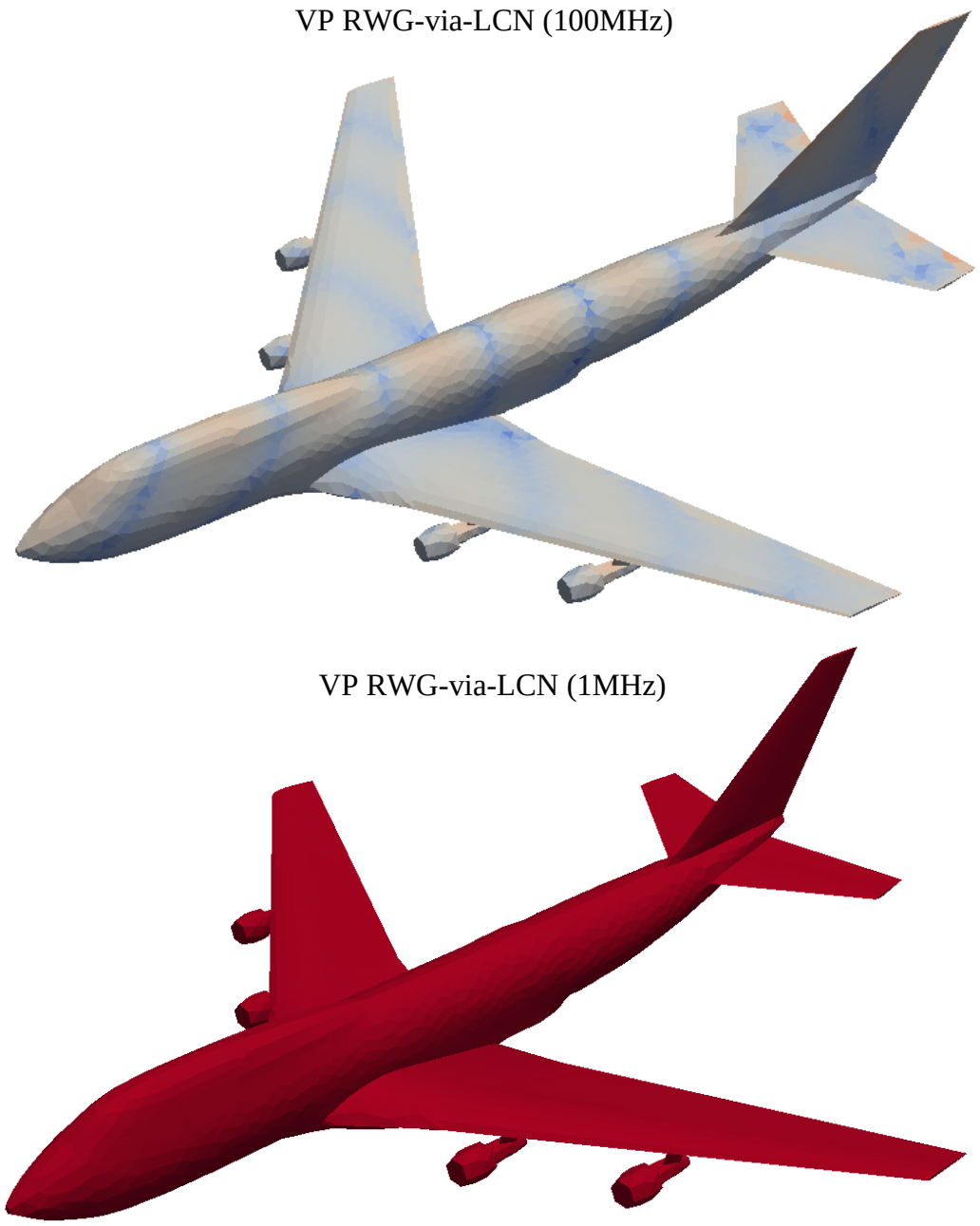

Figure 4.9: Time snapshots of the current density induced at $\mathtt{t} = 0$s on the surface of the Boeing 747 model obtained by VP RWG-via-LCN with a mesh containing $9,810$ triangles. The reference solution is illustrated in Fig. 4.7 and is obtained by Wave3D [35] using a $283,970$ element mesh. The First-order LCN and MP RWG-via-LCN solutions with the same mesh are depicted in Figs. 4.8 and 4.10, respectively. Results are quantified in Fig. 4.11.

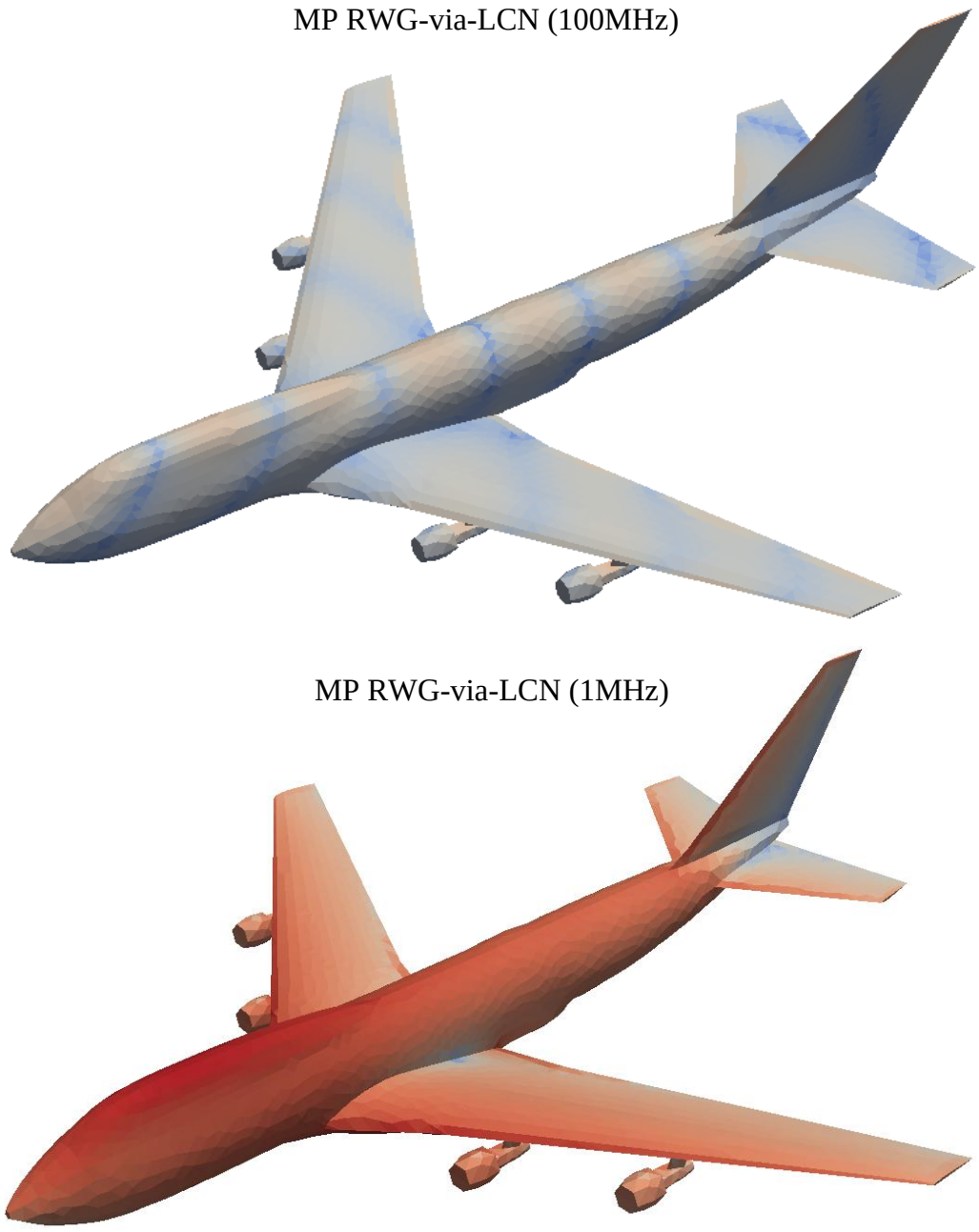

Figure 4.10: Time snapshots of the current density induced at $\mathtt{t} = 0$s on the surface of the Boeing 747 model obtained by MP RWG-via-LCN with a mesh containing $9,810$ triangles. The reference solution is illustrated in Fig. 4.7 and is obtained by Wave3D [35] using a $283,970$ element mesh. The First-order LCN and VP RWG-via-LCN solutions with the same mesh are depicted in Figs. 4.8 and 4.9, respectively. Results are quantified in Fig. 4.11.

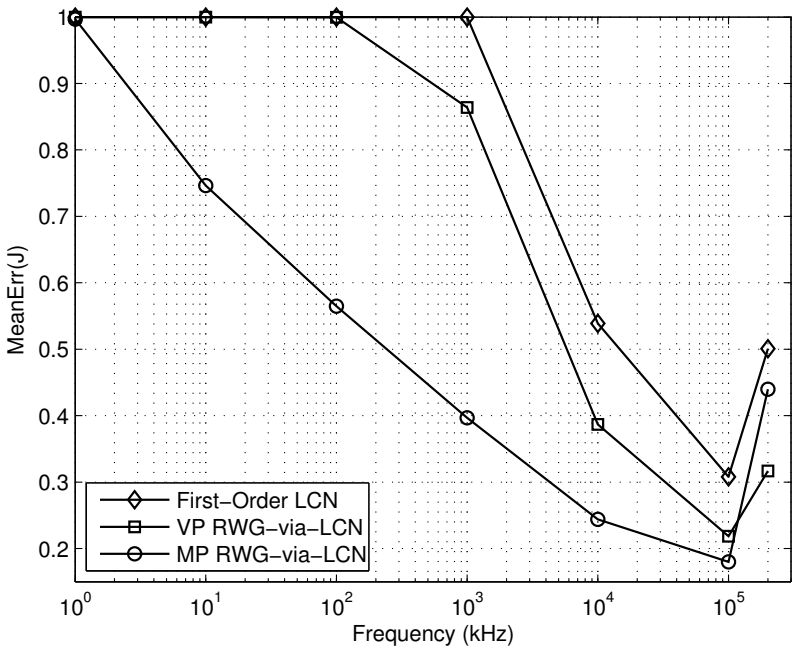

Figure 4.11: Mean relative error in the surface current MeanErr($\mathbf{J}$) obtained by (4.32) for the 9,810 element PEC Boeing 747 model. Wave3D [35] with 283,970 triangles is used as the reference solution.

solution of the first-order LCN.

Runtime detail for the data presented in Fig.4.11 is given in Table 4.1. It can be seen that the first-order LCN has much longer runtime which is mostly due to the LU-decomposition of a 4 times larger matrix compared to both RWG-via-LCN techniques. The VP RWG-via-LCN exhibits longer CPU times as the frequency decreases which can be explained by the fact that SP contributions require more iterations in the adaptive quadratures as the frequency decreases. The runtime for the proposed MP RWG-via-LCN on the other hand remains relatively the same at different frequencies.

The memory usage for the Boeing 747 example is tabulated in Table 4.2. The memory usage is directly affected by the size of the matrix and is independent of

Frequency	First-Order LCN	VP RWG-via-LCN	MP RWG-via-LCN
1kHz	66:43:25	17:15:18	6:32:03
10kHz	66:41:59	15:52:15	6:28:53
100kHz	66:42:26	14:58:19	7:37:25
1MHz	66:40:16	16:38:16	7:28:03
10MHz	61:38:07	5:26:47	6:27:06
100MHz	66:21:25	2:16:46	7:55:03
200MHz	66:58:14	3:12:55	6:35:01

Table 4.1: Runtime detail for the data presented in Fig.4.11 (hr:min:sec).

Frequency	First-Order LCN	VP RWG-via-LCN	MP RWG-via-LCN
1kHz	54,153,448	3,525,331	3,525,365
10kHz	54,153,448	3,525,331	3,525,321
100kHz	54,153,456	3,525,325	3,525,453
1MHz	54,153,450	3,525,333	3,525,332
10MHz	54,153,444	3,525,333	3,525,335
100MHz	54,153,444	3,525,331	3,525,335
200MHz	54,153,448	3,525,336	3,525,335

Table 4.2: Memory usage for the data presented in Fig.4.11 (kb).

the frequency since LU-decomposition is used herein. As a result, as can be seen in Table 4.2, the LCN method used about 54GB of memory while both RWG-via-LCN techniques used around 3.5GB of memory throughout the frequency range.

4.6 Conclusion

In this paper we established an exact relationship between RWG MoM in the mixed-potential form and the LCN schemes, resulting in a new current-continuity-enforcing LCN discretization of the MPIE termed MP RWG-via-LCN. The MP RWG-via-LCN is a point-based method, thus it can be efficiently accelerated by MLFMA similar to LCN. The new technique, similar to its VP RWG-via-LCN predecessor, enforces current continuity between triangles and produces 4 times smaller and bet-

ter conditioned matrix, compared to first-order LCN. The proposed MP RWG-via-LCN method is computationally more efficient and yields considerably more accurate results compared to the LCN and VP RWG-via-LCN techniques due to analytical cancellation of the line integrals appearing in the MPIE formulation. Moreover, the proposed MP RWG-via-LCN technique can be combined with preconditioning and Helmholtz decomposition techniques to solve low-frequency breakdown instead of resorting to AEFIE formulation which increases the DOF compared to the EFIE. The paper also provides detailed explanations for the effect of numerical versus exact cancellation of the line charge contributions in VP and MP forms of the EFIE and pertinent RWG MoM discretization schemes.

Chapter 5

On Achieving High-Order Convergence to the Correct Answer with the Locally Corrected Nyström Method

By *Mohammad Shafieipour* in partial fulfilment of the requirements of the degree of *Doctor of Philosophy (Ph.D.)*, March 2016.

5.1 Introduction

In the last two chapters we introduced two novel techniques for point-based Rao-Wilton-Glisson (RWG) method-of-moments (MoM) discretization of the electric field integral equation (EFIE) in its vector- and mixed-potential forms. Inherent to the nature of RWG basis functions, both schemes are low-order (LO) methods. Due to the maturity of the LO techniques, the industry is dominated by LO methods and the

techniques proposed in Chapters 3 and 4 might be adopted by the industry according to the industry's needs. However, both the industry and the research community is making a transition from LO methods to high-order (HO) methods as HO methods are exponentially more efficient than their LO counterparts as seen in [1] and further explained in this chapter. It is therefore essential to not only develop novel LO techniques (e.g. Chapter 3, and 4) for the industry's immediate needs, but also contribute to the development of the more efficient and newly emerging HO methods.

Although much research has already been carried out to explore the advantages of HO schemes [1, 19, 20, 49, 96–99], in this chapter, we discuss various aspects of achieving HO convergence to the correct answer (aka HO behaivour) using the HO locally corrected Nyström (LCN) method in discretizing the EFIE and two other surface integral equations (SIEs) for perfectly electric conducting (PEC) material, namely, the magnetic field integral equation (MFIE) and the combined field integral equation (CFIE). The MFIE can be obtained in a similar manner that EFIE was derived in Chapter 2 and the combined field integral equation (CFIE) is an algebraic combination of the two. Interested reader can refer to [5, 39–42] for more details on various SIE formulations.

5.2 Patch Size Limitation for the LCN Method

HO techniques reduce the number of unknowns since they can approximate the unknown fields on large patches [1, 19, 20, 96, 97]. Therefore the common max patch size h limitation based on the wavelength λ imposed on LO techniques ($h < \lambda/10$) does not have to be used in HO LCN method as it does not allow for utilization of larger elements. Reference [96] which proposed the use of HO curvilinear quadrilateral elements for HO MoM, did not attempt to formulate the patch size and showed

through numerical results that even at high frequencies, elements larger than 0.1λ can be used with HO MoM. The authors in [97, 99, 100] investigated the availability of large patches using Bézier meshes for highly curved geometries but did not study the limitation on the patch size with respect to the discretization scheme. A comprehensive note on HO frequency domain computational electromagnetics (CEM) [20], suggested as an empirical law that $h < 1.5\lambda$ can be used in HO CEM techniques.

In this section we demonstrate that for the LCN method to provide HO solutions, the element size should not only be limited by the wavelength, but it should also be defined based on the order of the discretization. The analysis is based on the *spatial sampling theorem* which is a consequence of the well known *Nyquist* criterion applied to the discretization of the RHS (right-hand-side) of the pertinent SIEs.

5.2.1 Spatial Sampling Theorem

It is well stablished in the field of digital signal processing [101–103] that according to the Nyquist criterion a band-limited signal can be reconstructed uniquely by its values sampled at uniform intervals of T_s such that

$$T_s \leq \frac{1}{2f} \quad \text{(sec)} \tag{5.1}$$

where f is the frequency of the signal in Hz. This is known as the *uniform sampling theorem* [101]. The uniform sampling theorem can also be applied to samples in the spatial domain rather than time, in which case the theorem is called *spatial sampling theorem* [104, 105]. Figure 5.1.a depicts a 1D spatial sampling of a traveling plane wave where samples are taken at equidistance points with distance d. According to the spatial sampling theorem, for the field of an incident plane wave to be exactly

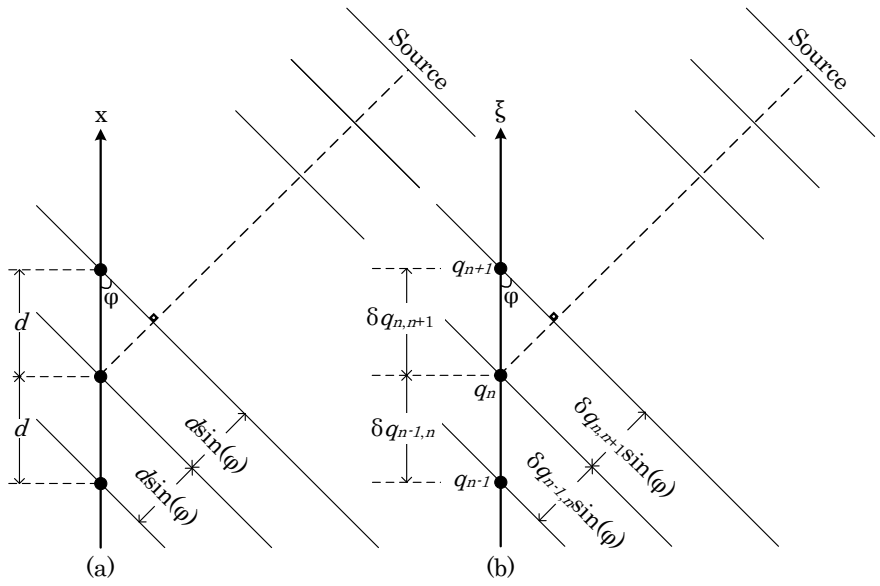

Figure 5.1: Illustration of 1D spatial sampling of a propagating wave using (a) Cartesian coordinate system, and (b) Barycentric coordinate system.

(without any error) reconstructible using the sample points, the following inequality has to be fulfilled

$$d\,|\sin(\varphi)| \leq \frac{1}{2\nu} \quad \text{(meter)}, \ \forall\varphi \tag{5.2}$$

where $\nu = \frac{1}{\lambda}$ is the spatial frequency of the wave. Knowing that $|\sin(\varphi)| \leq 1$, the spatial sampling interval can have the following form

$$d \leq \frac{\lambda}{2} \tag{5.3}$$

This theoretical limitation on the max distance between any two adjacent sampling points will be used in the sequel to explain the limitation on the patch size for the LCN method.

5.2.2 Limitation on the Patch Size for LCN

One way to explain the relationship between the maximum electrical size of the element $h_{\max}$ and the discretization order of the LCN is to analyse the quadrature sampled excitation function (i.e. the RHS) with respect to the inequality in 5.3. Consider the scalar LCN defined over the 1D domain

$$\int_a^b K(x,x')I(x')dx' = \phi^{\text{inc}}(x) \tag{5.4}$$

where K is the kernel, I is the unknown scalar quantity, $[a,b]$ is the interval in which I should be evaluated, x and x' are the observation and source points, respectively, in 1D Cartesian coordinates, and the RSH is the known forcing function. It is assumed that the entire interval $[a,b]$ is modelled using a single 1D element. As LCN is a point-based scheme, it enforces the observation points at the discrete quadrature abscissas x_{q_n} and thus we have

$$\int_a^b K(x_{q_n},x')I(x')dx' = \phi^{\text{inc}}(x_{q_n}) \tag{5.5}$$

The transition from (5.4) to (5.5) takes place in all forms of the LCN method and subsequent stages of discretization follow as discussed for example in [1, 18, 89]. It is important to realize that in converting (5.4) to (5.5) the excitation function $\phi^{\text{inc}}(x)$ is sampled as discrete quadrature points x_{q_n}. Fig. 5.1.b depicts such sampling where sampling of the incident field is shown at three consecutive quadrature points over the 1D Canonical coordinate (q_{n-1}, q_n, q_{n+1}). According to (5.3), for $\phi^{\text{inc}}(x_{q_n})$ in (5.5) to be able to uniquely represent $\phi^{\text{inc}}(x)$ in (5.4), the largest distance between any two quadrature points ($\delta q_{n-1,n}$ and $\delta q_{n,n+1}$ in Fig. 5.1.b) should not exceed $\frac{\lambda}{2}$. Therefore for the LCN method to exhibit HO convergence, the following "convergence criteria"

should be respected

$$h_{\max} \leq \frac{\lambda}{\delta q_p} \tag{5.6}$$

where $h_{\max}$ is the maximum electrical size of the element, and $0 < \delta q_p \leq 2$ is the maximum distance between two neighbouring quadrature abscissas of the pth order quadrature rule. The range $(0, 2]$ for δq_p is conveniently chosen to be consistent with the interval of $[-1, 1]$ in computational domain coordinate system. Note that the criteria (5.6), is necessary for the LCN method to achieve HO convergence, but may not be sufficient as other factors such as 2D or 3D modelling, element shape, curvature of the edges, etc, might prevent an LCN solution to exhibit HO convergence. From (5.6) it can be understood that the maximum electrical size of the element $h_{\max}$ is not only dependent on the wavelength λ, but it is also dependent on the order of the discretization as δq_p varies for different orders of a certain quadrature rule. Fig. 5.2 compares $1/\delta q_p$ for the commonly used product of 1D Gauss-Legendre rule at different orders $p = 0...19$. The abscissas of the Gauss-Legendre rule reside at the roots of the Legendre polynomials. At $p = 0$ where there is only one quadrature point, we have $\delta q_p = 2$, since the distance between two quadrature points is the distance between centroids of two adjacent patches. As the order p increases, quadrature abscissas tend to concentrate around the edge of the element. Therefore $1/\delta q_p$ does not grow linearly as p increases. Nevertheless, as can be seen in Fig. 5.2, at $p = 8$, the maximum electrical size of the element $h_{\max}$ may be as large as 3λ[1]. This convergence criteria, is larger than 1.5λ which was empirically suggested in [20] for HO CEM techniques.

[1]Note that usually Computer-Aided Design (CAD) tools (such as Gmsh [106]) provide the element size h in terms of the radius of the circumscribing circle r, in which case $h = \sqrt{2}r$.

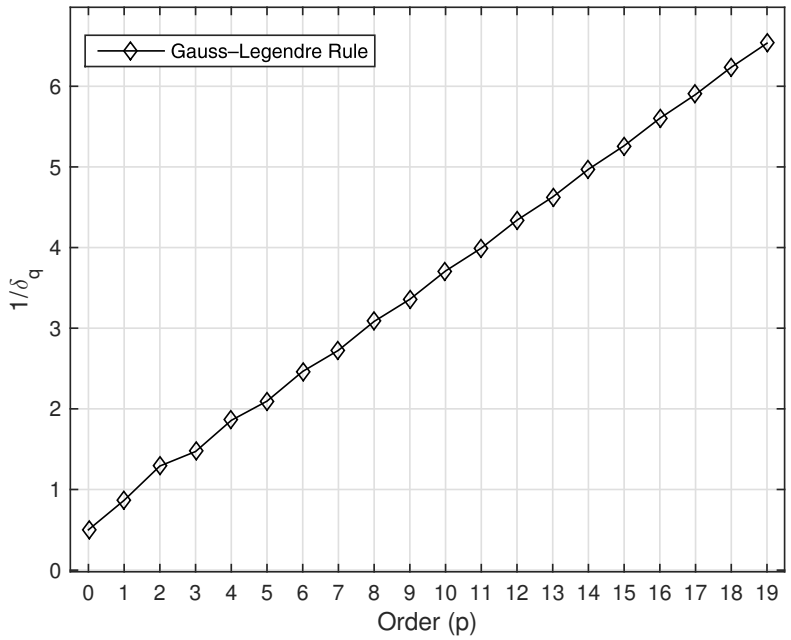

Figure 5.2: $1/\delta q_p$ for different orders of the Gauss-Legendre rule.

5.2.3 Numerical Results

In order to illustrate the validity of the convergence criteria presented in (5.6), we consider electromagnetic scattering on a sphere as its analytical solution is available by Mie series. The sphere is made of PEC material with radius of 1m which is modelled via analytic exact cube-to-sphere mapping. The excitation is a $\hat{z}$-directed electric dipole situated 10 meters above the center of the sphere with $f = 1$GHz. The CFIE with $\alpha = 0.5$ is used to obtain the solution and the basis functions are polynomial-complete to order $p + 1$ where product of 1D Gauss-Legendre rule is applied [1, 18]. The sphere is discretized using $6, 24, 54, 96$ and 216 elements which respectively have $h_{\max} = 3.85\lambda$, 2.45λ, 1.68λ, 1.3λ, and 0.89λ at the considered frequency (1GHz). The

mean error in the computed current MeanErr($\mathbf{J}$) is calculated as

$$\text{MeanErr}(\mathbf{J}) = \frac{1}{N}\sum_{i=1}^{N}\frac{|J_i^{\text{LCN}} - J_i^{\text{Mie}}|}{|J_i^{\text{Mie}}|} \tag{5.7}$$

where N is the number of quadrature points, J_i^{LCN} is the LCN computed current at the quadrature points, and J_i^{Mie} is the corresponding current evaluated by the Mie series solution. Fig. 5.3 plots MeanErr($\mathbf{J}$) for various orders where errors larger than 100% are capped at 100%. The dotted lines correspond to orders that do not meet (5.6) while solid lines represent orders that respect (5.6). As can be seen from the figure, for a certain mesh, convergence to the true solution occurs if the convergence criteria (5.6) is met (solid lines). As expected, the convergence rate is different for different mesh according to $\mathcal{O}(h^p)$ convergence rate [1, 19, 20]. On the other hand if the convergence criteria (5.6) is violated (dotted lines), the average error of the solution remains greater than 30% irrespective of the discretization parameters $(h_{\max}, p)$ indicating that the numerical results are not trustworthy. This completes the discussion on the patch size limitation for the HO LCN method.

5.3 Predicting the Optimal Number of Unknowns for the LCN Method

In this section we develop a procedure in which the minimum number of unknowns for a desired accuracy can be achieved using the HO LCN method. In doing so, it is necessary to discuss the convergence rate of the HO LCN.

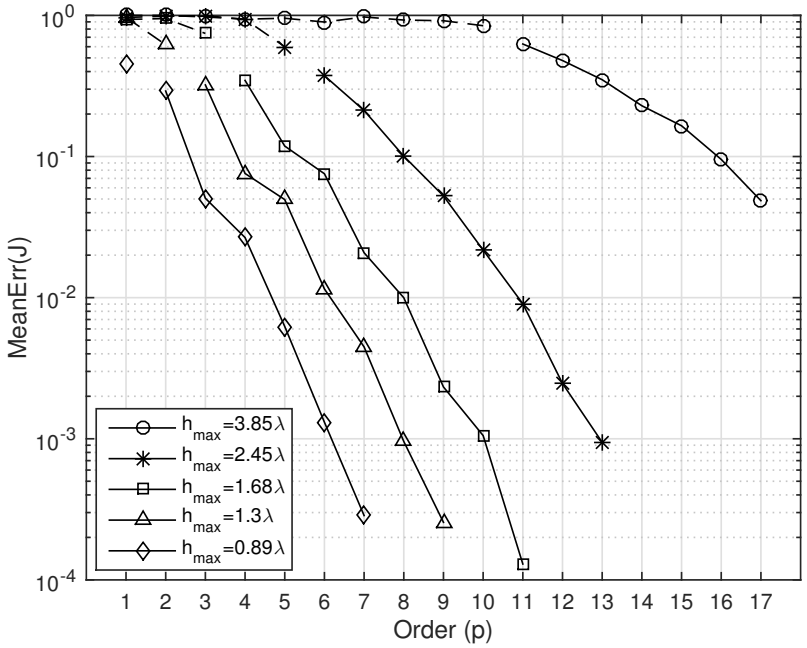

Figure 5.3: MeanErr(**J**) computed using (5.7) for different mesh and orders when compared with the Mie series solution. Results are obtained using CFIE ($\alpha = 0.5$). Dotted lines represent situations where (5.6) is violated and solid lines otherwise.

5.3.1 Theoretical Convergence Rate

In HO CEM literature, it is assumed that the convergence rate of a proper HO algorithm with order p using characteristic element size h is $\epsilon = \mathcal{O}(h^p)$ [1, 18–20, 96]. This assumption has been made as a general metric for the efficiency of the HO methods. However, according to the theory presented in [107], if basis functions interpolating the current are complete up to polynomial degree p in both dimensions of the surface coordinate system, the MoM's solution should exhibit $\mathcal{O}(h^{2(p+1)})$ convergence rate. This rate is considerably higher than $\mathcal{O}(h^p)$. Since MoM and LCN have been shown to be equivalent [18], the same convergence rate is also expected from the LCN method as demonstrated below.

Due to the availability of analytical solution, we present simulations of the scattering on a 1 meter radius sphere excited by a radial dipole located 9 meters above the sphere's north pole at 1GHz. The sphere example is also desirable since it does not have sharp edges and the LCN method has been shown to provide HO solutions for this problem [1, 18, 47, 48]. Here, we study the global convergence rate but due to the smoothness of the sphere, the same analysis could be applied to the local convergence rate as well. In order to eliminate any geometrical error, the geometry is obtained by analytical cube-to-sphere mapping that exactly models the smooth curvature of the sphere using quadrilateral patches. The quadrature rules were defined over these cells as a product of 1D Gauss-Legendre rules. Mean relative error is estimated using (5.7). Fig. 5.4 shows the mean relative error obtained by MFIE with h- and p-refinements. Errors more than 1 have been capped at 1 in order to have a clearer plot. The red lines represent situations where $h_{\max}$ violates (5.6) in at least one element whereas blue lines are results obtained from cases where all elements have sizes $h \leq \lambda/\delta q_p$. The black lines correspond to the analytical lines where $\epsilon = Ch^{2(p+1)}$. It turns out

(through experiments) that C in this example has the following closed form

$$C = 0.05k_0^{2(p+1)}||K|| \tag{5.8}$$

where $||K||$ is the L_1-norm of the Peano kernel [108] which can be written in terms of the solution order p as

$$||K|| = \frac{2^{2p+3}[(p+1)!]^4}{(2p+3)[(2p+2)!]^3} \tag{5.9}$$

It is clear from the blue lines, that at all orders, HO behaviour with convergence almost equal to $Ch^{2(p+1)}$ is exhibited when the criteria (5.6) is enforced. On the other hand where such restriction has not been enforced on h, in almost all cases, accurate results can not be obtained and large mean relative errors close to 100% are produced. This supports the statement that violating (5.6) is in fact violation of the Nyquist criteria in sampling of the RHS (incident field) and completely paralyzes the numerical method. However, there is one point in the plot at order 2 where despite the criteria being violated, a mean error less than 1 is obtained. This can be explained by the fact that for this case, most of the elements have sizes $h \leq \lambda/\delta q_2$ and actually met the criteria and the number of elements that violated it are very few leading to relative mean error less than 100%. In fact in this particular case we have $h = 0.391$m and $\lambda/\delta_{q_2} = 0.387$m which indicates that most of the elements have met the criteria. Nevertheless, the convergence rate at this point does not exhibit $Ch^{2(p+1)}$ due to the small deviation from (5.6) by very few (6 out of 96) elements. From the numerical results provided above, one can see that by respecting the criteria formulated in (5.6), the MFIE offers theoretical convergence rate with errors $\epsilon = \mathcal{O}(h^{2(p+1)})$ whereas previous work [18] reported less consistent convergence

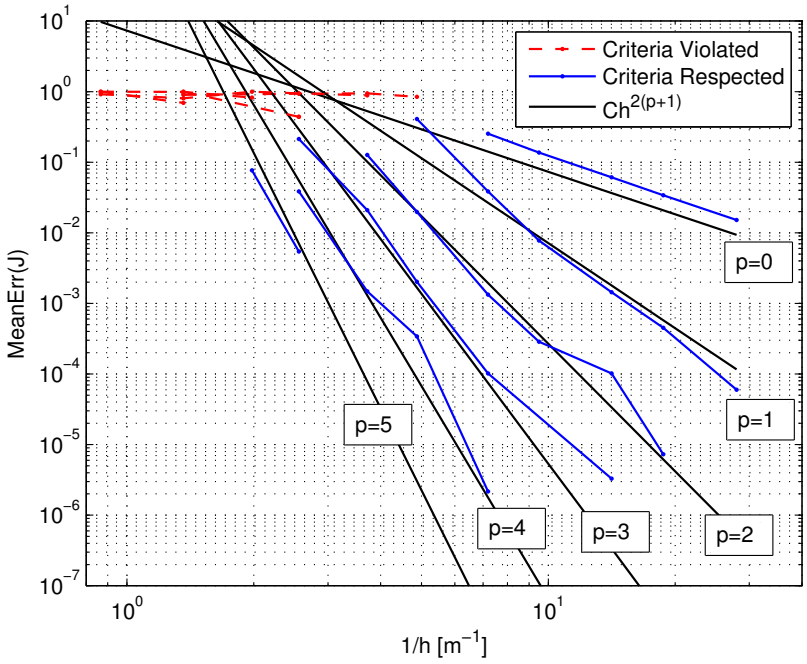

Figure 5.4: Respecting and Violating the Introduced Convergence Criteria

with the theory [107], perhaps due to some elements violating (5.6) similar to the case above where minor deviations from the criteria by few elements caused non-theoretical convergence rate. Therefore, although reference [18] reported less than theoretical convergence rate $p_{\text{conv}} > p + 1$ for the MFIE, as demonstrated above, the theoretical convergence rate can indeed be achieved for MFIE on sufficiently smooth objects if the criteria (5.6) is respected. Therefore by refining h and p, the error drops as $\epsilon = \mathcal{O}(h^{2(p+1)})$. For the EFIE, previous work [18] reported convergence with order $p_{\text{conv}} \leq p + 1$. Our HO LCN implementation is also unable to exhibit $\epsilon = \mathcal{O}(h^{2(p+1)})$ for the EFIE and CFIE even if the criteria is met. In fact, due to the non-self-adjoint nature of the electromagnetic integral operators, it is difficult (if not impossible) to derive a general closed form expression for the error convergence [18]. Therefore neither of h^p or $h^{2(p+1)}$ can be used in practical examples[1]. More generally,

[1]See Prof. Gedney's comment in Section 7.2.8.4.

an HO BEM method, has error convergence which can be represented by

$$\begin{aligned} \epsilon &= c_1 h^{bp+c_2} \\ \epsilon &= c_1 \cdot h^{c_2} \cdot h^{bp} \\ \epsilon &= a h^{bp} \end{aligned} \tag{5.10}$$

where $a = c_1 \cdot h^{c_2}$ and b are constant terms which depend on many different factors including but not limited to[1]

1. Formulation (i.e. EFIE, MFIE or CFIE).
2. The electrical size of the considered scattering object.
3. The shape of the considered scattering object.
4. Choice of triangular or quadrilateral elements using either curvilinear or flat faceted elements.
5. The chosen error estimation mechanism (i.e. mean error, max error, norm error).
6. The parameter in which error estimation is applied for (i.e. current or RCS).
7. Choice of basis functions (i.e. a_i or a^i using either complete polynomial or mixed-order which can be done either by monomials or Legendre polynomials).
8. Choice of quadrature rules (Gaussian or Newton-Cotes).

Therefore, a and b should be found experimentally for a specific problem and LCN implementation. In the next section we explain how this can be done.

[1]For the reasons that will be clear later, the characteristic element size h in the mesh is excluded from the list.

5.3.2 Finding the Convergence Rate Experimentally

Consider the electromagnetic scattering from an exact-sphere with 96 quadrilateral elements obtained by CFIE. We choose this example here as an analytical solution is available and we can compare the numerical solution with the analytical solution. But this procedure can be applied to an arbitrary smooth geometry. Observing Fig. 5.5, it can be seen that by using a minimum of three simulations, one can find the convergence rate of a particular electromagnetic scattering problem. From the figure, it can be seen that regardless of the reference solution being analytical (Mie series) or numerical (Highest Order), it is possible to accurately estimate average error in the solution. This is because, from the point of view of a solution that has average error $\epsilon = 10^{-k}$, a solution that has error 10^{-k-1} can act as a proper reference solution[1]. Therefore in Fig. 5.5, the computed error convergence rate (solid lines) is almost identical to the true convergence rate found by the analytical solution (dotted lines). Now using any 2 points ϵ_1, ϵ_2 and knowing that $\epsilon_1 = ah^{bp_1}$ and $\epsilon_2 = ah^{bp_2}$, the factors a and b can be computed. To find b we use ϵ_1, ϵ_2

$$\begin{aligned} \frac{\epsilon_1}{\epsilon_2} &= \frac{ah^{bp_1}}{ah^{bp_2}} = h^{b(p_1-p_2)} \\ b(p_1-p_2) &= \log_h(\frac{\epsilon_1}{\epsilon_2}) \\ b &= \frac{\log_h(\frac{\epsilon_1}{\epsilon_2})}{p_1-p_2} \end{aligned} \tag{5.11}$$

[1]As an example, if the exact solution is A and the true absolute error in solution B is $\epsilon_B = B - A = 10^{-1}$, a solution called C with $\epsilon_C = C - A = 10^{-2}$, can estimate the error in B as $B - (A + 10^{-2}) = 1.1 \times 10^{-1}$.

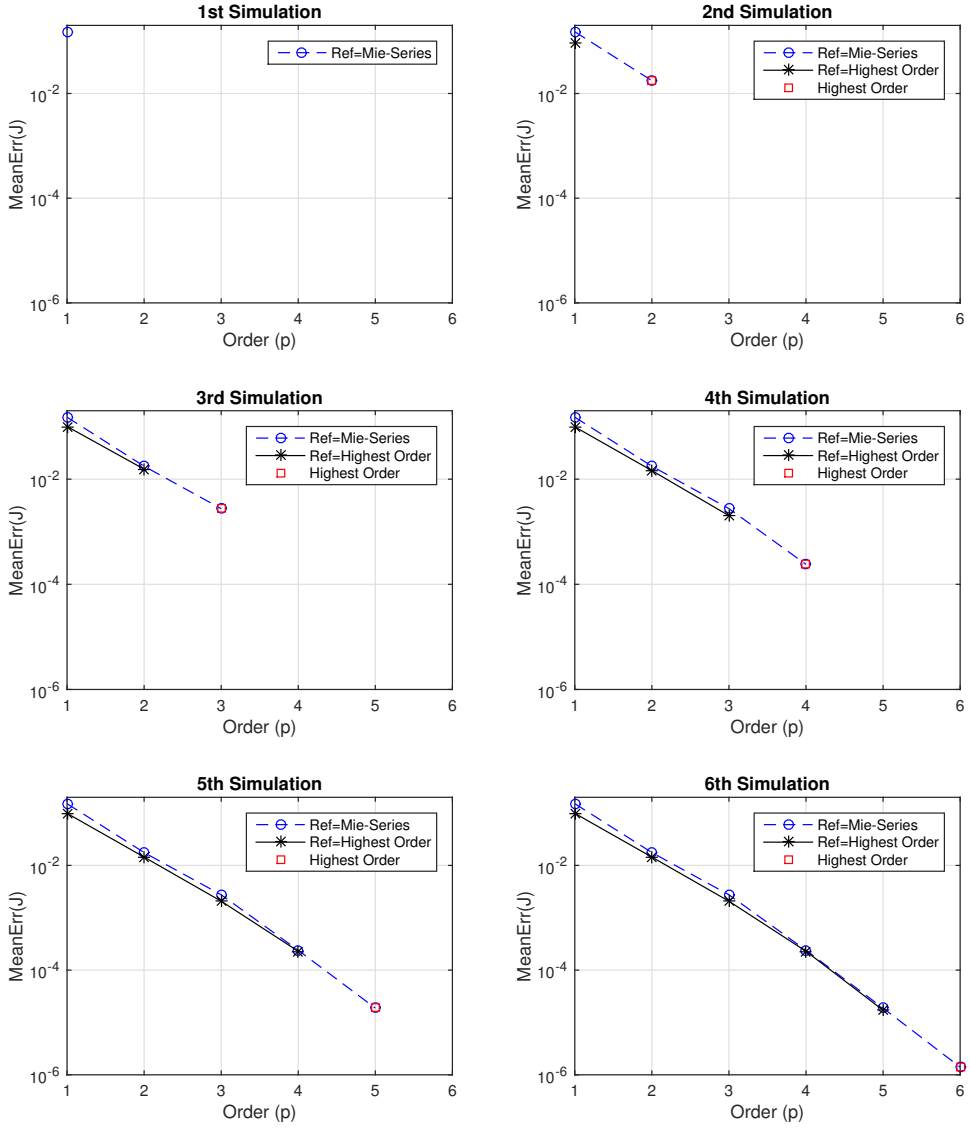

Figure 5.5: Demonstration of approximating the error in a solution using the available highest order numerical solution as the reference solution (solid lines) versus the true error (dotted lines) computed when the analytic Mie series solution is used as the reference solution.

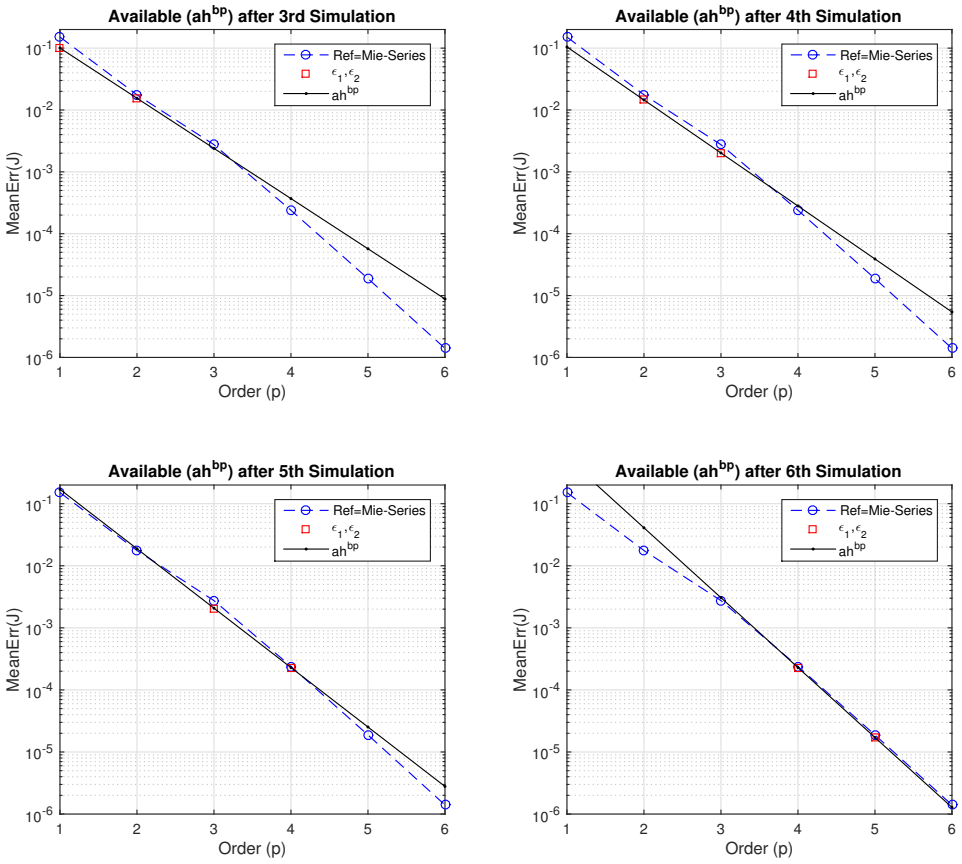

Figure 5.6: Demonstration of approximating the convergence rate experimentally (solid lines) versus the true convergence rate (dotted lines).

but a can be found using either ϵ_1 or ϵ_2

$$\begin{aligned} \epsilon_1 = ah^{bp_1} \quad &\Rightarrow a = \frac{\epsilon_1}{h^{bp_1}} \\ \epsilon_2 = ah^{bp_2} \quad &\Rightarrow a = \frac{\epsilon_2}{h^{bp_2}} \end{aligned} \tag{5.12}$$

Fig. 5.6, plots the estimated error convergences using the data obtained in 3rd to 6th simulations using (5.11) and first line of (5.12). As can be seen from the figure, the estimated curve becomes more accurate as higher orders are computed. Nevertheless,

the curve obtained using the first three simulations seems accurate enough to estimate a and b.

5.3.3 Computing the Number of Unknowns with respect to the Desired Accuracy

It was shown in [1] that the number of required unknowns from 2 algorithms with different orders can be related analytically by assuming that an HO method provide results that exhibit errors in the order of h^p. Here we derive (16) of [1] using the generalized convergence rate ah^{bp} in (5.10) and extend the discussion by introducing the desired accuracy into the formulation. As was discussed in Section 6 of [1], the number of unknowns n associated to the LCN with order p and element size h scales in the order of

$$n = \frac{p^2}{h^2} \tag{5.13}$$

Now assume that the solution to a problem with the LCN can be solved by an algorithm with max order P with characteristic element size H and it produces results with error ϵ using N unknowns. To come up with a solution to the same problem using order $p < P$ with characteristic element size h but with the same order of error ϵ using n unknowns we can write

$$\begin{aligned} ah^{bp} &= H^P \\ h^{bp} &= \frac{1}{a}H^P \\ h &= \sqrt[bp]{\frac{1}{a}H^P} \\ h^2 &= \left(\sqrt[bp]{\frac{1}{a}H^P}\right)^2 \end{aligned} \tag{5.14}$$

Substituting (5.14) into (5.13) we may write

$$\begin{aligned} n &= \frac{p^2}{\left(\sqrt[bp]{\frac{1}{a}H^P}\right)^2} \\ &= \frac{p^2}{\left(\frac{1}{a}H^P\right)^{(\frac{2}{bp})}} \\ &= \frac{p^2}{a^{(\frac{-2}{bp})} \cdot H^{(\frac{2P}{bp})}} \\ &= \frac{p^2}{a^{(\frac{-2}{bp})} \cdot (H^2)^{(\frac{P}{bp})}} \end{aligned} \tag{5.15}$$

We also know from (5.13) that $N = P^2/H^2$ thus by replacing H^2 in (5.15) we can write

$$\begin{aligned} n &= \frac{p^2}{a^{(\frac{-2}{bp})} \cdot (\frac{P^2}{N})^{(\frac{P}{bp})}} \\ &= N^{(\frac{P}{bp})} \cdot a^{(\frac{2}{bp})} \cdot \frac{p^2}{P^{(\frac{2P}{bp})}} \end{aligned} \tag{5.16}$$

which is equivalent to (16) of [1] if $a, b = 1$. To introduce the accuracy into the above formulae, we perform (5.14) on H^P instead of ah^{bp}

$$\begin{aligned} H^P &= ah^{bp} \\ H &= \sqrt[P]{ah^{bp}} \\ H^2 &= \left(\sqrt[P]{ah^{bp}}\right)^2 \end{aligned} \tag{5.17}$$

and similarly perform (5.15) on N

$$\begin{aligned} N &= \frac{P^2}{\left(\sqrt[P]{ah^{bp}}\right)^2} \\ &= \frac{P^2}{\left(ah^{bp}\right)^{(\frac{2}{P})}} \\ &= \frac{P^2}{\left(ah^{bp}\right)^{(\frac{2}{P})}} \\ &= \frac{P^2}{a^{(\frac{2}{P})} \cdot \left(h^2\right)^{(\frac{bp}{P})}} \\ &= \frac{P^2}{a^{(\frac{2}{P})} \cdot \left(\frac{a}{a}h^2\right)^{(\frac{bp}{P})}} \\ &= \frac{P^2}{\frac{a^{(\frac{2}{P})}}{a^{(\frac{bp}{P})}} \cdot \left(ah^{bp}\right)^{(\frac{2}{P})}} \end{aligned} \tag{5.18}$$

At this point we can use the error convergence $\epsilon = ah^{bp}$ and have

$$N = \frac{P^2}{\frac{a^{(\frac{2}{P})}}{a^{(\frac{bp}{P})}} \cdot \epsilon^{(\frac{2}{P})}} \tag{5.19}$$

By substituting (5.19) into (5.16) we have

$$n = \left(\frac{P^2}{\frac{a^{(\frac{2}{P})}}{a^{(\frac{bp}{P})}} \cdot \epsilon^{(\frac{2}{P})}} \right)^{(\frac{P}{bp})} \cdot a^{(\frac{2}{bp})} \cdot \frac{p^2}{P^{(\frac{2P}{bp})}} \tag{5.20}$$

After some algebraic manipulations on the exponent of a we arrive at

$$n = a \cdot \left(\frac{P^2}{\epsilon^{(\frac{2}{P})}} \right)^{(\frac{P}{bp})} \cdot \frac{p^2}{P^{(\frac{2P}{bp})}} \tag{5.21}$$

where it is noticed that the dependency to P cancels out and the number of unknowns n can be written as

$$n = a \cdot \epsilon^{(\frac{-2}{bp})} \cdot p^2 \tag{5.22}$$

The expression in (5.22), is significant, as it allows to compute the number of unknowns n at a given order p, considering that a and b are experimentally found using the procedure in Section 5.3.2 for a desired accuracy ϵ. Fig. 5.7 plots (5.22) by assuming that $p = 1, 2, ..., 10, a = 1$, and $b = 1$ with different ϵ. These parameters are chosen to be consistent in the example described in [1]. It is noticed that if a LO method ($p = 1$), requires solutions with high accuracies, the number of unknowns and therefore the complexity of the algorithm grows exponentially faster, compared to higher order methods. For example, if 10 digits of precision is required, a 10th order algorithm can deliver the solution with only 10^3 unknowns, while a 1st order algorithm, requires 10^{20} unknowns. The dotted red line in the figure, corresponds to the (16) of [1], if the number of unknowns for the max order $p = 10$ (N_2 therein) is $N_2 = 10,000$. It can be seen that by introducing the desired accuracy, (5.22) can provide a better metric for comparing the complexity of the algorithms compared to (16) of [1].

5.3.4 Predicting the Optimum Number of Unknowns for a Desired Accuracy

Formulating the number of unknowns for a desired accuracy at different orders (5.22), facilitates predicting the optimum discretization in terms of the element size h and order p and therefore can predict the minimum number of unknowns for a desired accuracy as demonstrated below.

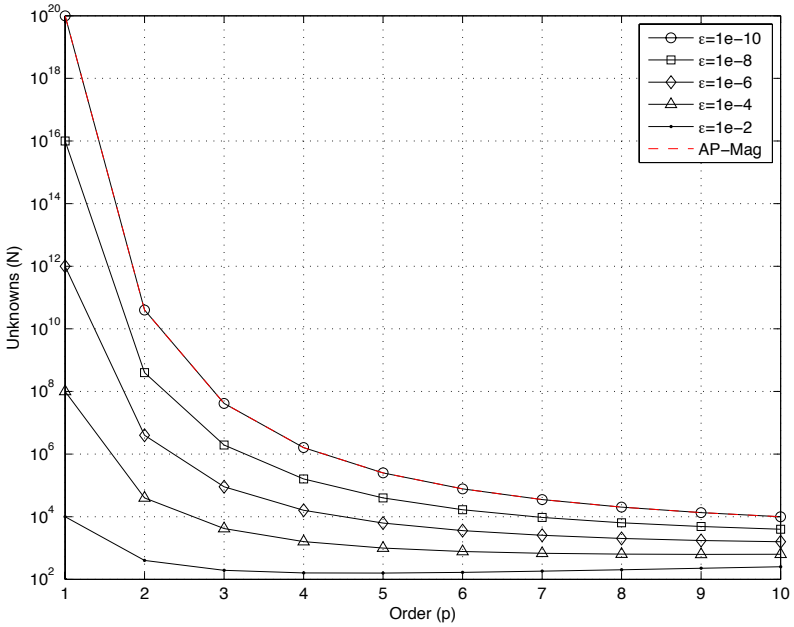

Figure 5.7: Comparison of the number of unknowns required to reach a prescribed accuracy using algorithms of various orders computed by (5.22).

Let's predict the optimum number of unknowns using the error convergence rate available after the third simulation in Fig. 5.5 which can be seen in Fig. 5.6. Therefore we have $\epsilon_1 = 0.1003, \epsilon_2 = 0.0155, p_1 = 1$, and $p_2 = 2$. Substituting them into (5.11) and (5.12) we find $a = 0.6495$ and $b = 1.4522$. Therefore the convergence rate for this particular example and LCN implementation is actually

$$\epsilon = 0.6495 h^{1.4522p} \tag{5.23}$$

and according to (5.22), the number of unknowns n for a given order p and the desired accuracy ϵ can be pre-computed as

$$n = 0.6495 \cdot \epsilon^{(\frac{-2}{1.4522p})} \cdot p^2 \tag{5.24}$$

Fig. 5.8, plots (5.24) for various accuracies and orders. The minimum number of unknowns is shown by the red curve. It can be seen that, for example, if 4 digits of precision is required, the order 6 solution is optimal to be used. It is interesting to see that (5.24) is independent of the characteristic element size h. Therefore, for a requested accuracy ϵ_{req}, the element size h_{req} can be computed

$$\begin{aligned} a h_{\text{req}}^{bp} &= \epsilon_{\text{req}} \\ h_{\text{req}} &= (\frac{\epsilon_{\text{req}}}{a})^{(\frac{1}{bp})} \end{aligned} \tag{5.25}$$

which is can be written in terms of the radius of the circumscribing circle r as

$$r_{\text{req}} = \sqrt{2}(\frac{\epsilon_{\text{req}}}{a})^{(\frac{1}{bp})} \tag{5.26}$$

With the above information, we know that if the requested solution accuracy is 4

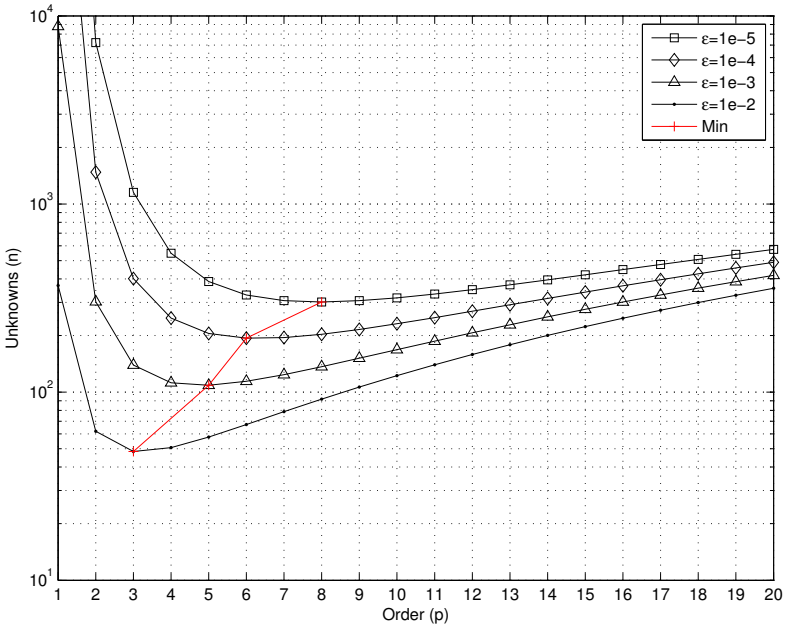

Figure 5.8: Predicting the optimal number of unknowns for a prescribed accuracy for the example studied in Figs. 5.5 and 5.6.

ϵ_{req}	p	r	Number of Elements	MeanErr($\mathbf{J}$)
1e-2	3	0.4753	24	9.57e-3
1e-3	5	0.5850	24	6.29e-4
1e-4	6	0.5603	24	8.64e-5
1e-5	8	0.6122	24	2.77e-6

Table 5.1: Demonstration of obtaining the desired accuracy by using the optimal algorithm when running HO LCN solver.

digits, it is optimal to run the LCN solver with the following parameters $p = 6, r = 0.5603$, which is essentially the 24 element exact-sphere at order 6. After running this optimum discretizaion and comparing its results with the analytic Mie series, we see that the computed mean relative error is 8.64×10^{-5} which is smaller than the requested 10^{-4}. Table 5.1, tabulates more results for various requested solution accuracies using optimal discretizations. It can be seen that the MeanErr($\mathbf{J}$) remains smaller than ϵ_{req} in all examples. For all the simulations, the 24 element exact-sphere is used, as all the r values in the table correspond to this mesh which has $r = 0.51$. The less-refined 6 element mesh and the more-refined 96 element mesh, have $r = 0.81$ and $r = 0.27$, respectively, and thus under- or over-discretize the geometry for the examples in the table. It should be pointed out that in the simulations of Table 5.1, 8 digits of precision was requested form the adaptive integration routines. However, this tolerance can be matched with the desired accuracy in practice. For example, if $\epsilon_{\text{rec}} = 10^{-4}$, only 4 digits of precision can be requested from the adaptive routines [18]. It is important to note that the LCN simulations considered here (Figs. 5.5 and 5.6) are obtained by CFIE which demonstrates the fact that the proposed procedure of finding the optimal unknown count can be applied to CFIE and implies its validation in MFIE and EFIE as well. This completes the procedure in which optimum number of unknowns can be predicted for a prescribed accuracy using the HO LCN method.

5.4 HO Imperative in electromagnetic (EM) Analysis

By carefully analysing Fig. 5.7, it is understood that if high-precision solutions are required, it is impractical to use LO techniques. For example, in the same figure, it can be seen that an LO ($p = 1$) method can provide 6 digits of precision with 10^{12} (1 Trillion) unknowns while a 10th order method can provide the same accuracy using less than $10,000$ unknowns. However, often in practice of engineering computations it is sufficient to predict dominant electromagnetic fields with two digits of accuracy. Therefore, from the same figure, one might argue that since in engineering problems 2 digits of precision is needed, the number of unknowns for an LO technique is not considerably higher than in HO techniques, and hence it is more judicious to keep working with the more mature LO techniques in engineering problems. For example in Fig. 5.7, it can be seen that if 2 digits of precision is required, a first-order method has to deal with about $10,000$ unknowns, while a 10th order method uses about 500 unknowns. This reduction in the number of unknowns is not significant and may not be a strong motivation to abandon a LO implementation and adopt a new HO method. The above argument typically applies to the engineering problems in which only the dominant fields are of interest while EM fields of strengths which are below a certain threshold are considered irrelevant. There is a plethora of important applications, however, such as design for stealth [115,116], EM interference (EMI) and EM compatibility (EMC) design [114], signal integrity analysis, and various others [113, 118], for which this is not the case and weak EM fields require as accurate prediction as the strong ones within the same model. In what follows, we demonstrate how this can be achieved by studying the effect of dynamic range in the accuracy of

a solution.

Consider the analytic Mie series solution for a PEC sphere with radius 1m, where the excitation is an electric dipole with time harmonic current at 5GHz placed 0.25m above the north pole of the sphere, hence the diameter of the sphere is 33.33λ. The top part of Fig. 5.9, depicts time-snapshot of the induced current on the surface of the sphere at time $\mathtt{t} = 0$s which is obtained from the complex current J_θ as $|J|\text{Cos}(0 + \arg(J))$. In the lower part of the figure, the same data is plotted, over the meridian of the sphere in terms of θ in degrees, where $\theta = 0$ corresponds to the north pole (near the dipole), and $\theta = 180$ corresponds to the south pole. Fig. 5.10, plots only the magnitude of the complex current $|J|$ for the same data shown in Fig. 5.9. It can be seen that the dynamic range in $|J|$ is $\frac{2.7\times10^{-3}}{3.92\times10^{-7}} = 6.83 \times 10^3$. The largest value $|J|_{\text{max}} = 2.7 \times 10^{-3}$ occurs in $0^\circ < \theta < 20^\circ$ range, while the smallest value $|J|_{\text{min}} = 3.92 \times 10^{-7}$ occurs in $160^\circ < \theta < 180^\circ$. It is easy to see that if a numerical technique can provide J values with 4 digits of precision (i.e. $\text{Err}(J) = 1 \times 10^{-4}$) in the range $0^\circ < \theta < 20^\circ$, the same numerical method can only provide results where $\text{Err}(J) = 1\times10^{-4}\times6.83\times10^3 = 6.83\times10^{-1}$ over $160^\circ < \theta < 180^\circ$ range. This type of area where the magnitude of the field is low compared to the other parts is sometimes referred to as the *shade area*. In the shade area, the error is about 70% despite the fact that the numerical method can provide results with 4 digits of precision where the error is the lowest. This poses difficulty when using LO methods. To demonstrate, we used a commercial software [35] which uses multilevel fast multipole algorithm (MLFMA) [5] accelerated RWG MoM to compute electromagnetic fields. First we discretize the sphere using $1,846,314$ flat triangular elements which corresponds to having 9 triangles per wavelength creating 2.77 Million RWG unknowns. Results are compared against the Mie series solution in Fig. 5.11. As summarized in Table

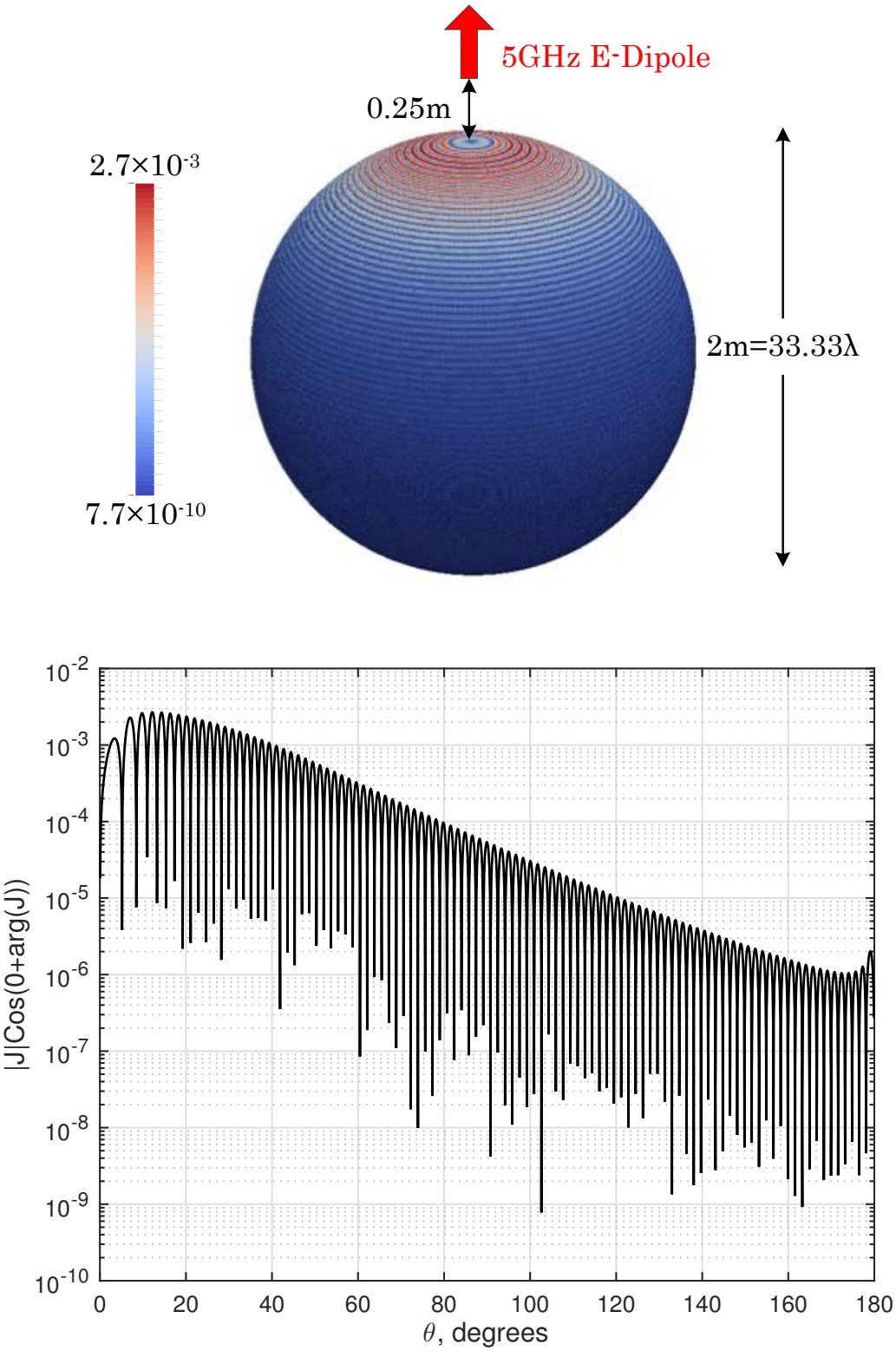

Figure 5.9: Demonstration of a large dynamic range in the solution obtained by Mie series at time $\mathtt{t} = 0$s.

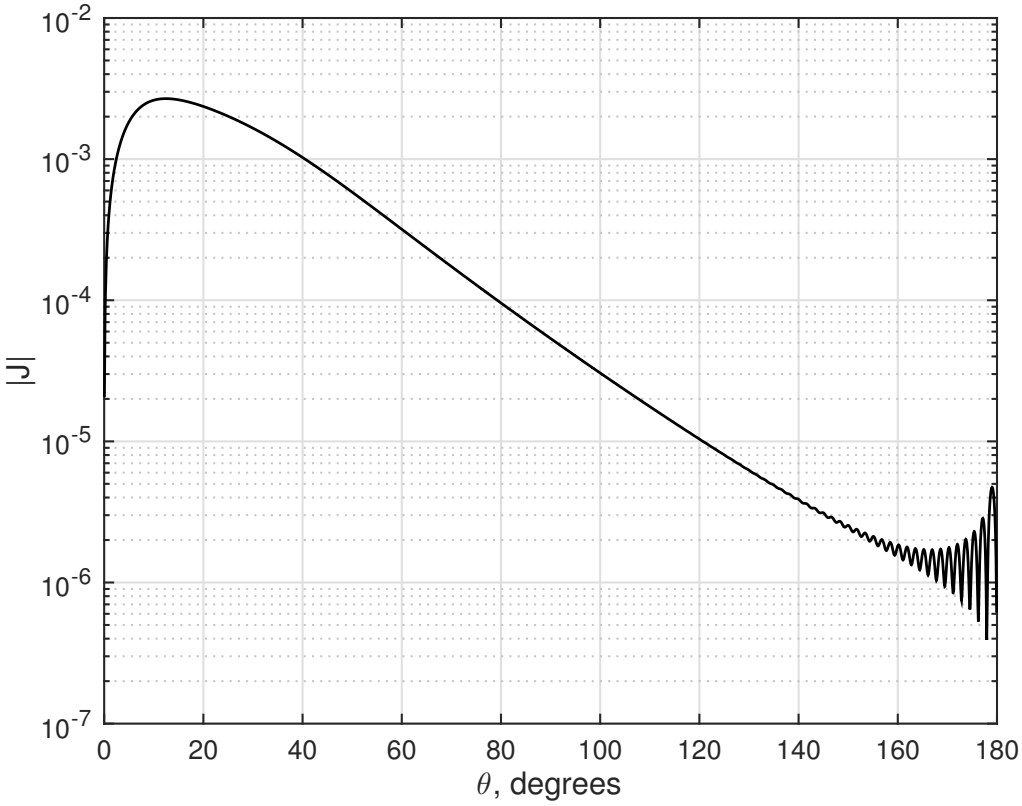

Figure 5.10: Demonstration of a large dynamic range in magnitude of the solution $|J|$ obtained by Mie series.

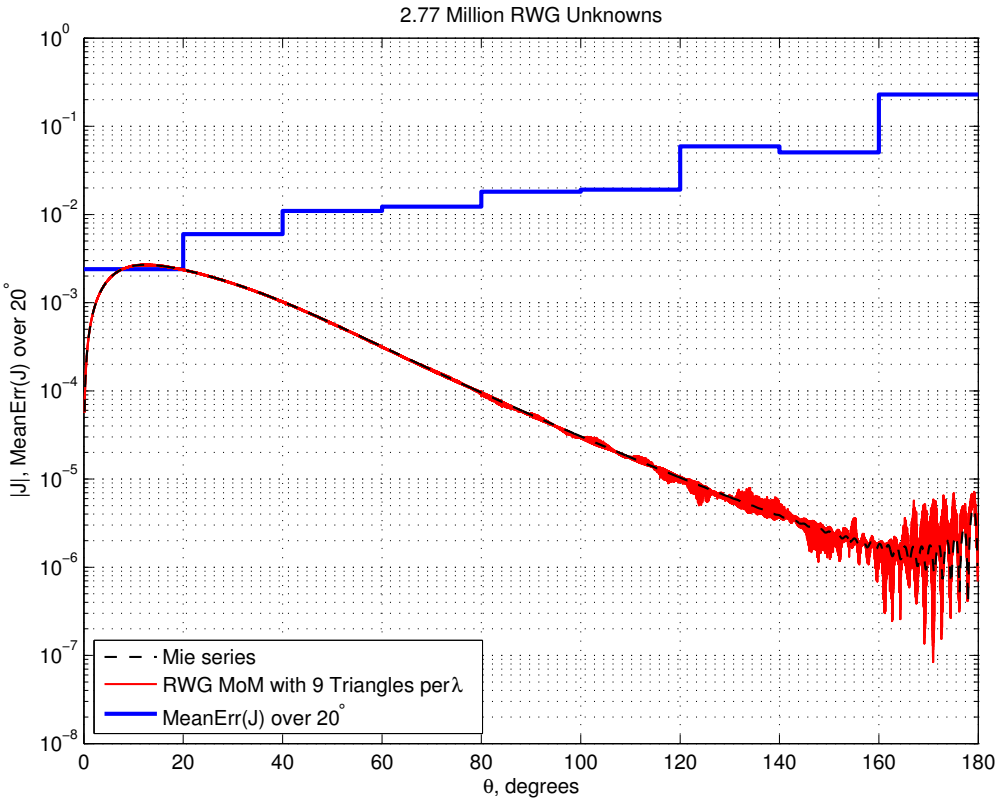

Figure 5.11: Comparison of the solution $|J|$ obtained by Mie series and the RWG MoM with 9 triangles per λ.

5.2, although there are 3 digits agreement between the RWG MoM solution and the Mie series solution over the $0° \leq \theta \leq 20°$ range, the error is about 22% in the $160° \leq \theta \leq 180°$ range which might be unacceptable for some applications. From Figs. 5.12 and 5.13, and Table 5.2, it can be seen that by refining the mesh there is improvement in the accuracy of the solution but the error in the shaded area remains higher than 14% despite using more than 4 million unknowns in the finest discretization. On the contrary, if we use MLFMA accelerated HO LCN [1] to do the same simulation using 846 element exact-sphere, as can be seen in Figs 5.14 to 5.19 and summarized in Table 5.3, arbitrary accuracy solutions can be obtained even

Triangles per λ	RWG Unknowns	MeanErr($\mathbf{J}$) $[0^\circ \leq \theta \leq 20^\circ]$	MeanErr($\mathbf{J}$) $[160^\circ \leq \theta \leq 180^\circ]$
9	$2,769,471$	0.0024	0.2293
11	$3,631,350$	0.0019	0.1763
12	$4,346,841$	0.0017	0.1475

Table 5.2: Summary of the LO RWG MoM performance in Figs 5.11 to 5.13.

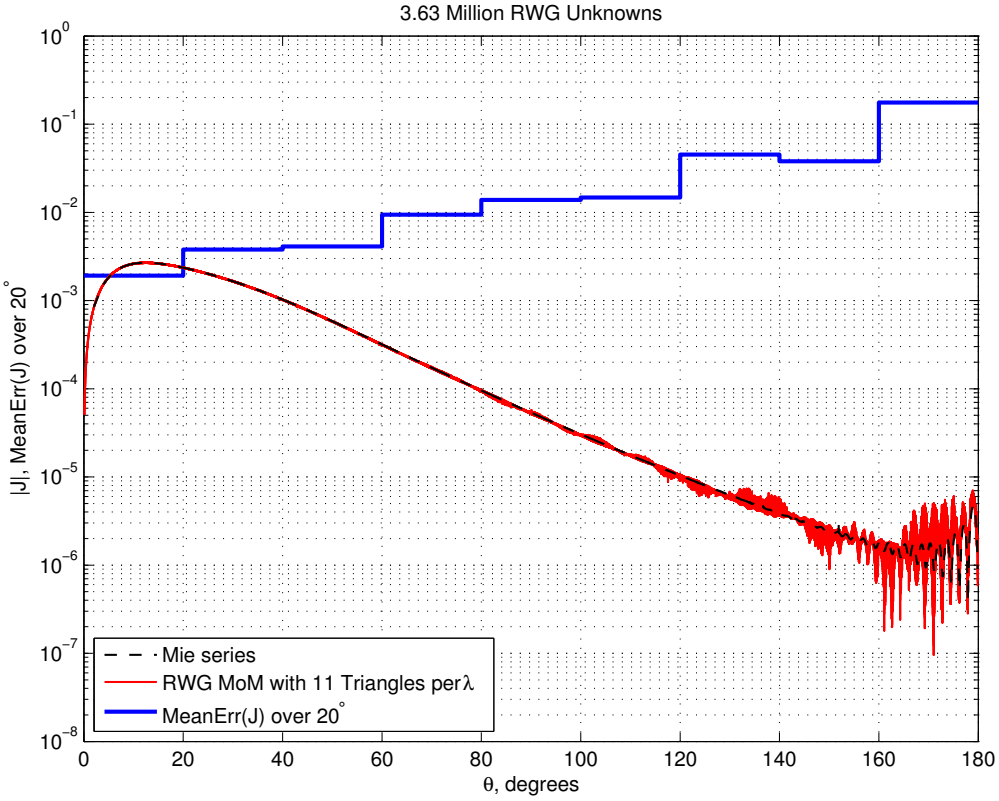

Figure 5.12: Comparison of the solution $|J|$ obtained by Mie series and the RWG MoM with 11 triangles per λ.

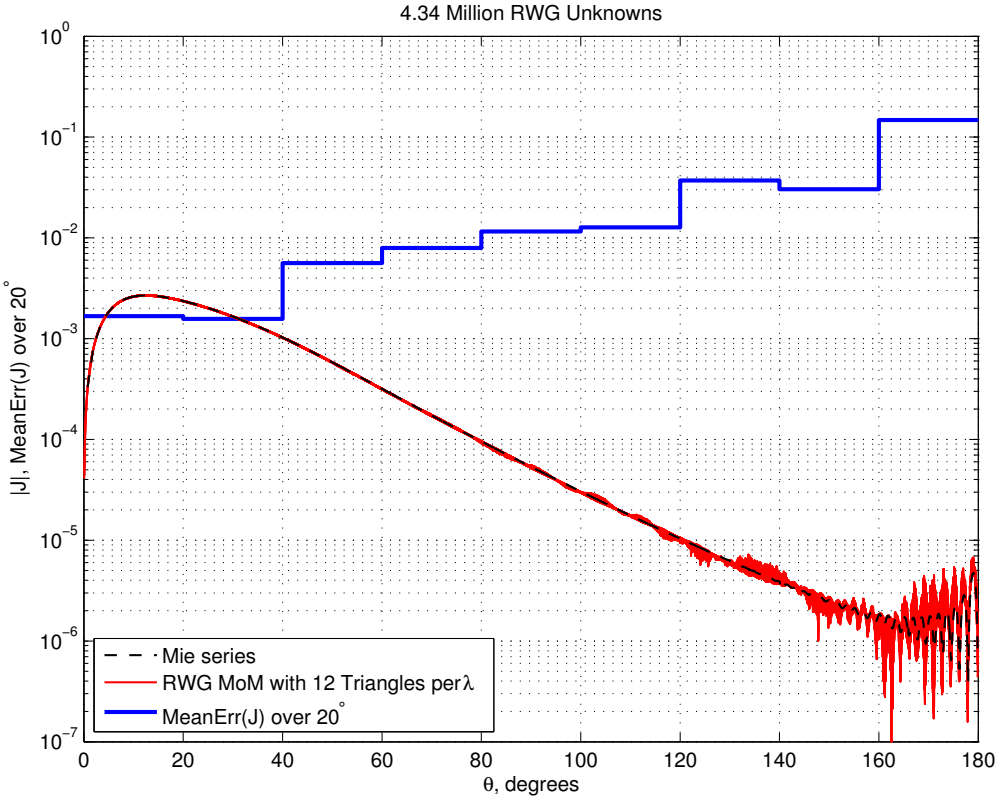

Figure 5.13: Comparison of the solution $|J|$ obtained by Mie series and the RWG MoM with 12 triangles per λ.

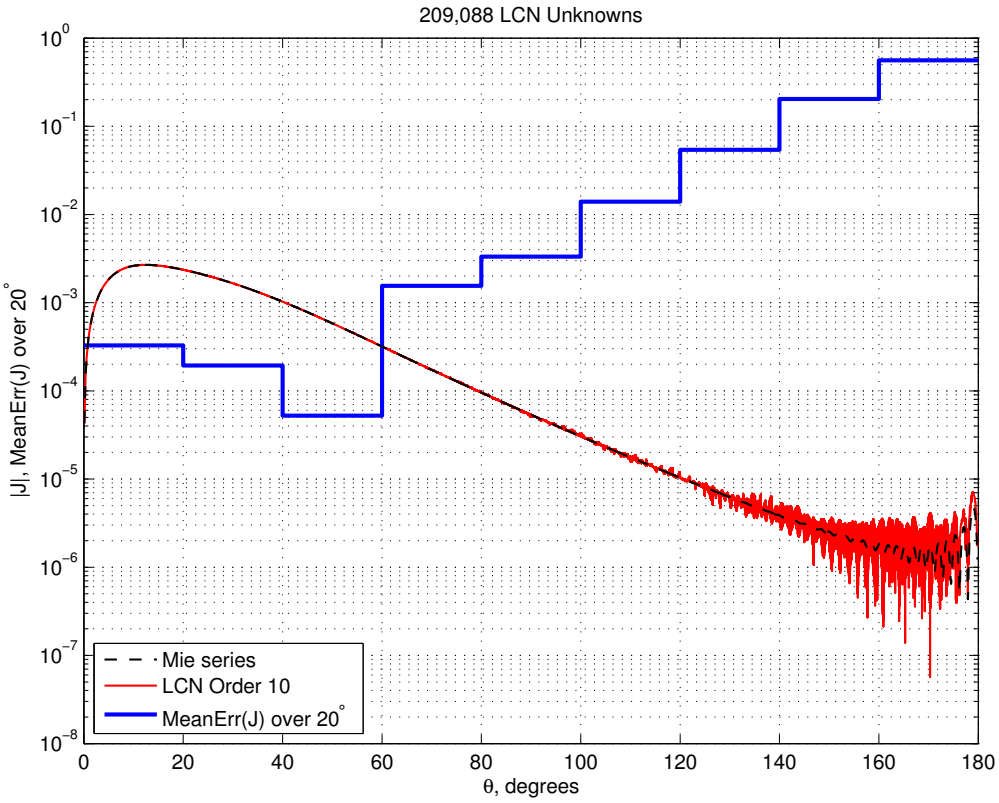

Figure 5.14: Comparison of the solution $|J|$ obtained by Mie series and the HO LCN at order 10.

in the shade area. It is to be note that the noise floor at about 10^{-6} is due to setting the adaptive integration tolerance as well as the MLFMA acceleration tolerance to 6 digits of precision. Finally, we substituted the values of $\epsilon_1 = 0.558$, $\epsilon_2 = 0.0554$, $p_1 = 10$, and $p_2 = 11$ in Table 5.3 to compute the number of unknowns using (5.22). Fig. 5.20 plots the number of unknowns for 2, 4, and 6 digits of precision results. Note that these solutions have been obtained using LCN at orders 11,13, and 15 as shown in Table 5.3. Fig. 5.20, once again, demonstrates the HO imperative in EM analysis. To obtain the solution with 2 digits of precision, an order 1 algorithm needs about 3 Million unknowns. If 4 digits of precision is required, the same algorithm

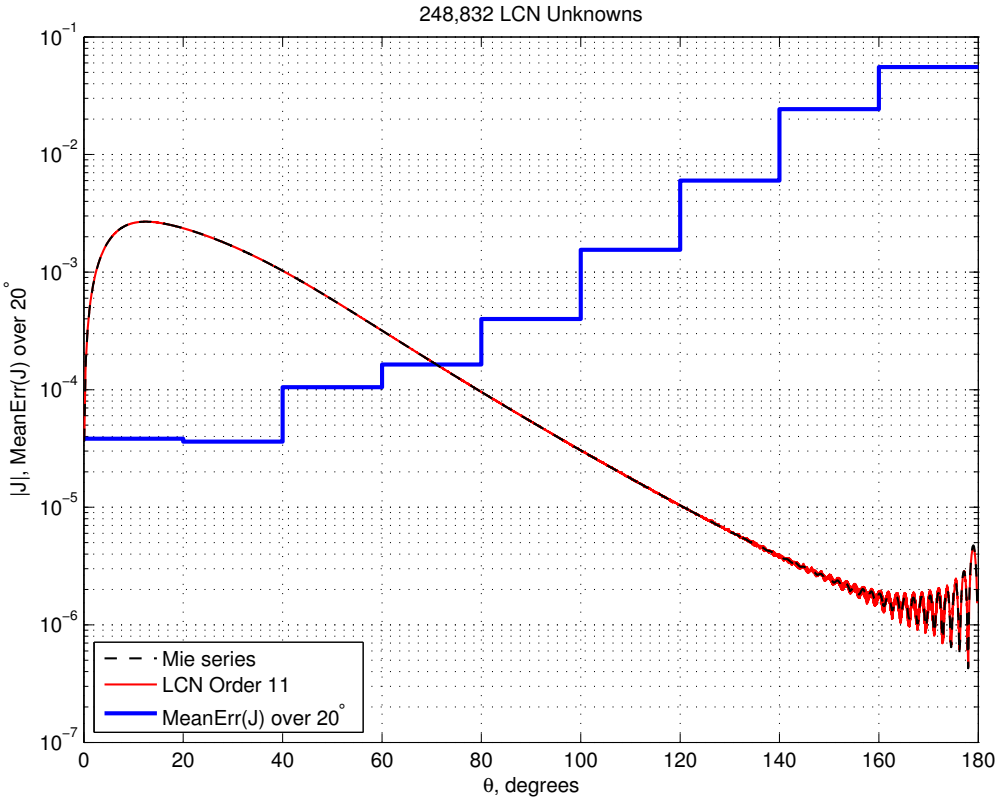

Figure 5.15: Comparison of the solution $|J|$ obtained by Mie series and the HO LCN at order 11.

LCN Order	LCN Unknowns	MeanErr($\mathbf{J}$) $[0° \leq \theta \leq 20°]$	MeanErr($\mathbf{J}$) $[160° \leq \theta \leq 180°]$
10	209,088	3.27×10^{-4}	0.558
11	248,832	3.82×10^{-5}	0.0554
12	292,032	3.86×10^{-6}	0.0047
13	338,688	1.01×10^{-6}	2.44×10^{-4}
14	388,800	1.00×10^{-6}	1.56×10^{-5}
15	442,368	1.00×10^{-6}	2.05×10^{-6}

Table 5.3: Summary of the HO LCN performance in Figs. 5.14 to 5.19.

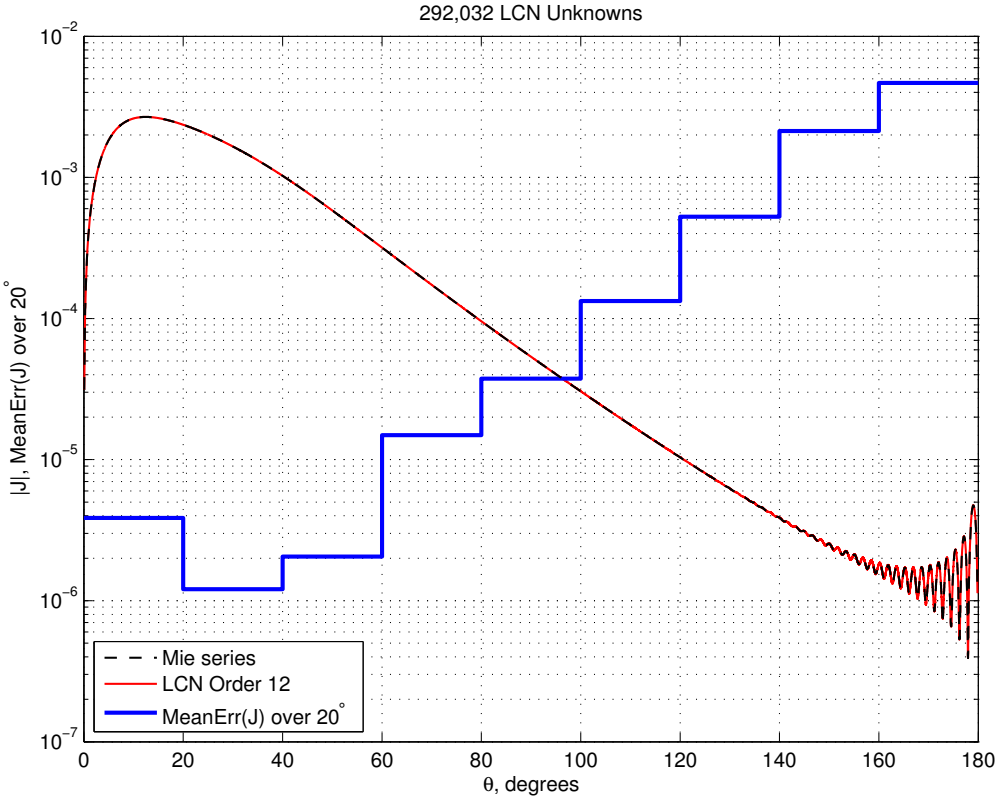

Figure 5.16: Comparison of the solution $|J|$ obtained by Mie series and the HO LCN at order 12.

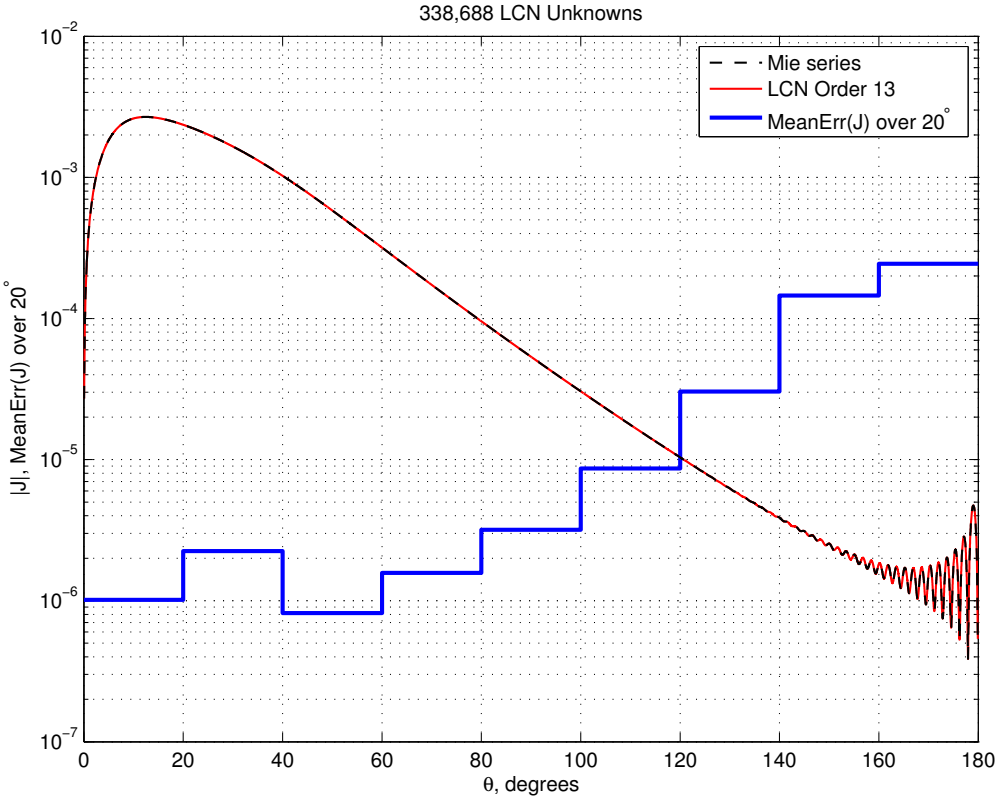

Figure 5.17: Comparison of the solution $|J|$ obtained by Mie series and the HO LCN at order 13.

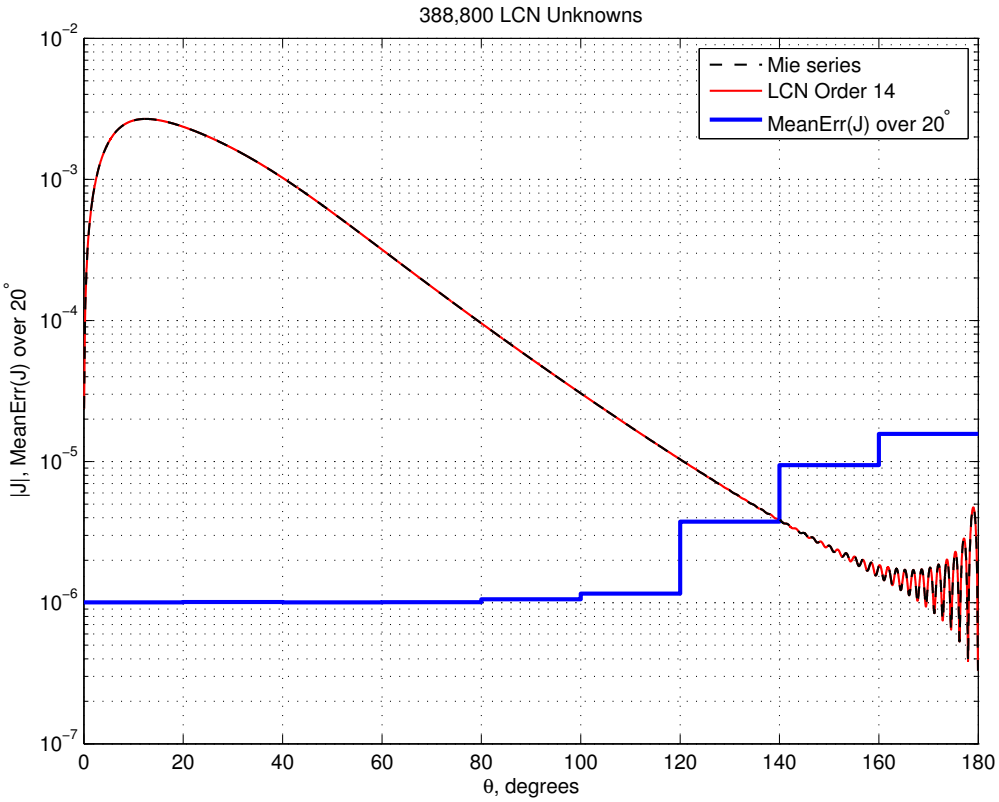

Figure 5.18: Comparison of the solution $|J|$ obtained by Mie series and the HO LCN at order 14.

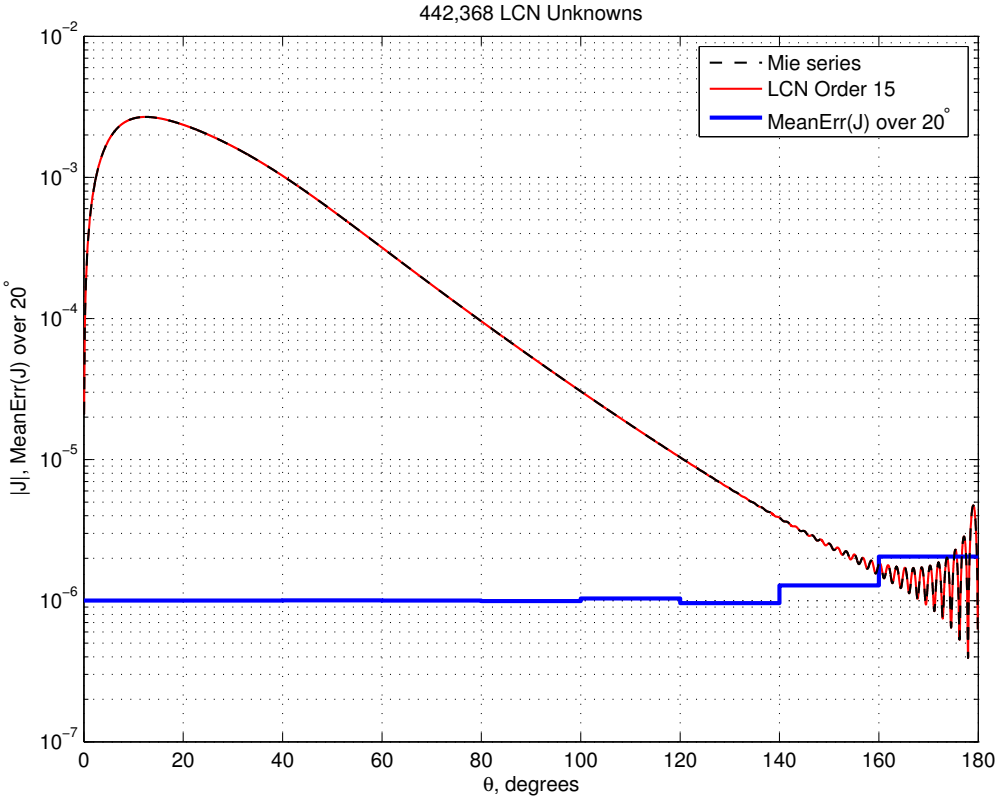

Figure 5.19: Comparison of the solution $|J|$ obtained by Mie series and the HO LCN at order 15.

requires about 4 Billion unknowns and 6 digits of precision can be achieved using this algorithm if more than 7 Trillion unknowns are involved in the solution. But the HO LCN can provide all these results with less than 0.5 Million unknowns with orders 11,13, and 15, as demonstrated in Table 5.3 and plotted in Fig. 5.20.

The large dynamic range in the solution demonstrated in this section for a PEC sphere can be interpreted as a general case where large dynamic range in the solution calls for adopting HO techniques in practical examples. In a related published work, we study a more practical example with similar observation on the surface of a B2 aircraft model [109]. Below we list more practical examples requiring controlled precision results due to large dynamic range in the solution.

- Accurate modelling of nano-scale plasmonic waveguides [110–113].
- Electromagnetic compatibility analysis of antenna to antenna coupling on electrically large platforms such as an aircraft [114].
- Design of stealth aircrafts [115, 116].
- Analysis of highly resonant structures [117, 118].

5.5 Conclusion

In this chapter we studied various aspects of HO LCN and summarized some insights as to why HO methods are preferred over LO methods by developing analytical expressions to formulate such gains. It was shown that the HO LCN can be used to provide exponentially more efficient results in CEM. However, the discussion in this chapter, remains entirely based on the geometry of a sphere modelled by analytical exact cube-to-sphere mapping. This geometry was used in the discussion of this

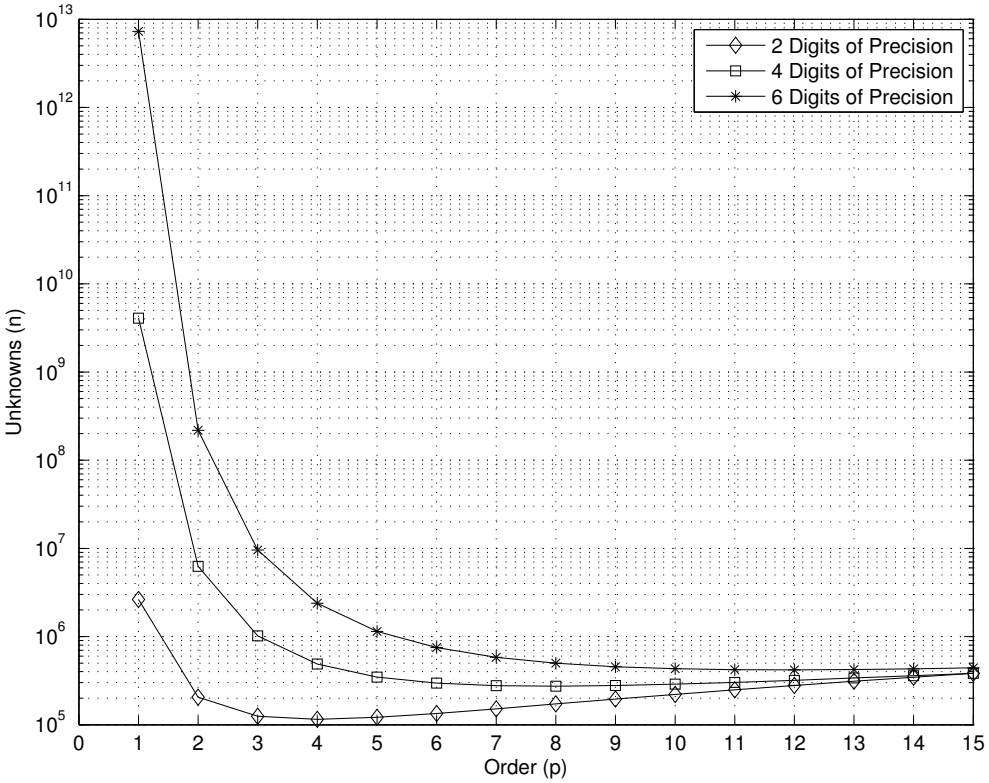

Figure 5.20: Comparison of the number of unknowns required to reach a prescribed accuracy using algorithms of various orders computed by (5.22). Using HO LCN, solutions with 2, 4, and 6 digits of precision using respectively orders 11, 13, and 15 has been computed all with less than 0.5 Million unknowns. Note that these precisions have been achieved in the shade area and as demonstrated earlier, it is practically not possible for RWG MoM to achieve such results.

chapter due to the availability of its analytical solution by Mie series. Furthermore, the exact-sphere model, ensured that no numerical inaccuracy was due to the geometry representation and thus facilitated a precise discussion on the accuracy of the discretization alone. Obviously, in practical problems, a more general HO geometry representation should be adopted. There are two choices. First, it is possible to use HO curvilinear elements as discussed in [72], and second, it is possible to adopt non-uniform rational b-spline (NURBS) representation of the surface as proposed in [99]. However, in [99] it was assumed that no triangular elements are present in the model despite the fact that NURBS surfaces usually contain both quadrilateral and triangular elements. This poses difficulty in using NURBS surfaces in conjunction with a general purpose HO LCN solver, as formulating LNC on triangles has limitations. In the following chapter, we discuss these limitations and propose a new technique for formulating LCN on triangular elements.

5.6 Acknowledgments

I would like to thank Dr. Jonatan Aronsson for providing me with the large scale Wave3D results presented in this chapter. Also special thanks to Compute Canada for providing extra resources on WestGrid's advanced research computing platform as part of the Resource Allocation Competition in 2015, without which the LCN large scale examples shown in this chapter would not have been possible.

Chapter 6

On New Triangle Quadrature Rules for the Locally Corrected Nyström Method Formulated on NURBS Generated Bézier Surfaces in 3D

Abstract

Non-uniform rational b-spline (NURBS) is the most widely used technique in today's geometric computer-aided design systems for modelling surfaces. Combining the locally corrected Nyström (LCN) method with NURBS, requires formulating LCN on both quadrilateral and triangular Bézier surfaces as a typical NURBS generated Bézier mesh includes elements of both types. While on quadrilateral elements the product of 1D Gaussian quadrature rules can be applied to LCN effectively, Gaussian integration rules available for triangles can not efficiently be applied to LCN for two reasons. First, they do not posses the same number of quadrature points as the number of functions in a complete set of polynomial basis at arbitrary order. Second, they exacerbate the condition number of the resulting matrix equation at higher orders due to an increasing density of quadrature points near the edges and corners of triangles. In this paper, we construct a new set of quadrature rules for Bézier triangles (i.e. degenerate quadrilaterals) based on the Newton-Cotes (equidistant) quadrature rules and apply these rules to the LCN solution of the electric, magnetic, and combined field integral equations. Results show that the new family of quadrature rules overcomes both aforementioned issues and can be applied to LCN effectively for orders from 0 to 9, inclusively.

6.1 Introduction

It has been shown that using non-uniform rational b-spline (NURBS) surfaces in computational electromagnetics (CEM) can lead to a substantial increase in efficiency. Benefits can be found for both high frequency methods such as physical optics [119] and uniform theory of diffraction [120], as well as rigorous boundary element methods (BEM) such as low-order (LO) method-of-moments (MoM) [100], high-order (HO) MoM [97, 121] and the locally corrected Nyström (LCN) method [99]. The advantages of incorporating NURBS surfaces into a BEM technique of CEM include: 1) precise representation of structures without introducing artificial edges [119], preventing BEMs from introducing infinite field singularities at such edges; 2) inclusion of larger patches irrespective of curvature which leads to a reduction in the number of unknowns [97,100,121]; and 3) desirable properties in terms of geometry design, storage efficiency, and parametric geometry characterization [122,123] widely adopted by the computer-aided design (CAD) tools industry [124–126].

When NURBS modelling is used in BEMs of CEM, a conversion from the NURBS surface representation to a Bézier mesh is required [97,99,100,121]. This is due to the fact that BEMs use surface tangents as basis functions while no numerically stable algorithms for such derivatives exists for NURBS surfaces [121]. A Bézier mesh, as shown in Figs. 6.1 and 6.2, typically contains both triangular and quadrilateral elements. Thus computation of the electromagnetic fields on both types of elements is required from NURBS based BEMs. This presents difficulty when NURBS surfaces are used in conjunction with an LCN discretization of surface integral equations as the LCN discretization on triangular elements has several limitations as will be explained shortly. As a result, in a previous implementation of LCN discretization on NURBS surfaces [99], triangular elements were completely avoided and numerical results were

shown only for canonical geometries consisting solely quadrilateral Bézier patches. In this paper, we introduce a novel formulation of the LCN on NURBS generated Bézier surfaces by developing quadrature rules for Bézier triangles which are in the form of degenerate quadrilaterals (Fig. 6.1b). A brief overview of the existing LCN approaches on the triangular elements provides the motivation for this work.

The LCN method was proposed in 1998 by Canino et. al. [19] as an alternative to the MoM for the numerical solution of electromagnetics integral equations such as the electric field integral equation (EFIE) and the magnetic field integral equation (MFIE). The point-based nature of the LCN method offers several advantages over element-based MoM including: 1) computing single reaction integrals as opposed to the double integrations of the MoM which greatly reduces the computational cost compared to MoM [18, 20], 2) providing more flexibility in building hierarchical geometric partitioning which increases the efficiency of fast algorithms [**?**], and 3) allowing for mesh elements to have a vertex in the middle of an edge which facilitates the handling of material junctions [48]. While LCN can be formulated for arbitrary geometry discretizations, in the seminal paper [19], Canino and his co-authors provided numerical results which were obtained on curvilinear triangular patches based on Lyness and Jespersen quadrature rules [127]. However, their results showed that such triangular quadrature rules can not be efficiently applied to LCN at arbitrary expansion/basis order as the number of testing functions formed by the product of polynomial basis functions (e.g. monomials) in the two surface parameters, and the number of sample points do not always match. A complete set of polynomial functions to a given order demands a set of quadrature points with equal cardinality for the resulting Vandermonde matrix [6] to be square. Otherwise an under-determined linear system is required and is likely to affect the error-controllability of the LCN scheme [1, 19].

Furthermore, quadrature abscissas of the Gaussian quadrature rules [127–129] tend to concentrate near the edges and corners of triangles as the order increases. Consequently at higher orders, the LCN sample points become too close together which makes the local correction system increasingly ill-conditioned. Too closely placed sample points in the LCN method causes the EFIE to produce impedance matrices with very high condition numbers which can prevent the LCN method from providing a correct solution. For example, in [19] it was reported that an integration rule with more than 15 points [127] causes the EFIE to become ill-conditioned. It was predicted [19] that inventing a new set of high-order rules on triangles with better sample distribution might be a solution for overcoming this difficulty. In [131], the authors took a different approach to formulating LCN on triangles. They showed that by using extra testing functions as mixed-order polynomials whose partial derivatives span the same space, it is possible to build square systems for the local corrections and at the same time alleviate issues regarding the inconsistent charge representation flowing from the implicit current expansion. In particular, they added extra monomials to a complete set of monomials up to order d in order to equalize the number of quadrature points with their custom set of monomials. However, this formulation only guarantees to integrate the monomials (hence the current) up to order d [1], regardless of the order of the quadrature rule, and ultimately introduces oversampling into the LCN scheme. For example, a 7th order triangle rule in [129] which has 13 points, promises to integrate the current up to order $d = 3$ with 10 polynomial functions. This reduces the order of the LCN method to $p = 3$ such that the extra 3 points and test functions in the formulation can be interpreted as oversampling. The above-mentioned limitations might have been the reason for the LCN literature to primarily adopt quadrilateral elements [1,18,47–49,88,90,130] rather than considering

LCN on triangular elements [19, 44, 131, 132].

In this paper we formulate LCN on Bézier triangles using a new set of quadrature rules based on the Newton-Cotes quadrature formulae. The family of Newton-Cotes quadrature rules is based on equidistant quadrature abscissas [133]. A natural generalization of the Newton-Cotes formulae to the $\mathcal{N}$-dimensional case for simplexes was formulated in 1970 [134] and equidistant quadrature rules on triangles were studied for both open and closed types[1]. While Newton-Cotes rules are simple to implement, they are inefficient compared to Gaussian quadrature rules [134, 135] because a 1D Gaussian rule with $n+1$ points can exactly integrate a polynomial of order $2n+1$ or less, whereas a 1D Newton-Cotes rule with $n+1$ points can exactly integrate polynomials of up to order n when $n+1$ is even, and up to order $n+1$ when $n+1$ is odd [136]. Therefore Newton-Cotes rules are not widely used when numerical evaluation of integrals is required. Also, Newton-Cotes rules of high-orders (order 10 and above [133]), may become numerically unstable. Nevertheless, in this paper we show that in the context of the LCN scheme, constructing quadrature rules for triangles based on the 1D equidistant rule [134] prevents the discretized EFIE from suffering an increased condition number of the matrix equation. One such family of quadrature rules on triangles has $Q = (n+1)(n+2)/2$ nodes and is inherently suitable to be used in LCN on triangular elements as Q is the cardinality of a complete polynomial basis of order n in 2D, resulting in a square local correction matrix. These rules integrate the current up to an arbitrary order without introducing oversampling and support a current representation with a self-consistent polynomial basis for the charge. Defining LCN over triangular Bézier elements based on a uniform distribution of points was

[1] An *open* type Newton-Cotes quadrature formula samples function values at equidistant points by ignoring the boundaries whereas a *closed* type Newton-Cotes formulation uses function values at equidistant points including the starting and ending points [134].

first presented in [137]. However, as the generalization in [134] allows for creating rules other than open and closed types, in this paper, we create a new subset of the generalized rules given in [134]. This new family of quadrature rules, like the 1D Newton-Cotes rule in general, results in numerically stable Vandermonde system, is accurate to machine precision for orders up to 9, and therefore facilitates LCN on triangular Bézier elements for orders 0 to 9.

6.2 Geometry Representation Based on NURBS surfaces and Bézier Meshes

6.2.1 NURBS Surfaces

The position-vector on a surface defined by NURBS which has degree $\mathtt{P}$ in the u direction and degree $\mathtt{Q}$ in the v direction can be written as [138]

$$\mathbf{r}(u,v) = \frac{\sum_{i=0}^{\mathtt{M}} \sum_{j=0}^{\mathtt{N}} \mathtt{W}_{i,j} \mathbf{P}_{i,j} N_i^{\mathtt{P}}(u) N_j^{\mathtt{Q}}(v)}{\sum_{i=0}^{\mathtt{M}} \sum_{j=0}^{\mathtt{N}} \mathtt{W}_{i,j} N_i^{\mathtt{P}}(u) N_j^{\mathtt{Q}}(v)}, \quad u,v \in [0,1] \tag{6.1}$$

where $\mathbf{P}_{i,j}$ are the control points, $\mathtt{W}_{i,j}$ are the weights, and $N_i^{\mathtt{P}}$ is the ith nonrational B-spline basis function of degree $\mathtt{P}$ which can be obtained recursively as

$$\begin{aligned} N_i^{\mathtt{P}}(t) &= \frac{t - t_i}{t_{i+\mathtt{P}} - t_i} N_i^{\mathtt{P}-1}(t) + \frac{t_{i+\mathtt{P}+1} - t}{t_{i+\mathtt{P}+1} - t_{i+1}} N_{i+1}^{\mathtt{P}-1}(t), \\ N_i^0(t) &= \begin{cases} 1, & t_i \le t \le t_{i+1} \\ 0, & \text{otherwise} \end{cases} \end{aligned} \tag{6.2}$$

where t_i are the knots which form a knot vector $U = \{t_0, t_1, ..., t_{\mathtt{M}+\mathtt{P}+1}\}$. Similarly, $N_j^{\mathtt{Q}}$ is defined on the knot vector V. It can be shown that the choice of U and $\mathtt{P}$

can control the differentiability of the resulting NURBS surface along the u direction, and similarly the choice of V and $\mathtt{Q}$ can control parametric continuity along the v direction [122]. Therefore, it is possible to ensure parametric continuity over the surface of a NURBS patch up to an arbitrary nth degree (C^n continuity). It is also possible to enforce geometric continuity up to the second degree (G^2 continuity) between adjacent NURBS surfaces [125,139]. If a surface is C^n continuous at a point, then both the direction and magnitude of the spatial derivatives of the radius-vector $\mathbf{r}(u,v)$ in the u and v directions are equal in the vicinity of that point, up to the nth degree. However, if the surface is G^n continuous at a point, only the direction of the spatial derivatives of $\mathbf{r}(u,v)$ remain unchanged in the vicinity of that point, up to the nth degree [140]. Hence, when creating a model geometry using NURBS, it is possible to preserve G^2 continuity throughout the entire model. This property is desirable for CEM algorithms as it prevents the geometry modelling to introduce artificial edges on the surface of a smooth model. Such edges cause crowding of the electromagnetic fields and prevent HO methods from achieving the desired $\mathcal{O}(h^p)$ error convergence in the solution, where h is the characteristic size of the mesh elements and p is the order of the discretization. Note, that the G^2 continuity property provided by NURBS is unavailable in alternative geometry modelling CAD approaches based on surface representations in terms of independent curvilinear mesh elements [96,106].

6.2.2 Bézier Mesh

Geometry representation in BEMs requires surface tangent vectors $\partial\mathbf{r}(u,v)/\partial u$ and $\partial\mathbf{r}(u,v)/\partial v$ which are used to form the basis functions. No numerically stable algorithms for such derivatives exists for NURBS surfaces [121] defined by (6.1). The MoM and LCN circumvent this difficulty by transforming NURBS surfaces into a

Bézier mesh followed by obtaining $\partial \mathbf{r}(u,v)/\partial u$ and $\partial \mathbf{r}(u,v)/\partial v$ on individual Bézier patches [97, 99, 100, 121]. The position-vector on each Bézier patch is defined as [122, 123], [121]

$$\mathbf{r}(\xi,\eta) = \frac{\sum_{i=0}^{\mathtt{m}} \sum_{j=0}^{\mathtt{n}} \mathtt{w}_{i,j} \mathbf{p}_{i,j} B_i^{\mathtt{m}}\left(\frac{\xi+1}{2}\right) B_j^{\mathtt{n}}\left(\frac{\eta+1}{2}\right)}{\sum_{i=0}^{\mathtt{m}} \sum_{j=0}^{\mathtt{n}} \mathtt{w}_{i,j} B_i^{\mathtt{m}}\left(\frac{\xi+1}{2}\right) B_j^{\mathtt{n}}\left(\frac{\eta+1}{2}\right)}, \qquad \xi,\eta \in [-1,1], \tag{6.3}$$

where $\mathbf{p}_{i,j}$ are the control points, $\mathtt{w}_{i,j}$ are the weights, and $B_i^{\mathtt{m}}(t)$ are the Bernstein polynomials of degree $\mathtt{m}$ defined as

$$B_i^{\mathtt{m}}(t) = \frac{\mathtt{m}!}{i!(\mathtt{m}-i)!} t^i (1-t)^{\mathtt{m}-i}, \quad t \in [0,1]. \tag{6.4}$$

Fig. 6.1a depicts a typical representatives of a Bézier patch. Since such a patch has four edges $l_0, ..., l_3$, we refer to it as a *quadrilateral* Bézier patch. However, almost all NURBS generated Bézier meshes contain not only quadrilateral Bézier patches, but also *triangular* Bézier patches (Fig. 6.1b) where one edge is of zero length (degenerate quadrilateral). This is referred to as a singular patch [125, 143]. From Fig. 6.2, it can be seen that a NURBS generated Bézier mesh of a simple geometry (sphere), as well as the model of a B2-Aircraft, contain both quadrilateral and triangular Bézier patches. Thus, when incorporating NURBS surfaces into BEMs, they must support formulations on both quadrilateral and triangular elements.

6.3 The LCN Discretization on NURBS Surfaces

Details of the standard HO LCN method for solving the EFIE, MFIE and the combined filed integral equation (CFIE) can be found in [1, 18, 19]. In this section we

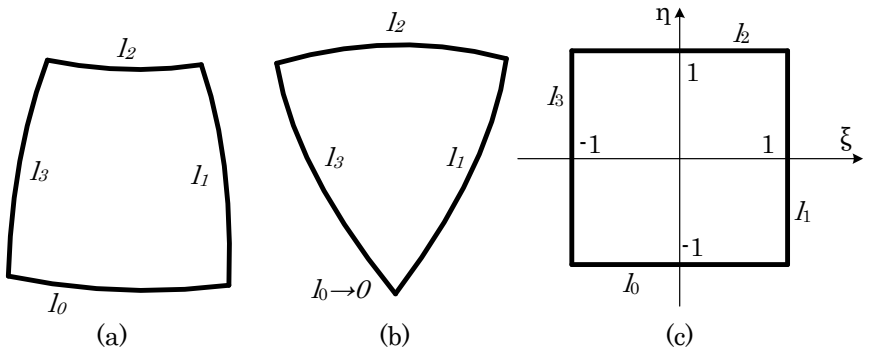

Figure 6.1: (a) A typical (quadrilateral) Bézier patch, (b) A singular (triangular) Bézier patch with singularity at edge l_0. Both (a) and (b) can be mapped to the canonical quadrilateral illustrated in (c) where it can be seen that l_0 is the ξ-curve at $\eta = -1$, l_1 is the η-curve at $\xi = 1$, l_2 is the ξ-curve at $\eta = 1$, and l_3 is the η-curve at $\xi = -1$.

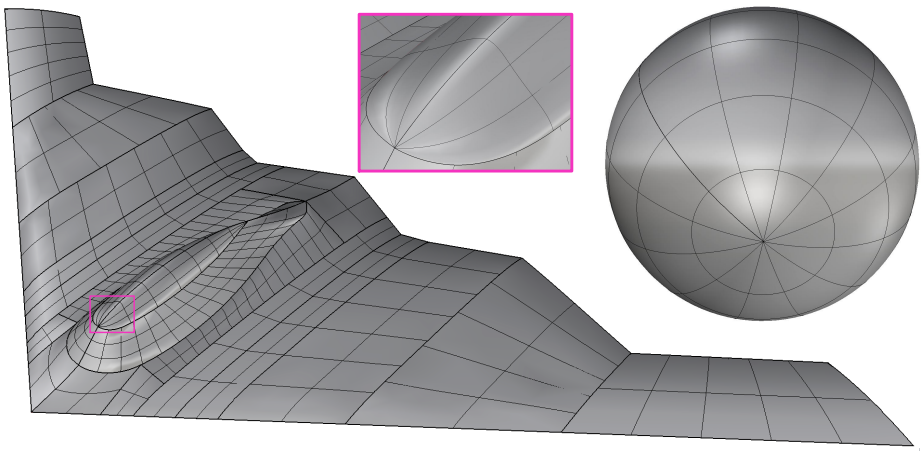

Figure 6.2: A NURBS generated Bézier mesh created by a commercial tool [125] for a sphere and a B2-Aircraft model. The sphere comprises only one NURBS with a Bézier mesh that contains 72 quadrilateral and 24 triangular Bézier patches. The maximum deviation from the true geometry for the sphere is 10^{-10}m. The B2-Aircraft model has 36 NURBS which are represented by 566 quadrilateral Bézier elements and 16 triangular (singular) Bézier elements. The magnification on the B2-Aircraft model is presented to emphasize the presence of triangular elements. Note that the B2-Aircraft model, which has Bézier elements with non-aligned boundaries, can still be used in LCN as it does not enforce current continuity across elements.

describe additional detail for constructing the proposed LCN discretization scheme based on NURBS surfaces containing quadrilateral and/or triangular Bézier elements.

6.3.1 Incorporating NURBS and Bézier Mesh into BEMs

Incorporating NURBS surfaces into the standard LCN discretization scheme involves the following: 1) the transformation of NURBS surfaces to Bézier patches using the Cox-De Boor algorithm [122, 141], and 2) computing the position vector $\mathbf{r}(\xi,\eta)$ and covariant basis functions $\mathbf{a}_1(\xi,\eta) = \partial\mathbf{r}(\xi,\eta)/\partial\xi$ and $\mathbf{a}_2(\xi,\eta) = \partial\mathbf{r}(\xi,\eta)/\partial\eta$ for a Bézier patch by using the algorithm of De Casteljau [123, 142]. While these algorithms can be implemented directly, their implementation is not trivial and one can resort to the use of libraries such as *openNURBS* [143]. The library seamlessly operates with the NURBS models created in *Rhinoceros3D* CAD environment [125] (Fig. 6.2). To have a proper transition from parameters of a standard Bézier element (u,v) [122, 143], parametric coordinates are fed to the library's $\mathbf{r}(u,v)$ and $\mathbf{a}_{1,2}(u,v)$ functions as $u = (\xi+1)/2$ and $v = (\eta+1)/2$. The accuracy of converting the surface definition from NURBS to Bézier elements can be controlled with the tolerance parameter set in the openNURBS library at the stage of geometry conversion. The *3dm* file format was used in this work.

6.3.2 LCN Formulation on Quadrilateral Bézier Elements

On quadrilateral Bézier elements (Fig. 6.1a), the product of 1D Gaussian (i.e. Gauss-Legendre) rules with polynomial-complete basis functions is applied according to [1, 18]. It is also possible to use mixed-order basis function set as suggested in [47, 130].

6.3.3 LCN Formulation on Triangular Bézier Elements

In this work a new set of quadrature rules for Bézier triangles (i.e. degenerate quadrilaterals as depicted in Fig. 6.1b) is derived from the generalized rules presented in [134]. The new quadrature rules are applied to triangular Bézier patches in the LCN local interactions.

6.3.3.1 Preliminaries

As the standard LCN does not apply quadrature points on the elements' boundaries, we limit our attention to the class of quadrature rules for which the nodes lie entirely within the boundaries of the domain $-1 < \xi, \eta < 1$. When forming a 1D quadrature rule based on equidistant points of *open* type [134], the entire domain is uniformly covered by the quadrature abscissas. Therefore, the distance between a point and its adjacent boundary is equal to its distance with its adjacent quadrature point. However, these types of abscissas are not ideal for LCN. It is more advantageous to define quadrature points that maintain large distances from each other, both within a given element, and with respect to quadrature points in the neighbouring elements. This improves condition number of the Vandermonde matrix in the local correction system of equations (as shown in Table 6.2) as well as the overall LCN impedance matrix [19]. For these reasons we formulate LCN on triangular Bézier elements based on a new set of 1D equidistant quadrature abscissas. Consider $n+1$ quadrature points over the 1D domain with the ith quadrature abscissa denoted as x_i^n and defined as[1]

$$x_i^n = (-n + 2i)/(n + 1), \quad i = 0, 1, ..., n. \tag{6.5}$$

[1]Equation (6.5) is equivalent to having $N = 1$ and $\mu = 0.5$ in (10) of [134] when the 1D domain is considered to be $(0 < x < 1, x \neq 0, 1)$.

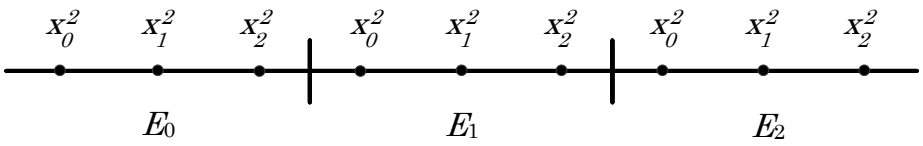

Figure 6.3: 1D equidistant quadrature nodes x_i^n defined in (6.5) with $n = 2$ for three consecutive 1D elements E_0, E_1, and E_2.

Fig. 6.3 depicts the abscissas in (6.5) with $n = 2$ for three consecutive 1D elements. As can be seen from the figure, the distance between a quadrature point that lies adjacent to the boundary of one element (x_0^2 on E_1), has the same distance with the quadrature point within its own element (x_1^2 on E_1), as well as the quadrature point that is adjacent to the same edge from the neighbouring element (x_2^2 on E_0). In what follows, this form of equidistant points is generalized to construct quadrature rule on Bézier triangles.

6.3.3.2 Definition

We are interested in building a set of quadrature rules for the triangle shown in Fig. 6.1b, where the edge l_0 is singular ($l_0 \to 0$)[1]. This singular Bézier patch can be mapped to the canonical quadrilateral shown in Fig. 6.1c, where $\xi, \eta \in [-1, 1]$. Therefore we construct the quadrature rules of the form

$$\sum_{q=0}^{Q-1} w_q f(\xi_q, \eta_q) \simeq \int_{-1}^{1}\int_{-1}^{1} f(\xi, \eta) d\xi d\eta \tag{6.6}$$

where Q is the number of quadrature points. The quadrature abscissas are represented by ξ_q, η_q which are defined based on distribution of 1D abscissas in (6.5) over the

[1] A Bézier patch can also be singular at the other three edges (l_1, l_2, l_3). For a singular Bézier patch with singularity at an edge other than l_0, rotation is required.

canonical quadrilateral shown in Fig. 6.1c as follows:

$$\begin{aligned} \xi_q =& x_j^i, \quad \eta_q = x_i^n, \\ i = 0...n, \quad & j = 0...i, \quad q(i,j) = i(i+1)/2 + j, \end{aligned} \tag{6.7}$$

with the total number of quadrature points Q on a triangle equal to $Q = (n+1)(n+2)/2$. Fig. 6.4 depicts the quadrature points for the rule with $n = 2, 3, 8$ and 9. Note that the resulting quadrature rules are complete to order $p = n$ as explained in Section 6.3.3.3. In (6.6), w_q are the weights which can be obtained by solving the linear system

$$\begin{bmatrix} S_0^0 & S_1^0 & \dots & S_{Q-1}^0 \\ S_0^1 & S_1^1 & \dots & S_{Q-1}^1 \\ \vdots & \vdots & \ddots & \vdots \\ S_0^{K-1} & S_1^{K-1} & \dots & S_{Q-1}^{K-1} \end{bmatrix} \begin{bmatrix} w_0 \\ w_1 \\ \vdots \\ w_{Q-1} \end{bmatrix} = \begin{bmatrix} b_0 \\ b_1 \\ \vdots \\ b_{K-1} \end{bmatrix} \tag{6.8}$$

where the matrix on the left-hand side $[S]$ has entries $S_q^k = F^k(\xi_q, \eta_q)$. Here, $\{F^k(\xi, \eta)\}$ is a full set of K polynomial functions complete to order p over the 2D domain. Hence, $p = n$ makes $[S]$ a square matrix as a set of 2D polynomial functions complete to order p has $K = (p+1)(p+2)/2$ functions [131]. Entries of the right-hand side b_k are

$$b_k = \int_{-1}^{1} \int_{-1}^{1} F^k(\xi, \eta) d\xi d\eta, \quad k = 0, ..., K-1 \tag{6.9}$$

where the double integration can be computed adaptively using high-order quadrature rules. A sufficient condition for the unique solution of matrix equation (6.8) is that $[S]$ is non-singular. Since $[S]$ is a 2D Vandermonde-type system [6] this condition is fulfilled for a finite p. TABLE 6.1 presents the computed weights for rules with

Table 6.1: Order p, total number of quadrature points Q, local coordinates ξ_q, η_q, and the weight w_q for the qth quadrature node defined in (6.6).

p	Q	q	ξ_q	η_q	w_q
0	1	0	0	0	4.0000000000000000E+00
1	3	0	0	-1/2	2.0000000000000000E+00
1	3	1	-1/2	1/2	1.0000000000000000E+00
1	3	2	1/2	1/2	1.0000000000000000E+00
2	6	0	0	-2/3	1.5000000000000000E+00
2	6	1	-1/2	0	5.0000000000000000E-01
2	6	2	1/2	0	5.0000000000000010E-01
2	6	3	-2/3	2/3	1.2187500000000002E+00
2	6	4	0	2/3	-9.3750000000000040E-01
2	6	5	2/3	2/3	1.2187500000000002E+00
3	10	0	0	-3/4	1.0833333333333324E+00
3	10	1	-1/2	-1/4	4.5833333333333480E-01
3	10	2	1/2	-1/4	4.5833333333333375E-01
3	10	3	-2/3	1/4	1.7343750000000004E+00
3	10	4	0	1/4	-2.5520833333333340E+00
3	10	5	2/3	1/4	1.7343750000000009E+00
3	10	6	-3/4	3/4	-5.0520833333333440E-01
3	10	7	-1/4	3/4	1.0468750000000009E+00
3	10	8	1/4	3/4	1.0468750000000009E+00
3	10	9	3/4	3/4	-5.0520833333333390E-01

$Q = 1, 3, 6$ and 10 quadrature points where the base polynomials are chosen to be the set that span the space of monomials $F^k(\xi, \eta) = \xi^i \eta^j$ up to a given order, i.e. $i = 0, ..., p$ and $j = 0, ..., p - i$.

6.3.3.3 Order

A 1D Newton-Cotes rule with an even number of points (i.e. $n + 1$ is even) has order n, while a rule with odd number of points has order $n + 1$ [136]. However, to have a square matrix $[S]$ in (6.8), we applied polynomial functions complete to order $p = n$ to make $K = Q$. As a result, the weights $w_0, ..., w_{Q-1}$ obtained by solving the linear system of (6.8) provide integration results with order $p = n$.

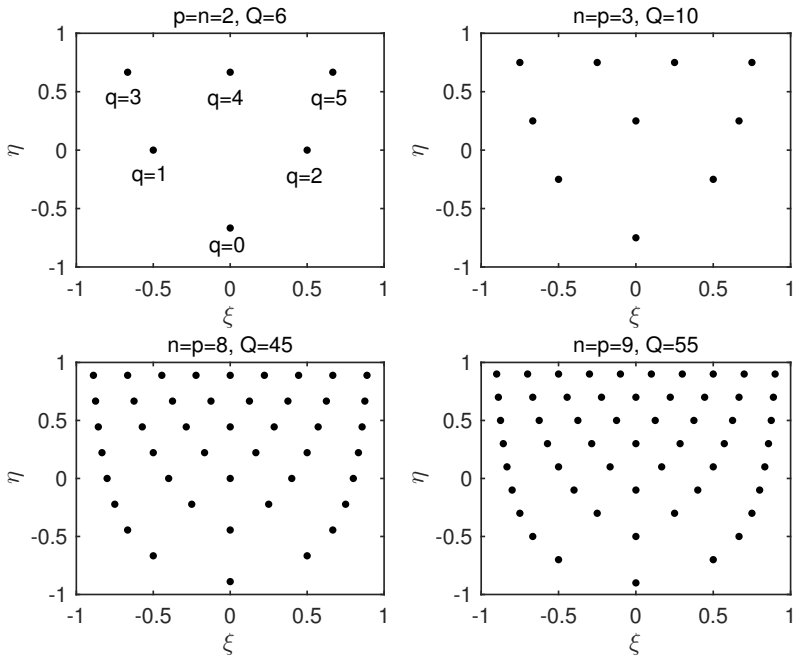

Figure 6.4: The abscissas of the quadrature rule formulated in (6.6) for orders $p = n = 2, 3, 8$ and 9, which respectively have $Q = 6, 10, 45$ and 55 quadrature points.

6.3.3.4 Numerical Instability

Generally, 1D Newton-Cotes quadrature rules are susceptible to numerical instabilities at orders higher than 9 [133] due two reasons; 1) large round-off errors due to inexact arithmetic stemming from weights that are large but differ in sign[1], and 2) failure to converge the underlying polynomial interpolation at equidistant points. To study such effect in the proposed rules, TABLE 6.2 tabulates the relative error ε in sum of all the corresponding monomials for each quadrature of orders $p = 0, 1, .., 15$ along with the condition number κ of the corresponding Vandermonde matrix $[S]$. The reference solution (the right hand side of (6.6)) is obtained by adaptive integrations with a maximum tolerance of 10^{-12}. As can be seen from the table, the proposed rules provide machine precision results for $p = 0, 1, ..., 9$ but the error becomes larger

[1]Note that the weights in Table 6.1 are not necessarily positive.

than 10^{-12} for $p \geq 10$. This suggests that the Newton-Cotes based quadrature rules defined in (6.6)-(6.9), like the 1D equidistant rules, may become inaccurate for orders $p > 9$ regardless of the fact that the condition number κ has a typical exponential growth for progressively higher orders and does not exhibit an unusual increase from order 9 to 10.

Nevertheless, in practical 3D modelling, LCN does not usually utilize such high orders due to constraints on computational resources. Moreover, as it is suggested generally for Newton-Cotes rules, one can build a *composite rule* if the integration domain is too large [144]. In the context of LCN, this can be done by means of h-refinement according to LCN's convergence rate which is known to be $\mathcal{O}(h^p)$ [1, 18]. Particularly, in the event that a triangular Bézier element (e.g. E_0 in Fig. 6.5) with a large patch size h_0 demands for order $p_0 > 9$ to achieve a desired accuracy, one can perform h-refinement on E_0 (no uniformity is required) and use different orders p_1, p_2 on the resulting elements E_1, E_2 to maintain the solution error as $\epsilon = \mathcal{O}(h_0^{p_0})$. Fig. 6.5 depicts such h-refinement. Specifically, the desired accuracy can be achieved as long as $h_1^{p_1}, h_2^{p_2} \leq h_0^{p_0}$, where h_1 and h_2 are the element size for E_1 and E_2, respectively. Therefore, the introduced rule, despite its unpredictable nature for orders higher than 9, can be applied for construction of general purpose HO LCN.

6.3.3.5 Application in LCN Local Interactions

As detailed in [1, 18, 19], the LCN local interactions are separated into two parts; the far region where the quadrature rule is applied directly, and the near region where the quadrature rules are built for singular integrals. This procedure is known as local correction. When constructing the LCN's local corrections based on the proposed rule, the abscissas in (6.7) are used to form the local correction system.

Table 6.2: The relative error ε associated with a pth order quadrature rule with Q points defined in (6.6)-(6.9). The corresponding Vandermonde matrix $[S]$ in (6.8) has condition number κ and is formed by $K = Q$ polynomial functions.

p	Q	ε	κ	p	Q	ε	κ
0	1	0.0E+00	1.0E+00	8	45	8.8E-13	4.3E+04
1	3	0.0E+00	2.4E+00	9	55	3.0E-13	1.9E+05
2	6	0.0E+00	8.3E+00	10	66	5.1E-11	8.7E+05
3	10	0.0E+00	3.2E+01	11	78	8.3E-10	3.9E+06
4	15	2.2E-15	1.2E+02	12	91	3.2E-09	1.8E+07
5	21	0.0E+00	5.2E+02	13	105	3.4E-08	8.2E+07
6	28	3.4E-15	2.2E+03	14	120	4.1E-07	3.8E+08
7	36	1.0E-13	9.8E+03	15	136	5.0E-07	1.8E+09

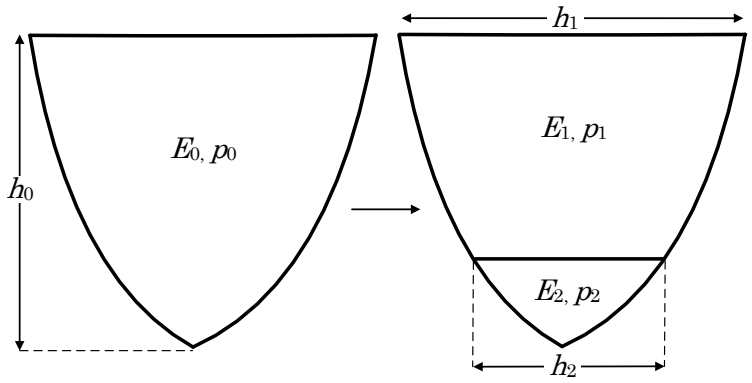

Figure 6.5: Non-uniform sub-division of the triangular Bézier patch E_0 to ensure that the solution error remains as $\epsilon = \mathcal{O}(h_0^{p_0})$ by enforcing $h_1^{p_1}, h_2^{p_2} \leq h_0^{p_0}$, where h_i and p_i are respectively the element size and the quadrature order for E_i. The division is done in a manner to yield only one singular element E_2. This ensures that the other element E_1 is quadrilateral and therefore p_1 can be chosen arbitrarily. The only constraints is to keep $p_2 \leq 9$.

This has two important implications. First, well-conditioned square local correction systems can be formed at arbitrary orders without introducing oversampling[1]. Second, the resulting LCN local interactions are not prone to an inconsistent basis for the charge density. The first implication is because a pth order triangle rule in (6.6) has $Q = (p+1)(p+2)/2$ integration nodes and can form a square Vandermonde matrix using a set of polynomial testing functions complete to order p with $K = Q$ functions. The resulting local correction system is expected to be well-conditioned as the equidistant points of the proposed quadrature rule produce Vandermonde systems with reasonable condition numbers (Table 6.2). This is contrary to where the existing Gaussian triangle rules are used to form local correction systems. Table 6.3 summarizes the condition numbers κ of Vandermonde systems formed by two different Q point Gaussian quadrature rules (i.e. [127, 129]) and K polynomial functions along with the condition numbers of the Vandermonde systems proposed in [131] for both directions of the coordinate system (ξ, η). For several orders, Gaussian quadrature rules have $Q \neq K$ which results in non-square local correction systems [19] unless extra test functions (hence extra unknowns) are introduced [131]. Moreover, the aggravating condition numbers of the resulting Vandermonde systems are the limiting factor for applying HO Gaussian triangle rules to the LCN local interactions as a sudden increase in the condition number (i.e. $\kappa > 10^{16}$) can be observed for all Gaussian based Vandermonde systems as the order increases. This agrees with [19] where Lyness and Jespersen quadrature rules with $Q > 15$ were reported to pose conditioning issues when forming the LCN impedance matrix. The second implication stems from using a complete set of polynomial testing functions which yields a current representation that also has a self-consistent polynomial basis for the charge [131].

[1]For instability reasons explained in Section 6.3.3.4, the resulting local correction systems are limited to orders $p = 0, 1, ..., 9$.

Table 6.3: The condition number κ of a pth order Vandermonde matrix formed by Gaussian Q point quadrature rules and K polynomial functions.

	Lyness & Jespersen [127]			Dunavant [129]		
p	K	Q	κ	K	Q	κ
0	1	1	1.00E+00	1	1	1.00E+00
1	3	3	7.36E+00	3	3	7.36E+00
2	6	6	6.02E+01	6	6	6.02E+01
3	10	12	3.30E+02	10	12	5.25E+02
4	15	15	4.00E+03	15	16	4.43E+03
5	21	21	2.58E+17	21	25	5.35E+04
6	28	28	7.84E+17	28	33	4.35E+05
7	–			36	37	3.72E+16

	Wildman & Weile(ξ) [131]		Wildman & Weile(η) [131]	
p	$K = Q$	κ	$K = Q$	κ
3	12	9.82E+03	12	5.19E+03
4	16	6.84E+03	16	9.19E+03
5	25	1.52E+06	25	5.27E+05
6	33	2.00E+07	33	6.68E+06
7	37	9.25E+16	37	3.71E+17

For a Bézier patch with a singularity at l_0, the proposed rule can be applied as discussed in this paper directly. For Bézier elements with a singularity at one of the other edges l_1, l_2, and l_3, a rotation is required. In our implementation, we created four different sets of triangular quadrature rules and applied them to the appropriate singular Bézier elements. For testing functions, it is possible to use either monomials [1, 19] or Legendre polynomials [18]. We used Legendre polynomials as they yield a better condition number of the Vandermonde matrix due to orthogonality [19].

6.3.4 Computational Complexity

6.3.4.1 NURBS and Bézier Elements

Incorporating NURBS surfaces into an HO scheme increases the matrix fill time compared to having bilinear, or interpolation-based, curvilinear elements [97]. Such

an increase however, does not substantially impact the complexity of the HO LCN scheme. In order to fill the matrix for a particular frequency, transformation of NURBS surfaces into a Bézier mesh has to be performed once, which keeps the overall computation time almost unchanged. Obtaining the position vector and its spatial derivatives has a larger effect on the matrix fill time. However, since the LCN method computes integrals over the source elements only, the matrix fill time is still negligible compared to that of solving the resulting large dense matrix equation. As such, it does not contribute substantially to the computational complexity of the LCN method, unlike HO MoM which has to deal with high-precision integrations over both source and test elements. Evaluating Bézier parameters in this case may notably contribute to the computation time.

6.3.4.2 Adaptive Integration

Computing the right-hand side in the local corrections procedure [1], requires adaptive integration [18]. The choice of HO rule used in the adaptive procedure is independent of the rule used in the LCN local interactions. Therefore, as the product of 1D Gauss-Legendre rules with $(n+1)^2$ points provides integration rule in the order of $2n+1$, it is preferred over the Newton-Cotes based triangle rule described in this paper. The latter, with $(n+1)(n+2)/2$ nodes, provides the rules of order n, making it less efficient than the product of 1D Gauss-Legendre rules in terms of order per number of nodes. Consequently, when splitting a triangular Bézier patch into the regions for adaptive integrations, the canonical quadrilateral shown in Fig. 6.1c, is recursively sub-divided into four elements over ξ and η axis. Therefore, by using the triangular rules proposed in this paper, the complexity of the adaptive integrations remains unchanged.

6.3.4.3 Near and Far Regions

It is important to note that the choice of quadrature rule in the LCN procedure directly affects the boundary between near and far regions. This boundary can be determined experimentally as explained in [47]. The higher the order of the quadrature rule, the smaller the near region. A smaller near region leads to better computational efficiency, especially when fast algorithms are employed [1]. However, having triangular elements in the model and applying the proposed triangle rule with order p leads to an increase in the size of the near matrix compared to having a model that only has quadrilaterals with the product of 1D Gauss-Legendre rules. This is because the latter approximates the integrands with order $2p+1$ polynomials. Nevertheless, since near and far regions can be defined uniquely for each source cell [47], in the proposed LCN discretization technique, the size of the near matrix will not severely increase as usually there are more quadrilateral elements than triangular elements in a NURBS generated Bézier mesh. For example the B2-Aircraft model, shown in Fig. 6.2, has 566 quadrilateral Bézier elements and only 16 triangular Bézier elements. When h-refinement is required, it is possible to keep the number of triangular elements unchanged by refining a singular Bézier element in a way so as to produce only one smaller singular element, where the rest of the elements are quadrilaterals. This refinement process is depicted in Fig. 6.6.

6.4 Numerical Results

In this section, the properties of the proposed LCN method are studied for both canonical and realistic examples. In all simulations herein, LU-decomposition is used to directly solve the LCN system of linear algebraic equations, leading to an error

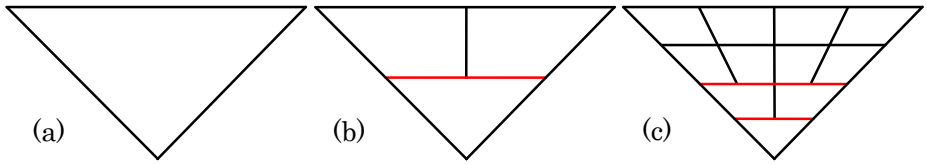

Figure 6.6: Uniform $h-$refinement imposed on a flat singular Bézier patch (a) such that $h^b_{\max} \simeq 0.5h^{\mathrm{a}}_{\max}$ and $h^c_{\max} \simeq 0.25h^{\mathrm{a}}_{\max}$ where $h^a_{\max}$ is the maximum element size in (a) and similarly for (b) and (c). This ensures that only one smaller singular Bézier patch is produced and the rest of the Bézier elements are all quadrilaterals (b,c) effectively keeping the near matrix as small as possible. Note that the non-aligned (highlighted in red) boundaries in (b,c) do not pose complications in LCN as no current continuity enforcement is required.

free matrix inversion that facilitates a reliable error analysis. The tolerance requested from the openNURBS routines was set to 10^{-6}.

6.4.1 Sphere

The HO methods of CEM converge to the correct field values under h- and p-refinements with errors that exhibit $\epsilon = \mathcal{O}(h^p)$ behaviour [1, 18–20, 96]. One reliable way to evaluation of the error behaviour of an HO 3D BEM scheme such as LCN is through numerical computation of the electromagnetic fields on a sphere, which can be compared to the analytical solution available in the form of the Mie series. The error in the surface current density $\mathbf{J}$ is typically quantified in terms of the following 2-norm [55]

$$\text{2-normErr}(\mathbf{J}) = \frac{\sqrt{\frac{1}{N}\sum_{n=1}^{N} |J_i^{\mathrm{LCN}} - J_i^{\mathrm{Mie}}|^2}}{|J^{\mathrm{Mie}}|_{\max}} \tag{6.10}$$

where J^{LCN} and J^{Mie} are the current magnitudes $|\mathbf{J}|$ at all of the quadrature points obtained by the LCN and Mie series, respectively, with N being the total number of points.

Figures 6.7 and 6.8 plot 2-normErr($\mathbf{J}$) for the LCN solution of scattering from

a perfectly electric conducting (PEC) sphere obtained through discretization of the EFIE and MFIE, respectively[1]. The highlighted point in Fig. 6.7 corresponds to the data shown in Fig. 6.9. The sphere of 1m radius was excited with a radial $\hat{z}$-directed electric dipole placed 9m above the north pole of the sphere. The time-harmonic frequency was taken to be 100MHz. The sphere was represented with a single NURBS surface (6.1) of degree 8 in both u and v directions ($\mathtt{P} = \mathtt{Q} = 8$). This resulted in a sphere model having maximum deviation in the radius not exceeding 10^{-10}m compared to the exact value of 1m. Four different meshes with 24, 48, 96, and 336 Bézier elements were obtained from this NURBS model. In forming the coarsest Bézier mesh, no quadrilateral elements were used and all 24 elements were triangular Bézier elements that span from the poles of the sphere to its equator. As was suggested in Section 6.3.4.3, h-refinement was used in a manner that kept the number of triangular elements unchanged. Therefore, in the other three meshes, there are 24 triangular Bézier elements adjacent to the south and north poles, and quadrilateral elements representing the remaining surface. The 96 element case is depicted in Fig. 6.2 and the 336 element mesh can be seen in the insets of Fig. 6.9. The maximum element size $h_{\max}$ for each Bézier mesh is given in the figures[2]. As can be seen from Figs. 6.7 and 6.8, the HO convergence to the correct answer has been achieved according to an $\mathcal{O}(h^p)$ rate for orders $p \leq 9$ but the error starts to grow for orders $p > 9$. This is consistent with the data shown in TABLE 6.2 where it is observed that the proposed triangle rule is accurate to machine precision for orders 0 to 9 but becomes unstable for orders higher than 9. For the 24 element case

[1]Note that the errors are plotted against the order p (rather than h) for readability reasons, i.e. in order to clearly show the stability of the introduced rules for orders from 0 to 9 and their instability for orders higher than 9.

[2]In this paper, the maximum element size corresponds to the maximum edge length as shown in Fig. 6.5. In some CAD tools such as Gmsh [106], the element size is provided in terms of the radius of the circumscribing circle r, in which case $h \simeq \sqrt{2}r$.

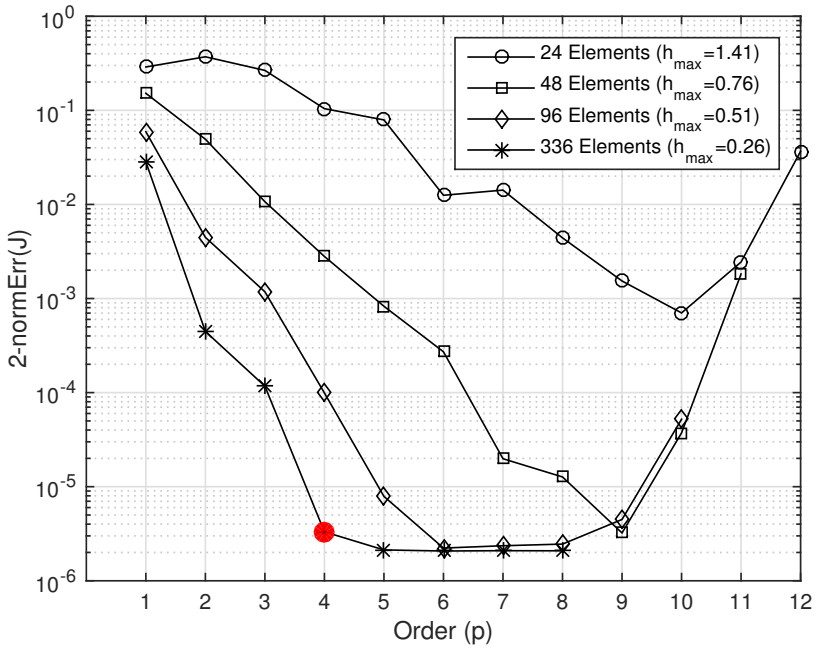

Figure 6.7: The 2-norm error (6.10) of LCN solution of EFIE for scattering on a 1m radius sphere at 100MHz. The 24 element model has only triangular Bézier elements. The other three models with $48, 96$ and 336 elements have both triangular and quadrilateral elements as in Fig. 6.2. The highlighted point on the 336 Element model at order $p = 4$ corresponds to the results shown in Fig. 6.9.

which only has triangular Bézier elements, if we consider EFIE's order 1 and 9, the convergence rate is $0.55(h^{0.88p})$ where $h = h_{\max}/\lambda = 0.47$. For the same Bézier mesh, by using orders 0 and 9, the MFIE's convergence rate is estimated to be $0.6(h^{1.43p})$. This is consistent with the numerical results reported in [18] where EFIE under-converged, whereas MFIE super-converged. The error floor appearing at about 10^{-6} can be explained by the fact that the geometry related computations are requested from openNURBS to be accurate up to 6 digits of precision.

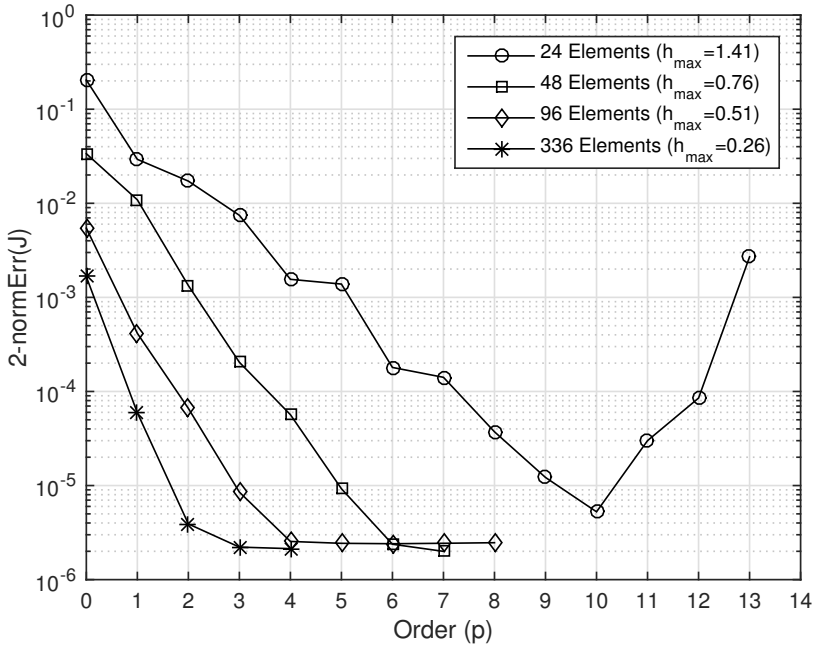

Figure 6.8: The 2-norm error (6.10) of LCN solution of MFIE for scattering on a 1m radius sphere at 100MHz. The 24 element model has only triangular Bézier elements. The other three models with $48, 96$ and 336 elements have both triangular and quadrilateral elements as in Fig. 6.2.

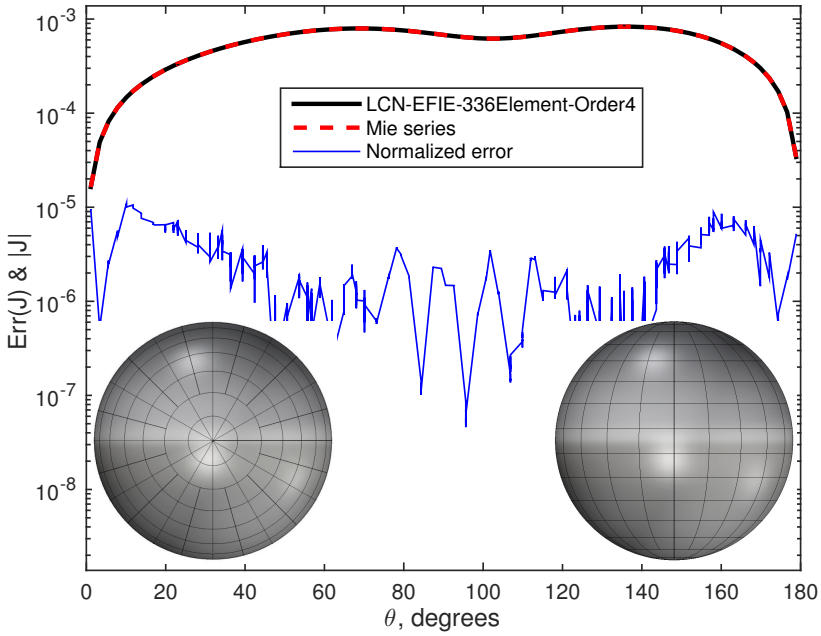

Figure 6.9: The current magnitude $|J|$ and its normalized error $\mathrm{Err}(J_\theta) = |J_\theta^{\mathrm{LCN}} - J_\theta^{\mathrm{Mie}}|/|J^{\mathrm{Mie}}|_{\max}$ corresponding to the highlighted fourth order configuration in Fig. 6.7 which has 336 Bézier elements, 24 of which are triangular elements. As can be seen from the left inset, 12 triangular Bézier elements are adjacent to the south pole (the north pole is identical). The right inset depicts the model from the side.

6.4.2 Archimedean Spiral Antenna

To demonstrate that the proposed LCN scheme exhibits HO error behaviour for geometries formed by multiple NURBS surfaces, we analyze the radiation intensity U [145] of an Archimedean spiral antenna shown in Fig. 6.10. The model features three NURBS surfaces in each of its arms which are made of a spiral cylinder terminated by two half spheres. Dimensions in terms of the wavelength λ are given in the figure. In the CAD tool Rhinoceros3D, the G^2 continuity (aka curvature continuity [125]) is ensured between all three NURBS in each arm of the spiral. This guarantees that there is no directional tangent discontinuity between NURBS surfaces of each arm, up to the second degree. The radiation intensity U was computed using the proposed LCN scheme when applied to CFIE ($\alpha = 0.5$) for two different Bézier discretizations. The coarser mesh is depicted in Fig. 6.10a which constitutes 48 triangular Bézier cells and 624 quadrilateral Bézier elements. The finer mesh also has 48 triangles but 2780 quadrilaterals due to the Bézier discretization technique introduced in Section 6.3.4.3. The proposed LCN discretization technique was applied to the 672 element mesh with orders p from 1 to 7, and orders from 1 to 3 for the finer mesh with 2828 elements. The limiting factor in p for both cases is due to the size of the resulting global matrix that was inverted directly[1]. Estimation of the computed solutions accuracy is done by comparing them against the most finely discretized solution taken as the *reference solution* [19]. In this example, the reference solution is chosen to be the LCN solution with the highest order $p = 7$. Fig. 6.10b illustrates the surface current density of the antenna computed by the reference solution at time $\mathtt{t} = 0$s. The mean and maximum

[1]The maximum number of unknowns came from the finer mesh at order $p = 3$ which can be computed as $2\{[2780(3+1)^2] + [48(3+1)(3+2)/2]\} = 89920$.

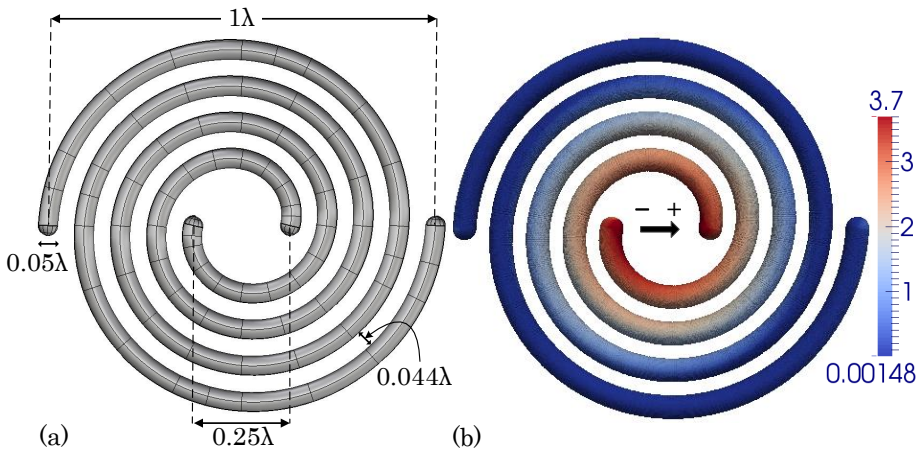

Figure 6.10: (a) The modelling of the Archimedean spiral antenna using 6 NURBS which resulted in a mesh that has 48 triangular Bézier elements and 624 quadrilateral Bézier elements. (b) Surface current density at time $\mathtt{t} = 0$s over the antenna simulated by the proposed LCN method applied to CFIE with $\alpha = 0.5$ at order 7. The feed is an electric dipole represented by an arrow at the center which induces voltage across the the two arms of the spiral. The radiation intensity U resulted from this solution is used as the reference solution in (6.11) and Fig. 6.11

relative errors in U are computed as

$$\begin{aligned} \text{MeanErr}(U) &= \frac{1}{N_{\text{a}}} \sum_{i=1}^{N_a} \frac{|U^{\text{LCN}}(\theta_i, \phi_i) - U^{\text{Ref}}(\theta_i, \phi_i)|}{|U^{\text{Ref}}(\theta_i, \phi_i)|}, \\ \text{MaxErr}(U) &= \max \left[\frac{|U^{\text{LCN}}(\theta_i, \phi_i) - U^{\text{Ref}}(\theta_i, \phi_i)|}{|U^{\text{Ref}}(\theta_i, \phi_i)|} \right] \end{aligned} \tag{6.11}$$

where N_a is the number of angles, $U^{\text{LCN}}(\theta_i, \phi_i)$ is the radiation intensity computed via the LCN method at discrete angle (θ_i, ϕ_i), and $U^{\text{Ref}}(\theta_i, \phi_i)$ is the radiation intensity of the reference solution. Fig. 6.11 plots the relative errors. It can be seen that the proposed LCN solution shows HO convergence to the reference solution according to $\mathcal{O}(h^p)$ behaviour for both mean and maximum relative errors. This indicates that by using the proposed LCN scheme, it is possible to compute radiation properties of an antenna with arbitrary accuracies (up to machine precision) at all considered directions.

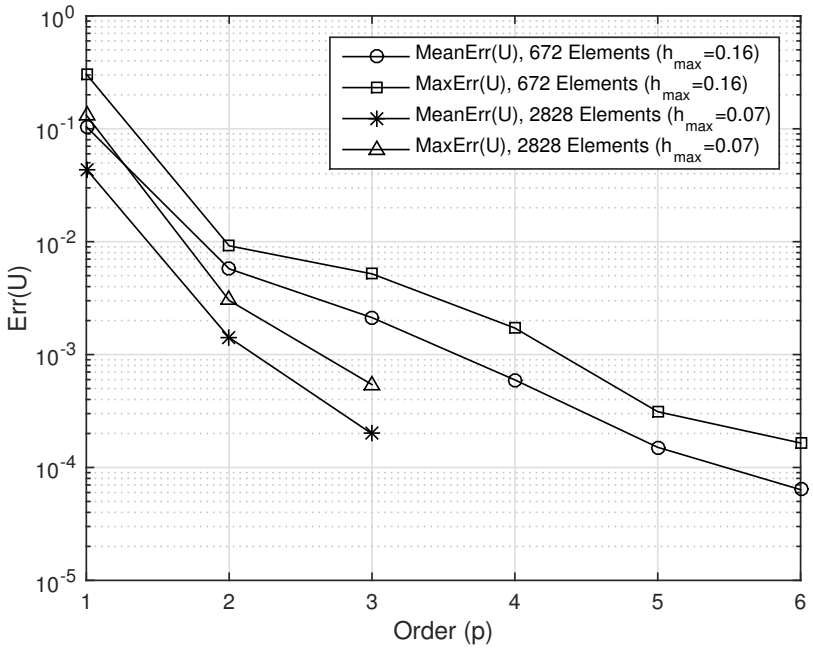

Figure 6.11: Mean and maximum relative errors in the radiation intensity U approximated as in (6.11) for the spiral antenna where the proposed LCN scheme is applied to CFIE with $\alpha = 0.5$. The model with 672 Bézier elements is depicted in Fig. 6.10a which is used to compute the reference solution at order $p = 7$ with its current density depicted in Fig. 6.10b.

6.4.3 B2-Aircraft Model

A very important feature offered by HO methods is in their ability to provide comparable results with LO methods with solution accuracies of 2 to 3 digits of precision but with fewer unknowns [20]. To demonstrate that the proposed scheme (i.e. LCN modelled with NURBS) can reduce the number of unknowns compared to an LO method, in this section, we consider electromagnetic scattering from a PEC B2-Aircraft model (Fig. 6.2) obtained by LCN where the proposed discretization scheme is applied to CFIE with $\alpha = 0.2$. The excitation is the same dipole as used in Section 6.4.1, positioned 10 meters above the nose tip of the aircraft. The wingspan of the aircraft is 57.3λ (see Fig. 6.12). A commercial tool (Wave3D [35]) was used to obtain the reference solution using RWG MoM with $812,952$ flat triangular elements ($h_{\max}^{\text{RWG}} = 0.1\lambda$) which resulted in $1,219,428$ RWG MoM unknowns. The proposed solution uses a NURBS representation of the model that is depicted in Fig. 6.2. One way to formulate LCN on the Bézier mesh depicted in Fig. 6.2, is to use the same order on all of the Bézier elements as was done in Sections 6.4.1 and 6.4.2. However, due to the non-uniform nature of the Bézier elements in terms of their size, it is more efficient to formulate LCN with different orders on different elements according to their size. The Bézier patch with the largest element size $h_{\max}$ was formulated with order 5 and the rest of the elements according to the desired $\mathcal{O}(h^p)$ error behaviour. Therefore, the ith Bézier patch with element size h_i should be formulated with order p_i such that $h_{\max}^5 \simeq h_i^{p_i}$. However, as the product of 1D Gaussian rules is most efficient on square patches, it becomes more computationally advantageous (less unknowns) to perform h-refinement along the lengthy direction (i.e. u or v) of the elongated Bézier elements, and use smaller orders on the resulting almost-square Bézier cells. In the B2-Aircraft case shown in Fig. 6.2, such h-refinement resulted in 884 quadrilateral

Bézier elements and 16 triangular Bézier elements[1]. Consequently, 10 of the triangular elements had order 1, 4 had order 2 and the remaining 2 had order 4. Quadrilateral elements were formulated with orders $1, 2, 3, 4$, and 5, on respectively, $56, 108, 190, 308$, and 222 Bézier cells. This resulted in a total of $40,024$ unknowns where the largest Bézier element had element size $h_{\max} = 2.08\lambda$. It is worth noting that the process of h-refinement explained above, is greatly facilitated by the openNURBS, as the library allows for splitting individual Bézier elements in either of the u and v directions with arbitrary ratios (for more examples see [69]). The surface current computed by both techniques at time $\mathtt{t} = 0$s are depicted in Fig. 6.12. From the figure, it can be seen that except for some values near the geometry edges, there is a close agreement between the two solutions despite the fact that the proposed solution uses over 30 times fewer unknowns compared to the RWG MoM reference solution. In order to numerically compare the two solutions, the surface current magnitude along the red line shown in Fig. 6.12 is plotted in Fig. 6.13. By comparing the position of this line in Fig. 6.12 and Fig. 6.2, it can be realized that this line is chosen in such a way so that it goes over both triangular and quadrilateral Bézier elements. In Fig. 6.13, the two solutions match with 2 to 3 digits of precision at all considered points where the number of compared values is limited by the number of LCN's quadrature points that reside over the considered line.

6.5 Conclusion

In this paper we proposed a new family of quadrature rules to be applied to triangular Bézier elements for LCN discretization of the EFIE, MFIE, and CFIE.

[1]Note that despite the h-refinement, the number of triangular Bézier elements remains 16 which is the same as those in Fig. 6.2. As explained in Section 6.3.4.3, this keeps the near matrix as small as possible.

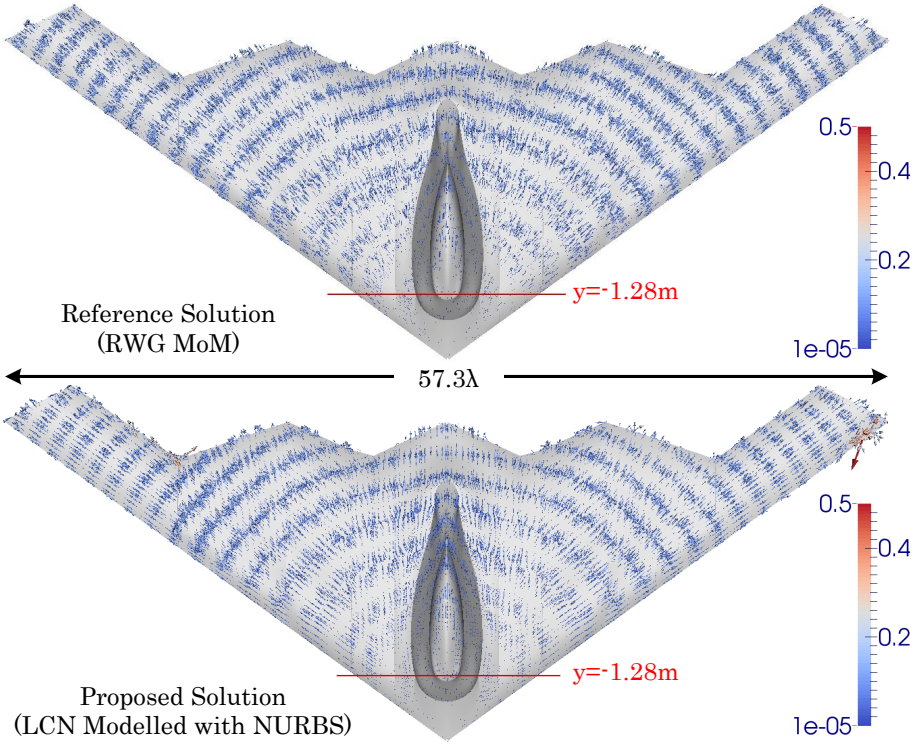

Figure 6.12: Current density on the surface of the B2-Aircraft at time $\mathtt{t} = 0$s computed by the RWG MoM obtained by a commercial tool [35] and the proposed LCN scheme. The proposed solution has resulted in over 30 times reduction in the number of unknowns compared to the reference RWG MoM solution. The red line over the surface at $y = -1.28$m has been used to plot the current magnitude in Fig. 6.13.

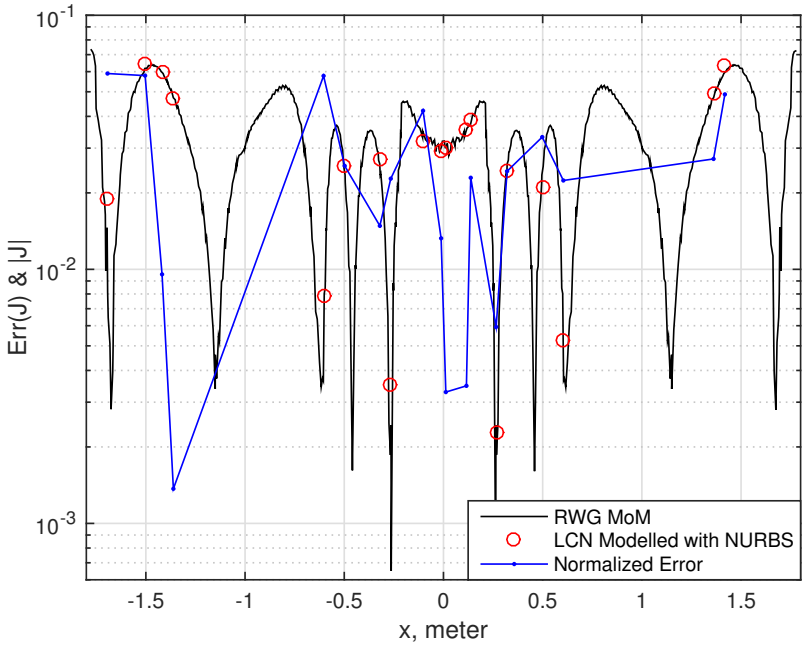

Figure 6.13: Comparison of the current magnitude $|J|$ over the red line at $y = -1.28$m in Fig. 6.12. The normalized error is $\mathrm{Err}(J_i) = |J_i^{\mathrm{LCN}} - J_i^{\mathrm{RWG\ MoM}}|/|J^{\mathrm{RWG\ MoM}}|_{\max}$.

The rule is derived from the generalized Newton-Cotes quadrature formula which is based on equidistant points. It prevents aggravating conditioning problems for the EFIE, unlike the Gaussian quadrature rules for triangles which have dense concentrations of points near the edges and vertices of triangles. The proposed triangle rule has the same number of quadrature points as the number of polynomial basis functions complete to a given order, resulting in a square local correction system of linear algebraic equations. The scheme has a self-consistent polynomial basis for the charge description and can be reliably used in the HO LCN for orders ranging from 0 to 9. Numerical results show that the proposed rule facilitates achieving HO error convergence to the correct field values according to an $\mathcal{O}(h^p)$ behaviour. The prerequisite to such error behaviour is that the LCN uses geometry models composed of NURBS generated Bézier meshes consisting either a single NURBS surface or multi-

ple NURBS surfaces, the latter being subject to G^2 continuity requirement between adjacent NURBS surfaces. Therefore, the introduced LCN scheme can provide solutions with arbitrary accuracies up to machine precision for smooth geometries. The proposed method when compared with the more traditional RWG MoM, has resulted in a 30 times reduction in the number of unknowns as it allows for patches as large as 2.08λ when engineering solutions with 2 to 3 digits of precisions are required.

6.6 Acknowledgments

The authors would like to thank Prof. A. F. Peterson from the Georgia Institute of Technology and Drs. D. L. Faircloth, and T. N. Killian from IERUS Technologies Inc. for helpful technical discussions that lead to developing the presented work. We also thank Alexander Krylov for his shared expertise in 3D CAD tools, which helped us create the geometries in Rhinoceros3D.

Chapter 7

Conclusions, Comments and Future Work

By *Mohammad Shafieipour* in partial fulfilment of the requirements of the degree of *Doctor of Philosophy (Ph.D.)*, March 2016.

In this Ph.D. program, the focus was on the boundary element methods (BEMs) used to discretize surface integral equations (SIEs) in computational electromagnetics (CEM). In this chapter, the accomplishments and conclusions are summarized and suggestions for possible future work are discussed. This chapter also provides Prof. Gedney's comments and the author's responses about the entire dissertation.

7.1 Conclusions

This thesis started by reviewing the motivation towards BEMs in CEM in Chapter 1, followed by studying the theory behind SIEs and the desirable properties of Rao-Willton-Glisson (RWG) basis functions when discretizing the electric field integral equation (EFIE). The overview of RWG MoM discretization of the EFIE was given

in an attempt to show the advantages of the current continuity enforcing nature of the RWG basis functions so as to motivate the reader for the use of such basis functions in the low-order (LO) locally corrected Nyström method (LCN) method. A new description of the LCN scheme was also given as a complementary note to existing LCN descriptions.

In Chapter 3, we argued that the LCN method at LOs, is inefficient compared to its LO RWG method-of-moments (MoM) counterpart due to the fact that it does not enforce continuity of current. A novel method to enforce current continuity on first-order LCN was developed by establishing the equivalence between the first-order LCN method and the RWG MoM. It was shown that such equivalence can increase the computational efficiency by 4 times reducing the number of unknowns and at the same time improving the accuracy of the method. In order to achieve the sought equivalence, the vector-potential (VP) EFIE was used as LCN discretizes the VP EFIE. The introduced method can also be seen as a point-based discretization of the RWG MoM for the VP EFIE as an alternative to the VP EFIE discretized with the point-matched MoM which is typically preferred over the element-based RWG MoM when fast algorithms are employed.

Chapter 4, dealt with establishing the relationship of LCN and RWG MoM in discretizing the mixed-potential (MP) EFIE. The MP EFIE formulation, when discretized with RWG MoM, facilitates analytical (exact) cancellation of line charge contributions. The exact relationship between LCN and RWG MoM was derived to build a point-based RWG MoM discretization of MP EFIE. It was shown that by using MP EFIE instead of VP EFIE, notably higher accuracies can be achieved and at the same time the computational complexity is reduced due to analytical cancellation of line integrals appearing in MP EFIE. A detailed study was carried out

to shed light on why analytical cancellations are preferred over numerical cancellations and their impact on the solution accuracy. The introduced method can also be equipped with low-frequency stable formulations for wideband applications as it is equivalent to a point-based RWG MoM discretization of the MP EFIE. This is unlike the constrained LCN (CLCN) [90] approach, where low-frequency stable formulation is achieved by the augmented EFIE (AFIE) which increases the degrees of freedom. The introduced MP RWG-via-LCN, similar to the VP RWG-via-LCN method is a point-based method and is typically preferred over element-based techniques in the presence of fast algorithms such as the multilevel fast multipole algorithm (MLFMA).

As of today, the CEM computer-aided design industry predominantly relies on the well established LO techniques. Therefore, the novel LO techniques developed in Chapters 3, and 4 might be good contenders in becoming industry ready products. However, it is known that high-order (HO) methods are more efficient than their LO counterparts and a natural progress at this point of research was to try to generalize the work of Chapters 3 and 4 to HOs. However, it is known that the effect of current continuity diminishes as the order increases. In fact, a new method for enforcing current continuity for arbitrary order LCN has recently been proposed [90] which according to one of its co-authors was inspired by the work presented in Chapter 3 which was published as a journal paper in 2014 [89]. However, numerical results of the authors confirmed that the effect of current continuity at HOs is not profound especially for practical examples. In the numerical results, practical examples were given only at orders zero and one and higher orders were not even studied except for canonical examples. For these reasons, in this PhD work a different approach was taken in order to contribute to HO LCN scheme as a reliable BEM.

In Chapter 5, different aspects of HO LCN was studied. For example, the lim-

itation on the patch size was derived and based on that a method was introduced than can predict the optimum number of unknowns according to the desired accuracy of the solution. The effect of large dynamic range in the solution was also studied and the motivation towards using HO LCN compared to classical RWG MoM was addressed, both analytically and numerically. Through extensive numerical results, the imperative of adopting HO techniques were investigated by comparing LO RWG MoM and HO LCN method in computing the electromagnetic scattering from a sphere where the analytical solution is available for validating the accuracy of the results. Using both numerical results and analytical expressions, it was demonstrated that HO methods are exponentially more efficient than LO methods.

In Chapter 6, the work in HO LCN was continued by introducing a new family of quadrature rules for triangles to be used in HO LCN when modelled with non-uniform rational b-spline (NURBS) surfaces. A previous implementation of HO LCN modelled with NURBS avoided using triangular elements and only applied quadrilateral elements despite the fact that NURBS surfaces typically contain elements of both types. Due to the limitations of Gaussian quadrature rules on triangles, a new set of quadrature rules for triangles based on the equidistant Newton-Cotes quadrature formula was developed. The resulting numerical scheme is capable of producing machine precision results for arbitrary smooth geometries created by convenient CAD tools. When compared to RWG MoM, the proposed method can reduce the number of unknowns significantly. For example, in modelling a B2-Aircraft, over 30 times reduction in the number of unknowns was demonstrated.

7.2 Addressing Prof. Gedney's Comments

Prof. Stephen D. Gedney of the University of Colorado was the external examiner of this work. Having such a top expert in the field as the external examiner was an almost perfect match for this work as he is the author of [18] and many more related publications which this work is heavily based-upon and related. His feedback is so valuable that some of his comments are addressed here in their original forms. In the remainder of this section, Prof. Gedney's notes are in *italic font*, while responses are in normal font.

7.2.1 Summary

Prof. Gedney: *The overall focus of this dissertation is on the further development of the application of the locally corrected Nyström method to solving surface integral equation methods for the computational simulation of the scattering of electromagnetic waves by conducting objects. The main contributions of the dissertation are 1) the mapping of a first-order LCN discretization, to a Galerkin method of moments scheme based on Rao-Wilton-Glisson (RWG), H(0)-divergence conforming basis functions, 2) the derivation of a mixed-potential form of the LCN method that also maps to the RWG basis, 3) the quantification of the error convergence of the LCN method for smooth structures, and the ability to predict the discretization for a desired accuracy, and 4) the LCN discretization using Bézier cells for the high-order modelling of smooth structures. The work embodied in this dissertation is deemed to be novel, based on my own opinion, as well as the opinion of several qualified peer reviewers who have reviewed and approved the publication of at least 3 journal papers in the IEEE Transactions on Antennas and Propagation, within which 3 chapters of this dissertation have been published. It is an excellent contribution to the field of com-*

putational electromagnetics, and should be commended. **Response:** Thank you very much for the well-crafted summary of this dissertation and your kind recognition of the contributions. I would like to note that the work of Chapter 6 has not been published to date, but rather has been submitted (with major revisions) to the said journal [147]. We hope that this work will be accepted and published in the near future.

7.2.2 Strengths and Weaknesses of the Thesis

7.2.2.1 Strengths

Prof. Gedney: *The work in this thesis presents a few significant contributions. In my opinion, Chapters 4 and 5 are the most significant.* **Response:** It is interesting to me that you find the work of Chapter 5 as one of the most significant contributions as this work has not been published or submitted for publication as a journal paper. In fact, writing this chapter was challenging as a lot of concepts have been covered which makes it difficult to put together as a chapter. I am glad that such difficulties did not prevent me from writing this chapter.

Prof. Gedney: *Chapter 4 presents a means of applying the LCN method to a mixed-potential form of the electric field integral equation (EFIE). While this method is limited to a low-order application of the LCN method, I think it can be extended to a high-order formulation, improving the overall quality of the LCN solution of the EFIE by reducing the hypersingularity of the EFIE kernel.* **Response:** Such work would be very interesting and seems to be possible. In fact, a similar work is suggested as a future work (Section 7.3.6).

Prof. Gedney: *Chapter 5 presents an analytical procedure for predicting the convergence behaviour of an LCN solution for a smooth body using the magnetic field*

integral equation (MFIE). A closed form expression for the error convergence is derived that while relying on experimental data, allows one to predict the discretization needed for a desired accuracy for a class of problems. This has not been presented before. **Response:** Predicting the convergence behaviour is not limited to MFIE and can be used for EFIE and CFIE as the experimental finding of a and b (Section 5.3.2) is not restricted to MFIE. In fact the numerical example given in Section 5.3.4 uses LCN discretization of the CFIE. The fact that the numerical results in Section 5.4 are limited to MFIE is due to the unavailability of effective preconditioners to make EFIE or CFIE converge to the desired GMRES tolerance as MLFMA acceleration is used. Predicting the optimal number of unknowns is applicable to MFIE, EFIE, and CFIE.

Prof. Gedney: *Chapter 6 is also an excellent contribution by applying the LCN method to more sophisticated curvilinear structures using NURBS based discretizations. Such discretizations truly lends itself to applying the full potential of a high-order method such as the LCN method.* **Response:** Thanks for the accurate and interesting comments.

7.2.2.2 Weaknesses

Prof. Gedney: *There are some weak points of the dissertation that should be addressed. The first is the application of the error analysis to the EFIE of the combined field integral equation (CFIE). The latter is more practical for large structures where the MFIE could suffer from interior resonance issues.* **Response:** We assume that this comment is about Chapter 5 as Chapters 3, 4, and 6 do cover EFIE. In fact, chapters 3 and 4 only cover EFIE for the reasons that are briefly explained in Section 7.3.1. In Chapter 5, overall, the discussion is applicable to MFIE/EFIE/CFIE and

as mentioned earlier, numerical results are given for CFIE and MFIE. For large-scale examples however, MFIE is considered due to the unavailability of efficient preconditioners to help GMRES tolerance reach the desired accuracy.

Prof. Gedney: *Another weak point is the Newton-Cotes triangle rule applied to degenerate triangles formed by Bézier surface representation of the NURBS elements. This method has potential, but as applied also has some limitations. Perhaps a true triangle Bézier surface can be derived, and Gauss-triangle rules could be used instead.* **Response:** As mentioned in Chapter 6, already existing Gaussian triangle rules do not always result in square Vandermonde matrices and produce matrices with exceedingly high condition numbers at high orders. These two issues should be resolved (by perhaps inventing a new type of Gaussian quadrature rules) before what is suggested here can be realized and may be a subject of future research. Such method would indeed be preferable over the method introduced in Chapter 6. The reasons are two fold; 1) there would be no limitation to increasing the order of the Gaussian quadrature rule as opposed to Newton-Cotes rules where the order is limited to $p < 10$, and 2) the product of 1D Gaussian rules with $(n+1)^2$ points provides integration results in the order of $2n+1$ and is preferred over the Newton-Cotes based triangle rule with $(n+1)(n+2)/2$ nodes which provides the rules of order n.

Prof. Gedney: *The strengths far outweigh the weaknesses in this work. It is a strong dissertation.* **Response:** Thank you very much. In the author's opinion, *all* the methods introduced in this dissertation while have been agreed to be novel and to the best of CEM community's knowledge to date, are subject to improvements. What is suggested in the future works, are those that can be envisioned at the time of this writing and perhaps more can be suggested as further research reveals more insights about these techniques. It would be my pleasure to see other people adopting

these techniques and improving them.

7.2.3 Suitability of the Thesis for Awards

Prof. Gedney: *This is hard for me to comment on, as I do not know the category of awards that the University of Manitoba has. I think that this is an excellent dissertation with a number of novel contributions, as stated above. If it were my student I would nominate this dissertation for an award.* **Response:** Seeing these types of comments from a top expert in the filed reminds me why I entered this program and adds ample joy to the success of graduation.

7.2.4 Chapter 1: Introduction

Prof. Gedney: *Overall, summarizes the dissertation well and provides more than ample background. I like the fact that Rokhlin's dogmas are stated. This is an important starting point.* **Response:** Rokhlin's dogmas are indeed important and yet not widespread in the literature. We hope that the prospective readers of this dissertation realize their importance and apply them to their field of scientific computing.

7.2.4.1 Comment 1

Prof. Gedney: *Page 7: You state: "otherwise the method is formulated using method-of-moments (MoM) [20–23] where interactions are defined based on elements and these methods are commonly referred to as element-based methods"*
Comment: The method of moments is based on an expansion of interpolation functions over the problem domain, and following the method of weighted residuals, computing moments of the operator. Entire domain functions spanning the entire domain

can be used or those bound by elements (cf, Peterson, Mittra, and Ray, Computational Methods for Electromagnetics, [39]). Interpolation functions bound by elements are more precisely referred to as finite element methods which can be used to solve differential or integro-differential operators (c.f., P. Silverster and R. Ferrari, Finite Elements for Electrical Engineers [57]). Though, in modern taxonomy finite element methods are interpreted as being the solution of a differential equation. Perhaps a clearer distinction between methods, is quadrature point based versus interpolation-function (or expansion-function?) based methods. **Response:** Thank you very much for pointing this out. The suggested terms are indeed more presice. However, using *point-based* instead of *quadrature-point-based* does not alter our discussion since the fact that the points of the LCN method reside at the quadrature points do not contribute to its efficient acceleration by fast algorithms. The term *element-based* on the other hand may cause ambiguity due to the reasons mentioned in the comment. Some references (e.g. [5]) have used the term "basis-based" and that is what we also included in Chapter 3.

7.2.4.2 Comment 2

Prof. Gedney: *Page 8: Some disadvantages of the LCN method should also be listed. Don't be afraid to address the cons.* **Response:** Initially, the reason for not listing LCN's disadvantages here was that this particular discussion is about point-based methods in general and LCN is given as an example of a point-based method. However, as suggested, we agree that the disadvantages of LCN should also be addressed. For that, please refer to the last paragraph of Section 4.1.

7.2.4.3 Comment 3

Prof. Gedney: *Page 8: You state: "In order to accomplish better conditioned matrices several techniques have been suggested for particular examples [27–29] but a general solution is not available to date and constitutes an open research problem [1]." There are much more recent and pertinent references than [27–29] for well-conditioned formulations. There is still a volume of on-going research on this topic. However, I believe that within the next 5 years, this question will be settled and more easily applied to LCN methods.* **Response:** Thank you very much for letting us know about this. A more recent literature review on this topic is left for prospective readers.

7.2.5 Chapter 2: Mathematical Formulation

Prof. Gedney: *This chapter summarizes the derivation of the EFIE, RWG basis, etc. This chapter is more a pre-curser to chapter 3 rather than for the entire dissertation. I expected a more general presentation of the formulations used in the dissertation, e.g., MFIE, CFIE, and LCN method. This is the author's prerogative.* **Response:** During my time as a Ph.D. student in the University of Manitoba, I started realizing that some concepts of the EM field can be explained in ways other than the ones available in the literature which could facilitate easier understanding or at least from a different point-of-view which could complement the already existing texts. Therefore, I decided to include in this chapter those topics that were related to the thesis and at the same time I had my own way of explaining them. Derivation of the EFIE from the Maxwell's equations and basics of LCN (suggested by one of the internal examiners, Dr. LoVetri) are included for this reason. Notes related to RWG MoM and RWG basis functions were added to the chapter to facilitate easier transition to the next chapter as pointed out in the comment.

7.2.6 Chapter 3: On the Equivalence of RWG Method of Moments and the Locally Corrected Nyström Method for Solving the Electric Field Integral Equation

Prof. Gedney: *This chapter focuses on deriving a mapping between an H(0)-div RWG based MoM scheme with the LCN method using p=1 basis. I am familiar with the publication of this work in the IEEE Trans. On Ant. Prop., 2014, and believe this to be a nice contribution. Nevertheless, I have some comments for the author.*

7.2.6.1 Comment 1

Prof. Gedney: *Page 50: You state: "In particular, a first-order LCN solution of the EFIE is often substantially less accurate when compared to its first-order Rao-Wilton-Glisson (RWG) MoM counterpart [1], despite using four times as many degrees of freedom per element."*
Comment: I believe this statement to be somewhat misleading. An equivalent $H(0)$ *basis for LCN on triangles would be a 1 point quadrature rule. This would integrate triangle functions to degree 1. This would lead to two degrees of freedom per triangle (quadrature-point, with two vectors). Case and point, a 1 point rule will integrate the RWG basis function exactly. This would converge with* $O(h^2)$ *on smooth surfaces. This requires* $2P$ *unknowns compared to* $1.5P$ *for RWG basis.* **Response:** The reason for calling first-order LCN a counterpart for RWG MoM is due to the discussion made in Section 3.4.1. Particularly, as shown in (3.30), to correlate the ramp-functions of the RWG MoM to scalar basis functions of LCN $F_k(\mathbf{r})$, it is required to choose first-order LCN as it has $(k = 1, 2, 3)$ where $F_1(\mathbf{r}) = 1$, $F_2(\mathbf{r}) = \xi(\mathbf{r})$ and $F_3(\mathbf{r}) = \eta(\mathbf{r})$. However, the point made in the comment is valid and should have been addressed. Thank you for your precise comment.

Prof. Gedney: *I believe that what is being implied here is that the four time reduction in matrix dimension is specific to this method where a three-point quadrature rule for the triangle rule is being mapped to the RWG basis. This leads to a 4 fold reduction in the dimension of the matrix. What is interesting is that this quadrature rule is higher-order than the RWG basis.* **Response:** Very interesting observation. In fact, during the writing of this contribution, we looked at the relationships between RWG basis and scalar basis functions of LCN $F_k(\mathbf{r})$, as opposed to looking at the minimum order quadrature rule that can exactly integrate RWG basis. By doing the latter, the RWG MoM does relate to zeroth-order LCN with $2P$ unknowns and the work of Chapter 3, establishes exact relationship between RWG MoM and an LCN solution at a higher order.

7.2.6.2 Comment 2

Prof. Gedney: *Page 54: "the singular kernel are integrated exactly to a given precision". Integrated exactly to a given precision is contradictory.* **Response:** True indeed! This should be corrected.

7.2.6.3 Comment 3

Prof. Gedney: *Page 56: "Note that unlike standard LCN, the observation weight ω_{q_m} is included in* (3.9) *in order to permit observation patch integrals analogous to RWG MoM"; Most LCN codes I am aware of weight the rows by the field quadrature weight. Though, the reason this is done in standard LCN is for symmetry of the system matrix.* **Response:** By looking at the standard LCN [1, 18, 19], it can not be realized that an LCN code weights the rows by the field quadrature weight for symmetry of the system matrix. This comment bears an important insight about

implementing LCN which was not known by the author prior to seeing this comment. Thank you very much.

7.2.6.4 Comment 4

Prof. Gedney: *Page 64: Equation* (3.33) *is not correct. Note that the unitary vectors have units of length, reciprocal unitary are 1/length, and the unit vector is unit-less. Thus, your units don't match up. Rather,* $\mathbf{a}^1 = \frac{\mathbf{a}_2 \times \hat{\mathbf{n}}}{\sqrt{g}}$, $\mathbf{a}^2 = \frac{\hat{\mathbf{n}} \times \mathbf{a}_1}{\sqrt{g}}$, *and* $\sqrt{g} = 2A$ *for the flat triangular patch. In this case the identity in* (3.34) *is true. (Note, that unitary vectors have units of length, and reciprocal unitary vectors have units of 1/length.)* **Response:** Thank you very much for this correction. As explained in the footnote2 of page 53, in this chapter $\sqrt{g}$ is omitted from notations. However, it is agreed that (3.33) should be corrected as explained in the comment.

7.2.6.5 Comment 5

Prof. Gedney: *Page 77: "For lower frequencies, enforcement of current continuity greatly influences the accuracy of the RWG-via-LCN method where the LCN method fails to provide satisfactory performance."*

Comment: The phenomena shown in Fig. 3.6 is interesting. Though, this would not be consistent with results shown for smoother discretizations in Chapters 4 and 5 of the dissertation, nor with my experience with curvilinear patches. It appears that a low-frequency break down of the LCN discretization of the EFIE is being accelerated by the flat faceted patch. While it is true that the lack of current continuity for the LCN method is the reason for this, the faceted geometry is amplifying this error. In normal LCN, one would use a curvilinear patch, and would control the geometry error. Hence, by not doing so Rohklin's dogmas 2 and 3 are being violated! I think

that this should be discussed in the text. Secondly, due to the facet angles, the LCN method is modeling charge density that accumulates at the edges. This is fictitious for the sphere, but not for a faceted geometry with corners. I would be curious to see how your results change for smooth patching. **Response:** Addressing this comment needs modification to the developed RWG-via-LCN C++ code and further numerical results are needed. Such study would in fact be interesting. However, as part of the code used during this Ph.D. program is now under restrictions by the government of Canada, we are unable to conduct this study.

7.2.7 Chapter 4: Exact Relationship between the Locally Corrected Nyström Scheme and RWG Moment Method for the Mixed-Potential Integral Equation

Prof. Gedney: *This is an interesting chapter that progresses from the previous chapter, applying a mapping from a LCN discretization to an RWG method for the mixed potential integral equation (MPIE). What is interesting here is that the scalar potential part of the MPIE receives a different LCN discretization for the vector potential and the scalar potential contributions. The two LCN matrices are then mapped to the MoM impedance matrix using appropriate transformations. This is interesting, and the first that I have seen this.*

What is most interesting in this study is the impact on the low-frequency breakdown of the LCN operator. Not surprisingly, the breakdown is associated with the scalar potential term. It is determined that the chief source of the loss of accuracy is in the line integrals that result from transfer of the divergence from the current onto the Green's function. The author nicely demonstrates that errors in the line integral are greatly amplified. This is consistent with my experience that the line integrals have

a large contribution to the scalar potential piece of the kernel, and that cancellation error can be critical. The author indicates that additional error is due to the low order approximation of the test integrals, where additional precision is lost at lower frequencies. It appears that this is amplified by the use of a faceted mesh. **Response:** Thank you for your comment. To the best of our knowledge, the important study of the error in the line charge contributions of RWG MoM for both vector-potential and mixed-potential EFIEs can only be found in this chapter which is a reprint of [132] and at the time of this writing is not available elsewhere in the EM literature.

7.2.8 Chapter 5: On Achieving High-Order Convergence to the Correct Answer with the Locally Corrected Nyström Method

Prof. Gedney: *This is a very interesting contribution. The most important being equation* (5.22) *(Though, it seems there has to be a simpler derivation of this!), which allows the prediction of the number of unknowns required to achieve a desired level of accuracy for a given order. The use of this to predict an optimal order in terms of unknowns is quite interesting, and the validation of this for the MFIE with the exact sphere mesh is also very nicely done. I have some remaining questions and comments.* **Response:** There may be a simpler derivation of (5.22) but this particular derivation was chosen to also result in (5.16), which is a more general case of (16) in [1].

7.2.8.1 Comment 1

Prof. Gedney: *When solving the large sphere problem, the integration error was set to a very low tolerance, and an exact mesh was used. Both of these were set very*

conservatively such that the error observed was due to the discretization. However, due to the problem size, I have to assume that a fast solver was used. Thus, how was the error in the FMM solution contained? That is, what were the group sizes used? How was it ensured that non-touching near neighbor reactions were performed to the desired precision? **Response:** For LCN large scale examples shown in this chapter the multilevel fast multiple algorithm (MLFMA) was used based on [1]. This is mentioned in the text. Therefore, one can refer to [1] for such detail.

Prof. Gedney: *Also, what was the residual error used for the convergence of the iterative solution? Or, was this solved using a direct solver? Some details on this seem necessary.* **Response:** The residual error used for the convergence of the iterative solution was set conservatively as pointed out in the comment. It was set to 10^{-6}.

7.2.8.2 Comment 2

Prof. Gedney: *Predicting the optimal number of unknowns is very useful in that it bounds the memory required for the solution using a direct solver. However, when using fast solvers, this actually does not necessarily optimize memory. For SIE methods, the near field block will grow as $\mathcal{O}(p^2)$. Also, as the desired error is dropping, the group dimension of the FMM octree will also need to increase to ensure desired accuracy. This also will increase memory.* **Response:** These are valid points and should be addressed in a more general study. However as this dissertation does not study MLFMA and only use it for proof of concepts where large scale examples are needed, we considered such effects beyond the scope of this dissertation. Nevertheless, as pointed out in the comment, finding the minimum value of N for a desired accuracy of the solution using a direct solver is important and might substantially increase the

efficiency of CEM when fast direct solvers [10, 12, 14, 84] are used.

7.2.8.3 Comment 3

Prof. Gedney: *From a practical point of view, there are other metrics that are not necessary optimized simultaneously with N. This would include the CPU time. Higher orders of p typically lead to larger compute times for the near field blocks that group larger than $\mathcal{O}(N)$ due to the larger size of the element matrices and the increased number of basis per cell. Also, as the tolerance is dropped, the adaptive quadrature integrations take longer to converge. The error tolerance of fast solvers must also be decreased. This requires larger group dimensions and an increased number of spectral angles. Without a question, this is a more complex problem, but one that comes into play. Finally, higher-orders p lead to higher condition numbers, which leads to an increase in the number of iterations in the iterative solver.* **Response:** The same response made for the previous comment can be applied here.

7.2.8.4 Comment 4

Prof. Gedney: *On page 137, the comment is made: "Our HO LCN implementation is also unable to exhibit $\epsilon = \mathcal{O}(h^{2(p+1)})$ for the EFIE and CFIE even if the criteria is met. In fact, due to the non-self-adjoint nature of the electromagnetic integral operators, it is difficult (if not impossible) to derive a general closed form expression for the error convergence [18]. Therefore neither of h^p or $h^{2(p+1)}$ can be used in practical examples" (underline added.); This sentence seems to imply that the analysis provided cannot be applied to the EFIE or CFIE. Is this true?* **Response:** The analysis provided can be applied to MFIE, EFIE, and CFIE which is made possible by the availability of the experimental finding of a and b in (5.10) explained in Sec-

tion 5.3.2. In fact, the example given in Section 5.3.3 uses CFIE to demonstrate the validation of the method.

Prof. Gedney: *If it is, then bullet item 1 in list on page 138 would not be applicable. Or are you trying to state that it is something other than these? This should be clarified.* **Response:** According to the response given above, the bullet item 1 in page 138 is applicable.

7.2.9 Chapter 6: On New Triangle Quadrature Rules for the Locally Corrected Nyström Method Formulated on NURBS Generated Bézier Surfaces in 3D

Prof. Gedney: *This chapter introduces the application of the LCN method to a NURBS discretization of a surface that have been represented by a combination of quadrilateral and triangular Bézier cells. A major focus of this effort is on the handling of the triangular Bézier cells by introducing a Newton-Cotes type of quadrature rule.*

The application of the LCN method to triangular cells is certainly more limited than to quadrilateral cells. As the author points out, this is due to the fact that for many triangle orders, optimal Gaussian quadrature rules do not yet exist for all orders that integrate to the desired degree with a triangle number. As a consequence, in the application of the LCN method, the local element matrices are typically under determined, requiring a pseudo-inverse, such as a minimum norm solution. Wildman and Weile suggest adding functions to square the system. However, this is limited to low orders, and not of practical value. We fairly routinely use mixed meshes. However, as pointed out by the author, it is best to minimize the number of triangles in your mesh. Also, as pointed out in this chapter, Newton-Cote's rules for triangles

do exist. Pete Silvester published a set of open rules in 1970. These rules provide the correct triangle number of points for a given order. However, the polynomial degree is the limiting factor.

The author presents a new type of Newton-Cotes rule. However, what is not clearly stated is that it is not a true triangle rule. Rather, it is a triangle rule that is developed for a degenerate quadrilateral. That is, it is custom fit to the Bézier triangles, which are degenerate quadrilaterals. The motivation for doing this is that if a standard Gauss-quadrature rule for a quadrilateral were used, there would be a clustering of points near the degenerate edge, leading to ill-conditioning of the system matrix. **Response:** It is now mentioned in the text that the proposed rules are applicable to Bézier triangles which are in the form of degenerate quadrilaterals.

7.2.9.1 Comment 1

Prof. Gedney: *I do have a concern about using degenerate quadrilaterals. That is, by definition, the Jacobian goes to zero at the degenerate (or singular) edge. As a consequence, the underlying basis, which is proportional to* $\frac{1}{\sqrt{(g)}}$*, is singular. Granted, this normalizes out due to the product of Jacobians. However, it is a concern. The effect of this appears to be lessened by the use of the proposed Newton-Cotes rule as opposed to a standard quadrilateral quadrature rule.* **Response:** The severe effect of conditioning issues (caused by the mentioned concern) when applying Gauss-Legendre rules on degenerate quadrilaterals was a motivation to this work. In fact if we try to formulate LCN on Bézier elements (which are in the form of degenerate quadrilaterals) with the product of 1D Gauss-Legendre rules, the EFIE will not produce meaningful results. However, the numerical results presented in this chapter show that by using the proposed Newton-Cotes rules for Bézier triangles (i.e. degenerate

quadrilaterals), although the Jacobian tends to zero right at the edge, its value is not severely decreased at the quadrature points (including the nearest quadrature point to the singular edge). Therefore, normalization of basis vectors to the Jacobian will not raise conditioning issues as it would have when existing Gaussian rules are applied to degenerate quadrilaterals.

7.2.9.2 Comment 2

Prof. Gedney: *One interesting thing about using degenerate quadrilaterals, is that the line integral resulting from the scalar potential term (c.f., (3.52)) along the degenerate edge (of zero length) is non-zero. Though, one has to be careful integrating this term b/c the ratio of the edge Jacobian (0) and the face Jacobian (also 0) must be done correctly. The author has obviously already figured that out.* **Response:** The issue of having a zero by zero division when computing a non-zero line integral over the singular edge is only valid for the value of absolute zero. The method introduced in Chapter 6 does not encounter such difficulty. This is because when computing the position vectors on the surface of a Bézier patch, due to the tolerance set at the geometry conversion from NURBS surfaces to Bézier patches (Section 6.3.1), the singular edge of a singular Bézier element does not have length of absolute zero but its length is close to the set tolerance. In this chapter this tolerance was set to 10^{-6}, and hence values of both surface and edge Jacobians at the singular edge of the singular Bézier elements are close to 10^{-6} and their ratio is valid and can numerically be computed. To make sure that this ratio is computed properly, the same integrations were carried out in dyadic form (over the surface without having to compute line integrals over the edges) and results matched with machine precision. Further experiments showed that if the tolerance is set to lower values such as 10^{-16},

this computation remains valid and does not pose numerical issues in the method. Nevertheless, to have a more robust implementation, it is recommended to analytically compute this ratio as was suggested in the comment, but it was not done for the presented numerical results of Chapter 6.

Prof. Gedney: *It is not clear if the order of the triangle is consistent with the order of the quadrilaterals. Namely, a* $[(p+1)\times(p+1)]$ *point Gaussian quadrature rule on a quadrilateral will integrate polynomials of degree* $2p+1$*, and at least for the MFIE should converge with order* $\mathcal{O}(h^{2(p+1)})$*. However, a p-th order Newton-Cotes rule on the triangle will only integrate polynomials of degree p, and will converge at best with order* $\mathcal{O}(h^{p+1})$*. Based on the theory presented in Chapter 5, then mixing a p-th order rule on quads with a p-th order NC rule on triangles, will lead to an inconsistent convergence rate. (At least this is what appears to have been done, and what is observed in Figs 6.7 and 6.8.) Would it not make more sense to use a* $(2p+1)$*-th order Newton-Cotes rule on the triangle in combination with p-th order rule on the quadrilateral?* **Response:** Very interesting issue raised here! In fact, only after this comment the inconsistent convergence rate was brought to our attention. Therefore it would make sense to apply this comment to results of the MFIE (Fig. 6.8). However, as discussed in Chapter 5, the convergence of LCN depends on many factors and would not always remains $\mathcal{O}(h^{2(p+1)})$. For example, the convergence rate of EFIE (Fig. 6.8) would remain less than $\mathcal{O}(h^{2(p+1)})$ regardless of the order of the triangle rules. Therefore in Chapter 6, it is assumed that the convergence rate is $\mathcal{O}(h^p)$ and triangle rules are applied accordingly. Moreover, as was suggested in Section 6.4.3, the order of each Bézier element can be chosen according to its size and $\mathcal{O}(h^p)$ making the order of each element according to the desired accuracy.

7.2.9.3 Comment 3

Prof. Gedney: *Observing Figures 6.7 and 6.8, it is clear that the triangle rules and the quadrilateral rules are converging with different rates. The case with only triangles (24 elements) is converging at a much slower rate than the case with mostly quadrilaterals (336 elements). On these two figures, if I extrapolate the 24 element case by choosing orders 3, 5, 7, 9 for the triangles to represent Nystrom orders p = 1, 2, 3, 4, respectively, you certainly get closer to the ideal slope. It would be very interesting to see how this impacts the 48, 96, and 336 element case.* **Response:** By comparing the results of Fig. 5.3 with Figs. 6.7 and 6.8, it can be realized that the low convergence rate of the 24 element cases in Figs. 6.7 and 6.8 is similar to the low convergence rate of the 6 element sphere in Fig. 5.3 with $h_{\max} = 3.85\lambda$ which is computed by Gauss-Legendre rules on quadrilateral elements. Therefore, not only the order of the rule applied to triangular elements has its effect on the convergence rate, the size of the elements is also important. Nevertheless, as was pointed out earlier, one might match the order of Newton-Cotes rules with Gauss-Legendre rules as was suggested in the comment.

Thank you for all the valuable comments. They definitely add to the quality of the work.

7.3 Future Works

Below are the possible research that can be conducted based on the author's experience and understandings that resulted from this research work.

1. Mathematically and numerically demonstrate that it is possible to use same converters as in Chapter 3 to convert first-order LCN to RWG MoM when dis-

cretizing the magnetic field integral equation (MFIE). Although never stated in this thesis or elsewhere, the equivalence established in Chapter 3, were initially developed based on MFIE formulation and numerical results confirmed the equivalence for the MFIE. Due to the *compact plus constant* nature of the MFIE operator however, the LCN method produces more accurate results than the EFIE at first order. Subsequently, we found that by converting MFIE's impedance matrix of the first-order LCN to RWG MoM, the accuracy of the solution degrades. The reason for it is perhaps due to the fact that RWG basis functions assume that the current is always normal to triangles' edges while the LCN method has covariant basis functions in both u and v directions and allow for arbitrary vector current on the surface of the triangle. Nevertheless, it is known that by combining the EFIE and the MFIE, the combined filed integral equation (CFIE) can be formulated. Therefore it would be an interesting future work to study the effect of current continuity for first-order LCN when discretizing the CFIE. It would then be interesting to compare the RWG-via-LCN discretization of the CFIE using both VP EFIE (Chapter 3) and the MP EFIE (Chapter 4).

2. Extend the work of Chapter 6 to show HO convergence to the correct answer for arbitrary geometries containing sharp edges. While such work might seem challenging, the infrastructure developed and tested in Chapter 6 has several characteristics that greatly motivates further work on this topic. First, it does show HO behaviour for arbitrary smooth geometries and by elimination, we know that the only reason for us not to have a practical general purpose HO BEM is to not properly handle sharp edges. Second, by knowing that a possible remedy to this problem is through *hp*-refinement [146] at the corners of the

geometry, the fact that NURBS facilitates on-the-fly h-refinement and HO LCN does so for the p-refinement, such a great accomplishment seem to be not-so-out-of-reach due to the progress made in this research program.

3. By looking at the work presented in Chapter 6, it is realized that the fact that the standard HO LCN does not require current continuity enforcement, the process of h-refinement is easily done by using the OpenNURBS library. Therefore, any future hp-refinement procedure, would rely on Bézier mesh that allow for non-aligned boundaries. However, current continuity enforcement techniques such as CLCN or continuity enforcing hierarchical basis functions [21], require to have matching edges throughout the mesh which are sometimes called *clean meshes*. This poses difficulty to enforce current continuity and at the same time perform hp-refinement. Nevertheless, is was shown in Chapter 6 that it is possible to enforce geometric G^2 continuity over the entire NURBS generated Bézier meshes. Therefore, it would be an interesting study to compare the performance of current continuity enforcing CLCN and the method introduced in Chapter 6 to see the effect of G^2 continuity (Chapter 6) versus C^1 continuity (CLCN) in the LCN discretization especially at HOs. If both techniques show similar performance, the latter is less preferred as it only allows for clean meshes, but if CLCN shows significant improvements, it would be a good idea to try to develop novel current continuity enforcing techniques that allows for non-aligned boundaries in the mesh.

4. There has been publications to handle dielectric materials by discretizing SIEs such as PMCHWT and Müller formulations using LCN [47, 48]. We are not entirely sure why these formulations were used in the previous work but an educated guess leads us to believe that these formulations have been used in

MoM and the authors in [47, 48] adopted these formulations due to their successful applications when discretized with MoM. However, it is important to note that these formulations were developed with the MoM discretization in mind and more generalized formulations are also available in the literature. For example, in [113], we successfully used the dielectric EFIE and MFIE formulations of [39] to model dielectric materials. This is despite the fact that these formulations do not lead to accurate results when discretized with RWG MoM. Our understanding is that due to the nature of RWG basis functions, these simpler formulations are not properly tested by RWG functions and thus one has to deal with more complicated (and probably more computationally expensive) PMCHWT and Müller formulations. The LCN method on the other hand has covariant basis functions in both dimensions of the surface parameters and can be used to discretize simple dielectric EFIE/MFIE formulations as demonstrated in [113]. A study that compares the performance of LCN discretization of PMCHWT, Müller, and CFIE formulations seem appropriate by studying the accuracy, number of unknowns, and other aspect of the pertinent schemes.

5. The abscissas of 1D Gaussian quadrature rules tend to concentrate near the edges and hence the maximum largest distance in a given order between any two points becomes larger than that of 1D Newton-Cotes rules. As a future work one can apply the product of 1D Newton-Cotes rules in Chapter 6 to quadrilateral elements and study the reduction in the number of unknowns due to the convergence criteria introduced in Chapter 5.

6. Although the current continuity enforcing CLCN [90] might be a discouragement towards generalizing the work of Chapter 3 to HOs, generalizing MP RWG-via-LCN of Chapter 4 to HOs would be an interesting future work as it uses the

MP EFIE rather than the VP EFIE inherent in HO LCN and HO CLCN. Such work will shed light on the advantages of discretizing the MP EFIE rather than VP EFIE at HOs using the point-based LCN method and might improve the performance of LCN/CLCN when arbitrary geometries are considered.

Saadi Shirazi, the 13th century Persian poet says[1]:

به پایان آمد این دفتر حکایت همچنان باقی به صد دفتر نشاید گفت شرح حال مشتاقی

It means that this text is over but the story goes on; even hundred texts might not be enough to describe the feelings of an enthusiast. This is exactly what I feel and in my opinion the Computational Electromagnetics has just begun!

[1]In Persian culture poets are alive by means of their poems! Hence the use of present tense verb.

References

[1] I. Jeffrey, J. Aronsson, M. Shafieipour, and V. Okhmatovski, "Error Controllable Solutions of Large Scale Problems in Elecromagnetics: MLFMA Accelerated Locally Corrected Nyström Solutions of CFIE in 3D," *IEEE Antennas Propag. Mag.* vol. 55, no. 3, pp. 294-308, June 2013.

[2] Frank La Rue, "Report of the Special Rapporteur on the promotion and protection of the right to freedom of opinion and expression" *Human Rights Council, General Assembly, United Nations,* Seventeenth session, Agenda item 3, May 2011.

[3] J. -M. Jin, "The Finite Element Method in Electromagnetics, 2nd ed." *New York: Wiley* 2002.

[4] A. Taflove and S. C. Hagness, "The Finite-Difference Time-Domain Method", 3rd ed. *Norwood: Artech House* 2005.

[5] W. C. Chew, J. - M. Jin, E. Michielssen, and J. Song, (ed.) *Fast and Efficient Algorithms in Computational Electromagnetics,* Norwood: Artech House, 2001.

[6] E. Bleszynski, M. Bleszynski, and T. Jaroszewicz, "AIM: Adaptive Inte-

gral Method for Solving Large-Scale Electromagnetic Scattering and Radiation Problems," *Radio Sci.,* lov. 31, no. 5, pp. 1225-1251, 1996.

[7] Hongwei Cheng, William Y. Crutchfield, Zydrunas Gimbutas, Leslie F. Greengard, J. Frank Ethridge, Jingfang Huang, Vladimir Rokhlin, Norman Yarvin, and Junsheng Zhao, "A Wideband Fast Multipole Method for the Helmholtz Equation in Three Dimensions," *J. Comp. Phys.* vol. 216, no. 1, pp. 300-325, July 2006.

[8] N. A. Gumerov and R. Duraiswami, *Fast Multipole Methods for the Helmholtz Equation in Three Dimensions,* Elsevier, Amsterdam, 2006.

[9] A. Boag, "Compression of the Method of Moments Matrices using the Non-Uniform Grid Approach," *Int. Conf. on Electromagnetics in Adv. Applications*, Turin, Italy, Sept. 2007.

[10] J. Shaeffer, "Direct Solve of Electrically Large Integral Equations for Problem Sizes to 1M Unknowns," *IEEE Trans. Antennas Propag.,* vol. 56, pp. 2306-2313, 2008.

[11] L. Greengard, D. Gueyffier, P. G. Martinsson, and V. Rokhlin, "Fast direct solvers for integral equations in complex three-dimensional domains," *Acta Numerica*, vol. 18, pp. 243-275, 2009.

[12] S. Borm, *Efficient Numerical Methods for Non-local Operators: H^2-Matrix Compression, Algorithms, and Analysis*, European Math. Soc.: EMS Tracts in Mathematics, vol. 14, Dec. 2010.

[13] R. J. Adams, Y. Xu, X. Xu, S. D. Gedney, and F. X. Canning, "Modular fast

direct electromagnetic analysis using local-global solution modes," *IEEE Trans. Antennas Propag.,* vol. 56, no. 8, pp. 2427-2441, Aug. 2008.

[14] H. Guo, J. Hu, E. Michielssen, "On MLMDA/Butterfly Compressibility of Inverse Integral Operators," *IEEE Antennas and Wireless Propag. Lett.*, vol.12, pp. 31-34, 2013.

[15] V. Rokhlin, "Rapid solution of integral equations of classical potential theory," *Journal of Computational Physics,* vol.60, no.2, pp. 187-207, Sep. 1985.

[16] S. Wandzura, "Fast methods for fast computers," Workshop on Fast Approximate Algorithms, Center for Scientific Computation and Mathematical Modeling, University of Maryland, April 19-30, 2004, online: *www.cscamm.umd.edu/programs/fam04/FastTalk_wandzura_fam04.pdf* (Accessed on March 1, 2014).

[17] M. Djordievic and B. M. Notaros, "Double higher order method of moments for surface integral equation modeling of metalic and dielectric antennas and scatterers," *IEEE Trans. Antennas Propag.,* vol. 52, pp. 2118-2129, Aug. 2004.

[18] S. D. Gedney, "On Deriving a Locally Corrected Nyström Scheme From a Quadrature Sampled Moment Method," *IEEE Trans. Antennas Propag.,* vol. 51, no. 9, p. 2402-2412, September 2003.

[19] L. F. Canino, J. J. Ottusch, M. A. Stalzer, J. L. Visher, and S. M. Wandzura, "Numerical solution of the Helmholtz equation in 2D and 3D using a high-order Nyström discretization," *J. Comp. Phys.* vol. 146, no. 2, pp. 627-663, 1998.

[20] B. M. Notaroš, "Higher Order Frequency-Domain Computational Electromag-

netics," *IEEE Trans. Antennas Propag.,* vol. 56, no. 8, pp. 2251-2276, Aug. 2008.

[21] E. Jorgensen, J. L. Volakis, P. Meincke, O. Breinbjerg, "Higher order hierarchical Legendre basis functions for electromagnetic modeling," *IEEE Trans. Antennas Propag.,* vol.52, no.11, pp.2985-2995, Nov. 2004.

[22] R. D. Graglia, D. R. Wilton, and A. F. Peterson, "Higher Order Interpolatory Vector Bases for Computational Electromagnetics," *IEEE Transactions on Antennas and Propagation,* **AP-45**, 3, March 1997, pp. 329-342.

[23] S. M. Rao, D. R. Wilton, and A. W. Glisson, "Electromagnetic Scattering by Surface of Arbitrary Shape," *IEEE Trans. Antennas Propag.,* vol. AP-30, no. 3, p. 409-418, May 1982.

[24] M. Vikram, H. Huang, B. Shanker, and T. Van, "A Novel Wideband FMM for Fast Integral Equation Solution of Multiscale Problems in Electromagnetics," *IEEE Trans. Antennas Propag.,* vol. 57, no. 7, pp. 2094-2104, July 2009.

[25] G. Kang, J. M. Song, W. C. Chew, K. Donepudi, and J. M. Jin, "A novel grid-robust higher-order vector basis function for the method of moments," *IEEE Trans. Antennas Propag.,* vol. 49, no. 6, p. 908-915, Jun 2001.

[26] K. C. Donepudi, J. Song, J. M. Jin, G. Kang, and W. C. Chew, "A Novel Implementation of Multilevel Fast Multipole Algorithm for Higher Order GalerkinÕs Method," *IEEE Trans. Antennas Propag.,* vol. 48, no. 8, pp. 1192-1197, Aug. 2000.

[27] G. C. Hsiao and R. E. Kleinman, "Mathematical Foundations for Error Estimation in Numerical Solutions of Integral Equations in Electromagnetics," *IEEE*

Transactions on Antennas and Propagation, vol. 45, no. 3, March 1997, pp. 316-328.

[28] R. J. Adams, "Physical and analytical properties of a stabilized electric field integral equation," *IEEE Transactions on Antennas and Propagation,* vol. 52, no. 2, February 2004, pp. 362-372.

[29] H. Contopanagos, B. Dembart, M. Epton, J. Ottusch, V. Rokhlin, J. Visher, and S. M. Wandzura, "Well-conditioned boundary integral equations for three-dimensional electromagnetic scattering," *IEEE Transactions on Antennas and Propagation,* vol. 50, no. 12, December 2002, pp. 1824-1930.

[30] Y. Zhang, T. K. Sarkar, X. Zhao, D. Garcia-Donoro, W. Zhao, M. Salazar, and S. Ting, *Higher Order Basis Based Integral Equation Solver (HOBBIES).* Hoboken, NJ: Wiley, 2012.

[31] Altair Engineering Inc., Stellenbosch, South Africa, "FEKO," Oct. 2, 2015 [Online]. Available: www.feko.info

[32] Sonnet Software Inc., New York, USA, "Sonnet Suites," Oct. 2, 2015 [Online]. Available: www.sonnetsoftware.com/products/sonnet-suites

[33] V. Okhmatovski, M. Yuan, I. Jeffrey, R. Phelps "A Three-Dimensional Pre-corrected FFT Algorithm for Fast Method of Moments Solutions of the Mixed-Potential Integral Equation in Layered Media ," *IEEE Trans. Microwave Theory and Techniques.,* vol. 57, no. 12, pp. 3505-3517, Dec. 2009.

[34] B. Kolundzija and D. Sumic, "Electromagnetic simulation of complex and electrically large structures in WIPL-D Pro [Application Notes]," *IEEE Microw. Mag.,* vol. 9, no. 6, pp. 159-162, Dec. 2008.

[35] CEMWorks Inc., Winnipeg, Canada, "Wave3D," Jul. 18, 2014 [Online]. Available: www.cemworks.com

[36] PTC ,Software & Solutions "PTC Mathcad," Mar. 29, 2016 [Online]. Available: www.ptc.com/engineering-math-software/mathcad

[37] Compute Canada, WestGrid Canada, "Grex," Oct. 4, 2015 [Online]. Available: www.westgrid.ca/support/systems/Grex/

[38] R. P. Crease, "The great equations", *W. W. Norton & Company, New York, USA,* 2010.

[39] A. F. Peterson, S. L. Ray, and R. Mittra, "Computational Methods for Electromagnetics." *New York: IEEE Press* 1998.

[40] C. T. Tai, "Dyadic Green Functions in Electromagnetic Theory (2nd edition)." *New York: IEEE Press* 1994.

[41] C. T. Tai, "Generalized Vector and Dyadic Analysis (2nd edition)." *New York: IEEE Press* 1997.

[42] J. A. Stratton, "Electromagnetic Theory." *New Jersey: IEEE Press* 2007.

[43] Maxwell's Equations, Feb. 19, 2014 [Online]. Available: www.maxwells-equations.com

[44] M. Shafieipour, I. Jeffrey, J. Aronsson, and V. Okhmatovski, "On the Equivalence of RWG Method of Moments and the Locally Corrected Nyström Method for Solving the Electric Field Integral Equation," *IEEE Transactions on Antennas and Propagation*, vol. 62, no. 2, pp. 772-782, Feb. 2014.

[45] M. Shafieipour, I. Jeffrey, J. Aronsson, and V. Okhmatovski, "Exact Relationship between the Locally Corrected Nyström Scheme and RWG Moment Method for the Mixed-Potential Integral Equation," *IEEE Trans. Antennas Propag.,* vol. 63, no. 11, pp. 4932-4943, Nov. 2015.

[46] A. F. Peterson, "Accuracy of Currents Produced by the Locally-Corrected Nyström Method and the Method of Moments when used with Higher-Order Representations," *Applied Computational Electromagnetics Society (ACES) Journal,* vol. 17, pp. 74-83, Mar. 2002.

[47] S. D. Gedney, A. Zhu, and C. -C. Lu, "Study of Mixed-Order Basis Functions for the Locally Corrected Nyström Method," *IEEE Trans. Antennas Propag.,* vol. 52, no. 11, p. 2996-3004, Nov. 2004.

[48] A. Zhu, S. D. Gedney, and J. L. Visher, "A Study of Combined Field Formulations for Material Scattering for a Locally Corrected Nyström Discretization," *IEEE Trans. Antennas Propag.,* vol. 53, no. 12, p. 4111-4120, Dec. 2005.

[49] V. Rawat, J. P. Webb, "Scattering From Dielectric and Metallic Bodies Using a High-Order, Nyström, Multilevel Fast Mutipole Algorithm," *IEEE Trans. Magnetics,* vol. 42, no. 4, p. 521-526, April 2006.

[50] W. H. Press, S. A. Teukolsky, W. T. Vetterling, B. P. Flannery, "Numerical Recipes 3rd Edition: The Art of Scientific Computing." *Cambridge University Press* 2007.

[51] V. Okhmatovski, M. Yuan, I. Jeffrey, R. Phelps "A Three-Dimensional Precorrected FFT Algorithm for Fast Method of Moments Solutions of the Mixed-

Potential Integral Equation in Layered Media ," *IEEE Trans. Microwave Theory and Techniques.,* vol. 57, no. 12, pp. 3505-3517, Dec. 2009.

[52] E. J. Nyström, "Über die praktische Auflüsung von Integral-gleichungen mit Anwendungen auf Randwertaufgaben," *Acta Math.,* vol. 54, pp. 185-204, 1930.

[53] Gaussian Quadrature Weights and Abscissae, Feb. 21, 2016 [Online]. Available: pomax.github.io/bezierinfo/legendre-gauss.html

[54] Mapping a Cube to a Sphere, Mar. 15, 2016 [Online]. Available: mathproofs.blogspot.ca/2005/07/mapping-cube-to-sphere.html

[55] Andrew F. Peterson, and Malcolm M. Bibby "An Introduction to the Locally-Corrected Nyström Method" *Synthesis Lectures on Computational Electromagnetics: Morgan & Claypool* 2010.

[56] K. A. Michalski and D. Zheng, "Electromagnetic Scattering and Radiation by Surfaces of Arbitrary Shape in Layered Media, Part I: Theory," *IEEE Trans. Antennas Propag.,* vol. 38, no. 3, pp. 335-344, March 1990.

[57] P. P. Silvester and R. L. Ferrari, "Finite Element for Electrical Engineers," *Cambridge: Cambridge University Press* 1983, pp. 1-32, 73-88, 143-186.

[58] R. Penrose, "A generalized inverse for matrices," *Mathematical Proceedings of the Cambridge Philosophical Society.* 51 : pp. 406-413, 1955.

[59] D. R. Wilton, S. M. Rao, A. W. Glisson, D. H. Schaubert, O. M. Al-bundak and C. M. Butler, "Potential Integrals for Uniform and Linear Source Distributions on Polygonal and Polyhedral Domains," *IEEE Trans. Antennas Propag.,* vol. AP-32, no. 3, p. 409-418, Mar. 1984.

[60] M. G. Duffy, "Quadrature Over a Pyramid or Cube of Integrands with a Singularity at a Vertex," *SIAM J. Numer. Anal.,* vol. 19, pp. 1260-1262, Dec. 1982.

[61] M. A. Khayat, D. R. Wilton, and P. W. Fink, "An Improved Transformation and Optimized Sampling Scheme for the Numerical Evaluation of Singular and Near-Singular Potentials," *IEEE Antennas and Wireless Propag. Lett.*, vol. 7, pp. 377-380, 2008.

[62] F. Vipiana and D. R. Wilton, "Numerical Evaluation via Singularity Cancellation Schemes of Near-Singular Integrals Involving the Gradient of Helmholtz-Type Potentials," *IEEE Trans. Antennas Propag.,* vol. 61, no. 3, pp. 1255-1265, Mar. 2013.

[63] M. Al-Qedra, P. Saleh, F. Ling, V. Okhmatovski, "Barnes-Hut Accelerated Capacitance Extraction Via Locally Corrected Nyström Discretization," *2006 IEEE Electrical Performance of Electronic Packaging,* pp. 107-110, Oct. 2006.

[64] R. Coifman, V. Rokhlin, and S. Wandzura, "The Fast Multipole Method for the Wave Equation: A Pedestrian Prescription," *IEEE Antennas Propag. Mag.* vol. 35, no. 3, pp. 7-12, June 1993.

[65] R. F. Harrington, "Time-Harmonic Electromagnetic Fields," *New York: McGraw-Hill* 1961.

[66] R. F. Harrington, *Field Computation by Moment Methods.* New York: IEEE Press, 1993.

[67] O. Ergül and L. Gürel, *The Multilevel Fast Multipole Algorithm (MLFMA)*

for Solving Large-Scale Computational Electromagnetics Problems. Wiley-IEEE Press, 2014.

[68] V. Okhmatovski, M. Shafieipour, and J. Aronsson, "New Era Algorithms and Supercomputers: Forging the Third Industrial Revolution," *G20 Youth Forum 2014 Conference,* Garmisch-Partenkirchen, Germany, May 7-11, 2014.

[69] M. Shafieipour, J. Aronsson, C. Niu, I. Jeffrey, and V. Okhmatovski, "Error-controllable higher-order electromagnetic analysis of complex 3D interconnects with boundary element Locally Corrected Nyström method," *2014 IEEE 18th Workshop on Signal and Power Integrity (SPI),* Ghent, Belgium, May 2014.

[70] J. Aronsson, M. Shafieipour, and V. Okhmatovski, "Solution of large multi-scale EMC problems with method of moments accelerated via low-frequency MLFMA," *IEEE Intl. Symp. Electromagnetic Compatibility,* Long Beanch, CA, August 2011.

[71] J. Aronsson, M. Shafieipour, and V. Okhmatovski, "Study of Preconditioners For RWG MoM Analysis of Large Scale Scatterers Containing Junctions with Open Surfaces and Delta-Gap Voltage Sources," *Applied Computational Electromagnetic Society,* Columbus, OH, April 2012.

[72] A. Zhu, S. D. Gedney, and J. L. Visher, "A Study of Combined Field Formulations for Material Scattering for a Locally Corrected Nyström Discretization," *IEEE Trans. Antennas Propag.,* vol. 53, no. 12, p. 4111-4120, Dec. 2005.

[73] J. L. Tsalamengas, "Exponentially Converging Nystrom Methods in Scattering From Infinite Curved Smooth Strips-Part 1: TM-Case," *IEEE Trans. Antennas Propag.,* vol. 58, no. 10, pp. 3265-3274, Oct. 2010.

[74] J. L. Tsalamengas, "Exponentially Converging Nystrom Methods in Scattering From Infinite Curved Smooth Strips-Part 2: TE-Case," *IEEE Trans. Antennas Propag.,* vol. 58, no. 10, pp. 3275-3281, Oct. 2010.

[75] K. Butt, I. Jeffrey, M. Al-Qedra, L. Feng, and V. Okhmatovski, "Accurate capacitance extraction in the entire package model using a parallel kernel independent hierarchical extractor," *IEEE Workshop on Signal Propagation on Interconnects (SPI),* Ruta Di Camogli (Genova), Italy, May 13Ð16, 2007.

[76] AA Kishk and L. Shafai, "Different formulations for numerical solution of single or multibodies of revolution with mixed boundary conditions," *IEEE Trans. Antennas Propag.,* vol. 34, no. 5, pp. 666-673, May 1986.

[77] J. -M. Jin, *The Finite Element Method in Electromagnetics,* 2nd ed. New York: Wiley, 2002.

[78] A. Taflove and S. C. Hagness, *The Finite-Difference Time-Domain Method,* 3rd ed. Norwood: Artech House, 2005.

[79] A. Skarlatos, R. Schuhmann, and T. Weiland, "Solution of radiation and scattering problems in complex environments using a hybrid finite integration technique - uniform theory of diffraction approach," *IEEE Trans. Antennas Propag.,* vol. 53, no. 10, pp. 3347-3357, Oct. 2005.

[80] C. T. Tai, *Dyadic Green Functions in Electromagnetic Theory,* 2nd ed. New York: IEEE Press, 1994.

[81] V. Okhmatovski, J. Aronsson, and L. Shafai, "A well-conditioned non-iterative approach to solution of the inverse problem," *IEEE Trans. Antennas Propag.,* vol. 60, no. 5, pp. 2418-2430, Mar. 2012.

[82] F. P. Andriulli, K. Cools, H. Bagci, F. Olyslager, A. Buffa, S. Christiansen, and E. Michielssen, "A Multiplicative Calderon Preconditioner for the Electric Field Integral Equation," *IEEE Trans. Antennas Propag.,* vol. 56, no. 8, p. 2398-2412, Aug. 2008.

[83] W. Chew, M. -S. Tong, and B. Hu, *Integral Equation Methods for Electromagnetic and Elastic Waves.* Morgan & Claypool Publishers, 2008 (Updated 2012).

[84] W. Chai and D. Jiao, "Fast *calH*-Matrix-Based Direct Integral Equation Solver With Reduced Computational Cost for Large-Scale Interconnect Extraction," *IEEE Trans. Compo., Packag. and Manuf. Technol.,* vol. 3, no. 2, pp. 289-298, Feb. 2013.

[85] J. -S. Zhao and W. C. Chew, "Integral equation solution of Maxwell's equations from zero frequency to microwave frequencies," *IEEE Trans. Antennas Propag.,* vol. 49, no. 10, pp. 1635-1645, Oct. 2000.

[86] V. Okhmatovski, J. Morsey, and A.C. Cangellaris, "Loop-tree implementation of the adaptive integral method (AIM) for numerically-stable, broadband, fast electromagnetic modelling," *IEEE Trans. Antennas Propag.,* Vol. 52, No. 8, pp. 2130-2140, Oct. 2000.

[87] F. Vipiana, and M. A. Francavilla, "EFIE Modeling of High-Definition Multiscale Structures," *IEEE Trans. Antennas Propag.,* vol. 58, no. 7, pp. 2362-2374, Jul. 2010.

[88] J. C. Young, Y. Xu, R. J. Adams, and S. D. Gedney, "High-Order NystrŽm

Implementation of an Augmented Electric Field Integral Equation," *IEEE Antennas Wire. Propag. Lett.* vol. 11, pp. 846-849, 2012.

[89] M. Shafieipour, I. Jeffrey, J. Aronsson, and V. I. Okhmatovski, "On the Equivalence of RWG Method of Moments and the Locally Corrected Nyström Method for Solving the Electric Field Integral Equation," *IEEE Trans. Antennas Propag.,* vol. 62, no. 2, pp. 772-782, Feb. 2014.

[90] N. Hendijani, J. Cheng, R. J. Adams, and J. C. Young, "Constrained Locally Corrected Nyström Method," *IEEE Trans. Antennas Propag.,* In Press.

[91] C. A. Balanis, *Advanced Engineering Electromagnetics,* 2nd ed. Hoboken, NJ: Wiley, 2012.

[92] J. G. Van Bladel, *Electromagnetic Fields,* 2nd ed. Wiley-IEEE Press, May 2007.

[93] H. Mang, L. Jinbo, and Z. Kang, "Improving the Spherical Harmonics Expansion-Based Multilevel Fast Multipole Algorithm (SE-MLFMA)," *IEEE Antennas and Wireless Propag. Lett.*, vol. 12, pp. 551-554, 2013.

[94] D. T. Schobert and T. F. Eibert, "Fast Integral Equation Solution by Multilevel Green's Function Interpolation Combined With Multilevel Fast Multipole Method," *IEEE Trans. Antennas Propag.,* vol. 60, no. 9, pp. 4458-4463, Sept. 2012.

[95] B. M. Kolundzija, M. S. Pavlovic, and B. Mrdakovic, "Optimum choice of currents' expansion order in MLFMM algorithm for electromagnetic scattering," *IEEE Intl. Symp. Antennas Propag. Society (APS/URSI),* pp. 1-4, 2009.

[96] M. Djordjević, and B. M. Notaroš, "Double Higher Order Method of Moments for Surface Integral Equation Modeling of Metallic and Dielectric Antennas and Scatteres," *IEEE Trans. Antennas Propag.,* vol. 52, no. 8, pp. 2118-2128, Aug. 2004.

[97] Haobo Yuan, Nan Wang, and Changhong Liang, "Combining the higher order method of moments with geometric modelling by NURBS Surfaces," *IEEE Trans. Antennas Propag.,* vol. 57, no. 11, pp. 3558-3563, November 2000.

[98] L. R. Hamilton, J. J. Ottusch, M. A. Stalzer, R. S. Turley, J. L. Visher, and S. M. Wandzura, "Numerical Solution of 2-D Scattering Problems Using High-Order Methods," *IEEE Trans. Antennas Propag.,* vol. 47, no. 4, p. 683-691, Apr. 1999.

[99] B. Lai, H. B. Yuan, and C. H. Liang, "NURBS Surfaces Modeled Locally Corrected Nystrom Method," *Microw. Opt. Technol. Lett.,* vol. 53, no. 7, pp. 1637-1638, 2011.

[100] L. Valle, F. Rivas, and M. F. Cátedra, "Combining the moment method with geometrical modelling by NURBS surfaces and Bézier patches," *IEEE Trans. Antennas Propag.,* vol. 42, no. 3, pp. 373-381, March 1994.

[101] B. Sklar, "Digital Communications Fundamentals and Applications, 2nd ed." *Prentice-Hall, Inc. : Upper Saddle River, New Jersey 07458* 2001.

[102] P. B. Lathi, "Modern Digital and Analog Communication Systems, 3rd ed." *Oxford University Press, Inc. : 198 Madison Avenue, New York, New York 10016* 1998.

[103] F. Marvasti, "Nonunifonn Sampling: Theory and Practice" *Kluwer Academic/Plenum Publishers* 2001.

[104] R. Scholte, B. Roozen, and I. Lopez, "On Spatial Sampling and Aliasing In Acoustic Imaging," *Twelfth International Congress on Sound and Vibration,* ICSV12 Libson, 11-14 July, 2005.

[105] Y. Miyazaki, "Spatial Sampling Characteristics of Beam Wave Eigen Functions Representation for Optical CT," *PIERS Proceedings,* Kuala Lumpur, Malaysia, March 27-30, 2012.

[106] Christophe Geuzaine and Jean-FranDois Remacle, *"Gmsh,"* Feb. 24, 2014 [Online]. Available: www.geuz.org/gmsh/

[107] A. F. Peterson, D. R. Wilton, and R. E. Jorgenson, "Variational Nature of Galerkin and Non-Galerkin Moment Method Solutions," *IEEE Trans. Antennas Propag.,* vol. 44, no. 4, pp. 500-503, Apr. 1996.

[108] F. G. Lether "Cubature Error Bounds for Gauss-Legendre Product Rules," *SIAM J. Numer. Anal.,* vol. 8, no.1 , pp. 36-42, Mar. 1971.

[109] M. Shafieipour, J. Aronsson, and V. Okhmatovski, "On Error Controlled Computing of the Near Electromagnetic Fields in the Shade Regions of Electrically Large 3D Objects," *International Symposium on Electromagnetic Theory,* Espoo, Finland, Aug. 2016. (Accepted)

[110] A. Alu and N. Engheta, *Theory of linear chains of metamaterial/plasmonic particles as subdiffraction nanotransmission lines*, Physical Review B, v. 74, no. 205436, pp. 1-18, 2006.

[111] M. G. Silveirinha, A. Alu, J Li, and N. Engheta, "Nanoinsulators and nanoconnectors for optical nanocircuits," *Journal of Applied Physics,* vol.103, no.6, 2008.

[112] N. J. Halas, S. Lal, W. S. Chang, S. Link, and P. Nordlander, "Plasmons in Strongly Coupled Metallic Nanostructures," *Chemical Reviews,* vol. 111, pp. 3913-3961, 2011.

[113] M. Shafieipour, and V. Okhmatovski, "Error-Controlled Boundary Element Modeling of 3D Plasmonic Nano-Structures via Higher-Order Locally Corrected Nyström Method," *IEEE Antennas and Propagation Society International Symposium,* Vancouver, BC, Canada, July 2015.

[114] D. Weston, *Comparison of Techniques for Prediction and Measurement of Antenna to Antenna Coupling on an Aircraft*, York, UK, EMC Europe, 2011.

[115] Doug Richardson, *Stealth Warplanes: Deception, Evasion, and Concealment in the Air*, MBI Publishing Company, New York, 2001.

[116] S. Cadirci, "RF Stealth (Or Low Observable) and Counter-RF Stealth Technologies: Implications of Counter-RF Stealth Solutions for Turkish Air Force," *M.Sc. Thesis*, Naval Postgraduate School, Monterey, CA, 2009.

[117] R. K. Mongia and P. Bhartia, "Dielectric Resonator Antennas - A Review and General Design Relations for Resonant Frequency and Bandwidth," *International Journal of RF and Microwave Computer-Aided Engineering*, **4**, 3, July 1994, pp. 230-247.

[118] D. Kaifez and P. Guillon, *Dielectric Resonators*, Dedham, MA: Artech, 1986.

[119] Jun Yan, Jun Hu, and Zaiping Nie, "Calculation of the Physical Optics Scattering by Trimmed NURBS Surfaces," *IEEE Trans. Antennas Propag.,* vol. 61, no. 8, pp. 4194-4203, 2013.

[120] Xi Chen, Si-Yuan He, Ding-Feng Yu, Hong-Cheng Yin, Wei-Dong Hu, and Guo-Qiang Zhu, "Geodesic Computation on NURBS Surfaces for UTD Analysis," *IEEE Antennas Wire. Propag. Lett.* vol. 12, no., pp. 194-197, 2013.

[121] Z. L. Liu, and J. Yang, "Analysis of electromagnetic scattering with higher-order moment method and NURBS model," *Progress In Electromagnetics Research (PIER),* vol. 96, pp. 83-100, 2009.

[122] L. Piegl, and W. Tiller, "The NURBS Book." *Berlin Heidelberg: Springer-Verlag* 1996.

[123] G. E. Farin, "NURBS from Projective Geometry to Practical Use, 2nd ed." *A K Peters, Ltd. : Natick, MA, USA* 1999.

[124] J. S. M. Vergeest, "CAD surface data exchange using STEP," *Computer-Aided Design, Elsevier* vol. 23, no. 4, pp. 269-281, May 1991.

[125] Robert McNeel & Associates., Seattle, USA, *"Rhinoceros3D,"* Feb. 14, 2014 [Online]. Available: www.en.na.mcneel.com

[126] Autodesk Inc., *"AutoCAD software,"* Mar. 24, 2014 [Online]. Available: www.autodesk.com

[127] J. N. Lyness and D. Jespersen, "Moderate degree symmetric quadrature rules for the triangle," *J. Inst. Math. Appl.* vol. 15, pp. 19-32, 1975.

[128] S. Wandzurat, H. Xiao, "Symmetric quadrature rules on a triangle", *Computers & Mathematics with Applications,* Volume 45, Issue 12, June 2003, Pages 1829-1840, ISSN 0898-1221.

[129] D. A. Dunavant, "High degree efficient symmetrical gaussian quadrature rules for the triangle," *Int. J. Numer. Meth. Eng.,* vol. 21, pp. 1129-1148, 1985.

[130] F. Caliskan and A. F. Peterson, "The need for mixed-order representations with the locally corrected Nyström method," *IEEE Antennas Wire. Propag. Lett.* vol. 2, no. 1, pp. 72-73, 2003.

[131] R. A. Wildman and Daniel S. Weile, "Mixed-Order Testing Functions on Triangular Patches for the Locally Corrected Nyström Method," *IEEE Ant. Wire. Propag. Let.,* vol. 5, no. 1, pp. 370-372, Dec. 2006.

[132] M. Shafieipour, I. Jeffrey, J. Aronsson, and V. Okhmatovski, "Exact Relationship between the Locally Corrected Nyström Scheme and RWG Moment Method for the Mixed-Potential Integral Equation," *IEEE Trans. Antennas Propag.,* In Print.

[133] Daan Huybrechs, "Stable high-order quadrature rules with equidistant points", *Journal of Computational and Applied Mathematics,* Volume 231, Issue 2, 15 September 2009, Pages 933-947, ISSN 0377-0427.

[134] P. Silvester, "Symmetric quadrature formulae for simplexes," *Mathematics of Computations,* vol., no., pp. 95-100, 1970.

[135] J. S. Savage, and A. F. Peterson, "Quadrature rules for numerical integration over triangles and tetrahedra," *IEEE Antennas Propag. Mag.* vol. 38, no. 3, pp. 100-102, June 1996.

[136] M. Abramowitz and I. A. Stegun, "Handbook of Mathematical Functions with Formulae, Graphs, and Mathematical Tables" *New York: Dover* 1972.

[137] A. F. Peterson, D. L. Faircloth, and T. N. Killian, "The Nyström Method Applied to Arbitrary Three-Dimensional Conductors Using NURBS-Based Triangular Patches," *IEEE Antennas and Propagation Society International Symposium,* Toronto, Ontario, Canada, 11-17 July 2010.

[138] M. G. Cox, "The numerical evaluation of B-splines," *IMA Journal of Applied Mathematics* vol. 10, pp. 134-149, 1972.

[139] Zhao Shufeng, "A Practical Method to Construct G1/G2 Continuous NURBS Patches," *Journal of Engineering Graphics* vol. 2, pp. 105-115, 2003.

[140] David F. Rogers, "An Introduction to NURBS: With Historical Perspective" *Morgan Kaufmann, 1 edition* July 21, 2000.

[141] C. de Boor, "A Practical Guide to Splines" *Springer* 1978.

[142] K. Spitzmüller, "Technical note - Partial derivatives of Bézier surfaces," *Computer-Aided Design, Elsevier* vol. 28, No. 1, pp. 67-72, 1996.

[143] Robert McNeel & Associates., Seattle, USA, *"openNURBS,"* Feb. 24, 2014 [Online]. Available: www.rhino3d.com/opennurbs

[144] Gene H. Golub and James M. Ortega, "Scientific Computing and Differential Equations: An Introduction to Numerical Methods" *Academic Press* 1991.

[145] Constantine A. Balanis, "Antenna Theory: Analysis and Design," *Wiley-Interscience, 3 edition* April 4, 2005.

[146] X. Dong, L. Demkowicz, and H. Ling, "A 3-D hp Finite/Infinite Element Method to Calculate Power Deposition in the Human Head," *IEEE Trans. Biomed.,* vol. 54, no. 4, pp. 734-741, April 2007.

[147] M. Shafieipour, J. Aronsson, I. Jeffrey, C. Nui, and V. Okhmatovski„ "On New Triangle Quadrature Rules for the Locally Corrected Nyström Method Formulated on NURBS Generated Bézier Surfaces in 3D," *IEEE Trans. Antennas Propag.,* (Under Review) 2016.